
PARTICLE ACCELERATION IN YOUNG SUPERNOVA REMNANTS
WITH NONTHERMAL X-RAY AND GAMMA-RAY OBSERVATIONS

NAOMI TSUJI

PH.D. THESIS

*DEPARTMENT OF PHYSICS
GRADUATE SCHOOL OF SCIENCE
RIKKYO UNIVERSITY*

NISHI IKEBUKURO, TOSHIMA-KU, TOKYO, 171-8501, JAPAN



JANUARY, 2020

Abstract

A supernova remnant (SNR) is a prominent candidate as an accelerator of galactic cosmic rays (CRs). In a widely accepted theory of diffusive shock acceleration (DSA), a particle is accelerated by diffusing back and forth across shock waves. The information on ongoing particle acceleration in shock waves of SNRs is accessible through observations of nonthermal radiation. The spectral cutoff shape of accelerated electrons is determined by diffusion and cooling and appears in the X-ray and TeV gamma-ray energy ranges, respectively, through synchrotron radiation and inverse Compton (IC) scattering. To measure the cutoff shape precisely and explore the corresponding diffusion coefficient and acceleration efficiency, we systematically analyze young SNRs that emit nonthermal X-rays and TeV gamma-rays to obtain a unified understanding of particle acceleration in SNRs.

The nonthermal (synchrotron) X-ray spectrum provides us with a powerful means of studying the nature of particle (electron) acceleration in a shock wave formed at the surface of an SNR. If energy loss of synchrotron cooling is efficient, the electron spectrum becomes steeper (E^{-3}) than predicted by the standard DSA (E^{-2}), and exponentially drops off ($\exp(-(E/E_0)^2)$) above the maximum energy of E_0 in the case of Bohm diffusion, where the diffusion coefficient, D , is proportional to the particle energy ($D \propto E^\alpha$ with $\alpha = 1$). In this thesis, the relevant synchrotron model is applied to 11 young SNRs. We measure the cutoff energy parameter (ε_0) in the synchrotron X-ray spectrum and estimate the Bohm factor (η) by a theoretically predicted relation of $\varepsilon_0 \propto v_{\text{sh}}^2 \eta^{-1}$, with v_{sh} being shock velocity. The η parameter is defined as a mean free path of an electron over its gyroradius and is indicative of acceleration efficiency (i.e., $\eta = 1$ indicates the most efficient acceleration derived from the minimum diffusion coefficient). We apply the method to the nonthermal X-ray spectra of 11 SNRs using broadband spectroscopy taken with *Chandra* and *NuSTAR*. The obtained ε_0 values and shock speeds from previous studies show variations that depend on SNRs and even on regions within each SNR. Six of 11 SNRs can be spatially resolved to investigate the ε_0 - v_{sh} relation, resulting in different behaviors of acceleration as follows: one behavior is well-reproduced through the theoretical prediction with a constant η (Kepler's and Tycho's SNRs), another behavior is determined based on the surroundings, in particular, magnetic field orientation (SN 1006) and ambient density (Cassiopeia A), and our cooling-limited assumption might not be applicable in the inner regions of the northwest rim of RX J1713.7-3946 and G1.9+0.3. With all 11 SNRs together, the η parameter tends to have a smaller value as the SNR evolves and becomes older. This evolution of acceleration efficiency could be related to turbulent production, which is expected to be self-generated by the accelerated particles.

We also apply the IC scattering model to the TeV gamma-ray observations of five SNRs. We found that in the same way as we derived the Bohm factor using X-ray observations, the gamma-ray spectrum was also utilized for estimating η in the leptonic scenario. Compared to the η parameters estimated by using X-ray observations, slightly higher values of η are obtained due to the smaller cutoff energies of electrons. The difference can be attributed to the different sizes of regions for spectral extraction between X-ray and gamma-ray observations. In addition, we should address the issue of the application of the IC (leptonic) model, in which gamma-rays are emitted from high-energy electrons, to the gamma-ray spectra that might contain hadronic components radiated from accelerated protons.

We construct a model for accelerated electrons in non-Bohm diffusion ($\alpha \neq 1$). The difference of α shows an apparent distinction in the cutoff shape of the electron spectrum as $\exp(-(E/E_0)^{\alpha+1})$, particularly in the higher energies. We derive the corresponding synchrotron and IC models to apply to nonthermal observations in X-rays and TeV gamma-rays, respectively. The models with different α values are not significantly distinguished due to the limited statistics of the present spectra in the higher energies. With deeper observations and/or a combination of X-ray and gamma-ray spectra with better spatial resolution, the α parameter would be more

constrained and provide feedback to theoretical studies of particle diffusion and turbulent generation.

Contents

1	Introduction	1
2	Review	3
2.1	Cosmic Ray	3
2.2	SNR paradigm	5
2.2.1	Supernova remnant	5
2.2.2	SNR paradigm	5
2.3	Particle acceleration	9
2.3.1	Shock wave	9
2.3.2	Diffusive shock acceleration	9
2.3.3	Acceleration timescale	11
2.3.4	Maximum attainable energy	11
2.4	Diffusion and turbulence	13
2.4.1	Diffusion	13
2.4.2	Turbulence	17
2.5	Radiation processes	21
2.5.1	Synchrotron radiation	21
2.5.2	Inverse Compton scattering	22
2.5.3	Bremsstrahlung	22
2.5.4	π^0 -decay	23
2.5.5	Broadband nonthermal radiation spectra	23
2.6	Spectral model around SNR shock	25
2.6.1	Spectral deformation	25
2.6.2	Electron	27
2.6.3	Synchrotron X-ray	31
2.6.4	Inverse Compton gamma-ray	34
2.6.5	Summary of leptonic models	36
3	Instruments	37
3.1	Chandra X-ray Observatory (<i>Chandra</i>)	37
3.1.1	High Resolution Mirror Assembly (HRMA)	37
3.1.2	Science Instrument Module (SIM)	37
3.2	Nuclear Spectroscopic Telescope Array (<i>NuSTAR</i>)	40
3.2.1	Optics module	40
3.2.2	Focal plane module	41
3.2.3	Detailed analysis of <i>NuSTAR</i>	42
3.3	TeV gamma-ray observation	49
3.3.1	Imaging Atmospheric Cherenkov Telescope	49
3.3.2	High Energy Spectroscopic System (H.E.S.S.)	50

4	Nonthermal X-ray observations of young supernova remnants: Bohm diffusion	53
4.1	Introduction	54
4.2	Observations and data reduction	55
4.3	Analysis and results	60
4.3.1	Images	60
4.3.2	Spectrum	65
4.4	Discussion	69
4.4.1	Cutoff energy v.s. shock speed	69
4.4.2	Acceleration efficiency in individual source	72
4.4.3	Acceleration efficiency in young SNRs	85
4.4.4	Limited by cooling or age?	89
4.4.5	Maximum attainable energy: Are SNRs PeVatrons?	90
4.5	Conclusions	91
5	Gamma-ray observations of young supernova remnants: Bohm diffusion	93
5.1	Gamma-ray observations	94
5.2	Spectral fitting and results	94
5.3	Discussion	97
6	Non-Bohm diffusion	101
6.1	Introduction	101
6.2	Model	103
6.2.1	Electron	103
6.2.2	Synchrotron X-ray	105
6.2.3	Inverse Compton gamma-ray	106
6.3	Nonthermal X-ray diagnostics	108
6.3.1	Application to X-ray observations and results	108
6.3.2	Discussion: Estimation of diffusion coefficient	111
6.4	Nonthermal gamma-ray diagnostics	115
6.4.1	Application to gamma-ray observations and results	115
6.4.2	Discussion: Comparison of X-ray and gamma-ray results	115
6.5	Conclusions	117
7	Summary and conclusions	121
Appendices		
A	Radiation spectrum from cutoff power-law electron	125
A.1	Synchrotron radiation	125
A.2	Inverse Compton in Thomson limit	127
B	Projection effect on proper-motion measurements	129
C	Synchrotron radiation in distributed field	133
C.1	Model	133
C.2	Application to observations	134
D	Inverse Compton scattering in Thomson regime	137
D.1	Thomson regime in Bohm diffusion	137
D.2	Thomson regime in non-Bohm diffusion	137
References		139

Chapter 1

Introduction

Astrophysical phenomena have attracted our attention and puzzled us for ages. Observations of electromagnetic (EM) waves, which are commonly employed in astronomy, have been utilized to explore ongoing astrophysical events far away from the Earth. Detected EM waves divide phenomena in the Universe into two types based on radiation mechanisms: a *thermal* process, which is characterized by a temperature in Maxwell distribution, and a *nonthermal* process, the energy distribution of which is described by a power-law form. Today, multi-wavelength EM observations range from radio to even TeV gamma-rays, allowing us to investigate the nature of the nonthermal Universe. In addition to classical means of observing EM radiation, recent successes in detecting neutrinos and gravitational waves have introduced a new era characterized by *multi-messenger* observations.

One unsolved astrophysical problem is the origin of cosmic rays (CRs), namely, nonthermal particles filling the Universe with energies ranging over 10 orders of magnitude from $\sim 10^9$ eV to $\sim 10^{20}$ eV. The power-law energy spectrum with the slope of -2.7 to -3.1 produces a bulk energy concentrated in a small number of high-energy CRs. Even after more than 100 years since the discovery in 1912, two simple questions regarding CRs remain unanswered — *where* do they come from and *how* do they obtain their energies? Many observational experiments have contributed to revealing that the CR energy spectrum has characteristic breaks at $\sim 10^{15}$ eV (“knee”) and $\sim 10^{18}$ eV (“ankle”). Recent improvements in instruments have updated the properties of the CR energy spectrum. Alpha Magnetic Spectrometer (AMS), which is a CR detector onboard International Space Station, has confirmed another spectral break and nonuniversal energy spectra of CRs (The AMS Collaboration, 2015b, 2014). Grand-based telescopes have revealed dipolar and hotspot-like features in the map of arrival directions of ultra high energy cosmic rays (UHECRs) (The Pierre Auger Collaboration, 2017; The Telescope Array Collaboration, 2018). Whereas progress has been made in producing more precise measurements of CRs in the vicinity of the Earth, multi-wavelength observations can shed light on the physics of particle acceleration at the sources.

The galactic cosmic rays with energies below the knee are believed to originate from supernova remnants (SNRs) in our galaxy. Electrons accelerated up to GeV and TeV energy ranges have been probed through detection of synchrotron photons in radio and X-ray energy bands, respectively. After the launch of *Fermi*, high-energy protons have also been confirmed by observing π^0 -decay features around the sub-GeV energy band. Recently, nonthermal particles in keV, MeV, and PeV can be accessible using the latest detectors: keV electrons were implied by the detection of X-ray nonthermal bremsstrahlung in W 49B (Tanaka et al., 2018), MeV particles (possible protons) were detected by neutral Fe line emission at 6.4 keV (Nobukawa et al., 2018), and PeV particles (possible protons) were found in the power-law spectrum in TeV gamma-rays without any sign of exponential cutoff (Abramowski et al., 2014).

Theoretical studies have been conducted accompanied by observations. A well-accepted theory of particle acceleration is diffusive shock acceleration (DSA). Based on the original idea proposed by Fermi (Fermi, 1949), it has been constructed that a particle stochastically gains energy by diffusing back and forth across a shock wave in an SNR (Axford et al., 1977; Krymskii, 1977; Blandford and Ostriker, 1978; Bell, 1978). Although DSA successfully produces high-energy particles and power-law energy distribution, many facets of this process remain ambiguous. Particularly the mechanisms of the start (“injection”) and end (“maximum energy”) of the process of DSA are not fully understood. The attainable maximum energy is determined by an acceleration

efficiency characterized by diffusion of particles. Because particles diffuse by being scattered with a turbulent magnetic field, the diffusion and turbulence are strongly related. The mechanism of turbulent production also remains unknown, and producing observational constraints is difficult. It has been theoretically predicted that the turbulence is self-generated by the cosmic ray, and instability of CR streaming enhances the field. This idea has been demonstrated by numerical calculations, including particle-in-cell simulations (e.g., Reville et al. (2008); Caprioli and Spitkovsky (2014a)).

The motion of cosmic ray is characterized by diffusion during the process in which a particle becomes cosmic ray, wherein the particle is accelerated at SNRs, escapes from the remnants at one moment, and propagates in the interstellar medium (ISM). The first step (acceleration) can be tested by EM observations and theories. Direct measurements of CR help to unveil the third step (identifying the properties of the propagation of the CR). As previously outlined, considerable progress has been made in measurements of CR near the Earth, EM observations of sources, and theories. However, we should address some gaps between them. One example is a spectral index: the directly measured CR shows that the energy spectrum of galactic cosmic rays approximately follows $\propto E^{-2.8}$, whereas the energy spectrum predicted by DSA is $\propto E^{-2}$. To fill the gaps, the diffusion of particles plays an important role. The diffusion coefficient at 1 TeV is roughly $10^{29} \text{ cm}^2 \text{ s}^{-1}$ in ISM, while it is expected to be $10^{24} \text{ cm}^2 \text{ s}^{-1}$ around the SNR shock, assuming Bohm diffusion. In addition, an interesting constraint on the escaping CR was lately reported by Abeysekara et al. (2017). They found “TeV halos” extended up to a radius of 20 pc around two nearby pulsars with a diffusion coefficient at 1 TeV of $10^{27} \text{ cm}^2 \text{ s}^{-1}$. After this new detection of a lower diffusion coefficient than that in the ISM, much attention has been drawn to the diffusion of particles around accelerators.

The diffusion in the vicinity of the SNR shock is a major factor in both the maximum energy achieved by the SNRs and the physics of particle acceleration. The attainable maximum energy would answer the critical question of the origin of galactic cosmic rays; whether the SNRs are indeed capable of accelerating particles up to the PeV energy band (“PeVatron”). Although PeVatron candidates have been reported in a few SNRs on the galactic plane (Abramowski et al., 2014; H. E. S. S. Collaboration, 2018a), most young SNRs have exponential cutoffs in their energy spectra in TeV (Funk, 2015), implying parental particles with a maximum energy of at most 100 TeV, substantially lower than the knee. The ambiguity concerning the maximum energy is mainly due to the uncertainty regarding the diffusion coefficient, which is difficult to estimate from theoretical studies. Regarding the acceleration mechanism, certain characteristic parameters are used to determine the acceleration such as a shock speed, cutoff energy, and acceleration efficiency that is dependent on the diffusion coefficient. These parameters have been measured in individual SNRs, but are not investigated in a unified manner. Turbulent magnetic fields, which represent another important factor in acceleration theory, are also poorly understood because practically no observational constraints exist. The turbulence is strongly connected to the diffusion of particles, and therefore is fundamental to the theory of DSA.

The scientific objective of this thesis is to place observational constraints on the diffusion coefficient at the very site of particle acceleration, namely, the shock wave of a supernova remnant. The diffusion in the SNR shock has been widely accepted to be Bohm-like, where a mean free path of a particle is proportional to its gyroradius. However, this validity has not been observationally verified, although the diffusion type is crucial in determining the relevant turbulent spectrum. We perform a systematic analysis of young SNRs at the relatively young stage at which the acceleration is believed to be most effective and the maximum energy is expected to be achieved. This is quite meaningful in two respects; the origin of galactic cosmic rays, particularly the origin of the knee, and the physics of the particle acceleration. The remainder of this thesis is organized as follows. Chapter 2 gives an overview of galactic cosmic rays, particle acceleration in SNRs, and models that are applicable to accelerated electrons in SNRs. Instruments used for imaging and spectral analyses of X-ray and TeV gamma-ray observations are introduced in Chapter 3. The systematic studies of young SNRs in X-rays and gamma-rays are presented in Chapter 4 and Chapter 5, respectively, based on the assumption of Bohm diffusion. Chapter 6 demonstrates non-Bohm diffusion regimes through a combination of nonthermal X-ray and gamma-ray observations. A summary and conclusions are provided in Chapter 7.

Chapter 2

Review

2.1 Cosmic Ray

The origin of cosmic rays (CRs) have puzzled us since the discovery in 1912 via balloon experiments by Victor F. Hess. Based on the fact that the strength of ionizing radiation increased at the higher altitude, he concluded that it was cosmic origin, and referred to “cosmic rays (CRs)” (see, e.g., Hess (2018) which is a translated version of the original paper). The following experiments found they were not electromagnetic waves, but energetic charged particles. After over a hundred years have passed since the discovery of CRs, lots of questions remain unanswered.

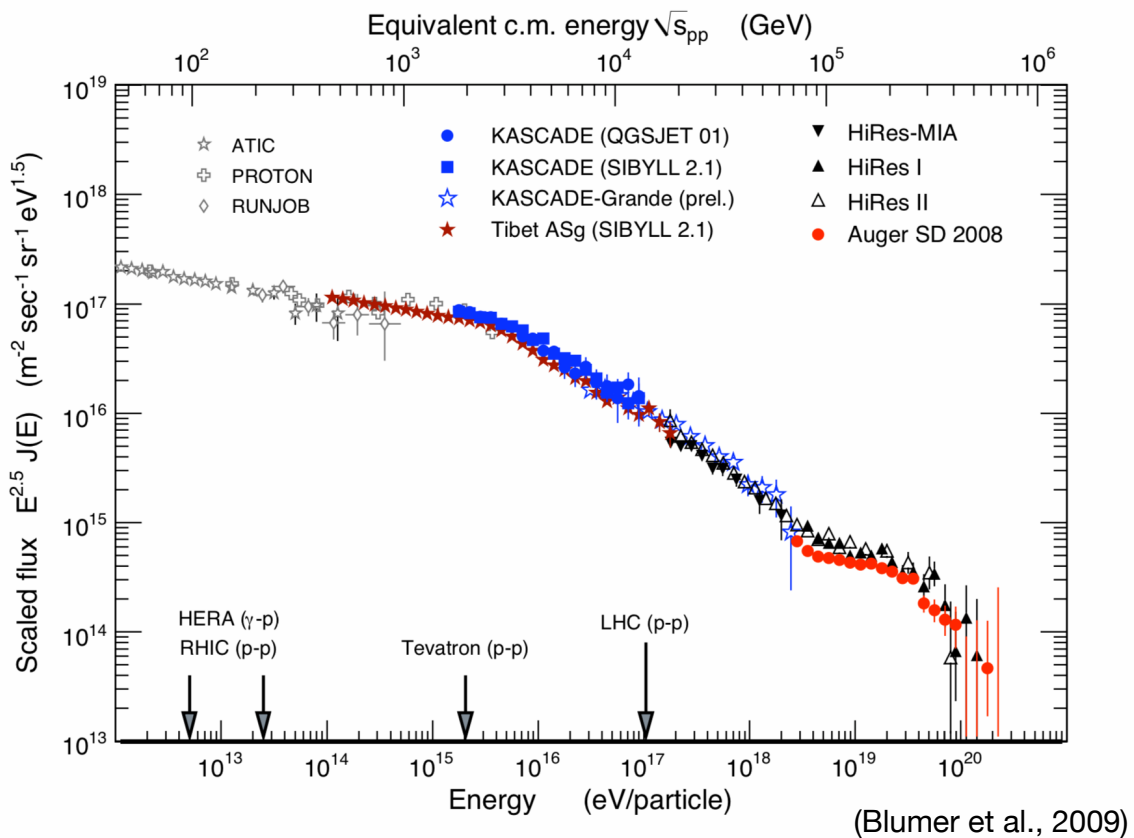


Figure 2.1: CR energy spectrum (taken from Blümer et al. (2009))

Many experiments and measurements, including balloon missions, space satellites, and ground-based

detectors, revealed some physical properties of CRs. The *old-fashioned* results, up to one decade ago, are as follows. The CRs composite of 90% protons, 10% helium nucleon, and a small amount of the other elements including heavier nucleon and electrons. The CR energies range from $\sim 10^9$ eV up to $\sim 10^{20}$ eV with energy density of ~ 1 eV cm $^{-3}$. The energy spectrum, shown in Figure 2.1, is overall described with a power-law function with some characteristic features. The spectral breaks are confirmed at $\sim 3 \times 10^{15}$ eV (“knee”) with the spectral index of $s = 2.7$ changing to 3.1^1 , $\sim 10^{17.5}$ eV (“second knee”), and $\sim 10^{18.5}$ eV (“ankle”) with $s = 3.1$ to 2.7 (see, e.g., Blümer et al. (2009) and references therein). At the ultra-high-energy regime above 10^{18} eV, the energy spectrum has an exponential cutoff (“Greisen-Zatsepin-Kuzmin (GZK) cutoff”) because the CR with such high energy decays due to interacting with Cosmic Microwave Background (CMB).

Recent improvements of new instruments for measuring the CR provided us with more precise and detailed natures of the CR and completely updated the old-fashioned picture of our understanding of the CR. With some developed measurements, such as Alpha Magnetic Spectrometer (AMS) onboard the International Space Station and Payload for Antimatter Matter Exploration and Light-nuclei Astrophysics (PAMELA), the energy spectrum below the knee turned out to deviate from the single power-law distribution. For instance, the energy spectrum of CR protons in 1 GeV to 1.8 TeV measured by AMS showed a spectral hardening at ~ 330 GeV with the spectral index of $s = 2.848$ changing to 2.716 (The AMS Collaboration, 2015b). The similar features have been reported in spectra of other CR nucleon such as CR helium (e.g., The AMS Collaboration (2015a)). Atkin et al. (2018) pointed out that there exists *new knee*, corresponding to spectral steepening around 10 TV, and this feature is universal for all the CR nuclei spectra obtained with the NUCLEON experiments. Besides, an excess of CR positrons was confirmed (The AMS Collaboration, 2014). These new features are not fully understood, and it is not conclusive whether they are originated from the sources, CR propagation, and/or re-acceleration.

The origin of the cosmic rays — *where do they come from?* — is still unsettled. The CRs with energies up to knee are likely galactic origin because gyroradii of these CRs are small enough to reside in our galaxy. Galactic supernova remnants (SNRs) are expected to play an important role in the observed galactic CRs, although problems regarding the new spectral features, which were brought with the new instruments, are yet untangled. The SNRs as the source of galactic CRs are summarized in Section 2.2.

The origin of the CRs above the knee, on the other hand, is more ambiguous. Because of the larger gyroradii, the CRs with energies above the ankle, referred to as ultra high energy cosmic rays (UHECRs), are considered as extragalactic origin. The ground-based telescopes for measuring the CRs, such as Pierre Auger Observatory and Telescope Array (TA), recently unveiled new features of UHECRs with the accumulated statistics that have been observed over a decade (see, e.g., Verzi et al. (2017) for a review). The Pierre Auger Collaboration (2017) reported the existence of a dipole structure (“Auger dipole”) in energies above 8×10^{18} eV with an amplitude of 6.5% and a position of $(\alpha_{J2000}, \delta_{J2000}) = (100 \pm 10^\circ, -24_{-13}^{+12}^\circ)$ at a confidence level of 5.2σ . TA detected a hotspot-like feature (“TA hotspot”) with a radius of 20° at a position of $(48.4^\circ, 44.5^\circ)$ at a confidence level of 6.2σ (The Telescope Array Collaboration, 2018). Both these discoveries are consistent with the extragalactic origin for UHECRs in terms of the arrival directions.

¹The spectral index s is defined as $dN/dE \propto E^{-s}$, where dN/dE and E indicate the differential energy spectrum and the CR energy, respectively.

2.2 SNR paradigm

The galactic supernova remnants have been prominent candidates for accelerating the cosmic rays with energies up to the knee. It is referred to as ‘‘SNR paradigm’’ to interpret the galactic CRs as particles being accelerated in SNRs via diffusive shock acceleration (DSA) and propagating in the Universe to reach the Earth. This section briefly presents an overview of SNR paradigm (see Reynolds (2008) for a review).

2.2.1 Supernova remnant

Supernova is one of the most energetic astrophysical phenomena, with kinematic energy of $\sim 10^{51}$ erg. It is triggered at the very last stage of a star’s lifetime after consuming out its nuclear fuel. There mainly exist two types of supernovae (SNe); 1. thermonuclear explosion (or Type Ia SN) which is an explosive nuclear reaction in a white dwarf, blowing the entire star away, and 2. core-collapse explosion which is an explosion of a massive star ($> 8 M_{\odot}$), leaving a central compact object (CCO), a neutron star or a black hole, at the explosion center. The leftover of the supernova explosion, known as a supernova remnant, is expanding and evolving in the interstellar medium (ISM).

The material ejected by SNe expands in the ambient ISM with the initial velocity of $\sim 10000 \text{ km s}^{-1}$, forming a supersonic wave at the surface because the sound speed in the typical ISM is given by $c_s \sim 10 \text{ km s}^{-1}$. This is called *forward shock* or *blast-wave shock*. The ejecta freely expands at the early phase (*ejecta-dominated* or *free-expansion* stage), and the forward shock sweeps up the ambient medium. The forward-shocked matter pushes the ejecta back, and another shock (*reverse shock*) is formed. The reverse shock compresses and heats the ejecta. At the boundary of the forward-shocked ISM and the reverse-shocked ejecta, another physical jump (known as *contact discontinuity*) is created. Therefore the interior of SNR has a laminar structure, as shown in Figure 2.2. Once the mass of the forward-shocked ISM and the ejecta become comparable, the forward shock decelerates. This moment is the beginning of the second stage (i.e., *Sedov-Taylor* phase). The behavior of the forward shock in Sedov-Taylor stage is described with self-similar solutions,

$$R \propto t^{2/5}, \quad (2.1)$$

$$V \propto t^{-3/5}, \quad (2.2)$$

where R , V , and t are a position of the forward shock (a radius from the explosion center), a speed, and an evolutionary age after the SNe, respectively. Hydrodynamical models to reproduce the trajectory of SNR shocks have been developed (see, e.g., Truelove and McKee (1999); Laming and Hwang (2003)). The properties strongly depend on initial parameters, such as a number density of ISM, density profile, ejecta energy, and ejecta mass. An example with one parameter set is illustrated in Figure 2.3.

2.2.2 SNR paradigm

The idea of SNR paradigm has been well accepted for decades since it was first proposed by Baade and Zwicky (1934). This is because SNRs are acceptable for the origin of the galactic CRs in terms of energy budget and energy spectrum. The CR energy density, $U_{\text{CR}} \sim 1 \text{ eV cm}^{-3}$, can be attainable if about 10% of the total energy of SNe is transferred to the accelerated particles. The well-studied theory of particle acceleration (diffusive shock acceleration) predicts a power-law distribution, that is consistent with the observed energy spectrum of the CRs.

The accelerated particles in the local sources (i.e., SNRs) have been indirectly detected through electromagnetic (EM) emission in different wavelengths. Table 2.1 summarizes previous observations of EM radiation from SNRs to diagnose the accelerated particles with different energies from keV to TeV.

In the 20th century, synchrotron radiation in the radio band had been detected from the galactic SNRs, indicating the existence of electrons accelerated up to the GeV regime (see, e.g., the updated version of Green catalog in Green (2019)). A breakthrough in X-ray astronomy was provided by ASCA, which provided us with the spectroscopic information up to 12 keV. The observations of SN 1006 with ASCA found the central region dominated by thermal line emissions and the bilateral limbs dominated by nonthermal radiation, suggesting that

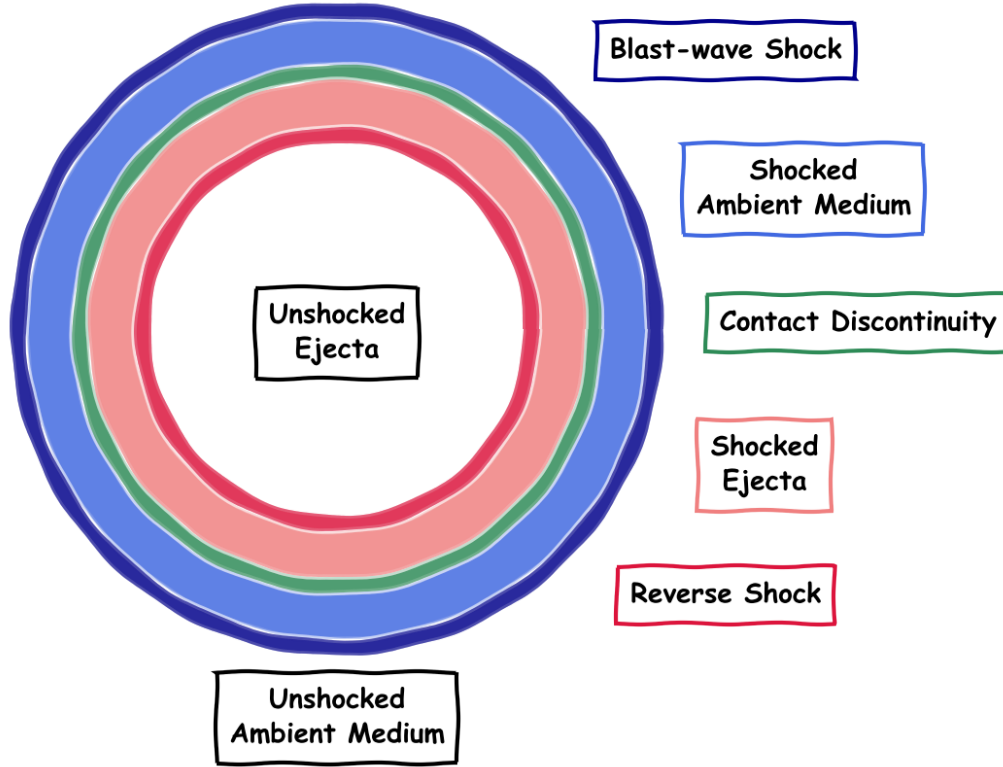


Figure 2.2: Interior structure of SNR. The forward-shocked ISM and the reverse-shocked ejecta are separated by the physical boundary (contact discontinuity).

Table 2.1: EM radiation diagnostics of CRs in SNRs

Particle energy	Electron		Proton	
	Radiation	Reference	Radiation	Reference
keV	X-ray nonthermal Bremsstrahlung	Tanaka et al. (2018)	—	—
MeV	Neutral Fe line emission	—	Neutral Fe line emission	Sato et al. (2014); Nobukawa et al. (2018)
GeV	Synchrotron radio	Green (2019)	π^0 -decay gamma-ray	Ackermann et al. (2013)
TeV	Synchrotron X-ray	Koyama et al. (1995)	π^0 -decay gamma-ray	Aharonian et al. (2004)
PeV	Inverse Compton gamma-ray	Aharonian et al. (2004)	—	—
PeV	—	—	π^0 -decay gamma-ray	Abramowski et al. (2014)

the nonthermal emission originated from the synchrotron X-ray emitted by multi-TeV electrons (Koyama et al., 1995).

In the 2000s, TeV gamma-ray astronomy has begun after the completion of new technology to detect gamma-rays on the ground with Imaging Atmospheric Cherenkov Telescopes (IACTs). High Energy Spectroscopic System (H.E.S.S.), which is one IACT in the southern hemisphere, revealed a TeV gamma-ray morphology

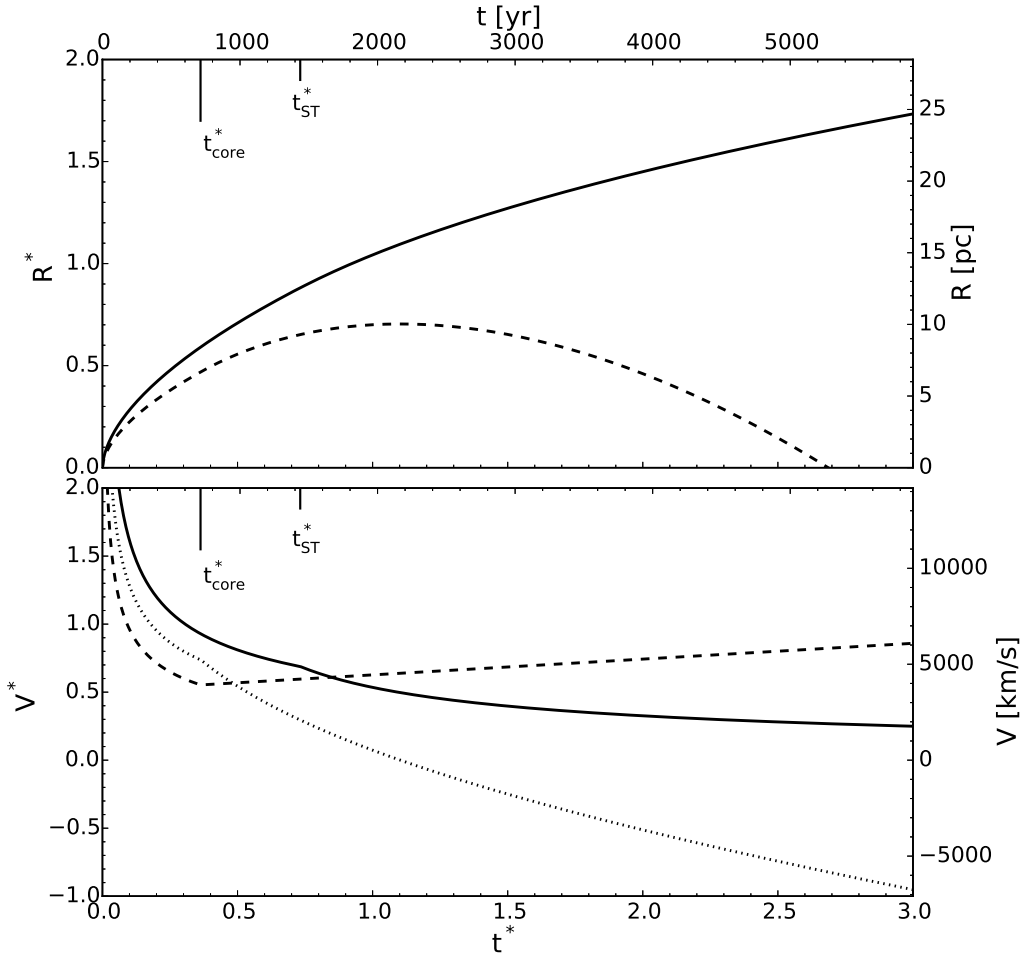


Figure 2.3: Evolution model of SNR (taken from Tsuji and Uchiyama (2016)). Time evolutions of the shock radii (top panel) and the shock speeds (bottom panel) are calculated for $(M_{\text{ej}}, E_{\text{ej}}, n) = (1 M_{\odot}, 10^{51} \text{ erg}, 0.01 \text{ cm}^{-3})$. The solid and dashed lines indicate the quantities of the blast-wave shock and the reverse shock, respectively. In the bottom panel, the dashed line is the reverse shock speed at the pre-shock ejecta frame, and the dotted line is the reverse shock speed at the ambient rest frame.

of SNR RX J1713.7–3946 (Aharonian et al., 2004). Despite the controversial matter of the particle type for radiating such high energy gamma-rays in this remnant (i.e., electrons in a leptonic scenario or protons in a hadronic scenario), the accelerated particles up to the multi-TeV band were confirmed. Years later, *Fermi* detected the π^0 bump, which is a characteristic feature accompanied by the interaction between CR protons and the interstellar nuclei (the hadronic scenario), in GeV gamma-ray spectra of SNR IC 443 and W 44 (Ackermann et al., 2013). This was the very first evidence of accelerated protons in SNRs. With deeper TeV gamma-ray observations by H.E.S.S., the power-law spectrum without an exponential cutoff was taken from a few SNRs in the galactic plane (Abramowski et al., 2014), implying the energy of the parental protons likely reaches the PeV regime. These objects are considered as “PeVatron” (an accelerator of PeV particles) candidates and important for the study of the knee in the CR energy spectrum.

Developed X-ray observations also updated our understanding of particle acceleration in SNRs. Using *Suzaku* observations, neutral Fe line emissions at 6.4 keV were found in some old SNRs, suggesting that the line emissions are attributed to protons in the MeV band (Sato et al., 2014; Nobukawa et al., 2018). The hard X-ray spectroscopy with Nuclear Spectroscopic Telescope Array (*NuSTAR*) detected a hard tail in the spectrum above ~ 14 keV from SNR W 49B, implying that it is nonthermal bremsstrahlung emitted from spectral-flattened (due to ionization loss) electrons in sub-MeV (Tanaka et al., 2018).

Propagation of the CRs is quite crucial in SNR paradigm because the CR energy spectrum is modified when propagating in the interstellar space due to energy loss and/or escape from the galaxy. For example, assuming a simple leaky-box model², the spectral index appears larger (i.e., the spectrum gets steepened) because of diffusion for the CRs to travel from the acceleration site to the Earth. The observed CR-proton spectrum in the vicinity of the Earth, $n(E)$, can be described with

$$n(E) \sim Q(E)\tau_{\text{esc}}(E) \propto E^{-(s+\alpha)}, \quad (2.3)$$

where $Q(E) \propto E^{-s}$ is an injected spectrum from the source, and $\tau_{\text{esc}}(E) \propto E^{-\alpha}$ is the timescale of CRs to escape with the diffusion coefficient of $D(E) \propto E^{-\alpha}$. Therefore compared to the original spectrum in the acceleration site, the spectrum obtained around the Earth is steepened by a term of α , which is sometimes presumed to be 1/3 for Kolmogorov diffusion (The AMS Collaboration, 2016; Verzi et al., 2017).

Although SNR paradigm seems well adopted and is supported by many observational facts, some fundamental issues should be addressed here.

SNRs as the galactic CR accelerators — (i) Energy transfer rate: the efficiency to transfer SNe energy to particle acceleration, expected to be $\sim 10\%$ accounting for the energy budget, is uncertain. (ii) Maximum energy (PeVatron): some PeVatron candidates were recently found by H.E.S.S., but most of SNRs show TeV spectra with exponential cutoffs. (iii) New spectral features: it remains veiled to explain the newly found spectral breaks in the CR spectrum with AMS.

SNRs as ideal laboratories to demonstrate DSA — SNR plays an important role as an ideal laboratory to test the theoretical studies about particle acceleration in terms of physical interests. (i) Injection problem: seed particles injected to Fermi acceleration cycle and process of injection are unknown. (ii) Nonlinear effect: the CRs around the shock cause pressure gradient, making the shock modified and the nonlinear effect non-negligible. (iii) Maximum energy: the attainable maximum energy is limited by cooling, dynamical age, or escape. (iv) Magnetic field amplification: regardless of the observational evidence of the amplified magnetic field (e.g., Uchiyama et al. (2007)), the mechanism is not well established. (v) Turbulent generation: the pressure gradient due to CR streaming itself makes the magnetic field turbulent, but details regarding this process are not well understood.

²A standard model for the galactic CRs which the CRs confined in the galactic plane gradually leak (escape) into the outside of the galaxy.

2.3 Particle acceleration

The idea of particle acceleration in a shock wave was first realized by Enrico Fermi — *Fermi acceleration* (Fermi, 1949). Shock waves are ubiquitous in astrophysical objects, such as supernova remnants or intercluster medium. Diffusive shock acceleration (DSA) is a theory of particle acceleration that utilizes Fermi acceleration and applies for astrophysical shocks (Axford et al., 1977; Krymskii, 1977; Blandford and Ostriker, 1978; Bell, 1978; Malkov and Drury, 2001; Longair, 2011). The physics regarding DSA is shortly introduced in this section.

2.3.1 Shock wave

A shock wave is defined as a discontinuous plane propagating with a supersonic speed (Figure 2.4). For hydrodynamical parameters (velocity v_i , density ρ_i , pressure p_i , and temperature T_i) of the upstream ($i = 1$) and downstream ($i = 2$) flows, conservation laws of mass flux, momentum flux, and energy flux should be satisfied. Then jump conditions (also known as Rankine-Hugoniot relations) are obtained as

$$\frac{\rho_2}{\rho_1} = \frac{v_1}{v_2} = \frac{(\gamma + 1)\mathcal{M}_1^2}{2 + (\gamma - 1)\mathcal{M}_1^2} \approx 4, \quad (2.4)$$

$$\frac{p_2}{p_1} = \frac{2\gamma\mathcal{M}_1^2 - (\gamma - 1)}{\gamma + 1} \gg 1, \quad (2.5)$$

$$\frac{T_2}{T_1} = \frac{[2\gamma\mathcal{M}_1^2 - (\gamma - 1)][(\gamma - 1)\mathcal{M}_1^2 + 2]}{(\gamma + 1)^2\mathcal{M}_1^2} \approx \frac{5}{16}\mathcal{M}_1^2, \quad (2.6)$$

where the last term of each equation is calculated for the ratio of specific heats of $\gamma = 5/3$ and Mach number of $\mathcal{M}_1 \gg 1$. Note that for such a strong shock ($\mathcal{M} \gg 1$), the compression ratio $\sigma (= \rho_2/\rho_1 = v_1/v_2)$ is 4.

2.3.2 Diffusive shock acceleration

In diffusive shock acceleration, a particle is accelerated by diffusing back and forth across a shock wave, producing a power-law energy distribution of accelerated particles. Let assume that one particle with energy of E in the upstream rest frame crosses the shock front, and moves into the downstream. Since the downstream speed seen in the upstream rest frame is given by $V = v_1 - v_2$, one can obtain the energy of the downstream particle (E') by Lorentz transformation,

$$E' = E \left(1 + \frac{V}{c} \cos \theta \right), \quad (2.7)$$

where θ denotes the angle between the momentum direction of the particle and the shock normal. In the downstream region, the particle is randomly reflected by magnetic field (see Section 2.4.1 for details), changes its direction, and crosses the shock to go back to the upstream region. By inverse-Lorentz transformation of the particle from the downstream system to the upstream system, the particle energy in the upstream (E'') is derived as

$$E'' = E' \left(1 + \frac{V}{c} \cos \theta \right). \quad (2.8)$$

Using Equation 2.7 and Equation 2.8, one can derive energy gain of one-round crossing the shock,

$$\frac{\Delta E}{E} = \frac{E'' - E}{E} = 2 \frac{V}{c} \cos \theta. \quad (2.9)$$

Note that the second-order term was ignored here. The angle-averaged one-round energy gain can be described as

$$\frac{\Delta E}{E} = 2 \frac{V}{c} \int_0^{\pi/2} \cos \theta \cdot p(\theta) d\theta = \frac{4}{3} \frac{V}{c}, \quad (2.10)$$

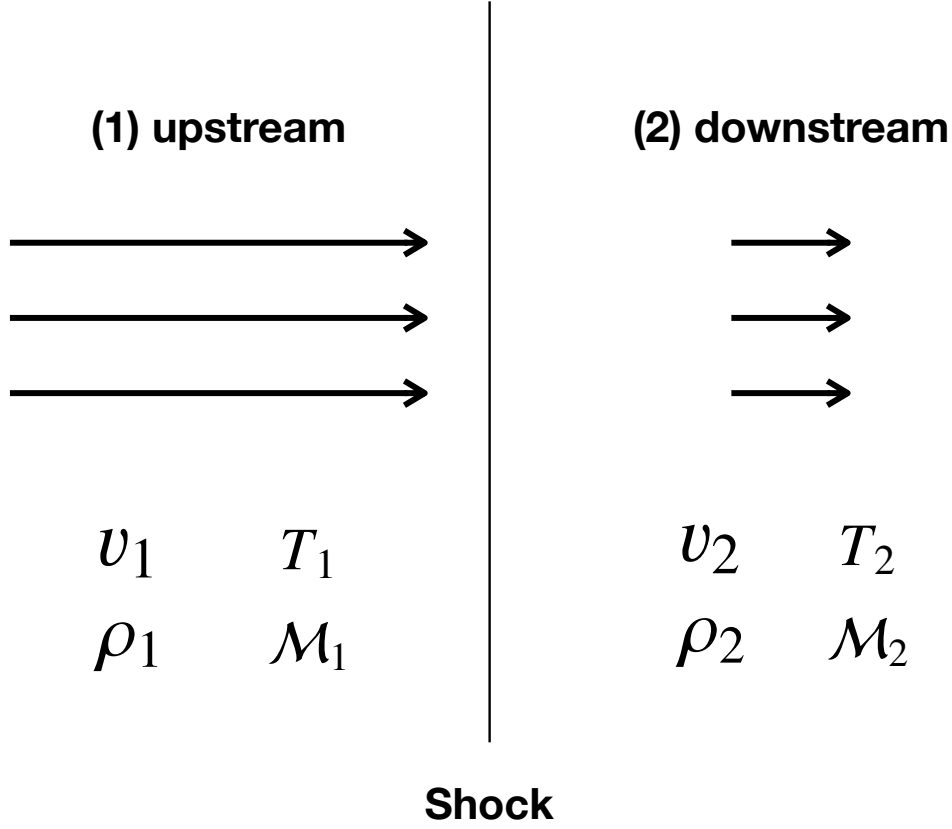


Figure 2.4: The schematic picture of the shock wave in its rest frame. The parameters of v , T , ρ , and \mathcal{M} indicate velocity, temperature, density, and Mach number of flow, respectively. The subscripts of 1 and 2, respectively, denote the quantities in the upstream and downstream regions.

where $p(\theta) = 2 \sin \theta \cos \theta$ indicates a probability of the particle to cross the shock between θ and $\theta + d\theta$.

The particles gain energies by diffusing back and forth across the shock many times, and at the same time escape from this cycle by diffusion and convection. After n cycles, the particle with the initial energy of E_0 is accelerated up to E_n , which can be written as

$$E_n = E_0 \left(1 + \frac{4V}{3c}\right)^n \sim E_0 \exp\left(\frac{4V}{3c}n\right). \quad (2.11)$$

The diffusion flux for the particles to travel from the upstream to the downstream is $f_1 = Nv/4$, where N is the number density and v ($\approx c$) is the speed of the particle. The convection flux for the downstream particles to escape from the acceleration cycle is given by $f_2 = Nv_2$. Since the probability for the particle to escape from the acceleration cycle per one-round trip is $f_2/f_1 = 4v_2/c$, the probability for the particle to remain near the shock after n -times cycles is given by

$$P_n(E) = \left(1 - \frac{4v_2}{c}\right)^n \sim \exp\left(-\frac{4v_2}{c}n\right). \quad (2.12)$$

Finally using Equation 2.11 and Equation 2.12, the differential energy spectrum is obtained to be

$$\frac{dN}{dE} \propto P_n E^{-1} \propto E^{-\frac{\sigma+2}{\sigma-1}}. \quad (2.13)$$

For the standard shock compression of $\sigma = 4$, the spectral index of the accelerated particles is 2.

2.3.3 Acceleration timescale

This subsection briefly summarizes timescale of particle acceleration via DSA (e.g., Malkov and Drury (2001)). The acceleration timescale, τ_{acc} , is roughly given by $\Delta t \left(\frac{E}{\Delta E} \right)$. Since the diffusion length of a particle is described with $\frac{D_i}{v_i}$ (the subscripts $i = 1$ and 2 denote the upstream and the downstream, respectively) with D being a diffusion coefficient of the particle, the typical time for the particle to stay upstream and downstream, defined as Δt , is $\frac{4D_1}{v_1 c} + \frac{4D_2}{v_2 c}$. Therefore the acceleration timescale is derived as

$$\tau_{\text{acc}} = \frac{3}{V} \left(\frac{D_1}{v_1} + \frac{D_2}{v_2} \right). \quad (2.14)$$

Bohm diffusion is widely accepted for particles around the SNR shock in DSA. Let us assume the equal diffusion coefficient upstream and downstream; $D_1 = D_2 = cr_g \eta / 3$ with gyroradius of $r_g = \frac{E}{ZqB}$ where Z is a charge number and q is a electric charge, and the so-called Bohm factor of η , which indicates a deviation of the mean free path of the particle from the gyroradius. For the shock with its velocity of $v_{\text{sh}} = v_1 = 4v_2$, one can obtain

$$\tau_{\text{acc}} = \frac{20}{3} \frac{cr_g}{v_{\text{sh}}^2} \eta. \quad (2.15)$$

2.3.4 Maximum attainable energy

Equation 2.15 gives the acceleration timescale of DSA. The acceleration is limited by the following four cases: dynamics, energy loss (cooling), age, and escape. In each framework, a practical form of maximum energy attainable via DSA can be obtained as follows.

Dynamics-limited: the acceleration timescale, given by Equation 2.15, should at most be smaller than characteristic dynamical timescale (i.e., $\tau_{\text{acc}} \leq \tau_{\text{dyn}} = R/V$ with the radius R and the shock speed V of the system). Hence, the dynamically limited maximum energy attainable via DSA is described as

$$E_{\text{max, dyn}} = \frac{3}{20} \frac{Zq}{c\eta} v_{\text{sh}} R B \sim 0.46 \frac{Z}{\eta} \left(\frac{v_{\text{sh}}}{10^4 \text{ km s}^{-1}} \right) \left(\frac{R}{10 \text{ pc}} \right) \left(\frac{B}{10 \mu\text{G}} \right) \text{ PeV}. \quad (2.16)$$

In order to accelerate particles up to the knee (a few PeV), the shock speed, the system size, and/or the strength of magnetic field should be large. Since the former two parameters cannot be larger by an order of magnitude, the magnetic field may be a key parameter for the maximum energy. Indeed the amplification of magnetic field by over an order of magnitude has been confirmed both observationally and theoretically.

Cooling-limited: the accelerated particle loses its energy due to radiation (see Section 2.5 for details). An electron, in particular, quickly and effectively loses the energy because of its light mass. The timescale of radiation process is presented in Section 2.5. Here we assume synchrotron cooling for the energy loss of an electron. Since the timescale of synchrotron radiation is described as $\tau_{\text{synch}} = 9(mc^2)^4 / 4q^4 B^2 E$, governing $\tau_{\text{acc}} = \tau_{\text{synch}}$ gives

$$E_{\text{max, synch}} = \sqrt{\frac{27}{80q^3 c}} (mc^2)^2 \eta^{-\frac{1}{2}} B^{-\frac{1}{2}} v_{\text{sh}} \sim 73 \eta^{-\frac{1}{2}} \left(\frac{v_{\text{sh}}}{3000 \text{ km s}^{-1}} \right) \left(\frac{B}{10 \mu\text{G}} \right)^{-\frac{1}{2}} \text{ TeV}. \quad (2.17)$$

Age-limited: for the age-limited case it is presumed that the acceleration is ongoing during the age of the source. This is especially applicable to a proton of which energy loss due to radiation is not strongly effective. The maximum energy in the age-limited case is obtained by assuming $\tau_{\text{acc}} = \tau_{\text{age}}$;

$$E_{\text{max, age}} = \frac{3}{20} \frac{q}{c} \tau_{\text{age}} v_{\text{sh}}^2 B \eta^{-1} \sim 43 \eta^{-1} \left(\frac{v_{\text{sh}}}{3000 \text{ km s}^{-1}} \right)^2 \left(\frac{\tau_{\text{age}}}{10^3 \text{ yr}} \right) \left(\frac{B}{10 \mu\text{G}} \right) \text{ TeV}. \quad (2.18)$$

Escape-limited: at late times, because the shock is decelerated, the particle is expected to escape from the source. With ℓ being the distance between the upstream particle and the shock front, the particle is assumed to escape freely for larger ℓ . If ℓ is small, the particle is confined around the shock and accelerated by DSA. Ohira

et al. (2010) derived the escape-limited maximum energy by governing $D_1/v_1 \approx \ell$, where D_1/v_1 indicates the diffusion length,

$$E_{\max, \text{esc}} = \frac{3q}{4c} \ell v_{\text{sh}} B \eta^{-1} \sim 69 \eta^{-1} \left(\frac{v_{\text{sh}}}{3000 \text{ km s}^{-1}} \right) \left(\frac{\ell}{1 \text{ pc}} \right) \left(\frac{B}{10 \mu\text{G}} \right) \text{TeV}. \quad (2.19)$$

2.4 Diffusion and turbulence

In the acceleration theory (DSA), a particle moves diffusively. The mean free path of the particle due to Coulomb collision becomes large in hot and rarefied plasma such as supernova remnants. Therefore an astrophysical shock is called a *collisionless* shock in this context, and the particle collides with magnetic field instead rather than with matters. This section summarizes diffusion in Section 2.4.1, and turbulent magnetic field in Section 2.4.2. The review by Blandford and Eichler (1987) and the textbook by Kulsrud (2005) were helpful for preparing materials in this section. See also, e.g., Blasi (2018); Gabici (2018).

2.4.1 Diffusion

Charged particle in regular magnetic field

In a *regular* magnetic field with no perturbation, a charged particle is in a helical motion along the field direction. The equation of motion of the charged particle is described with

$$\frac{d\mathbf{p}}{dt} = q \left(\mathbf{E} + \frac{\mathbf{v}}{c} \times \mathbf{B} \right), \quad (2.20)$$

where \mathbf{p} , \mathbf{v} , \mathbf{E} , \mathbf{B} , and c are momentum of the particle, speed of the particle, an electric field, a magnetic field, and the speed of light, respectively. Let assume that the magnetic field is oriented to the z -axis. Ignoring the electric field, the motion of particle is given by

$$\begin{cases} p_z = \text{const.} \\ v_x = v_0 \cos(\Omega t), \\ v_y = v_0 \sin(\Omega t) \end{cases} \quad (2.21)$$

where $\Omega = qB_0/\gamma mc$ indicates Larmor frequency. Larmor radius r_L is given by $v\gamma mc/qB_0$. If the magnetic field does not affect the energy of the particle, the relativistic particle moves with the averaged speed of $c/3$ in the z -axis.

Charged particle in irregular B-field

In an *irregular* magnetic field that has fluctuation ($\delta\mathbf{B}$) in addition to a regular field (\mathbf{B}_0), a charged particle interacts with the field and changes its direction due to being scattered by the field. Let assume Alfvén wave propagating in z -axis, $\delta B \ll B_0$, and $\delta\mathbf{B} \perp \mathbf{B}_0$ (Figure 2.5). The speed of Alfvén wave is described as

$$v_A = \frac{B}{\sqrt{4\pi\rho}} = 20 \left(\frac{B}{1 \mu\text{G}} \right) \left(\frac{n_1}{1 \text{ cm}^{-3}} \right)^{-1/2} \text{ km s}^{-1}. \quad (2.22)$$

Note that the Alfvén wave frequency is much smaller than the gyro frequency of ion ($\Omega_p = qB/m_p c$). Thus one assumes that Alfvén wave seen from a relativistic particle is static in first-order approximation. Ignoring the electric field of Alfvén wave, the equation of motion can be described with

$$\frac{d\mathbf{p}}{dt} = q \frac{\mathbf{v}}{c} \times (\mathbf{B}_0 + \delta\mathbf{B}). \quad (2.23)$$

The particle changes its direction of p_{\parallel} ($= p \cos \theta = p\mu$) due to the effect of $\delta\mathbf{B}$ in addition to \mathbf{B}_0 that contributes to the x and y components of the particle momentum. The equation of motion in the z -axis is written as

$$\frac{dp_{\parallel}}{dt} = \frac{q}{c} |\mathbf{v}_{\perp} \times \delta\mathbf{B}|. \quad (2.24)$$

Suppose that $\delta\mathbf{B}$ has a wave vector of k , a frequency of ω , and a phase of ψ , and the position of the particle is $z = z_0 + v_z t$. Then,

$$|\mathbf{v}_{\perp} \times \delta\mathbf{B}| = \frac{1}{2} v_{\perp} \delta B \{ \cos [(kv_z - \omega + \Omega)t + (kz_0 + \psi)] - \cos [(kv_z - \omega - \Omega)t + (kz_0 - \psi)] \}. \quad (2.25)$$

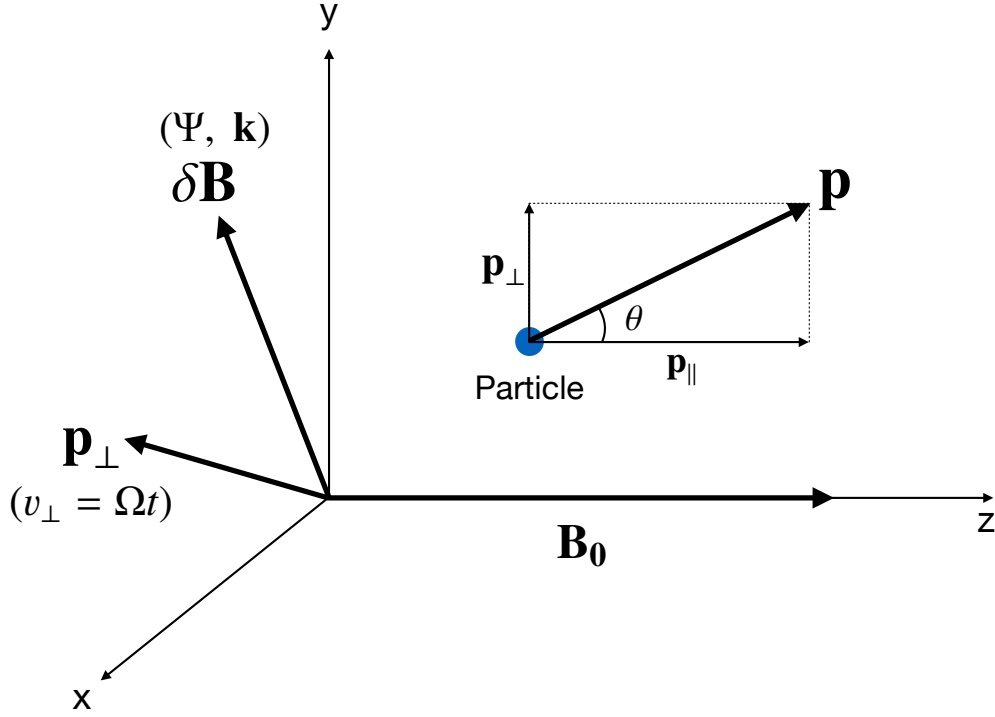


Figure 2.5: A charged particle in an irregular B-field. \mathbf{B}_0 is along the z -axis, and the pitch angle of particle is given by θ . The turbulent magnetic field, $\delta\mathbf{B}$, is on the x - y plane with a phase of Ψ and wave vector of \mathbf{k} .

Here, the first term is averaged out in time, but the second term is not if $kv_z - \omega - \Omega \approx 0$. Integrating Equation 2.25 over time for the particle with the speed of v_x to pass through the wave packet with a length of $L \approx 2\pi/k$, Equation 2.24 yields

$$\begin{aligned}\Delta p_{\parallel} &= \frac{1}{2} \frac{qv_{\perp} \delta B}{c} \frac{2\pi}{kv_z} \cos(kz_0 - \psi), \\ &= \pi p \sin \theta \left(\frac{\delta B}{B_0} \right) \cos \psi'.\end{aligned}\quad (2.26)$$

We assumed $\psi' = kz_0 - \psi$ and $\Omega = kv_z$. The change of the momentum parallel to the mean field is

$$dp_{\parallel} = d(p \cos \theta) = -p \sin \theta d\theta, \quad (2.27)$$

which should correspond to Equation 2.26. Therefore the change of the pitch angle is described as

$$d\theta = -\pi \left(\frac{\delta B}{B_0} \right) \cos \psi'. \quad (2.28)$$

When we ignore terms of order unity, $d\theta \sim \pm \frac{\delta B}{B_0}$, where the sign represents the phase. This indicates the change of the pitch angle in a single interaction. It should be noted that this interaction occurs when k is comparable to $\frac{\Omega}{v\mu}$: the characteristic wavenumber can be defined as

$$k_{\text{res}} = \frac{\Omega}{v\mu}. \quad (2.29)$$

This is referred to as *resonance scattering*. The scattering of the charged particle with the irregular magnetic field can be summarized as follows. As illustrated in Figure 2.6, the resonance scattering is realized for Larmor radius as large as a wavelength of the magnetic field, and the pitch angle changes by roughly $\delta B/B_0$ with a

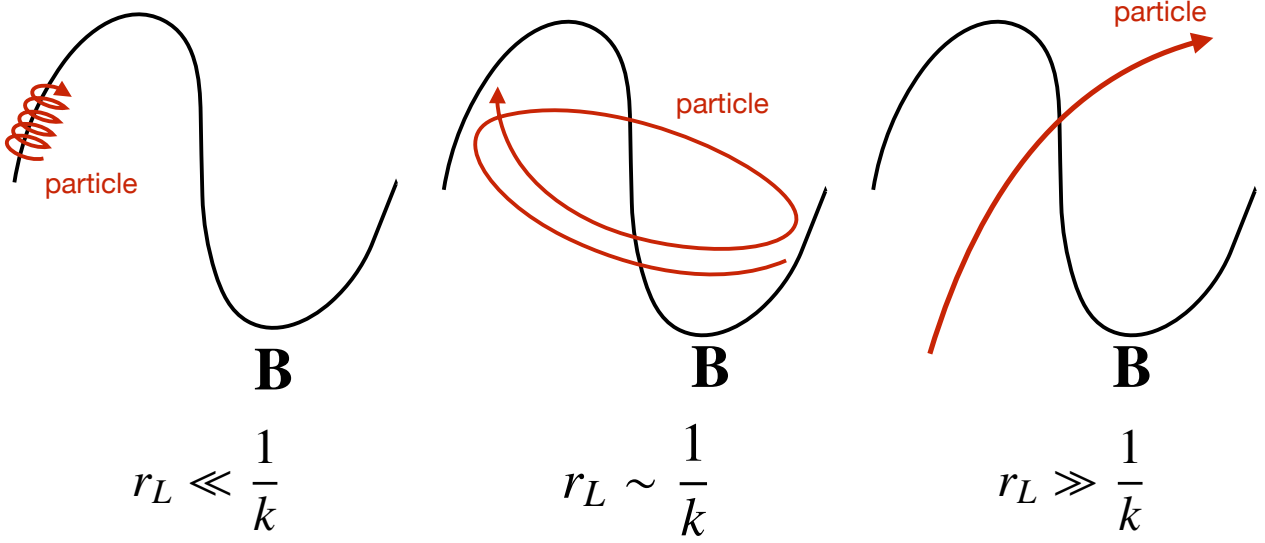


Figure 2.6: Schematic picture of the wave-particle interaction (see also Kulsrud (2005)). The particle is scattered with the field (resonance scattering) when $r_L \sim 1/k$.

random sign per scattering. If Larmor radius of particle is much smaller than the wavelength of the field (i.e., $r_L \ll \lambda \sim \frac{1}{k}$), the particle surfs adiabatically. On the other hand, the particle hardly feels the field in the case of $r_L \gg \lambda \sim \frac{1}{k}$.

We expand the single wave-particle interaction to many times interactions. It is presumed that timescale (τ) for the particle passing through the wave packet is comparable to wave period: $\tau = 2\pi/\Omega$, assuming $v_A \ll v_z$. In the interval of time t , t/τ times interactions occur. The averaged change of the pitch angle is obtained as

$$\langle (\Delta\theta)^2 \rangle = \frac{t}{\tau} \times \frac{\pi^2}{2} \left\langle \left(\frac{\delta B}{B_0} \right)^2 \right\rangle = \frac{t\pi\Omega}{4} \left\langle \left(\frac{\delta B}{B_0} \right)^2 \right\rangle. \quad (2.30)$$

Thus the diffusion in the pitch angle is characterized by

$$D_\theta = \frac{\langle (\Delta\theta)^2 \rangle}{2t} = \frac{\pi}{8} \Omega \left\langle \left(\frac{\delta B}{B_0} \right)^2 \right\rangle. \quad (2.31)$$

The field is not represented by a single wave, but many waves with a power spectrum:

$$\left\langle \left(\frac{\delta B_k}{B_0} \right)^2 \right\rangle \equiv kW(k). \quad (2.32)$$

Here $W(k)$ is a wave spectrum normalized by energy per unit of wave number. The subscript k represents the resonance condition. The total energy contained in the turbulent magnetic field can be obtained as

$$\left\langle \left(\frac{\delta B_{\text{tot}}}{B_0} \right)^2 \right\rangle = \int \frac{dk}{k} \left\langle \left(\frac{\delta B_k}{B_0} \right)^2 \right\rangle = \int dkW(k). \quad (2.33)$$

Transport equation of the particles with distribution function being f is given by

$$\frac{\partial f}{\partial t} + \mu v \frac{\partial f}{\partial z} = \frac{\partial}{\partial \mu} \left[(1 - \mu^2) D_\theta \frac{\partial f}{\partial \mu} \right]. \quad (2.34)$$

Suppose that the state is stationary (i.e., $\partial f/\partial t = 0$), and that the distribution is quasi-isotropic (i.e., $f = f^{(0)} + f_{\mu}^{(1)}$), where $f^{(0)}$ indicates an isotropic distribution and $f_{\mu}^{(1)}$ represents an anisotropic (but small) distribution). Integrating Equation 2.34 over μ from -1 to $+1$, one obtains diffusion equation:

$$\frac{\partial}{\partial z} \left[\frac{v^2}{2} \int_{-1}^1 d\mu' \mu' \int_{-1}^{\mu'} \frac{d\mu}{D_{\theta}} \frac{\partial f^{(0)}}{\partial z} \right] = 0. \quad (2.35)$$

In Equation 2.35, the spatial diffusion coefficient D is describes as

$$D = \frac{v^2}{2} \int_{-1}^1 d\mu' \mu' \int_{-1}^{\mu'} \frac{d\mu}{D_{\theta}}. \quad (2.36)$$

D_{θ} is independent on μ for an isotropic scattering. Then Equation 2.36 yields

$$D = \frac{1}{3} \frac{v^2}{D_{\theta}}. \quad (2.37)$$

Approximately, $D_{\theta} \sim \Omega \sim v/r_L$ if we assume that particles are isotropized for one gyration. In a quasi-linear theory,

$$D_{\theta} \approx \Omega \left(\frac{\delta B}{B_0} \right)^2 \approx \frac{v}{r_L} \left(\frac{\delta B}{B_0} \right)^2, \quad (2.38)$$

using Equation 2.31. Therefore the spatial diffusion coefficient can be obtained as

$$D = \frac{1}{3} r_L v \left(\frac{B_0}{\delta B} \right)^2 = D_{\text{Bohm}} \eta, \quad (2.39)$$

where $D_{\text{Bohm}} = r_L v/3$ is known as the coefficient in the Bohm diffusion, and $\eta \equiv (B_0/\delta B)^2$ is the so-called Bohm factor. Recalling Equation 2.32 and assuming that the wave spectrum has a form of $W(k) \propto k^{-p}$, the spatial diffusion coefficient is described as

$$D \approx \frac{1}{3} r_L v \frac{1}{k W(k)} \propto k^{p-2} \propto E^{-p+2}. \quad (2.40)$$

Here we recalled that $r_L \propto k^{-1}$ for the resonance scattering, and the Lamor radius is proportional to the energy of the particle ($r_L \propto E$). When the diffusion coefficient is defined as $D \propto E^{\alpha}$, the energy dependence (i.e., the α parameter) and the index of the wave spectrum (p) are related as

$$\alpha = -p + 2. \quad (2.41)$$

For example, typical diffusion regimes with $\alpha = 0, 1, 1/3, 1/2$, and 2 are referred to as constant, Bohm, Kolmogorov, Kraichnan, and wave damping.

2.4.2 Turbulence

Hydrodynamics, in realistic cases, is turbulent, making it very complicated to characterize its properties. The hydrodynamical motion is described by a flow and a wave, which are related to each other (i.e., the flow produces the wave and vice versa). The hydrodynamics is complex of these flows and waves, and therefore it consists of irregular motions, known as *turbulence*. See, e.g., Landau and Lifshitz (2013); Schekochihin and Cowley (2007) for details.

Hydrodynamical treatment

The hydrodynamical equations are as follows. Here it is assumed that the hydrodynamic is incompressible, which density is independent on pressure and temperature. The equation of motion of a complete fluid, also known as Euler's equation, is

$$\frac{\partial \mathbf{u}}{\partial t} + (\mathbf{u} \cdot \nabla) \mathbf{u} = -\frac{1}{\rho} \nabla P + \mathbf{K}, \quad (2.42)$$

where \mathbf{u} , ρ , P , and \mathbf{K} are speed, density, pressure of the fluid, and external force, respectively. The equation of motion of a viscous fluid is described as

$$\frac{\partial \mathbf{u}}{\partial t} + (\mathbf{u} \cdot \nabla) \mathbf{u} = -\frac{1}{\rho} \nabla P + \frac{1}{\rho} \left(\chi + \frac{1}{3} \eta \right) \nabla (\nabla \cdot \mathbf{u}) + \frac{\eta}{\rho} \Delta \mathbf{u} + \mathbf{K}, \quad (2.43)$$

where χ and η denote viscous rates depending on pressure and temperature. The basic equations of hydrodynamical motion consist of three equations: equation of motion (defined above), equation of continuity, and equation of state.

Reynolds number (Re) is indicative of viscosity:

$$\text{Re} = \frac{LU}{\nu} = \frac{\rho LU}{\eta}. \quad (2.44)$$

Here ν is defined as η/ρ . Reynolds's experiments found the transition from laminar flow to turbulent flow: laminar flow has relatively slow and stable fluid flux. As Re increases, instability is produced due to external disturbance, producing more turbulent flow.

The velocity and pressure of the turbulent flow are defined as

$$\mathbf{u} = \mathbf{U} + \hat{\mathbf{u}}; \quad \langle \hat{\mathbf{u}} \rangle = 0, \quad (2.45)$$

$$P = P + \hat{P}; \quad \langle \hat{P} \rangle = 0, \quad (2.46)$$

where the background average flow is described with \mathbf{U} and P , and the disturbance flow is described with $\hat{\mathbf{u}}$ and \hat{P} . Substituting them to Equation 2.43 and taking the average, the equations of motion of the background and turbulent flows are, respectively,

$$\frac{\partial \mathbf{U}}{\partial t} + (\mathbf{U} \cdot \nabla) \mathbf{U} + \langle (\hat{\mathbf{u}} \cdot \nabla) \hat{\mathbf{u}} \rangle = -\frac{1}{\rho} \nabla P + \nu \Delta \mathbf{U} + \mathbf{K}, \quad (2.47)$$

$$\frac{\partial \mathbf{u}}{\partial t} + (\mathbf{U} \cdot \nabla) \hat{\mathbf{u}} + (\hat{\mathbf{u}} \cdot \nabla) \mathbf{U} + (\hat{\mathbf{u}} \cdot \nabla) \hat{\mathbf{u}} - \langle (\hat{\mathbf{u}} \cdot \nabla) \hat{\mathbf{u}} \rangle = -\frac{1}{\rho} \nabla \hat{P} + \nu \Delta \hat{\mathbf{u}}. \quad (2.48)$$

Kolmogorov turbulence The turbulent fluid consists of various eddies at large and small scales. Starting from laminar flow, the turbulent energy is turned over from the first disturbance to the second disturbance via eddies, and this process is repeated until the fluid becomes fully turbulent. The large eddies possess laminar structure such as disturbance or eddy flow. The small eddies lose the characteristic structure and are spatially homogeneous and isotropic. This behavior was first predicted by Kolmogorov in 1941 (Kolmogorov, 1941) for large Reynolds number: i) *Kolmogorov's hypothesis of local isotropy* — turbulent motion at small scale is statistically isotropic. ii) *Kolmogorov's first similarity hypothesis* — turbulent motion at small scale is

universally and uniquely described with energy transfer rate ϵ and ν . iii) *Kolmogorov's second similarity hypothesis* — turbulent motion at subrange scale (i.e., intermediate range between large and small eddies) is universally described with energy transfer rate ϵ and independent on ν .

The turbulent energies are transferred from larger eddies to smaller eddies. Larger eddies, including the largest-scale eddy as large as the size of the system (L), contain most of the injected energy, referred to as “energy containing” or “energy production” range. Since the larger eddies are unstable, they are broken up to transfer the energies to smaller eddies. This energy cascade lasts until Re becomes sufficiently small and the eddy motions become stable. The intermediate range is called “inertial subrange”, and the energy spectrum has a characteristic power-law form with a spectral slope of $-5/3$, namely, $E(k) \propto k^{-5/3}$, which is known as Kolmogorov's $-5/3$ spectrum. In the smallest eddies, referred to as “dissipation range”, the energies are dissipated and transferred to heat. The parameters of each range are summarized in Table 2.2 based on Kolmogorov's theory. The entire energy spectrum of the turbulence is given by

$$E(k) = C\epsilon^{2/3}k^{-5/3}f_L f_\eta, \quad (2.49)$$

$$f_L = \left[\frac{k\ell_0}{((k\ell_0)^2 + C_L)^{1/2}} \right]^{p_0 + 5/3}, \quad (2.50)$$

$$f_\eta = \exp \left[-\beta \left\{ \left((k\ell_0)^4 + C_\eta^4 \right)^{1/4} \right\} \right], \quad (2.51)$$

where f_L and f_η describe, respectively, the functions in the energy containing (production) and dissipation ranges. Here ℓ_0 indicates the largest scale comparable with L . In the inertial subrange, $f_L \sim 1$ and $f_\eta \sim 1$. Experimentally the constant parameters are obtained as follows: $C_L \approx 6.78$, $C_\eta \approx 0.40$, $C = 1.5$, $p_0 = 2$, and $\beta = 5.2$. The schematic spectrum given by Equation 2.49 is illustrated in Figure 2.7.

Magnetohydrodynamical treatment

The magnetohydrodynamical (MHD) equation of motion for an incompressible fluid is described with

$$\frac{\partial \mathbf{u}}{\partial t} + (\mathbf{u} \cdot \nabla) \mathbf{u} = -\frac{1}{\rho} \nabla P + \frac{1}{c} \mathbf{j} \times \mathbf{B} + \nu \nabla^2 \mathbf{u} + \mathbf{K}, \quad (2.52)$$

where \mathbf{j} and \mathbf{B} represent current and magnetic field, respectively. The induction equation is given by

$$\frac{\partial \mathbf{B}}{\partial t} - \nabla \times (\mathbf{u} \times \mathbf{B}) = \eta \nabla^2 \mathbf{B}. \quad (2.53)$$

Elsasser field is defined as $\mathbf{z}^\pm = \mathbf{u} \pm \delta \mathbf{B}$ with fluctuation of magnetic field $\delta \mathbf{B}$. Substituting this to the equation of motion, Elsasser equations are derived as

$$\frac{\partial \mathbf{z}^\pm}{\partial t} + \mathbf{z}^\pm \cdot \nabla \mathbf{z}^\pm = -\nabla P + \frac{1}{2}(\nu + \eta) \nabla^2 \mathbf{z}^\pm + \frac{1}{2}(\nu - \eta) \nabla^2 \mathbf{z}^\pm + \mathbf{K}, \quad (2.54)$$

$$\nabla \cdot \mathbf{z}^\pm = 0. \quad (2.55)$$

Kraichnan turbulence The MHD properties of turbulence were first realized by Kraichnan (Kraichnan, 1965). He presumed that Alfvén wave timescale of $\tau_A \sim \frac{\ell}{v_A}$ is smaller than the hydrodynamical timescale of $\tau \sim \frac{\ell}{\delta u}$, and the energy transfer timescale is defined as $T \sim \frac{\tau^2}{\tau_A}$. In the inertial subrange, the turbulence energy spectrum is described by $E(k) \propto k^{-3/2}$. The parameters of Kraichnan turbulence are presented in Table 2.2.

Astrophysical turbulence

Astrophysical turbulence exists everywhere in the Universe; in our solar system (such as solar wind), our galaxy (individual astrophysical sources and interstellar medium), and extra galaxies. For instance, Armstrong et al. (1995) found a Kolmogorov-like spectrum of electron density in the nearby (within 1 kpc from the Earth) ISM,

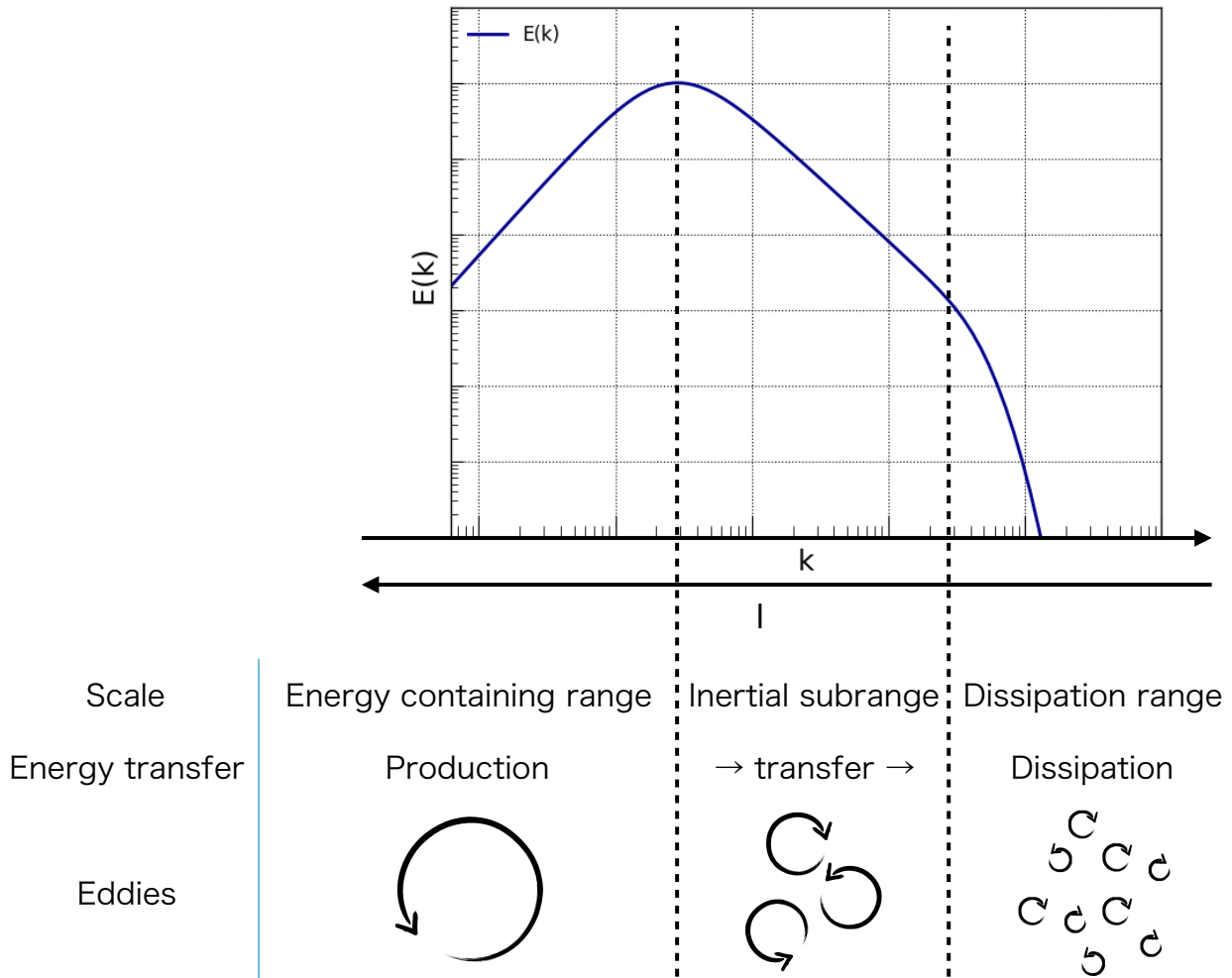


Figure 2.7: Turbulence energy spectrum (top) and schematic picture of turbulence (bottom).

raging in over five orders of magnitude from 10^{-13} m^{-1} to 10^{-8} m^{-1} in wavenumber space. This is interpreted as the subrange power-law feature seen in Kolmogorov turbulence, and the containing energies are injected from individual astrophysical sources, such as supernova explosions.

The turbulence in individual sources, however, is not well understood both observationally and theoretically. In a shock wave of a supernova remnant, which is our interest, the turbulence is believed to be self-generated by the particle that is accelerated in the shock. The hybrid simulation including a MHD shock and an individual relativistic particle is computationally difficult and challenging. With the limited computational boxes and time intervals, Bohm-like turbulence, of which $E(k)$ is proportional to k^{-1} , was shown to grow as the particle is accelerated via DSA (Caprioli and Spitkovsky, 2014a,b,c). It is also shown that for a strong shock ($\mathcal{M} \geq 60$) the diffusion coefficient of the particle becomes smaller than Bohm limit (Reville et al., 2008; Caprioli and Spitkovsky, 2014c). Although particle acceleration in a shock wave is strongly dependent on the diffusion and the corresponding turbulence, observational constraints have not been obtained yet.

Table 2.2: Parameters of turbulence

Hydrodynamical turbulence			
	Large eddy	Inertial subrange	Small eddy
Length	L	ℓ	ℓ_ν
Wavenumber	k_L	k	k_ν
Velocity [†]	δu_L	δu_ℓ	δu_ν
Time scale [‡]	$L/\delta u_L$	$\tau_\ell \sim \ell/\delta u_\ell$	
Energy	δu_L^2	δu_ℓ^2	
Energy transport (ϵ)	$= \langle \mathbf{u} \cdot \mathbf{f} \rangle \sim \delta u_L^3/L$	$\sim \delta u_\ell^2/\tau_\ell \sim \delta u_\ell^3/\ell$	
Energy dissipation			ν
Velocity scaling		$\delta u_\ell \sim (\epsilon \ell)^{1/3}$	
Length scaling*		$\ell_\nu \sim (\nu^3 \epsilon)^{1/4} \sim \text{Re}^{-3/4} L$	
Spectrum		$E(k) \sim \epsilon^{2/3} k^{-5/3}$	
Magnetohydrodynamical turbulence			
	Large eddy	Inertial subrange	Small eddy
Length	L	ℓ	ℓ_ν
Wavenumber	k_L	k	k_ν
Elasser field	δu_L	$\mathbf{z}^\pm = \mathbf{u} \pm \delta \mathbf{B}$	
Alfvénic velocity		$v_A = B_0/\sqrt{4\pi\rho}$	
Alfvénic time scale		$\tau_A \sim \ell_\parallel/v_A$	
Assumption		$\tau_A \ll \tau_s \sim \ell/\delta u_\ell$	
Time scale [‡]	$L/\delta u_L$	$\tau_\ell \sim \tau_s^2/\tau_A$	
Energy	δu_L^2	δu_ℓ^2	
Energy transport (ϵ)	$= \langle \mathbf{u} \cdot \mathbf{f} \rangle \sim \delta u_L^3/L$	$\sim \delta u_\ell^2/\tau_\ell \sim \ell_\parallel \delta u_\ell^4/\ell^2 v_A$	
Energy dissipation			ν
Velocity scaling		$\delta u_\ell \sim (\epsilon v_A)^{1/4} \ell_\parallel^{-1/4} \ell^{1/2}$ isotropy ($\ell \sim \ell_\parallel$): $\delta u_\ell \sim (\epsilon v_A \ell)^{1/4}$ anisotropy ($\ell \sim 1/k_{\parallel,0}$, $\ell \sim \ell_\perp$): $\delta u_\ell \sim (\epsilon v_A)^{1/4} k_{\parallel,0}^{1/4} \ell_\perp^{1/2}$	
Spectrum		isotropy: $E(k) \sim \epsilon^{2/3} k^{-5/3}$ anisotropy: $E(k) \sim (\epsilon v_A k_{\parallel,0})^{1/2} k_\perp^{-2}$	

[†] Velocity difference between the scale length.

[‡] Cascade time scale; time of energy transport.

* Viscous dissipation scale.

2.5 Radiation processes

Nonthermal radiation is a major tool to untangle the nature of astrophysics ongoing far away from us. This section briefly summarizes four main radiation processes: synchrotron radiation (Section 2.5.1), inverse Compton scattering (Section 2.5.2), bremsstrahlung (Section 2.5.3), which are emitted by electrons, and π^0 decay (Section 2.5.4), which is originated from protons. The details can be found, e.g., in Rybicki and Lightman (1986); Longair (2011); Kafexhiu et al. (2014).

2.5.1 Synchrotron radiation

For a charged particle in magnetic field, its direction is bent by the field, emitting electromagnetic wave of which frequency depends on the particle energy and the strength of the magnetic field. If the particle is relativistic, the radiation is called *synchrotron* radiation. The synchrotron radiation mainly arises from a relativistic electron because of its light mass. Hereafter the energies of an electron and a synchrotron photon are denoted by E_e (or its Lorentz factor of γ_e) and ε (or frequency of ω), respectively.

The radiative power of synchrotron radiation is given by

$$P_{\text{synch}} = - \left(\frac{dE_e}{dt} \right)_{\text{synch}} = \frac{4}{3} \sigma_T c \gamma_e^2 U_B, \quad (2.56)$$

with Thomson cross section of $\sigma_T = \frac{8\pi r_0^2}{3}$, where $r_0 = \frac{e^2}{m_e c^2}$ is the classical electron radius, and energy density of magnetic field of $U_B = \frac{B^2}{8\pi}$. The radiation from a relativistic particle is concentrated within the angle of $\sim 1/\gamma_e$ from the momentum direction due to the beaming effect. The synchrotron radiation power from a single electron is described with

$$P(\omega) = \frac{\sqrt{3}}{2\pi} \frac{q^3 B \sin \alpha}{m_e c^2} F \left(\frac{\omega}{\omega_c} \right), \quad (2.57)$$

$$\omega_c = \frac{3}{2} \frac{eB}{m_e c} \gamma_e^2 \sin \alpha. \quad (2.58)$$

Here ω_c is referred to as the characteristic frequency of synchrotron radiation. Using the modified Bessel function of $K_{5/3}$, the function $F(x)$ is given by

$$F(x) = x \int_x^\infty K_{5/3}(\xi) d\xi, \quad (2.59)$$

which is peaked at roughly $x = \frac{\omega}{\omega_c} \sim 0.29$.

One can obtain the synchrotron spectrum by integrating the product of Equation 2.57 and the electron distribution over the electron energy. Assuming that the energy distribution of the electron is power-law, $\frac{dN_e}{dE_e} \propto E_e^{-s}$, the energy spectrum of synchrotron radiation is described with

$$J(\omega) = \int_0^\infty P_{\text{synch}}(\omega) dN_e \quad (2.60)$$

$$\approx \omega^{-\frac{s-1}{2}}. \quad (2.61)$$

The photon number spectrum of synchrotron radiation is given by $J\omega^{-1} \approx \omega^{-(s+1)/2}$. Therefore the relation between the spectral indices of the electron (s) and photon (Γ) is derived as

$$\Gamma = \frac{(s+1)}{2}. \quad (2.62)$$

2.5.2 Inverse Compton scattering

High-energy electron interacts with an ambient photon, and scatters the photon up to higher energy, which is called inverse Compton (IC) scattering. In the rest frame of the electron, the energy of the target photon is $\gamma_e \varepsilon_i$, where ε_i is the initial photon energy in the observer frame. In Thomson regime ($\gamma_e \varepsilon_i \ll m_e c^2 = 0.511$ MeV), the photon energy does not change after the collision. Therefore the up-scattered photon (ε) gains energy by γ_e^2 in the process of inverse Compton scattering (i.e., $\varepsilon \sim \gamma_e^2 \varepsilon_i$).

The radiative power of IC scattering, P_{IC} , is given by

$$P_{\text{IC}} = - \left(\frac{dE_e}{dt} \right)_{\text{IC}} = \frac{4}{3} \sigma_T c \gamma_e^2 U_{\text{ph}}, \quad (2.63)$$

where U_{ph} indicates the energy density of the target photon field. It should be noted that P_{IC} has a similar form of P_{synch} , and the ratio is described with only U_B and U_{ph} :

$$\frac{P_{\text{synch}}}{P_{\text{IC}}} = \frac{U_B}{U_{\text{ph}}}. \quad (2.64)$$

This is used to estimate the B value from the observed flux of synchrotron radiation and inverse Compton scattering.

In general, the cross section of inverse Compton scattering including Klein-Nishina (KN) regime, where Thomson limit is not valid anymore, is described as

$$\sigma_{\text{KN}}(\varepsilon_i, \varepsilon, \gamma_e) = \frac{2\pi r_0^2 m_e c^2}{\varepsilon_i \gamma_e^2} \left[2q \ln q + 1 + q - 2q^2 + \frac{\delta_e^2 q^2 (1-q)}{2(1+\delta_e q)} \right], \quad (2.65)$$

where $\delta_e = 4\gamma_e \varepsilon_i / (m_e c^2)$ is a parameter that is indicative of the importance of KN effect, and $q = \frac{\varepsilon}{\delta_e (\gamma_e m_e c^2 - \varepsilon)}$ (see, e.g., Blumenthal and Gould (1970) for details, and see also Khangulyan et al. (2014) for analytical expressions). The IC emissivity is calculated by

$$\epsilon_{\text{IC}} = c \int d\gamma_e N_e(\gamma_e) \int d\varepsilon_i n(\varepsilon_i) \sigma_{\text{KN}}(\varepsilon_i, \varepsilon, \gamma_e), \quad (2.66)$$

where $n(\varepsilon)$ indicates the distribution of the target photon field. It is generally presumed that the seed photon field has Planckian distribution with temperature T ;

$$n(\varepsilon) = \frac{\varepsilon^2}{\pi^2 \hbar^3 m_e c^2} \left[\exp\left(\frac{\varepsilon}{kT}\right) - 1 \right]^{-1}. \quad (2.67)$$

For the seed photon field, star lights, such as optical or infrared photons, are sometimes used in addition to Cosmic Microwave Background filling the Universe with $T = 2.7$ K and $U_{\text{ph}} = 0.26$ eV cm⁻³.

In Thomson regime, the IC spectrum has a power-law distribution with the same photon index as the synchrotron spectrum (i.e., $\Gamma = (s + 1)/2$). In KN regime, the IC spectrum is suppressed especially at higher energies due to suppression of the cross section.

2.5.3 Bremsstrahlung

Nonthermal bremsstrahlung arises from a relativistic particle interacting with a thermal population. There are mainly two types of bremsstrahlung: electron-electron collision and electron-nucleon collision. The energy loss rate of electron-proton bremsstrahlung emission is

$$- \left(\frac{dE_e}{dt} \right)_{\text{brems}} = 2\alpha c \sigma_T n_{\text{H}} m_e c^2 \beta \gamma_e (\ln \gamma_e + 0.36), \quad (2.68)$$

where α is the fine-structure coefficient.

The emissivity of electron-electron and electron-nucleon bremsstrahlung is described as

$$\epsilon_{\text{brems}}(\varepsilon) = 4\pi n \Delta_{\text{He}}^{e,n} \int dE_e N_e(E_e) \sigma_{\text{brems}}, \quad (2.69)$$

with $N_e(E_e)$ being the energy distribution of electrons. Here $\Delta_{\text{He}}^{e,n}$ represents a correction factor for the presence of helium (i.e., $\Delta_{\text{He}}^e = 1.2$ and $\Delta_{\text{He}}^n = 1.4$). The differential cross section of bremsstrahlung is calculated in, e.g., Haug (1975), and omitted here because of its complexity. The bremsstrahlung spectrum repeats the parental energy spectrum of electron (i.e., $\Gamma \approx s$), because the differential cross section is inversely proportional to the photon energy and is hardly dependent on the electron energy in the relativistic regime.

2.5.4 π^0 -decay

Nonthermal radiation is attributed to not only relativistic electrons but also relativistic protons. Relativistic protons collide with ambient protons in the interstellar matter, which is referred to as pp interaction. The secondary products of this interaction contain pions (π^0), which decay into two gamma-ray photons within a lifetime of 8.30×10^{-17} s. In the rest frame of π^0 , the gamma-ray energy resulting from π^0 decay is 67.5 MeV because the rest mass of π^0 is 137 MeV.

The approximate formulation of the cross section of pp interaction, σ_{pp} , is described as

$$\sigma_{pp}(E_p) \approx 30 \left[0.95 + 0.06 \ln \left(\frac{E_p - m_p c^2}{1 \text{ GeV}} \right) \right] \text{ mb}, \quad (2.70)$$

where E_p denotes the proton energy. The π^0 emissivity of pp interaction is then calculated by

$$\epsilon_{\pi^0, pp}(E_{\pi^0}) = 4\pi n \int_{E_{p,\text{th}}}^{\infty} dE_p N_p \sigma_{pp}(E_p), \quad (2.71)$$

where n is the number density of the ambient protons, $E_{p,\text{th}}$ is the threshold energy of the proton which is energetic enough to produce π^0 via pp collision (i.e., $E_{p,\text{th}} = 2m_{\pi^0}c^2(1 + m_{\pi^0}/4m_p) \approx 280$ MeV with the pion mass of m_{π^0}), and N_p is the energy distribution of protons. The resulting gamma-ray emissivity is derived as

$$\epsilon_{\pi^0}(\varepsilon) = 2 \int_{E_{\text{min}}}^{\infty} dE_{\pi^0} \frac{\epsilon_{\pi^0, pp}(E_{\pi^0})}{\sqrt{E_{\pi^0}^2 - m_{\pi^0}^2 c^4}}, \quad (2.72)$$

where E_{min} is given by $\varepsilon + (m_{\pi^0}^2 c^4 / 4\varepsilon)$ with ε being the produced gamma-ray energy. Above ~ 1 GeV, the π^0 -decay spectrum obeys the almost same spectrum of protons (i.e., $\Gamma \approx s$). Below ~ 100 MeV, the π^0 -decay spectrum drops drastically in spite of the spectral parameters of protons. This feature is called π^0 *bump* and used as a probe of the hadronic radiation.

2.5.5 Broadband nonthermal radiation spectra

Calculation of the nonthermal radiation mentioned previously is implemented in ‘‘Naima’’³ (Zabalza, 2015). Figure 2.8 presents these nonthermal radiation spectra, calculated with Naima, from relativistic particles of which energy distribution is given by

$$\frac{dN}{dE} \propto E^{-s} \exp\left(-\frac{E}{E_c}\right), \quad (2.73)$$

with an exponential cutoff energy of E_c . To produce Figure 2.8, the parameters are set to the following values: the magnetic field B is 10 μG , the ambient number density n is 1 cm^{-3} , the spectral index s is 2, E_c is 10 TeV for both electron and proton populations, the total energy of electrons W_e is 10^{45} erg, and the total energy of protons W_p is 10^{47} erg. The IC spectrum is calculated for the case that the seed photon field is only CMB.

³<http://www.github.com/zblz/naima>

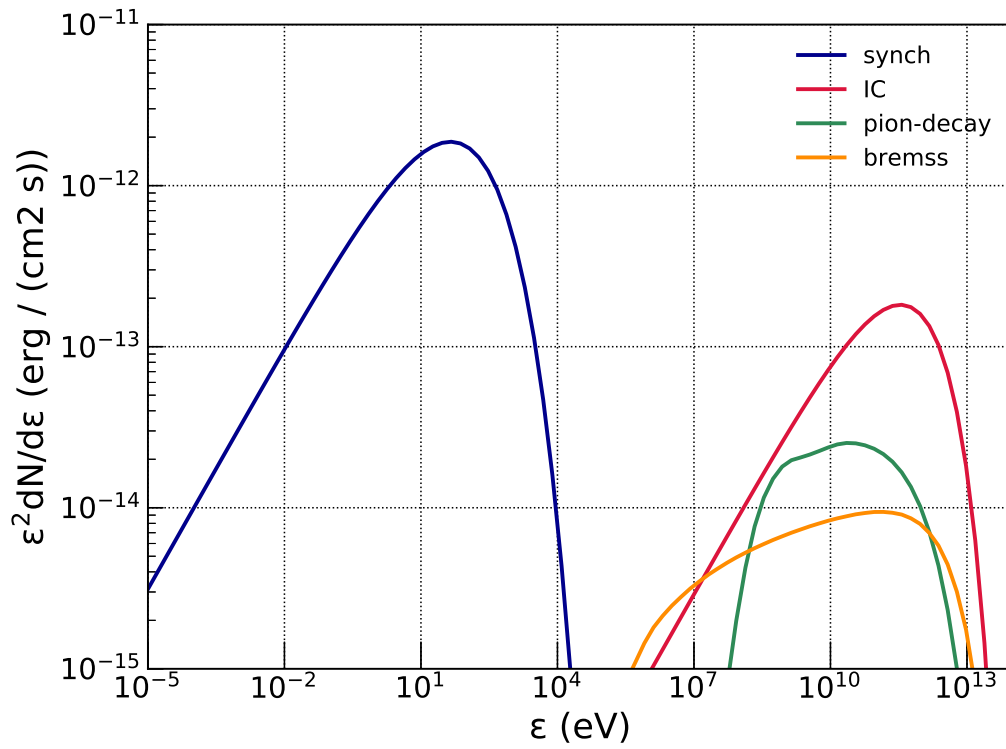


Figure 2.8: Radiation spectra of synchrotron emission, inverse Compton scattering, π^0 -decay, bremsstrahlung, calculated for $s = 2$, $E_c = 10$ TeV (for both electron and proton), $B = 10 \mu\text{G}$, $n = 1 \text{ cm}^{-3}$, $W_e = 10^{45}$ erg, and $W_p = 10^{47}$ erg, making use of Naima.

2.6 Spectral model around SNR shock

High-energy electrons, that are accelerated via diffusive shock acceleration at the shock front, are confined around the shock because of a balance between energy loss and diffusion. Taking the energy loss and diffusion into consideration, a transport equation of electrons yields a spectral model in the vicinity of the shock wave. First, we present spectral modification due to energy loss in Section 2.6.1. Second, we give an overview of Zirakashvili and Aharonian (2007), which derived asymptotic expressions of electrons (Section 2.6.2), and the corresponding synchrotron X-ray (Section 2.6.3) and inverse Compton (IC) gamma-ray (Section 2.6.4) in the framework of the cooling-limited electron in Bohm diffusion.

2.6.1 Spectral deformation

The energy spectrum of particles accelerated in an SNR is a key factor for both understandings of the origin of galactic cosmic rays and the acceleration mechanism in the SNR shock wave. The standard DSA predicts the spectral index, s , appears to be 2 for a strong shock. The particle spectrum in the SNR, however, deviates from the single power law with $s = 2$ because of the energy loss and has an exponential cutoff due to balance between acceleration and diffusion (escape). In the following, we summarize the energy loss rate of radiation and the spectral deformation due to the loss.

Energy loss

Once a particle is accelerated up to the relativistic regime, it emits nonthermal radiation (Section 2.5) and suffers from energy loss. An electron, in particular, loses its energy more quickly than a proton does. The energy-loss rate of an electron is given in Section 2.5: the synchrotron loss is Equation 2.65, the inverse Compton loss is Equation 2.63, and the bremsstrahlung loss is Equation 2.68. Besides, Coulomb collision between a relativistic electron and background particles plays an important role in energy loss. The energy loss due to Coulomb ionization is given by

$$-\left(\frac{dE}{dt}\right)_{\text{Cou}} = \frac{3}{2} c \sigma_T \frac{n_e m_e c^2}{\beta} \ln \Lambda, \quad (2.74)$$

where Λ is so-called Coulomb logarithm,

$$\Lambda = 1.12 \sqrt{\gamma_e} \beta^2 \frac{\alpha}{\sqrt{4\pi n_e r_0^3}} \approx 40. \quad (2.75)$$

Generally, the timescale of energy loss, τ , is described as

$$\tau = \frac{E}{\left|\frac{dE}{dt}\right|}. \quad (2.76)$$

Figure 2.9 presents the timescales of the nonthermal radiation processes, calculated for a typical parameter set for SNRs with $B = 10 \mu\text{G}$ and $n_e = n_H = 1 \text{ cm}^{-3}$. For young (\lesssim a few thousand years) SNRs, in which we are interested in this thesis, sub-MeV and multi-TeV electrons suffer from the energy loss of Coulomb collision and synchrotron radiation, respectively, because the radiation timescale becomes smaller than the age (i.e., $\tau \leq \tau_{\text{age}}$).

Spectral modification due to energy loss

Given the injection spectrum of accelerated particles ($Q(E)$), the particle distribution ($N(E)$) follows Fokker-Planck equation:

$$\frac{\partial N(E)}{\partial t} = -\frac{\partial}{\partial E} \left(\frac{\partial E}{\partial t} N(E) \right) + \frac{1}{2} \frac{\partial^2}{\partial E^2} \left(\frac{d\langle(\Delta E)^2\rangle}{dt} N(E) \right) - \frac{N(E)}{\tau_{\text{esc}}} + Q. \quad (2.77)$$

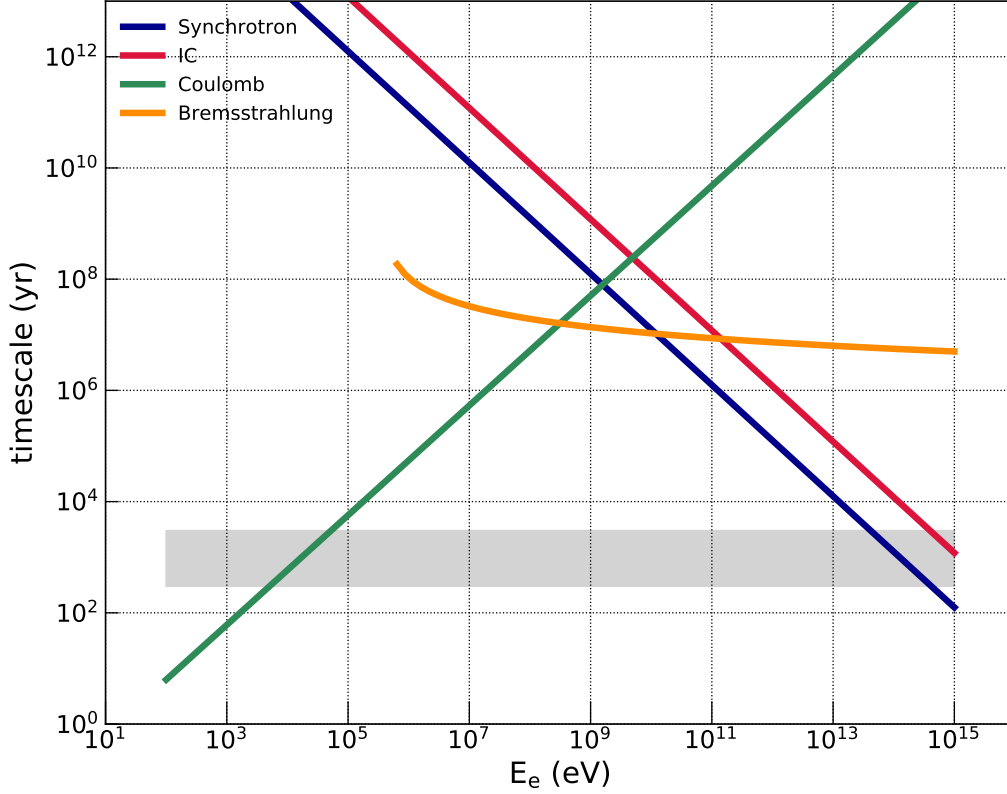


Figure 2.9: Timescale of energy losses of synchrotron radiation (shown in blue), inverse Compton scattering (red), Coulomb collision (green), and Bremsstrahlung (orange). calculated for $B = 10 \mu\text{G}$ and $n_e = n_H = 1 \text{ cm}^{-3}$. Only CMB is taken account for IC scattering timescale. The horizontal grey band indicates the age of 300–3000 yr.

In the right-hand side of Equation 2.77, the first term indicates the energy loss, the second term describes diffusion in energy space, and the third term represents escaping particles. Assuming that a steady state ($\partial N/\partial t = 0$) and the second and third terms are negligible, Equation 2.77 is reduced to

$$\frac{\partial}{\partial E} \left(\frac{\partial E}{\partial t} N(E) \right) = Q(E). \quad (2.78)$$

$Q(E)$ has a power-law form for the standard DSA (i.e., $Q(E) \propto E^{-s}$), and the solution of Equation 2.78 is derived as

$$N(E) = \frac{1}{s-1} \frac{E}{dE/dt} Q(E) = \frac{1}{s-1} \tau(E) Q(E), \quad (2.79)$$

where τ indicates the energy-loss timescale using Equation 2.76.

In Equation 2.79, if the timescale of energy loss depends on the energy, the energy distribution is significantly modified from the injection spectrum. For the synchrotron-limited case ($\tau_{\text{synch}} \leq t_{\text{age}}$), since τ_{synch} is proportional to E^{-1} by using Equation 2.56 and Equation 2.76, the distribution follows $E^{-(s+1)}$ by Equation 2.79. Thus the electron with energy above $E_{b,\text{synch}}$, which gives $\tau_{\text{synch}} = t_{\text{age}}$ and roughly appears in multi-TeV (Figure 2.9), is described with the *synchrotron-steepened* power law with the spectral index of $s + 1$. Since the X-ray synchrotron is dominantly radiated from TeV electrons, the X-ray synchrotron spectrum is also modified by the effect of synchrotron energy loss. The corresponding photon index of synchrotron spectrum is given by $\Gamma = (s + 2)/2$ using Equation 2.62. For the Coulomb-collision-limited case ($\tau_{\text{Cou}} \leq t_{\text{age}}$), the electron spectrum has a form of $E^{-(s-1)}$ because of $\tau_{\text{Cou}} \propto E$ by Equation 2.74 and Equation 2.76. The electron with energy below $E_{b,\text{Cou}}$, which gives $\tau_{\text{Cou}} = t_{\text{age}}$ and roughly appears in sub-MeV (Figure 2.9), is described with the *Coulomb-ionization-flattened* power law with the spectral index of $s - 1$.

2.6.2 Electron

This section summarizes the derivation of asymptotic expressions of accelerated electrons around the SNR shock (see Section 2 in Zirakashvili and Aharonian (2007) for details). The general solution is then applied for our assumption which energy loss of electrons is limited by synchrotron radiation, and diffusion of electrons is in the widely accepted Bohm regime. In Bohm diffusion, the mean free path of particle is roughly as large as its gyroradius.

Distribution function

Distribution function, f , is fundamental for describing the behaviour and property of particle distribution. It is defined in some different ways (see below) depending on the context:

$$dN = f_e dE \quad (\text{energy space}) \quad (2.80)$$

$$dN = f_p d^3 p = f_p 4\pi p^2 dp \quad (\text{momentum space}) \quad (2.81)$$

$$dN = f_x dE dx \quad (\text{coordinate}) \quad (2.82)$$

$$dN = f_r dE d^3 r = f_r 4\pi r^2 dr \quad (\text{coordinates}) \quad (2.83)$$

$$dN = f d^3 p d^3 r \quad (\text{phase - space coordinates}) \quad (2.84)$$

One needs to select an adequate distribution function for each problem.

To connect energy distribution (f_e) and momentum distribution (f_p), Equation 2.80 and Equation 2.81 yield

$$f_p(p) = f_e(E) \frac{1}{4\pi p^2} \frac{dE}{dp}. \quad (2.85)$$

In the relativistic regime, the energy is proportional to the momentum, $E \propto p$, one obtains

$$f_p(p) \propto f_e(E) E^{-2}. \quad (2.86)$$

Therefore, if the energy distribution is given by $f_e \propto E^{-2}$ in such as DSA, the corresponding momentum distribution is $f_p \propto p^{-4}$. In the non-relativistic case, the energy is described with $E \propto p^2$, Equation 2.85 gives a relation of

$$f_p(p) \propto f_e(E) E^{-1/2}. \quad (2.87)$$

General analytical spectrum in higher energies

One-dimensional diffusion-convection equation around a shock wave is described with

$$\frac{\partial}{\partial x} D \frac{\partial N}{\partial x} - u \frac{\partial N}{\partial x} + \frac{1}{p^2} \frac{\partial}{\partial p} [p^2 b(p) N] = 0, \quad (2.88)$$

where N , u , D , and $b(p)$ are the momentum distribution function, flow speed, diffusion coefficient of electron, and energy loss rate, respectively. The first, second, and third terms in Equation 2.88 indicate, respectively, diffusion, convection, and energy loss.

As shown in Figure 2.10, we consider the rest frame of the shock wave. Subscripts of 0, 1, and 2 denote, respectively, quantities at the shock front, upstream, and downstream. The boundary condition at the shock front is given by

$$u_1 \frac{p}{\gamma_s} \frac{\partial N_0}{\partial p} = D_2 \left. \frac{\partial N}{\partial x} \right|_{x=+0} - D_1 \left. \frac{\partial N}{\partial x} \right|_{x=-0}, \quad (2.89)$$

where γ_s denotes the power-law index of the momentum distribution (i.e., $\gamma_s = 3\sigma/(\sigma - 1)$ for the standard DSA). We assume some convenient expressions as follows. The solution of particle distribution has a form given by

$$N_{1,2} = K_{1,2}(x,p) \exp[S_{1,2}(x,p)], \quad (2.90)$$

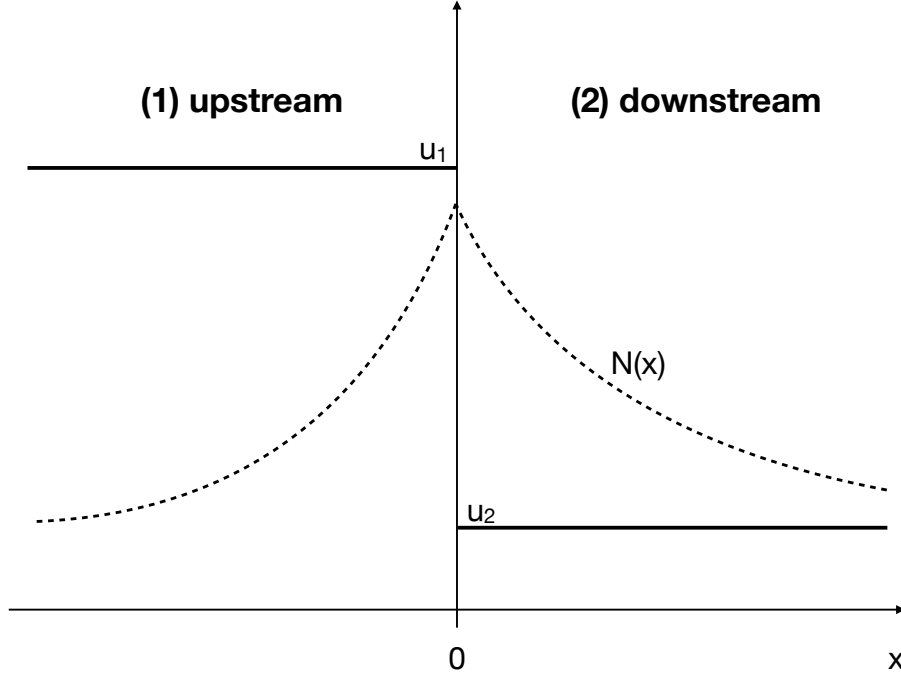


Figure 2.10: Diagram of SNR shock (imitating Figure 1 in Zirakashvili and Aharonian (2007)). $x < 0$ and $x > 0$ indicate the upstream and downstream regions, respectively. Distribution function, $N(x)$, is assumed to be peaked at the shock front ($x = 0$), and exponentially drops off.

where $S(x, p)$ is assumed to be proportional to $b(p)$. At the shock front, the functions $K(x, p)$ and $S(x, p)$ should satisfy conditions:

$$S_0(p) = S_1(p)|_{x=0} = S_2(p)|_{x=0}, \quad (2.91)$$

$$K_0(p) = K_1(p)|_{x=0} = K_2(p)|_{x=0}. \quad (2.92)$$

We solve the equations above to obtain S_0 and K_0 , which are respectively given by

$$S_0 = -\frac{\gamma_s^2}{u_1^2} \int_0^p \frac{dp'}{p'^2} \left(\sqrt{b_1(p')D_1(p')} + \sqrt{b_2(p')D_2(p')} \right)^2, \quad (2.93)$$

$$K_0 \propto p^{-1/2} \exp \left[\int dp \frac{\sqrt{D_2} \frac{\partial}{\partial p} \sqrt{b_2} + \sqrt{D_1} \frac{\partial}{\partial p} \sqrt{b_1}}{\sqrt{b_1 D_1} + \sqrt{b_2 D_2}} \right]. \quad (2.94)$$

Here we assume that the ratio of diffusion coefficients upstream and downstream is given by κ , and the ratio of energy losses upstream and downstream is given by ξ , namely,

$$D_2 = D = \kappa D_1, \quad (2.95)$$

$$b_2 = b = \xi b_1. \quad (2.96)$$

Finally Equation 2.90 can be reduced to the distribution at the shock front:

$$N_0 \propto \sqrt{\frac{b}{p}} \exp \left[-\frac{\gamma_s^2}{u_1^2} \left(1 + \frac{1}{\sqrt{\xi \kappa}} \right)^2 \int_0^p \frac{dp'}{p'^2} b(p') D(p') \right]. \quad (2.97)$$

The spectra upstream $F_1(p)$ and downstream $F_2(p)$ are obtained by the integrations of $N(x, p)$ over x :

$$F_1(p) = \int_{-\infty}^0 dx N(x, p) = \frac{\xi}{1 + \sqrt{\kappa \xi}} \frac{u_1 p}{\gamma_s b(p)} N_0(p), \quad (2.98)$$

$$F_2(p) = \int_0^{\infty} dx N(x, p) = \frac{\sqrt{\kappa \xi}}{1 + \sqrt{\kappa \xi}} \frac{u_1 p}{\gamma_s b(p)} N_0(p). \quad (2.99)$$

Equation 2.97, Equation 2.98, and Equation 2.99 represent the general spectral forms in the higher energies where the particles effectively lose their energies. In the lower energies, since the energy loss is negligible, the particles are simply distributed in the power-law form. Note that one should perform numerical calculations to obtain the spectral properties of a transition regime between the lower and higher energies. This is beyond the scope of this thesis, and the results of numerical calculations are taken from Zirakashvili and Aharonian (2007).

Spectrum in full-energy band

Now we apply Bohm-type diffusion for $D(p)$ and synchrotron cooling for $b(p)$ in the general expression of the distribution given by Equation 2.97. This application assumes accelerated electrons because the energy loss of electrons is dominated by synchrotron radiation in their higher energies. The diffusion coefficient in Bohm regime is described with

$$D_{\text{Bohm}}(p) = \frac{1}{3}\eta cr_g = \frac{1}{3}\eta \frac{c^2 p}{qB}. \quad (2.100)$$

where η is a constant factor indicating the deviation of mean free path of particle from gyro radius (r_g) (a.k.a., Bohm factor). The energy loss rate of synchrotron radiation is given by

$$b(p) = \frac{4}{9} \frac{q^4 B^2 p^2}{m^4 c^6}. \quad (2.101)$$

Here we obtain the relation of $\xi = \kappa^{-2}$ because of $b \propto B^2$ and $D \propto B^{-1}$.

In the lower energies, the particle distribution which is not effectively cooled by synchrotron radiation can be predicted from the standard DSA,

$$N_0 \propto p^{-\gamma_s}, \quad (2.102)$$

$$F_{1,2} \propto p^{-(\gamma_s+1)}. \quad (2.103)$$

Throughout this thesis, we assume $\gamma_s = 4$ for a strong shock with the compression ratio of $\sigma = 4$. Since the cooling length is proportional to p^{-1} , $F(p)$ is steeper than the distribution at the shock front.

In the higher energies, the synchrotron cooling becomes non-negligible. Inserting Equation 2.100 and Equation 2.101 to Equation 2.97, we obtain

$$N_0 \propto p^{\frac{1}{2}} \exp \left[- \left(\frac{p}{p_0} \right)^2 \right], \quad (2.104)$$

where a cutoff energy parameter, p_0 , is described as

$$p_0 = \left(1 + \frac{1}{\sqrt{\kappa\xi}} \right)^{-1} \frac{(mc)^2}{\gamma_s \sqrt{2q^3/27}} u_1 B^{-\frac{1}{2}} \eta^{-\frac{1}{2}}. \quad (2.105)$$

It should be noted that the exponential cutoff shape of the electron spectrum follows a form of $\exp(-p^2)$ rather than a simple form such as $\exp(-p)$.

In the entire energy band, Zirakashvili and Aharonian (2007) derived the analytical expression of the electron spectrum as

$$N_0 \propto p^{-4} \left[1 + 0.523 \left(\frac{p}{p_0} \right)^{\frac{9}{4}} \right]^2 \exp \left[- \left(\frac{p}{p_0} \right)^2 \right], \quad (2.106)$$

in the case of $\kappa = \sqrt{1/11}$, which represents a random compression of a shock over the obliquity. Assuming the equal values of D and B in the upstream and downstream regions (i.e., $\kappa = 1$), the spectrum is slightly modified as

$$N_0 \propto p^{-4} \left[1 + 0.66 \left(\frac{p}{p_0} \right)^{\frac{5}{2}} \right]^{\frac{9}{5}} \exp \left[- \left(\frac{p}{p_0} \right)^2 \right]. \quad (2.107)$$

The $\kappa = \sqrt{1/11}$ case is adopted in this thesis since it is more realistic. In the higher energies ($p \gg p_0$) in Equation 2.106, N_0 becomes proportional to $p^{1/2} \exp(-p^2)$, which is identical to the solution in the higher energies given by Equation 2.104. The transition function, which describes the part except for the cutoff power law, was determined by the numerical calculation of Equation 2.88 and requiring a smooth connection between the lower and higher energy bands. The schematic picture of the spectra in the lower, higher, and entire energies are illustrated in Figure 2.11.

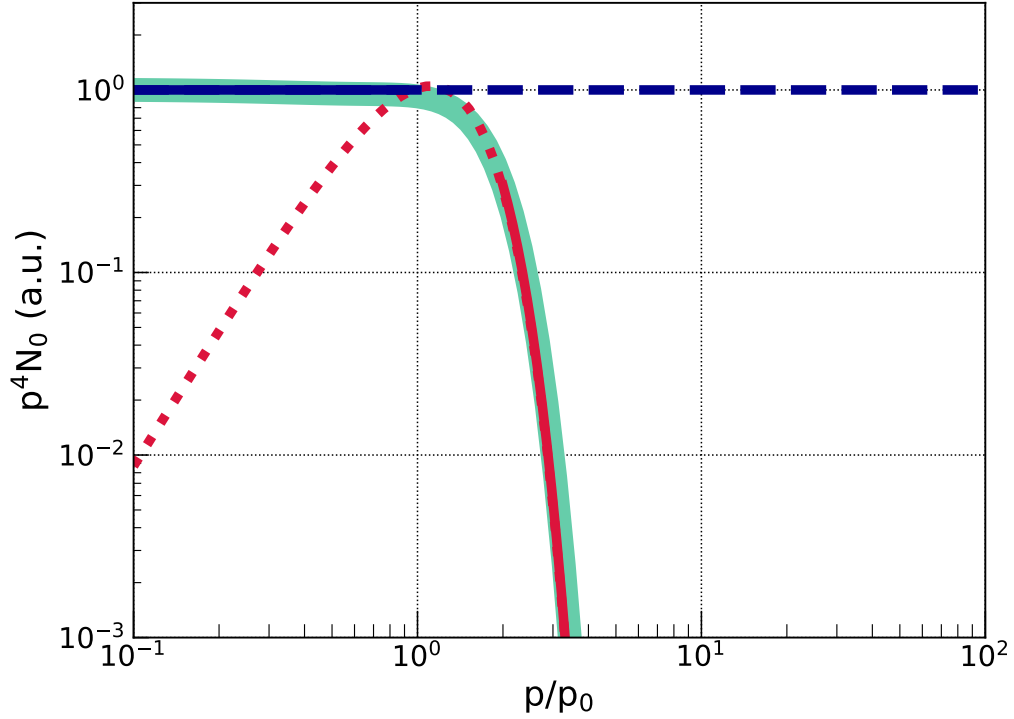


Figure 2.11: The electron spectrum in Bohm diffusion. The blue, red, and thick green lines indicate the analytical expressions in the lower (Equation 2.102), higher (Equation 2.104), and entire energies (Equation 2.106), respectively. The solid line shows the model in the relevant energy band, while the model in the other energy band is shown with the dashed line.

2.6.3 Synchrotron X-ray

Synchrotron emissivity

The synchrotron emissivity is described with

$$\epsilon(\omega) = \frac{\sqrt{3}Bq^3}{2\pi mc^2} \int p^2 dp N(p) R\left(\frac{\omega}{\omega_c}\right), \quad (2.108)$$

where characteristic frequency of synchrotron emission (ω_c) is $1.5qBp^2/m^3c^3$. Integrating the emissivity over the line of sight and the solid angle, and replacing $N(p)$ to the integrated spectrum of $F(p)$, the spectrum of synchrotron radiation is given by

$$J(\omega) = \frac{\sqrt{3}Bq^3}{2\pi mc^2} \int dp F(p) p^2 R\left(\frac{\omega}{\omega_c}\right). \quad (2.109)$$

Note that the photon number spectrum is given by $dN_X/d\varepsilon = J(\omega)\omega^{-1}$. The function to describe the synchrotron emission from a single electron can be described in an analytical form of

$$R\left(\frac{\omega}{\omega_c}\right) = \frac{1.81 \exp\left(-\frac{\omega}{\omega_c}\right)}{\sqrt{\left(\frac{\omega_c}{\omega}\right)^{2/3} + \left(\frac{3.62}{\pi}\right)^2}}. \quad (2.110)$$

This R function is often described using delta approximation which is peaked around 0.29: $R(x) \propto \delta(0.29 - x)$ for $x = \omega/\omega_c$. However, this approximation produces a somewhat different analytical expression compared to precise derivation, as mentioned in Zirakashvili and Aharonian (2007).

Spectrum in full-energy band

In the lower energy band, the synchrotron photon spectrum is radiated from the electron in the lower energies, described by $F(p) \propto p^{-(\gamma_s+1)}$. Therefore the synchrotron spectrum in the lower energies also has the power-law form:

$$\frac{dN_X}{d\varepsilon} \propto \varepsilon^{-\frac{\gamma_s}{2}}. \quad (2.111)$$

The relation between the spectral index of electrons (s) and that of synchrotron photons (Γ) is given by $\Gamma = (s + 1)/2$ (Equation 2.62) with $s = \gamma_s - 1$ in this case.

In the higher energy band, the synchrotron spectrum is radiated from the electron in the higher energies (Equation 2.104). When synchrotron X-rays are radiated from cutoff power-law electrons with a spectral index of s , cutoff momentum of p_0 , and cutoff slope of β , i.e.,

$$F(p) = p^{-s} \exp\left[-\left(\frac{p}{p_0}\right)^\beta\right], \quad (2.112)$$

the synchrotron spectrum is derived as

$$\frac{dN_X}{d\varepsilon} \propto \varepsilon^{-\frac{2s+3\beta-2}{2(\beta+2)}} \exp\left[-\left(\frac{\varepsilon}{\varepsilon_0}\right)^{\frac{\beta}{\beta+2}}\right], \quad (2.113)$$

where

$$\varepsilon_0 = \hbar\beta \left[4 \left(\frac{1}{2+\beta}\right)^{2+\beta}\right]^{1/\beta} \frac{3q}{2m^3c^3} B p_0^2. \quad (2.114)$$

Here the cutoff shape slope of the X-ray spectrum (β_X) is obtained as $\beta_X = \beta/(\beta + 2)$. See Appendix A for the detailed derivations of Equation 2.113 and Equation 2.114. Because the electron spectrum at the shock front in the higher energies is obtained to be Equation 2.104 and the integrated spectrum $F(p)$ is described with $N_0 p^{-1} \propto p^{-1/2} \exp[-(p/p_0)^2]$, applying the spectral index of $s = 1/2$ and the cutoff slope of $\beta = 2$ for Equation 2.113, the photon spectrum is derived:

$$\frac{dN_X}{d\varepsilon} \propto \varepsilon^{-5/8} \exp\left[-\left(\frac{\varepsilon}{\varepsilon_0}\right)^{1/2}\right]. \quad (2.115)$$

Equation 2.114 and Equation 2.105 yield the cutoff energy parameter in the synchrotron X-ray spectrum as

$$\varepsilon_0 = \frac{81mch}{16q^2\gamma_s^2} \left(1 + \frac{1}{\sqrt{\kappa\xi}}\right)^{-2} \eta^{-1} u_1^2. \quad (2.116)$$

Equation 2.116 suggests that the synchrotron cutoff energy is determined by the shock speed (u_1) and Bohm factor (η), and is independent on the magnetic field strength.

In the entire energy band, Zirakashvili and Aharonian (2007) obtained the asymptotic solution:

$$\frac{dN_X}{d\varepsilon} \propto \left(\frac{\varepsilon}{\varepsilon_0}\right)^{-2} \left[1 + 0.38 \left(\frac{\varepsilon}{\varepsilon_0}\right)^{0.5}\right]^{11/4} \exp\left(-\sqrt{\frac{\varepsilon}{\varepsilon_0}}\right) \quad (\kappa = \sqrt{1/11}), \quad (2.117)$$

$$\frac{dN_X}{d\varepsilon} \propto \left(\frac{\varepsilon}{\varepsilon_0}\right)^{-2} \left[1 + 0.46 \left(\frac{\varepsilon}{\varepsilon_0}\right)^{0.6}\right]^{11/4.8} \exp\left(-\sqrt{\frac{\varepsilon}{\varepsilon_0}}\right) \quad (\kappa = 1). \quad (2.118)$$

In the higher energies ($\varepsilon \gg \varepsilon_0$) in Equation 2.117 (and Equation 2.118), $dN_X/d\varepsilon$ becomes $\varepsilon^{-5/8} \exp(-\varepsilon^{1/2})$, which is compatible with the expression at the higher energies given by Equation 2.115. The transition function is determined by the numerical calculation and requiring the smooth connection between the lower and higher energy bands. Figure 2.12 illustrates the schematic picture of the synchrotron spectrum in the lower and higher energies, and how these two spectra are connected in the transition energies.

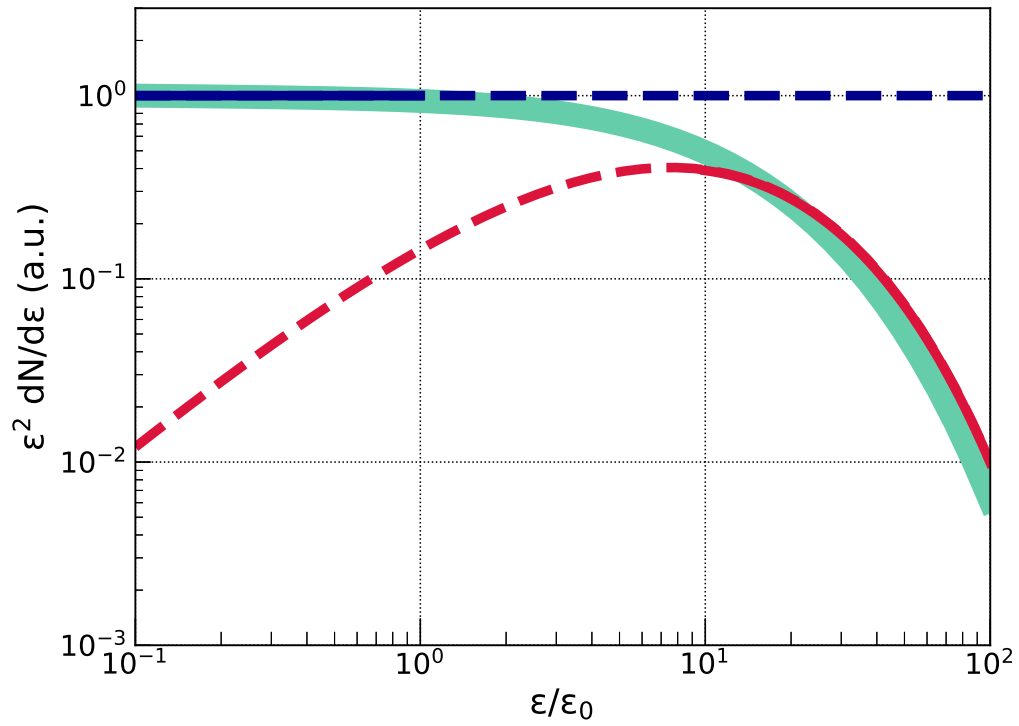


Figure 2.12: The synchrotron X-ray spectrum in Bohm diffusion. The blue, red, and thick green lines indicate the analytical expressions in the lower (Equation 2.111), higher (Equation 2.115), and entire energies (Equation 2.117), respectively. The solid line shows the model in the relevant energy band, while the model in the other energy band is shown with the dashed line.

2.6.4 Inverse Compton gamma-ray

Inverse Compton scattering emissivity

The emissivity of inverse Compton radiation from a single electron with Lorentz factor of γ in isotropic photon field is

$$\epsilon_{\text{IC}}(\omega) = 2\hbar c r_e^2 \int_{\omega_{\text{th}}}^{\infty} d\omega' n(\omega') \frac{\omega}{4\gamma^2 \omega'} \left[1 - 2\frac{\omega^2}{\omega_c^2} + \frac{\omega}{\omega_c} \left(1 + 2 \ln \frac{\omega}{\omega_c} \right) + \frac{\hbar^2 \omega^2}{2m^2 c^4 \gamma^2 \left(1 - \frac{\hbar\omega}{\gamma m c^2} \right)} \left(1 - \frac{\omega}{\omega_c} \right) \right], \quad (2.119)$$

where $\omega_c = 4\omega' \gamma^2 (1 - \hbar\omega/\gamma m c^2)$, r_e is the classical electron radius, and $n(\omega)$ is the energy distribution of the seed photon field (see, e.g., Blumenthal and Gould (1970)). We assume that the target photons have a Planckian distribution described as

$$n(\omega) = \frac{\omega^2 / (c^3 \pi^2)}{\exp(\hbar\omega/kT) - 1}, \quad (2.120)$$

with k and T being Boltzman constant and temperature of the radiation field, respectively.

Inverse Compton spectrum in Klein-Nishina regime

When the Klein-Nishina effect becomes important in the higher energies of electrons, one needs to calculate the integration of Equation 2.119 over the electron energy in order to obtain the IC spectrum. However, it is too complicated to obtain an analytical expression. We instead make use of Naima (Zabalza, 2015) to calculate the IC spectrum in KN regime radiated from the loss-limited electron in Bohm diffusion given by Equation 2.106. It should be noted that the analytical solution in Thomson regime can be obtained, as presented in the next subsection.

Figure 2.13 compares the IC spectra in KN regime with different cutoff energy parameters of electrons and that in Thomson limit. The KN effect is more important for the higher energy of electrons, resulting in a more suppressed IC spectrum in the higher energies in the case of $E_0 = 77$ TeV. Even if E_0 is 7.7 TeV, the IC spectrum in KN regime is suppressed compared to that in Thomson limit. Hence the IC spectrum in KN regime is preferred and adopted in this thesis.

Inverse Compton spectrum in Thomson regime

In Thomson limit, the analytical expression for the IC spectrum can be derived as follows. The assumption of Thomson regime holds when $b_{KN} = 4\frac{kT p_0}{m^2 c^3} \ll 1$. In the lower energy band, the IC spectrum is radiated from the electron in the lower energies, described by $F(p) \propto p^{-(\gamma_s+1)}$. Therefore the IC spectrum in the lower energies also has the power-law form:

$$\frac{dN_\gamma}{d\varepsilon} \propto \varepsilon^{-\frac{\gamma_s}{2}}. \quad (2.121)$$

The relation between the spectral index of electron (s) and that of IC photon (Γ) is given by $\Gamma = (s + 1)/2$ with $s = \gamma_s - 1$ in this case, as described in Section 2.5.2.

The emissivity of IC radiation in Thomson limit and at the higher energies ($\omega \gg \gamma^2 kT/\hbar$) is reduced from Equation 2.119 to

$$\epsilon_{\text{IC, Thomson}}(\omega) \propto \omega \exp\left(-\frac{\hbar\omega}{4\gamma^2 kT}\right). \quad (2.122)$$

Integrating this emissivity over the electron that is distributed in a cutoff power-law form, Equation 2.112, gives

$$\frac{dN_\gamma}{d\varepsilon} \propto \varepsilon^{-\frac{2s+3\beta-6}{2(\beta+2)}} \exp\left[-\left(\frac{\varepsilon}{\varepsilon_\gamma}\right)^{\frac{\beta}{\beta+2}}\right]. \quad (2.123)$$

See Appendix A for the detailed derivations. Applying the spectral index and the cutoff slope of the electron spectrum in the higher energies (i.e., $s = 1/2$ and $\beta = 2$) for Equation 2.123, the photon spectrum is obtained:

$$\frac{dN_\gamma}{d\varepsilon} \propto \varepsilon^{-1/8} \exp \left[- \left(\frac{\varepsilon}{\varepsilon_\gamma} \right)^{1/2} \right]. \quad (2.124)$$

The cutoff energy parameter in the IC spectrum in Thomson regime is derived as

$$\varepsilon_\gamma = \frac{kT}{m^2 c^2 p_0^2} \quad (\text{Thomson limit}), \quad (2.125)$$

$$= \frac{27(mc)^2 kT}{2\gamma_s^2 q^3} \left(1 + \frac{1}{\sqrt{\kappa\xi}} \right)^{-2} u_1^2 \eta^{-1} B^{-1} \quad (\text{Thomson limit}). \quad (2.126)$$

In the entire energy band, Zirakashvili and Aharonian (2007) obtained the analytical solution:

$$\frac{dN_\gamma}{d\varepsilon} \propto \varepsilon^{-2} \left[1 + 0.31 \left(\frac{\varepsilon}{\varepsilon_\gamma} \right)^{0.6} \right]^{25/8} \exp \left[- \left(\frac{\varepsilon}{\varepsilon_\gamma} \right)^{1/2} \right] \quad (\kappa = \sqrt{1/11}), \quad (2.127)$$

$$\frac{dN_\gamma}{d\varepsilon} \propto \varepsilon^{-2} \left[1 + 0.36 \left(\frac{\varepsilon}{\varepsilon_\gamma} \right)^{0.7} \right]^{15/5.6} \exp \left[- \left(\frac{\varepsilon}{\varepsilon_\gamma} \right)^{1/2} \right] \quad (\kappa = 1). \quad (2.128)$$

In the higher energies ($\varepsilon \gg \varepsilon_\gamma$) in Equation 2.127 (and Equation 2.128), $dN_\gamma/d\varepsilon$ becomes $\varepsilon^{-1/8} \exp(-\varepsilon^{1/2})$, which is consistent with Equation 2.124. The transition function is determined by the numerical calculation and requiring the smooth connection between the lower and higher energy bands.

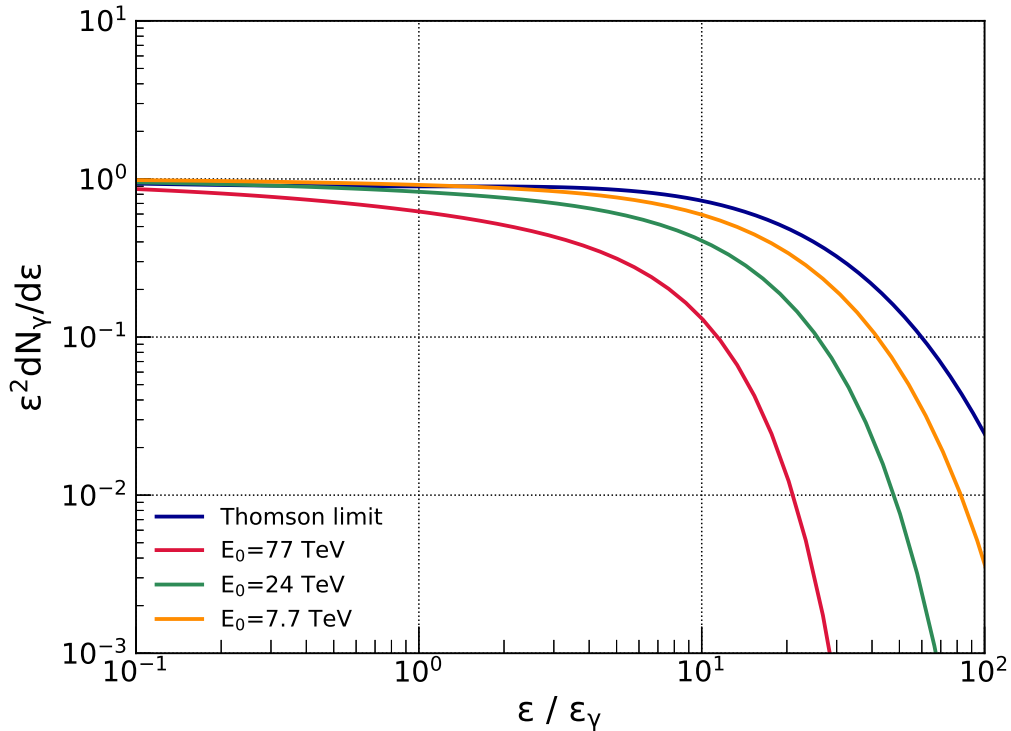


Figure 2.13: The IC gamma-ray spectrum in Klein-Nishina regime with E_0 of 77 TeV (shown in red), 24 TeV (green), and 7.7 TeV (orange), and in Thomson limit (blue).

2.6.5 Summary of leptonic models

Finally, Figure 2.14 illustrates the spectral models of the electron, synchrotron radiation, and inverse Compton scattering. It should be emphasized that the detailed analytical expressions significantly deviate from the simple cutoff power-law form, $\exp(-E)$, that is shown with the dashed black line in Figure 2.14. Therefore we apply our models to the observed spectra in the following chapters. We also use simple power-law and cutoff power-law models, although it is challenging to verify the difference between the physical and conventional models with the current observational data.

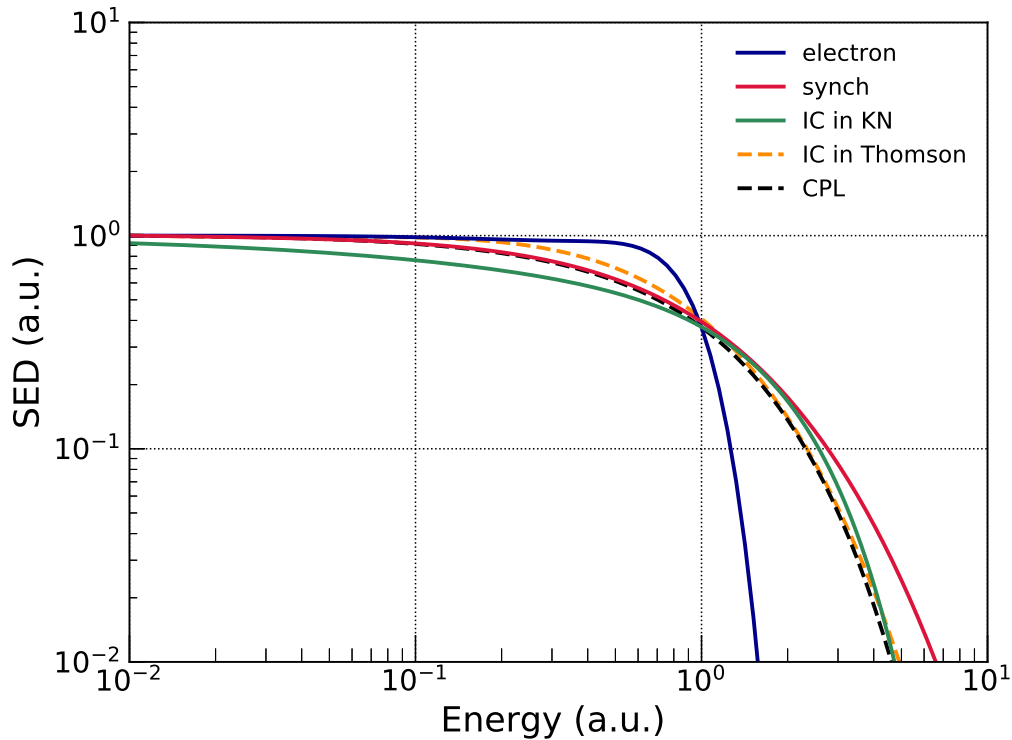


Figure 2.14: The model spectra of the electron (shown in blue), corresponding synchrotron (red), inverse Compton in KN regime (green) with $E_0 = 1$ TeV, and inverse Compton in Thomson regime (dashed orange), in the case of $\kappa = \sqrt{1/11}$. The x-axis is normalized by the energy which gives a e^{-1} drop off.

Chapter 3

Instruments

This thesis makes use of observational data taken with *Chandra* and *NuSTAR* satellites for X-ray observations and H. E. S. S. for TeV gamma-ray observations. Both *Chandra* and *NuSTAR* are equipped with X-ray reflecting mirrors, and provide us with imaging spectroscopy. *Chandra* observes the soft X-ray below 10 keV, while *NuSTAR* is the first satellite to detect spatially resolved hard X-ray up to 80 keV. This chapter briefly summarizes the properties and performances of these X-ray and TeV gamma-ray instruments.

3.1 Chandra X-ray Observatory (*Chandra*)

Chandra X-ray Observatory (hereafter *Chandra*) is an X-ray satellite that consists of an X-ray telescope with the unprecedented angular resolution of $0.5''$ and X-ray spectrometers. It was launched by NASA's first space shuttle Columbia on July 23rd, 1999, celebrating its 20th anniversary this year. *Chandra* is one mission of *Four Great Observatories* by NASA together with Hubble Space Telescope (*Hubble*), Compton Gamma Ray Observatory (*Compton*), and Spitzer Space Telescope (*Spitzer*). It is in an elliptical orbit with the orbital period of about 63.5 hours at the altitude of 16,000–139,000 km, lowering the background level by staying outside of the radiation belt for $\sim 80\%$ of the one period. The schematic picture of *Chandra* is shown in Figure 3.1. Its weight is 4,790 kg, and its overall length is 13 m. The onboard instruments are the X-ray telescope named High Resolution Mirror Assembly (HRMA) and Science Instrument Module (SIM) on the focal plane including Advanced CCD Imaging Spectrometer (ACIS), Low Energy Transmission Grating (LETG), and High Energy Transmission Grating (HETG). The scientific performances were summarized in Weisskopf et al. (2002).

3.1.1 High Resolution Mirror Assembly (HRMA)

The X-ray telescope, HRMA, is shown in Figure 3.1. Four paraboloid-hyperboloid (Wolter-I type) grazing incidence X-ray mirrors are nested. The diameter is 1.2 m, and the focal length is 10 m. In principle, the diffraction limit of the spatial resolution of a telescope is given by λ/D with wavelength and telescope aperture being λ and D , respectively. This gives the limit of about 10^{-4} arcsec for 1 keV photon and 1.2 m in diameter. The actual angular resolution of *Chandra*, however, is about 0.5 arcsec, which is the best resolution for X-ray observations ever achieved. This is because the incidence angle for X-ray photons to be reflected by the mirror is very small, and the reflection is strongly affected by the reflection rate and the shape accuracy of the surface of the mirror. The unprecedented spatial resolution of $0.5''$ was achieved by doubling the aperture size compared to the older Einstein satellite and the improved surface smoothness by polishing the mirrors. The cons of achieving the greatest angular resolution are the small effective area due to only four mirrors, of which each mirror is thicker, and the heavy total weight.

3.1.2 Science Instrument Module (SIM)

Science Instrument Module (SIM) contains ACIS and High Resolution Camera (HRC) on the focal plane, and transmission gratings (LETG and HETG) behind the telescope. Figure 3.1 illustrates the placement of these two detectors on the focal plane. SIM is movable in the $\pm Y$ and $\pm Z$ axis on the focal plane.

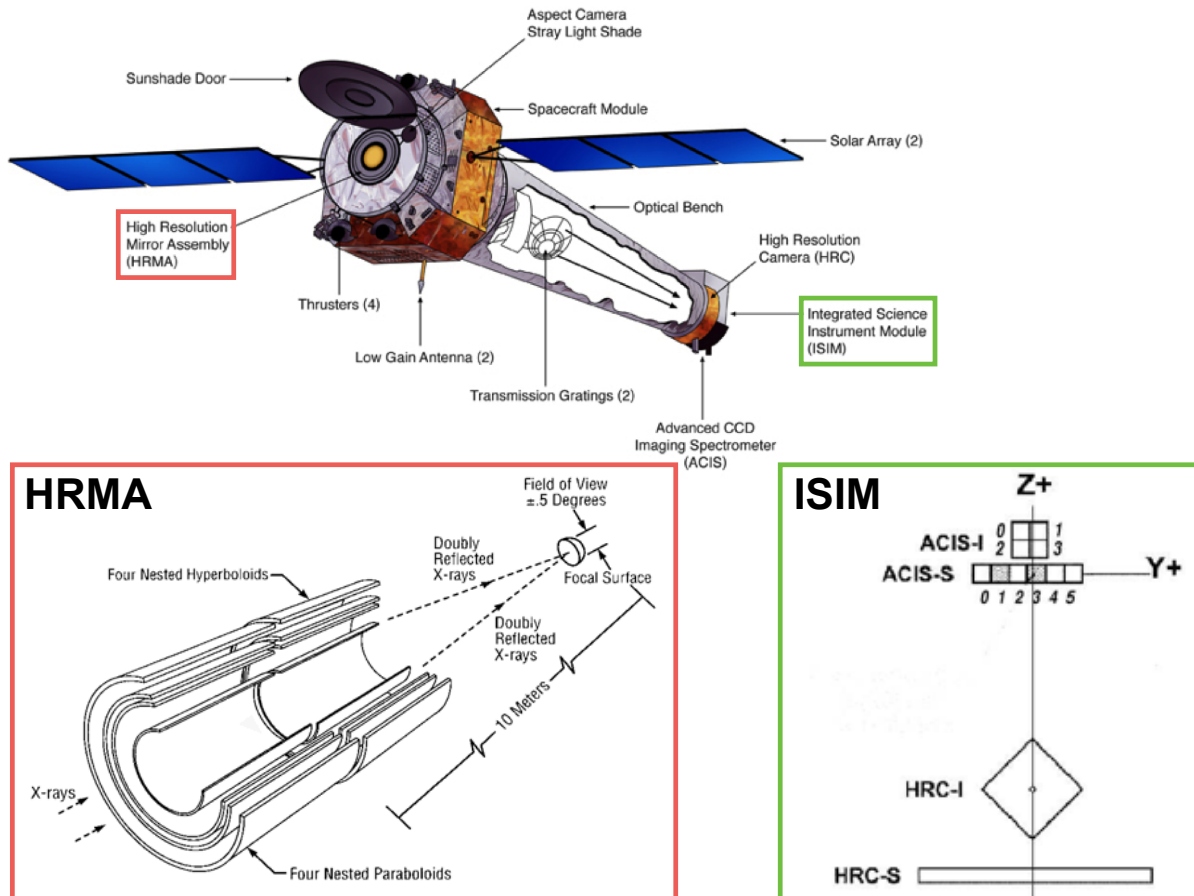


Figure 3.1: Schematic picture of *Chandra* X-ray Observatory (top), HRMA (bottom left), and SIM (bottom right), taken from *Chandra* X-ray Center (2018).

Advanced CCD Imaging Spectrometer (ACIS)

ACIS enables us to obtain images and spectra. *Chandra* has 10 CCD chips (ACIS), and each ACIS is a CCD camera with 1024×1024 pixels². As shown in Figure 3.1, there are ACIS-I with 2×2 CCD chips and ACIS-S with 1×6 CCD chips on the focal plane. Two tips of ACIS-S (S1 and S3) are backside illumination CCDs with the observable energy band of 0.4–10 keV, while the others are frontside illumination with 0.5–10 keV. It is allowed to perform observations using 6 CCDs simultaneously.

Figure 3.2 shows the performances achieved with actual observations with HRMA and ACIS. The on-axis¹ effective area is shown in the top left panel of Figure 3.2. The vignetting effect of *Chandra* observations is illustrated in the top right panel of Figure 3.2, where the vignetting is defined as the ratio of off-axis effective area to on-axis one. The larger the off-axis angle (θ) is, the smaller the vignetting ratio is. Also the vignetting depends on the X-ray energy: the higher the X-ray energy is, the smaller the vignetting ratio is. The bottom left and the bottom right panels of Figure 3.2 respectively present the encircled energy radius and the encircled fractional power, which are indicative of point spread function (PSF) of *Chandra* observations. The PSF, in general, can be represented by a half power diameter (HPD) or a full width of half maximum (FWHM). The *Chandra*'s HPD is about $0.4''$ for the on-axis source.

High Resolution Camera (HRC)

HRC consists of two microchannel plate imaging detectors, HRC-I and HRC-S. The field of view (FoV) of HRC is large; HRC-I and HRC-S have the FoV of 30×30 arcmin² and 6×99 arcmin², respectively. HRC-S is also

¹The position of the optical axis on the detector coordinate

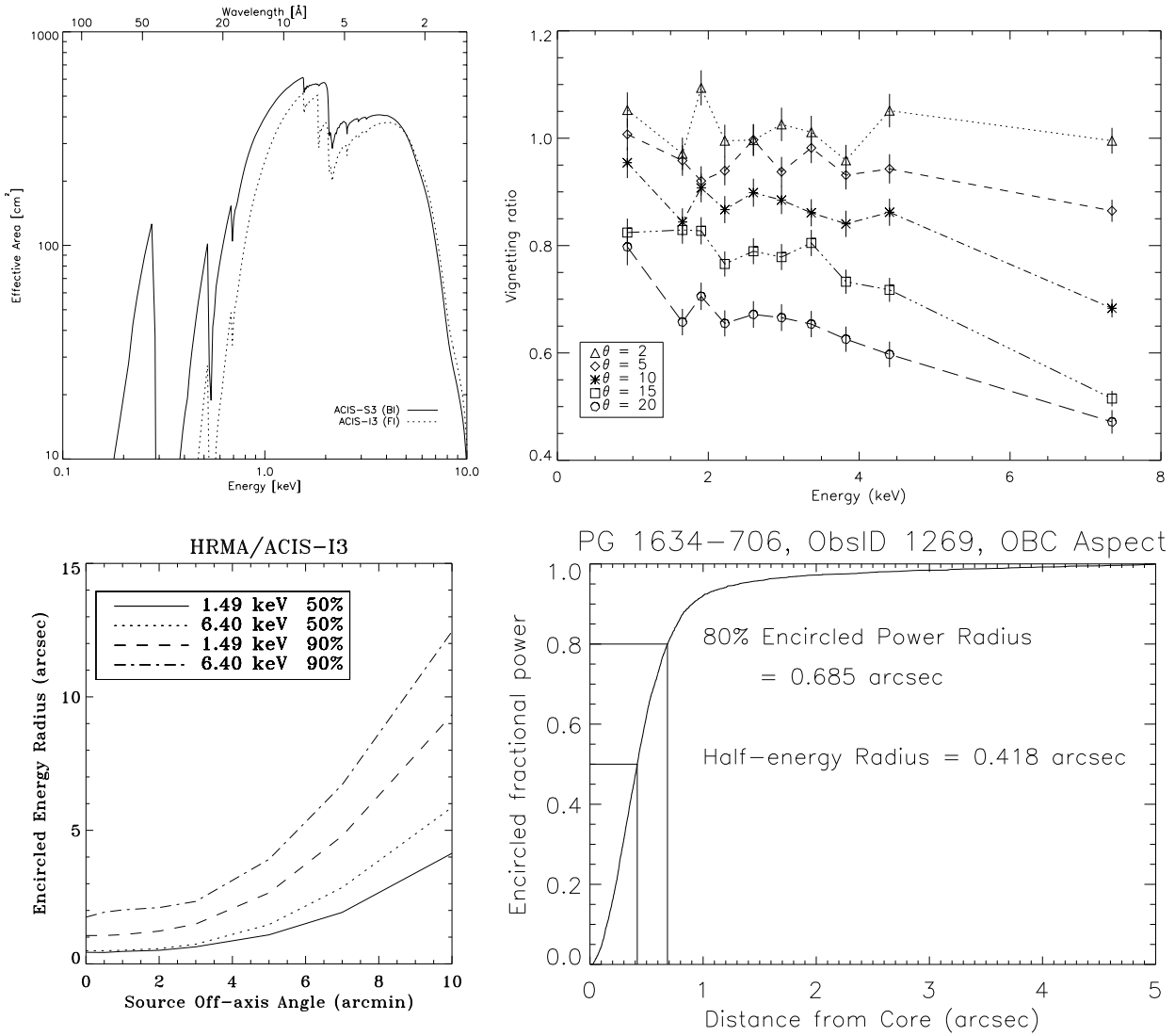


Figure 3.2: Performances of observation with HRMA/ACIS, taken from *Chandra* X-ray Center (2018). Top left: On-axis effective area. Top right: Off-axis vignetting effect, taken from observations of SNR G21.5. Bottom left: PSF of *Chandra* (encircled energy radius). Bottom right: PSF of *Chandra* (on-axis encircled fractional power).

in charge of a reading system for observations with LETG and HETG.

Transmission grating

Transmission grating provides us with precise spectroscopy by making use of X-ray transmission. *Chandra* has Low Energy Transmission Grating (LETG) and High Energy Transmission Grating (HETG) that are placed just behind HRMA (see Figure 3.1). The energy band of HETG is 0.4–10 keV with the energy resolution of $E/\Delta E = 1000$. The energy band of LETG is 0.08–0.2 keV with the energy resolution of $E/\Delta E = 1800$.

3.2 Nuclear Spectroscopic Telescope Array (*NuSTAR*)

Nuclear Spectroscopic Telescope Array (*NuSTAR*) is an orbiting satellite to focus on hard X-ray observations (e.g., Harrison et al. (2013)). It was launched from Reagan test site located in Kwajalein Atoll on June 13th, 2012. The detectable energy band is 3–79 keV, allowing us to access spatially resolved hard X-ray sky, for the first time, in particular above 10 keV that the previous X-ray satellites have never seen due to the limited reflectivity of an X-ray total reflection. *NuSTAR* is in a circular orbit at an altitude of 600 km. Figure 3.3 illustrates the schematic picture of *NuSTAR*. Its total weight is about 350 kg. The onboard instruments are two X-ray telescopes, optics module A (OMA) and B (OMB), and the co-aligned X-ray detectors, focal plane module A (FPMA) and B (FPMB).

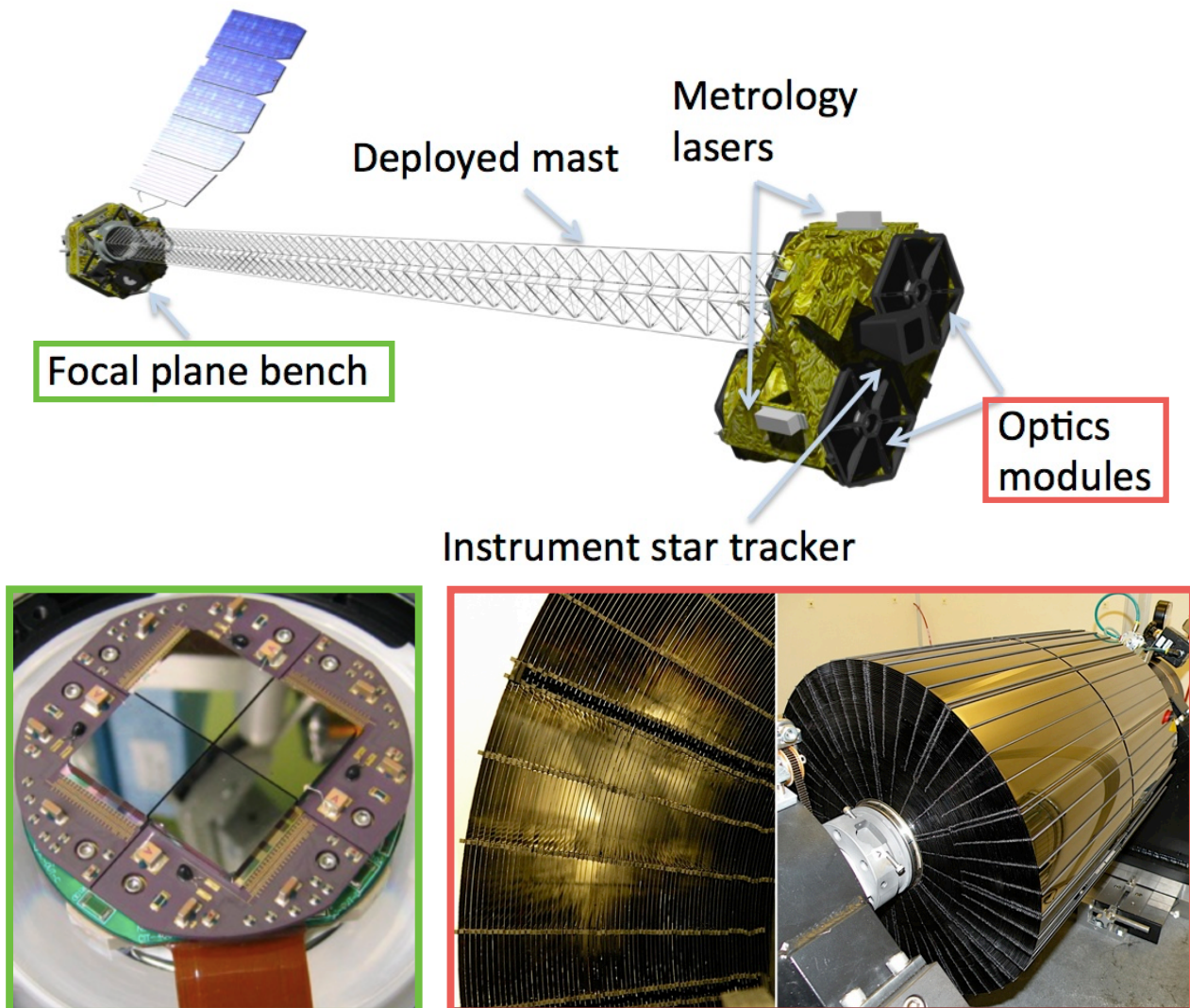


Figure 3.3: Schematic picture of *NuSTAR* (top), optics module (bottom right), and focal plane module (bottom left), taken from *NuSTAR* Science Operations Center (2016).

3.2.1 Optics module

The optics module is shown in Figure 3.3. 9 days after the launch, the mast was stretched and deployed to complete the satellite to earn the focal length of 10.14 m. The optics module consists of two Wolter-I type telescopes that have nested 133 layers of X-ray mirrors coated by W/Si and Pt/C multi layers.

Stray light

With *NuSTAR* observations, stray-light X-ray happens to be observed because of the 10 m separation between the optics module and the focal plane module, and its openness to the sky window. As illustrated in Figure 3.4, the X-ray from bright sources located within a radius of 5° from the target point is sometimes directly detected in the focal plane module through the aperture. This non-focused X-ray (stray light) is observed together with the focused X-ray that has passed through the optics module, and non-uniformly distributed in the focal plane module. Since the sky windows seen from FPMA and FPMB are different, the stray-light patterns on the detectors are also different (Figure 3.4). The stray-light contamination could be a serious problem for faint and extended X-ray sources such as SNRs. The detailed analysis to deal with the stray light is discussed in Section 3.2.3.

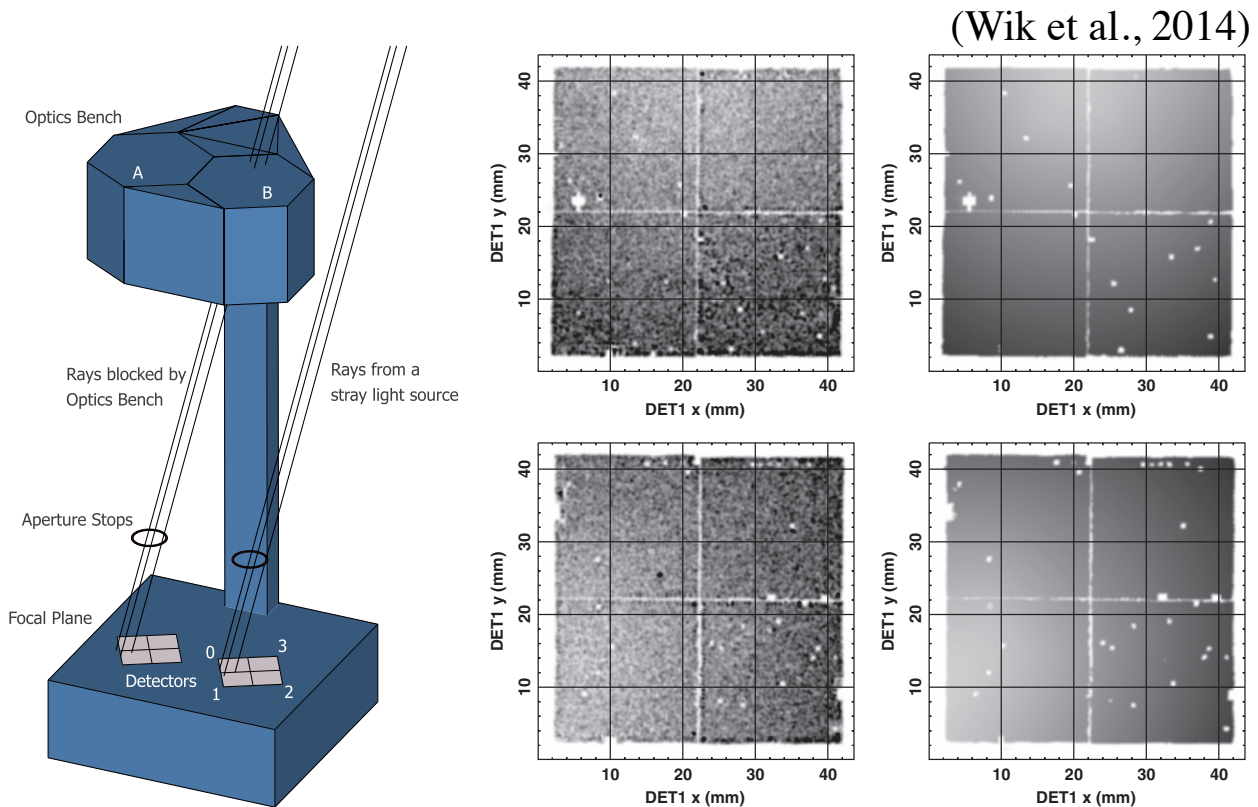


Figure 3.4: Left: Schematic structure of *NuSTAR* telescope, and how stray light is detected without passing through the optics. Right: Non-uniform distribution of stray light detected in an observation of the blank sky. The top left and right panels show the observation and model of FPMA, respectively. The bottom left and right panels show the observation and model of FPMB, respectively. They are taken from Wik et al. (2014).

3.2.2 Focal plane module

NuSTAR has the two X-ray detectors, FPMA and FPMB, which are co-aligned with the optics module, respectively, OMA and OMB. Both FPMA and FPMB are solid-state photon-counting detectors, which consist of 2×2 CdZnTe (CZT) crystal with a thickness of 2 mm. The FoV of each detector is 12.45×12.45 arcmin².

The scientific performances achieved with *NuSTAR* are presented in Figure 3.5. *NuSTAR* has a larger effective area up to ~ 80 keV compared to the other X-ray instruments (top left panel in Figure 3.5). The top right panel of Figure 3.5 presents the vignetting effect of *NuSTAR*. The effective area of different off-axis angles is shown in the bottom left panel of Figure 3.5. The PSF of *NuSTAR* is predominantly determined with the optics module, while a few percent errors arise from the motion of the deployed mast or reconstruction of the

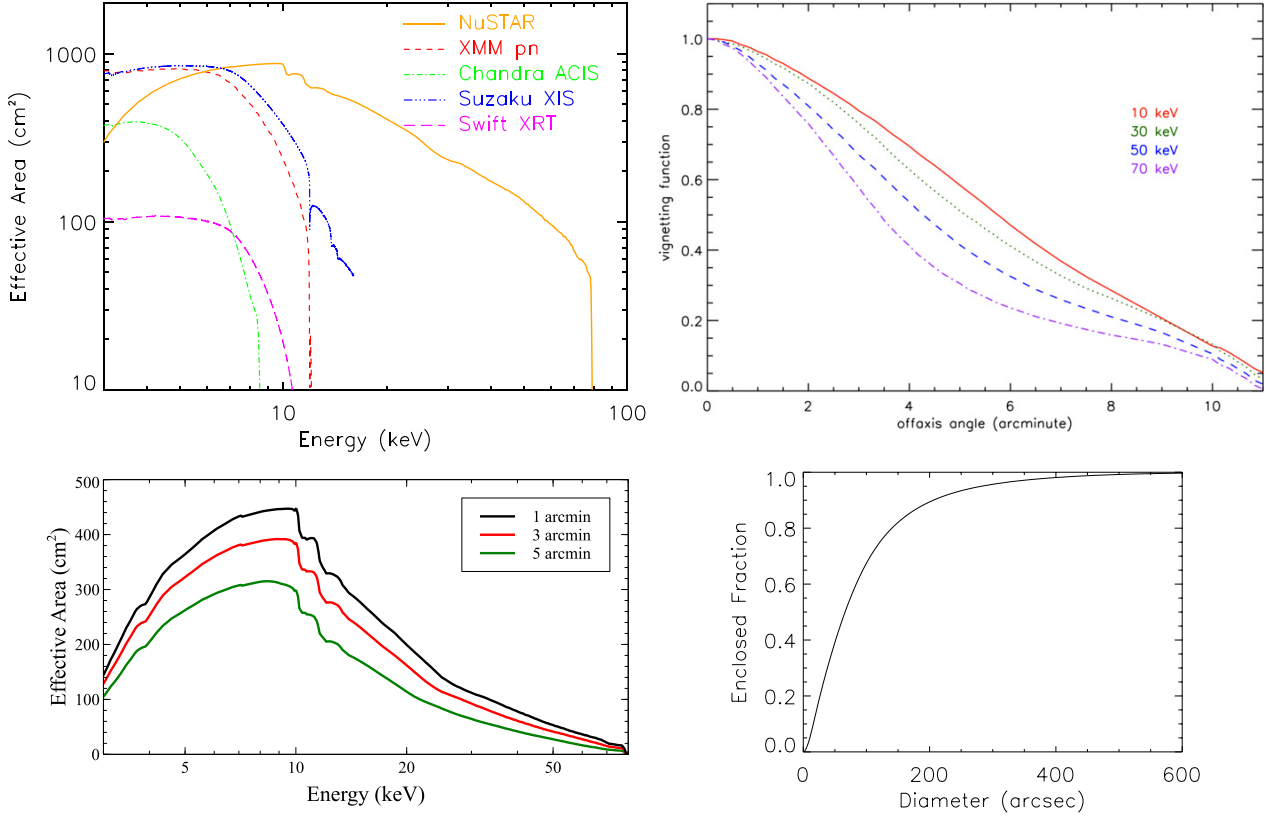


Figure 3.5: Performances of *NuSTAR*, taken from Harrison et al. (2013); *NuSTAR* Science Operations Center (2016). Top left: Effective area. Top right: Vignetting dependences on off-axis angles. Bottom left: Off-axis effective area. Bottom right: The PSF of *NuSTAR* (encircled fractional power), taken from observations of GRS 1915+105.

attitude. The bottom right panel of Figure 3.5 indicates the encircled count fraction observed with *NuSTAR*. The FWHM and the HPD are, respectively, 18'' and 58''.

The properties of *Chandra* and *NuSTAR* are listed in Table 3.1.

3.2.3 Detailed analysis of *NuSTAR*

NuSTAR has side aperture contamination. Due to the separation between the telescope modules and the detectors and its openness to the sky window, the X-ray emissions from the outside of the field of view (FoV) can be detected directly in the FPMs without passing through the optic modules. They are referred to as stray lights. They come from the region within a radius of 2.5° from the center of the FoV. The stray lights are caused by bright X-ray sources located in the vicinity of the target point and Cosmic X-ray Background (CXB), as well as Galactic Ridge X-ray Emission (GRXE; Revnivtsev et al. (2006); Krivonos et al. (2007); Yuasa et al. (2012)) when pointing at the galactic plane. This causes complex distributions of the background.

In the following, we present a detailed analysis of *NuSTAR* observations of supernova remnant (SNR) RX J1713.7–3946 as an example (see also Tsuji et al. (2019)). Using *NuSTAR*, we have performed observations of the NW region of RX J1713.7–3946 twice, in 2015 September (hereafter P1) and in 2016 March (P2) with exposure times of 50 and 57 ks, respectively. The *NuSTAR* observations of RX J1713.7–3946 require a cautious treatment to deal with the stray light and non-uniformly distributed background because the remnant is relatively faint and extended across the almost entire FoV, and the observations are heavily contaminated by the stray-light components and GRXE. The extent and location (on the galactic plane) of RX J1713.7–3946 make it one of the most complicated analyses of *NuSTAR*: the following statements contain all the tips needed for the detailed analysis with *NuSTAR*.

Table 3.1: Scientific performances of *Chandra* and *NuSTAR*

	<i>Chandra</i>	<i>NuSTAR</i>
Launch	July 23rd, 1999	June 13th, 2012
Weight	4,790 kg	350 kg
Altitude	16,000–139,000 km	650–610 km
Total length	13 m	
Energy band	0.5–10 keV	3–78.4 keV
Angular resolution (HPD)	0.5''	58''
Angular resolution (FWHM)	0.5''	18''
FoV	(8.3 arcmin) ² ×4 (ASIC-I) (8.3 arcmin) ² ×6 (ASIC-S)	(12.45 arcmin) ²
Sensitivity	4×10 ⁻¹⁵ erg/cm ² /s (0.4–6 keV, 10 ks, 3σ)	2×10 ⁻¹⁵ erg/cm ² /s (6–10 keV, 1000 ks, 3σ)
Energy resolution (FWHM)	130 eV at 1.49 keV 285 eV at 5.9 keV	400 eV at 10 keV 900 eV at 68 keV
Time resolution	1 ms	0.1 ms
Effective area	110 cm ² at 0.5 keV (FI) 600 cm ² at 1.5 keV (FI) 40 cm ² at 8.0 keV (FI)	300 cm ² at 3 keV 800 cm ² at 10 keV 100 cm ² at 58 keV
Optics		
Focal length	10 m	10.14 m
Layers	4	133
Internal radius	—	5.44 cm
External radius	1.2 m	19.1 cm
Layer length	22.5 cm	22.5 cm
Coating	Iridium	Pt/C (inside), W/Si (outside)

Since RX J1713.7–3946 is located on the galactic plane, there are some bright X-ray sources as possible stray-light contaminators. For instance, the stray light from HMXB 4U 1700–377 dominates in all the X-ray energy bands except for P1 observation with FPMA. In addition, there exist stray-light contaminations from GX 349+2, 4U 1708–40 in P1-FPMA, and 4U 1702–429 in P1-FPMA and P2-FPMB. Figure 3.6 illustrates the regions contaminated by the stray lights from these X-ray sources. The expected stray-light pattern in the FoV can be checked using “nuplan”, which is included in nuskybgd-master (nuskybgd toolkit; see below). We exclude these contaminated regions for the following imaging and spectral analysis.

Another component to cause stray-light contaminations is CXB. In addition to the focused CXB emission passing through the optics, CXB coming from the outside of the FoV without passing through the telescopes are detected non-uniformly in the FPMs. It should be noted that we need to take these nonuniform distributions into account because RX J1713.7–3946 is extended across most of the FoV. In order to deal with this issue, we use the toolkit named “nuskybgd”² (Wik et al., 2014).

Thanks to nuskybgd, we can construct the background for any region in which we are interested. The general usage of nuskybgd is as follows. First, we extract the spectra of “source-free” regions outside the SNR, where any stray lights from X-ray sources should not be contained. In nuskybgd, the model consists of the following four components: 1.) “aCXB” to describe the stray-light CXB through the aperture, 2.) “fCXB” to describe the focused CXB, 3.) “Inst” to describe instrument line emissions and reflected solar X-rays, and 4.) “Intn” to describe instrument Compton scattered continuum emissions. Using nuskybgd_fitab included in nuskybgd, we can fit the background spectrum by the model above. Based on the best-fit parameters, the background image and the background spectrum for an arbitrary region in the FoV are respectively produced

²<https://github.com/NuSTAR/nuskybgd>

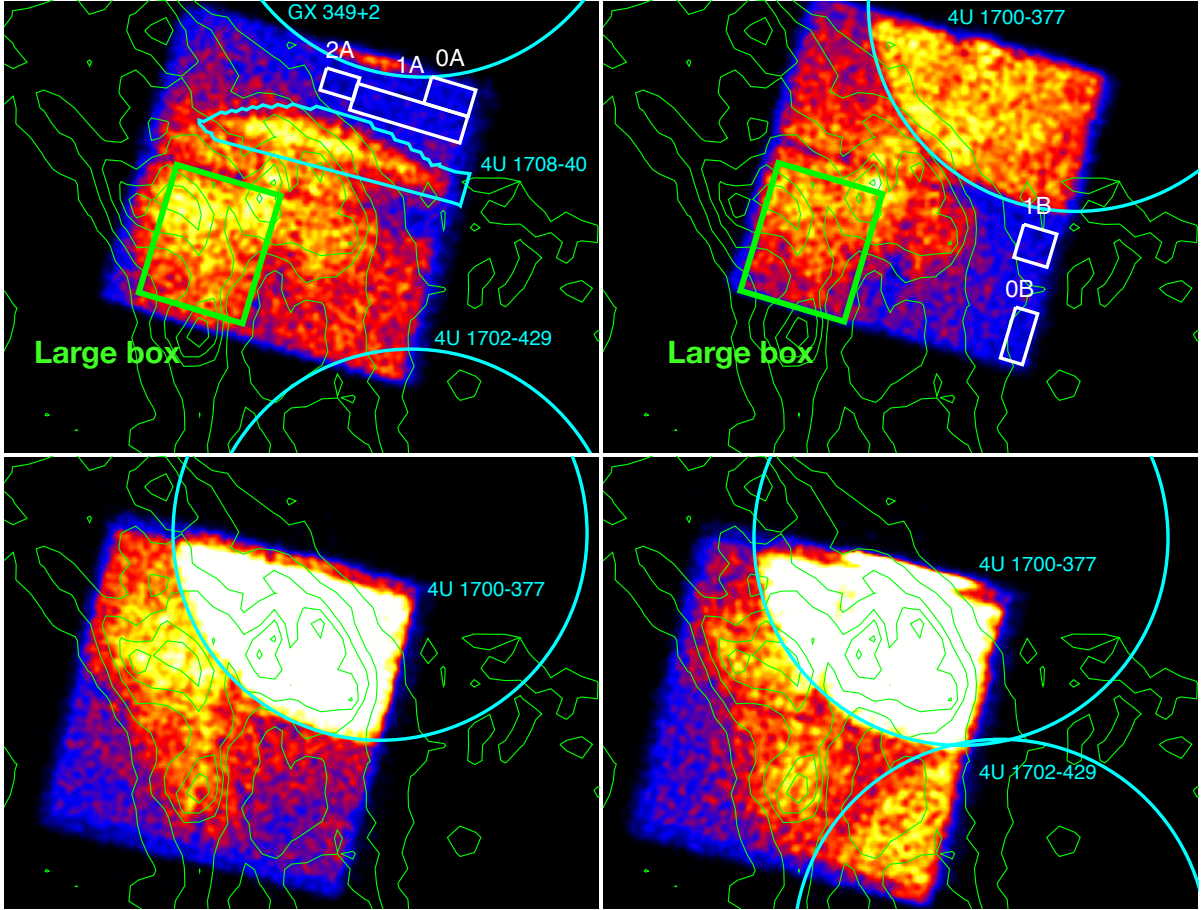


Figure 3.6: Top left: The count map of P1-FPMA. The cyan regions illustrate the expected stray-light patterns from known X-ray sources in the vicinity of RX J1713.7–3946. The background regions are shown with white boxes. The contours are taken from the *XMM-Newton* image in 0.5–8 keV. Top right: Same as the top left for P1-FPMB. Bottom left: Same as the top left for P2-FPMA. Bottom right: Same as the top left for P2-FPMB.

by using `nuskybgd_image` and `nuskybgd_spec` in `nuskybgd`.

GRXE is not negligible because RX J1713.7–3946 is located on the galactic plane. We use “`apec`” model in `XSPEC` with the electron temperature (kT) of 8 keV for GRXE. Indeed, off-set observations near RX J1713.7–3946 with *Suzaku* showed that CXB and GRXE, which is described by `apec` with $kT = 7.4\text{--}8.8$ keV, are dominant above 3 keV (Katsuda et al., 2015). Similar to CXB, GRXE has also a focused component (“`fGRXE`”) and an unfocused component (“`aGRXE`”). We assume `fGRXE` is uniform in the vicinity of RX J1713.7–3946, and fix the normalization to the value derived from *Suzaku* observations in Katsuda et al. (2015). The distribution of `aGRXE`, however, is not well known yet. Unlike `aCXB` coming from the flat sky, modeling `aGRXE` distribution on the detectors is a difficult task, since it mainly comes from the nonuniform galactic bulge. Here we assume `aGRXE` is simply uniform on the focal plane modules, and consider systematic uncertainties associated with this approximation (see below).

Our background estimation of RX J1713.7–3946 with *NuSTAR* is as follows. We extract the background spectra from the regions referred to 0A–2A in FPMA and 0B–1B in FPMB, shown in Figure 3.6. To estimate the background of FPMA, the spectra of 0A–2A are jointly fitted, tying the normalizations between them based on the relative brightnesses expected from the known nonuniform distribution. The spectra of 0B–1B are also jointly fitted to estimate the background of FPMB. Dividing the background region into a few pieces, such as 0A, 1A, and 2A, helps us to better estimate the background, as recommended in Wik et al. (2014). The background model consists of `aCXB`, `fCXB`, `Inst`, `Intn`, `aGRXE`, and `fGRXE`. We use `nuskybgd` for CXB and the instrumental components, while we add GRXE manually since the modeling of GRXE is not yet developed

in `nuskybgd`. When fitting the background spectra, the normalizations of `fCXB` and `aCXB` are fixed to the following values. The normalization of `fCXB` is fixed to the value defined in the literature (Boldt, 1987). Since `CXB` is uniform over the sky, the normalization of `aCXB` is derived from a high-latitude *NuSTAR* observation, where no `GRXE` is contained. The observation of a symbiotic star T CrB³ with the latitude of 48.18° is selected for this purpose. We fit the background spectra of T CrB, which are extracted from the same region in the detector coordinate as that of RX J1713.7–3946, using `nuskybgd` in order to get the level of `aCXB`. The obtained normalization is then used for the normalization of `aCXB` for the observations of RX J1713.7–3946.

The spectra of 0A–2A and 0B–1B are shown with all the components of the background model in Figure 3.7. The background spectra are well-fitted by our background model. It is notable that the background spectrum of 0B is extracted from the region where `aCXB` is weakest in FPMB, making the component of `aCXB` lower. The free parameters in low energy band and high energy band are, respectively, the normalization of `aGRXE` and the instrument emissions. The normalization of `aGRXE` is roughly obtained to be $\int n_e n_H dl = 7 \times 10^{19} \text{ cm}^{-5}$ for both FPMA and FPMB, based on the assumption of the distance of 1 kpc (Fukui et al., 2003).

In order to construct the background spectrum for the region of interest, we use `nuskybgd_spec` in `nuskybgd` for `aCXB`, `fCXB`, `Inst`, and `Intn` components. It takes into account the nonuniform distribution of the background, i.e. the background normalization for the region of interest is weighted by the nonuniform distribution on the detectors. On the other hand, for `fGRXE` and `aGRXE` we simply rescale the normalization by the size of the source region, assuming the flat `GRXE` distribution across the FoV. We discuss the validity of this assumption below.

For P2 epoch, the background is estimated based on the best-fit parameters of the background of P1 observation. Since the emission of RX J1713.7–3946 is extended across the entire FoV of P2, there is no region to extract for the background estimation. We assume that the background with *NuSTAR* is approximately stable over the period of these two observations, P1 (2015 September) and P2 (2016 March). The background of an arbitrary region in P2 observation is generated in the same procedure as P1, as mentioned above.

Results of imaging analysis with `nuskybgd`

In Figure 3.8, we present raw count maps, background images, and background-subtracted images of RX J1713.7–3946 NW in the energy band of 3–10 keV. The background images are constructed using `nuskybgd` (`nuskybgd_image`). We note that `GRXE` is included in these images, while the other components, namely the `CXB` and instrument background, are subtracted.

Results of spectral analysis with `nuskybgd`

Here we show an example spectrum extracted from the large box (the green box in Figure 3.6) in Figure 3.9. The background spectrum for this specific region in the FoV is reproduced by `nuskybgd_spec` in `nuskybgd` based on the best-fitted parameters of the background model. It should be noted that we manually generate and add the spectra of `aGRXE` and `fGRXE`, since the treatment of `GRXE` is not implemented in `nuskybgd`. Figure 3.9 presents the background, raw, and background-subtracted spectra in the large box.

We take the uncertainty of the background spectrum into consideration as a systematic error. When fitting the background spectra with `nuskybgd_fitab` in `nuskybgd`, the best-fit parameters have about 10% error. Therefore, we check how much the source spectrum from the region of interest depends on the choice of the background spectrum, by changing the normalization. If we change the normalization of the total background spectrum by 10%, the source spectrum changes by 10%. This uncertainty can be used as a systematic error. It should be noted that the uncertainty of the `aGRXE` component could be much larger than the statistical error because we simply assume the uniform distribution of `aGRXE`, as mentioned above. If we change only the normalization of the `aGRXE` spectrum by a factor of 3, the source spectrum changes by 10%. Thus our assumption on the uniform `aGRXE` does not largely affect the source spectrum as long as `aGRXE` is non-uniformly distributed by a factor of ≤ 3 . We note that in fact `CXB` is also expected to be fluctuated by $\sim 20\%$ in the FoV of *NuSTAR* (Moretti et al., 2009). Changing the normalization of `aCXB`, we also checked this

³T CrB was observed with *NuSTAR* in 2015 September with ObsID of 30101046002 and exposure of 80 ks.

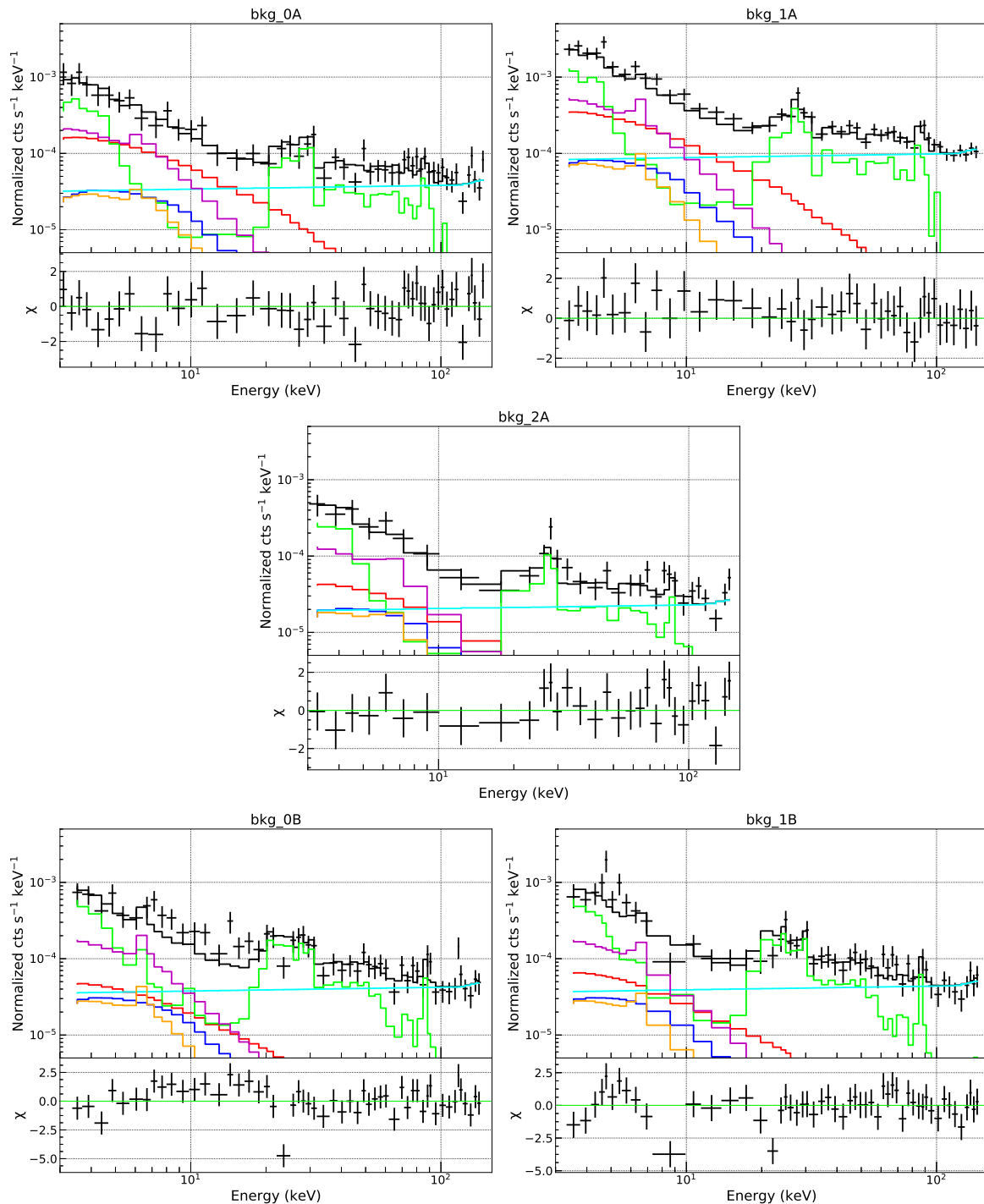


Figure 3.7: Top left: The background spectrum of 0A region with nuskybgd model plus GRXE. The black, red, blue, green, cyan lines respectively indicate the total background, aCXB, fCXB, Inst, and Intn, included in nuskybgd. The magenta and orange lines are aGRXE and fGRXE, respectively. The background spectrum with nuskybgd model plus GRXE. Top right: Same as the top left for the spectrum of 1A. Middle: Same as the top left for the spectrum of 2A. Bottom left: Same as the top left for the spectrum of 0B. Bottom right: Same as the top left for the spectrum of 1B.

uncertainty does not have a large effect on the source spectrum, i.e., the spectral parameters changes by less than 15% for the 20% fluctuation of aCXB.

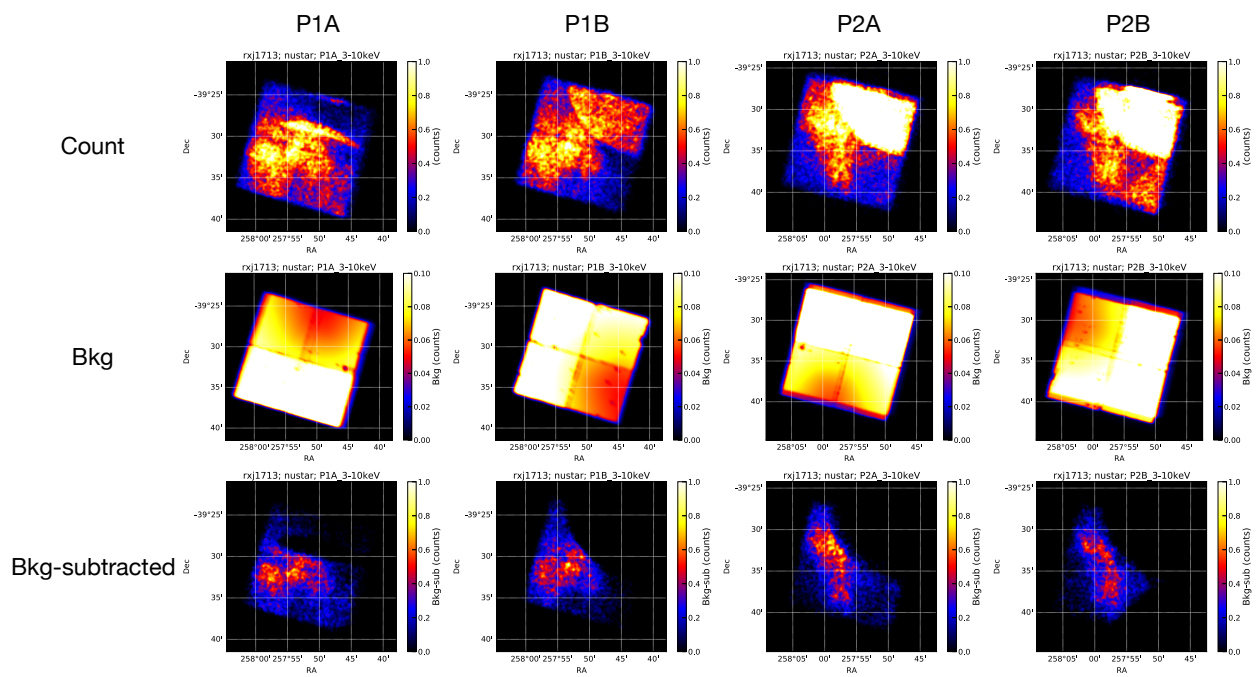


Figure 3.8: Top: Raw count maps in the 3–10 keV band. Middle: Background maps produced by nuskybgd. Bottom: Background subtracted and stray-light excluded images. P1-FPMA, P1-FPMB, P2-FPMA, and P2-FPMB are shown from the left.

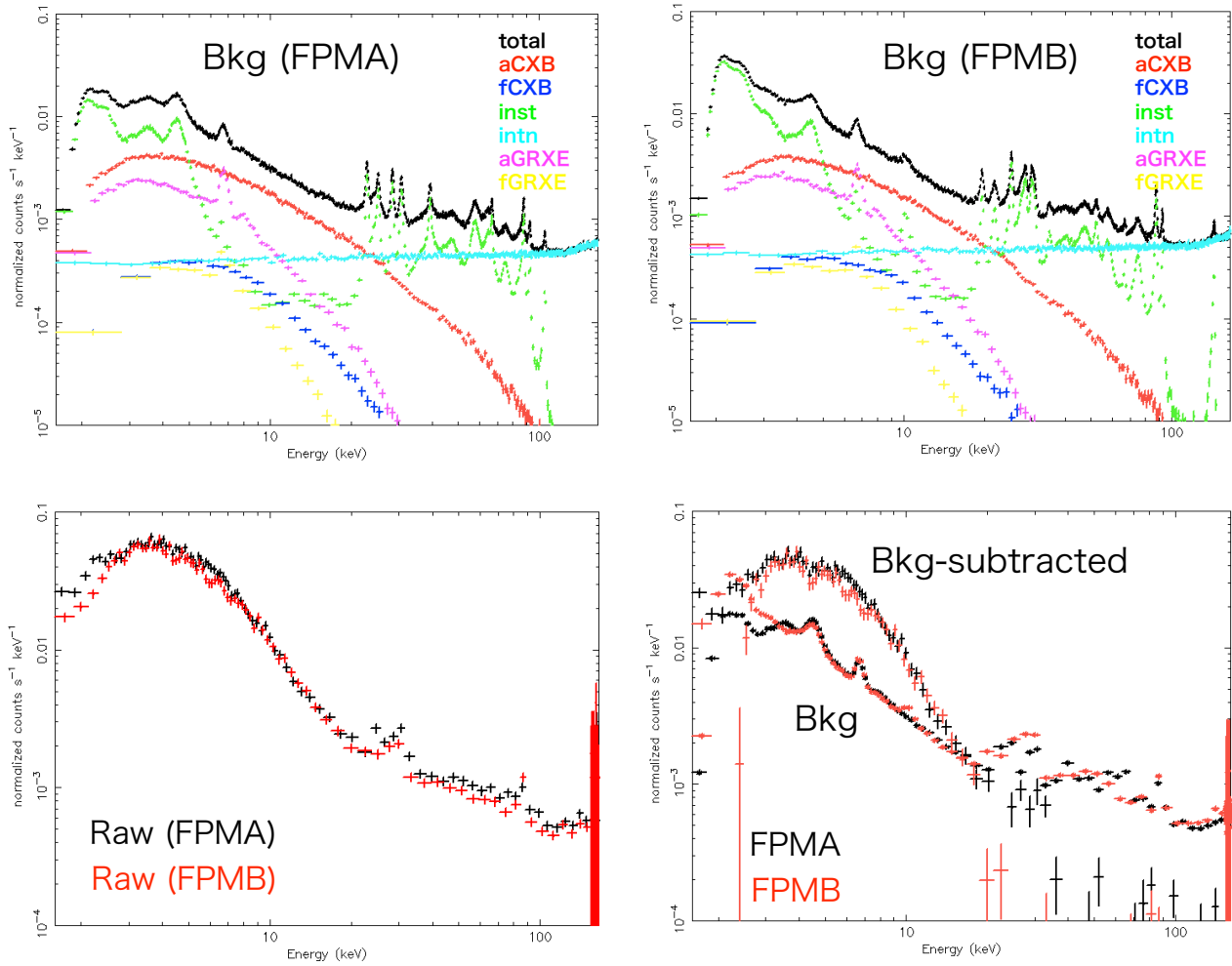


Figure 3.9: Top left: Background spectrum of P1-FPMA generated by nuskybgd in the region of the large box. Each component (aCXB, fCXB, Inst, Intrn, aGRXE, and fGRXE) is also shown. Top right: Same as the top left for P1-FPMB. Bottom left: Raw spectra of the large box (P1-FPMA in black and P1-FPMB in red). Bottom right: Background spectra (shown with asterisks) and background-subtracted spectra (crosses) in the large box. FPMA and FPMB are respectively presented in black and red.

3.3 TeV gamma-ray observation

Very-high-energy photons (e.g., radiation in the energy around the TeV range) are direct evidences of accelerated particles. TeV gamma-ray astronomy has begun since the detection of gamma-ray signal from Crab nebula by Whipple, a ground-based gamma-ray telescope system, in 1989 (Weekes et al., 1989). When a very-high-energy photon hits the atmosphere of the Earth, it occurs an air shower (electromagnetic cascade) which emits Cherenkov light. The ground-based telescope (i.e., Imaging Atmospheric Cherenkov Telescope (IACT)) collects the Cherenkov light, and then one can reconstruct the arrival direction and energy of the primary gamma-ray (Figure 3.10). The sky in the TeV energy band is dominated by individual sources, of which the number has reached to 225 up to now⁴. The detection technique of IACT is summarized in Section 3.3.1, and Section 3.3.2 presents a brief overview of H.E.S.S., of which data are used in this thesis.

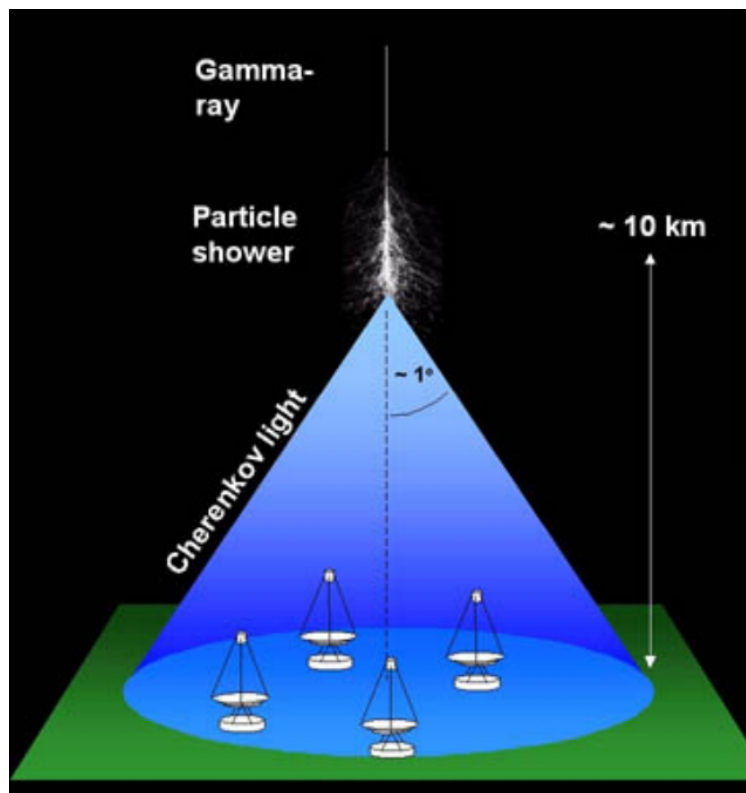


Figure 3.10: Schematic picture of IACT (see, e.g., <https://www.mpi-hd.mpg.de/hfm/HESS/>).

3.3.1 Imaging Atmospheric Cherenkov Telescope

A photon with energy of ≥ 1 MeV decays into a pair of electron and positron in the atmosphere of the Earth. These electrons and positrons emit subsequent gamma-rays via bremsstrahlung. This process (the pair creation and bremsstrahlung) repeats many times and produces an air shower, also known as an electromagnetic cascade. The particles in the shower radiate Cherenkov light, which is collected by the optical telescopes on the ground (Figure 3.10). Figure 3.11 illustrates the simulated images of the air shower, the Cherenkov light on the ground, and the Cherenkov-light image on the detector. The Cherenkov light is detected by more than one telescopes (stereo observation), allowing to estimate the arrival direction and the energy of the primary gamma-ray with higher accuracy.

Another component to produce air showers is cosmic ray (e.g., high-energy protons or heavier ions). They interact with the atmospheric nucleon and generate secondary particles, including Kaon, nucleon, and pion

⁴<http://tevcat.uchicago.edu/>

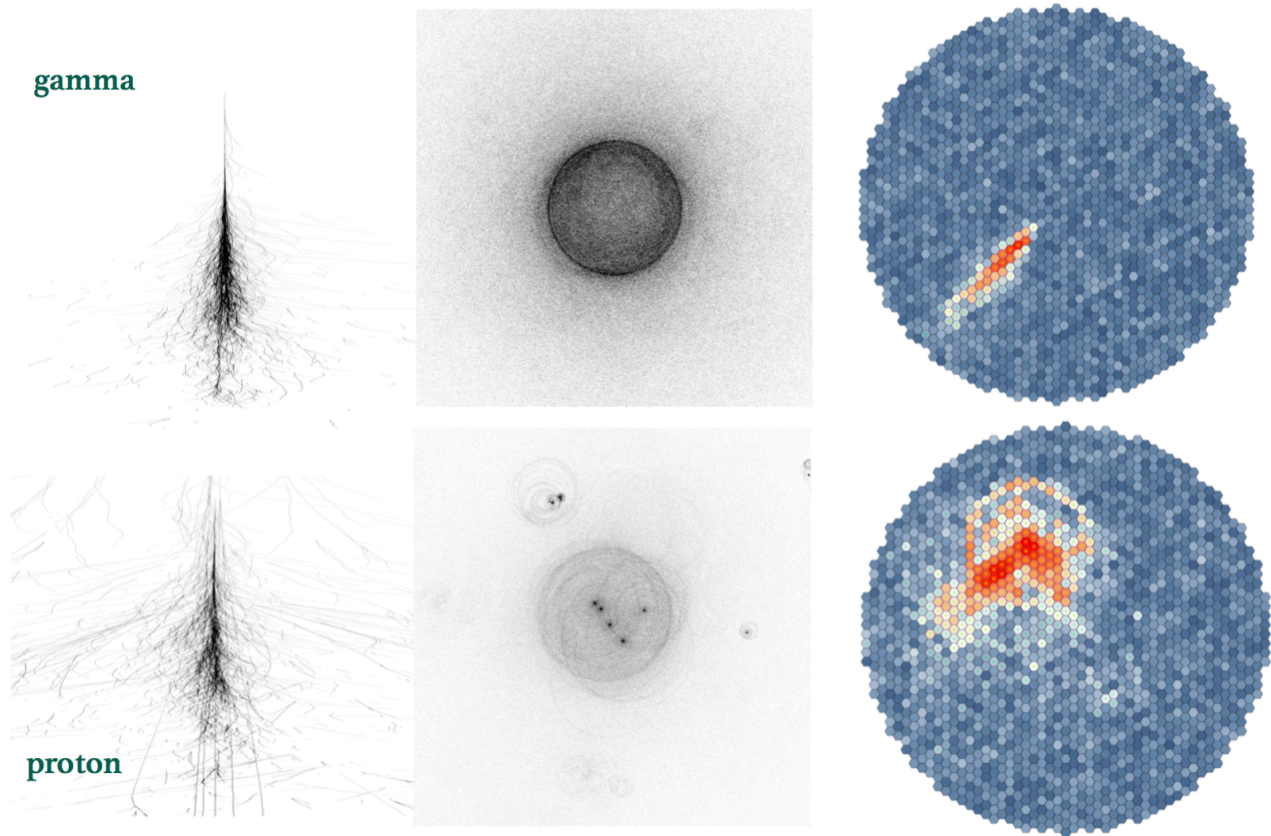


Figure 3.11: Top: Simulated images of an EM shower (left), Cherenkov light on the ground (middle), Cherenkov light on the detector (right). Bottom: Same as top panel for a hadronic shower. Both are taken from Hinton (2018).

which decays into gamma-rays and produces an EM shower. This shower originating from the CR is referred to as a hadronic shower (or a nuclear cascade). The simulated images of the hadronic shower are shown in Figure 3.11. It should be noted that the Cherenkov light image on the detector strongly depends on the type of the shower (i.e., electromagnetic or hadronic). This, therefore, allows us to distinguish the gamma-ray events from the CR background events.

3.3.2 High Energy Spectroscopic System (H.E.S.S.)



Figure 3.12: Picture of H.E.S.S. site (see, e.g., <https://www.mpi-hd.mpg.de/hfm/HESS/>).

High Energy Spectroscopic System (H.E.S.S.) is one of the currently operated IACT, as well as VERITAS and MAGIC. H.E.S.S. is located in the Khomas Highland of Namibia in southern Africa at an elevation of 1800 m from the sea level. In 2004 H.E.S.S. started its full operation consisting of four telescopes (CT1–4) with each interval between the telescopes of 120 m (H.E.S.S.-I phase). The detectable gamma-ray energy ranges from 0.1 to 100 TeV with the FoV of 5° in diameter. The energy and angular resolution are respectively 15% and 0.1° . The completion of another bigger telescope (CT5) at the center of the former four telescopes in 2012 enabled a hybrid observation, lowering the energy threshold to tens of GeV (H.E.S.S.-II phase). The picture of the telescopes at H.E.S.S. site is shown in Figure 3.12.

The information of the cosmic gamma-ray is acquired by reconstruction of the air shower based on the detected Cherenkov light. The analysis process is summarized in Aharonian et al. (2006). The details of the optics of CT1–4 and the trigger system can be found, e.g., in Bernlöhner et al. (2003) and Funk et al. (2004), respectively. Hillas parameters (width and length of the Cherenkov image on the detector and the distance between the image center and the camera center, as shown in Figure 3.13) have been used for the shower reconstruction. The arrival direction of the primary gamma-ray can be reconstructed by a combination of the major axis of the Cherenkov image obtained for each telescope. The gamma-ray and hadronic separation can be made by a comparison of the mean width and length of the Cherenkov-light image. The gamma-ray energy depends on the intensity of the Cherenkov light (because the gamma-ray deposits its energy in the shower) and an impact parameter⁵. Lately the accuracy of reconstruction was greatly improved by a new method using the simulated templates and comparing them with the observed images (see, e.g., Parsons and Hinton (2014)). There are two ways of background estimation, *ring* background model and *reflected* background model, as shown in Figure 3.13 (see also Berge et al. (2007)). Ring background model is used for imaging analysis, while reflected background model is utilized for spectral analysis. Note that reflected background model takes into accounts “acceptance”⁶ which varies with the radius from the observation pointing.

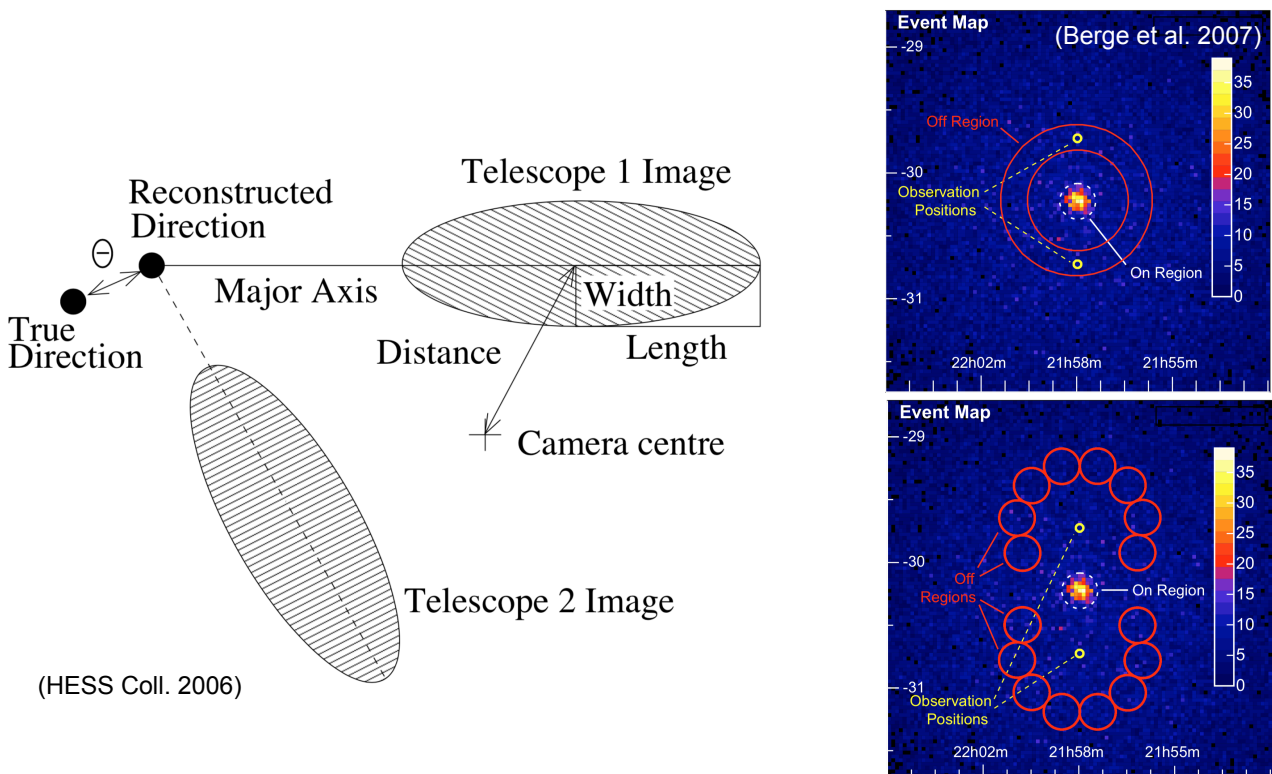


Figure 3.13: Left: Hillas parameters, taken from Aharonian et al. (2006). Right: Ring (top) and reflected (bottom) background models, taken from Berge et al. (2007).

⁵Impact parameter indicates the distance between the center of the shower on the ground and the telescope.

⁶A radial profile of the background event with the center being at the observation pointing.

Chapter 4

Nonthermal X-ray observations of young supernova remnants: Bohm diffusion

Cutoff energy in the synchrotron spectrum of an SNR contains a key parameter of ongoing particle acceleration. In this chapter, we systematically analyze 11 young SNRs, including all historical SNRs, to measure the cutoff energy, thus shedding light on the nature of particle acceleration at the early stage of SNR evolution. The nonthermal-dominated spectra in filament-like narrow structures are selectively extracted and used for spectral fitting because our model assumes that accelerated electrons are concentrated in the vicinity of the shock front due to synchrotron cooling. The cutoff energy parameter (ε_0) and shock speed (v_{sh}) are related as $\varepsilon_0 \propto v_{\text{sh}}^2 \eta^{-1}$ with a Bohm factor of η . Six SNRs provide us with spatially resolved ε_0 - v_{sh} plots across the remnants, indicating a variety of particle acceleration. The observed ε_0 - v_{sh} relation is nicely reproduced with the theoretical prediction with a constant value of η (Kepler's and Tycho's SNRs). The estimated η parameters are dependent on the shock obliquity (SN 1006) and on the variable number density (Cassiopeia A). Our assumption of the cooling-limited electron might not be applicable to G1.9+0.3 and the inner region in the NW rim of RX J1713.7-3946. With all SNRs considered together, the systematic tendency of η clarifies a correlation between η and age of t (or the expansion parameter of m) as $\eta \propto t^{-0.46}$ ($\eta \propto m^{4.5}$) (i.e., η decreases as the SNR evolves). This is interpreted as the magnetic field becomes more turbulent and self-generated, as particles are accelerated at a greater rate with time. We also present the properties of η with different types of supernova explosions and with reverse shock. In addition, we demonstrate a possibility of PeVatron because the maximum energy achieved in SNRs can be higher if we consider the newly observed time dependence on η .

4.1 Introduction

Supernova remnants are believed to be prominent accelerators of the galactic cosmic rays with energies up to a few PeV. However, the acceleration mechanism (i.e., DSA) has some critical problems, including the inability to detect PeV particles in SNRs. Because nearly all SNRs observed in gamma-rays have a power-law energy distribution with exponential cutoff energies of at most tens of TeV, whether SNRs are indeed capable of accelerating PeV particles (“PeVatron”) is questionable. Theoretically, the maximum attainable energy in DSA is not well constrained because of some unknown physical parameters such as a diffusion coefficient of the accelerated particle and magnetic field turbulence.

In DSA, which is widely accepted as an acceleration mechanism in SNRs, particles gradually and stochastically gain energies by crossing shock waves forward and backward. A particle changes its direction by being scattered with a magnetic field. Assuming Bohm diffusion, we can characterize the diffusion coefficient of the particle using a mean free path that is represented by the product of gyroradius and the so-called Bohm factor (η). In the case of $\eta = 1$ (also known as the Bohm limit), the mean free path of the particle takes the minimum value, and thus the particle is accelerated most efficiently. The diffusion coefficient (or the η parameter) is strongly related to the turbulent magnetic field that scatters the particle. Theoretical studies and numerical simulations propose that the turbulence is generated by the instability resulting from the pressure gradient derived from CR streaming (e.g., Bell (1978); Caprioli and Spitkovsky (2014a)). However, many facets of the mechanism of turbulent production are poorly understood.

Synchrotron radiation traces electrons accelerated in an SNR shock. The synchrotron X-ray, in particular, is emitted by multi-TeV electrons. Therefore, observations of synchrotron radiation in the X-ray domain are a great means for diagnosing the nature of the acceleration of the maximum energy attainable in an SNR. Young SNRs with ages less than a few thousand years are expected to radiate synchrotron X-rays. The detection of synchrotron emission has been reported in a few tens of galactic SNRs to date.

One can indirectly estimate η from measuring shock speed and cutoff energy in a synchrotron X-ray spectrum (e.g., Reynolds (1998); Zirakashvili and Aharonian (2007)). A TeV gamma-ray emitter, namely, SNR RX J1713.7–3946, is recognized as an accelerator producing the most efficient rate (i.e., the acceleration proceeds in the regime close to the Bohm limit of $\eta = 1$ (Tanaka et al., 2008; Tsuji et al., 2019)). Since *NuSTAR* was launched in 2012, it has provided us with spatially resolved hard X-ray spectra, thus enabling precise measurements of the cutoff energy. The young (\lesssim a few kyr) SNRs are believed to be efficient accelerators. However, some recent observations with *NuSTAR* have in fact revealed that the acceleration efficiency η is significantly variable and dependent on the acceleration site and/or source. Based on observations using *NuSTAR*, it has been determined that η is ~ 1 in the forward shock and 3–8 in the reverse shock or reflection shock in Cassiopeia A (Sato et al., 2018). In addition, η is ~ 20 in the youngest galactic SNR, G1.9+0.3 (Aharonian et al., 2017). For a unified understanding of particle acceleration in young SNRs, the gaps between G1.9+0.3 (~ 190 year), Cassiopeia A (~ 330 year), and RX J1713.7–3946 (~ 1600 year) must be filled.

In this chapter, we present a systematic analysis and measurement of the cutoff energy in the synchrotron spectrum of young 11 SNRs: G1.9+0.3, Cassiopeia A, Kepler’s SNR (Kepler), Tycho’s SNR (Tycho), G330.2+1.0, SN 1006, RX J1713.7–3946, RCW 86, Vela Jr., HESS J1731–347, and SN 1987A. Most of them are historical, and thus their ages are well constrained. The dataset of observations analyzed in this thesis, and the data reduction are presented in Section 4.2. Section 4.3 presents detailed imaging as well as spectral analyses and results. Our analysis for the first time reveals a variety of instances of particle acceleration in the remnants and reveals a systematic tendency of acceleration efficiency (Section 4.4). A conclusion is provided in Section 4.5.

4.2 Observations and data reduction

We systematically analyzed 11 young SNRs using X-ray observations. To reveal a tendency of acceleration efficiency in the young SNRs, they should be strong synchrotron emitters, and their physical parameters, such as age, distance, and shock speed, should be well constrained. The following 11 SNRs were selected based on the aforementioned criteria: G1.9+0.3, Cassiopeia A, Kepler, Tycho, G330.2+1.0, SN 1006, RX J1713.7–3946, RCW 86, Vela Jr., and HESS J1731–347 in our galaxy, and SN 1987A in the Large Magellanic Cloud (LMC). The other candidates that are dominated by synchrotron radiation (e.g., G32.45+0.1 and HESS J1640–465) were not included because they have large uncertainties regarding their ages and distances. The known parameters of these 11 SNRs are listed in Table 4.1.

Table 4.1: Properties of SNRs analyzed in this thesis.

Name	Age (yr)	Distance (kpc)	References
G1.9+0.3	190±50	~8.5	Borkowski et al. (2010)
Cassiopeia A	335±20	3.4	Patnaude and Fesen (2009)
Kepler	415	4±1	Cassam-Chenaï et al. (2004)
Tycho	440	2.3	Williams et al. (2013)
G330.2+1.0	700±300	~5	Park et al. (2006)
SN 1006	1010	1.9±0.3	Winkler et al. (2014)
RX J1713.7–3946	1600 ±10	1	Tsuji and Uchiyama (2016)
RCW 86	1835	2.8	Rosado et al. (1996)
Vela Jr.	3000±1000	0.5–0.9	Allen et al. (2015)
HESS J1731–347	2500–14000	3.6±0.4	H. E. S. S. Collaboration (2011)
SN 1987A	30	51.4	Frank et al. (2016)

We utilized archival X-ray observations using *Chandra* and *NuSTAR*. The dataset used in the analysis is summarized in Table 4.2 and Table 4.3.

We reduced all the observational data using the following software and calibration: The *Chandra* data were processed using CALDB version 4.7.6 in CIAO version 4.9. The *NuSTAR* data were calibrated and screened using nupipeline of *NuSTAR Data Analysis Software* (NuSTARDAS version 1.4.1 with CALDB version 20180814) included in HEASoft version 6.19. To screen the *NuSTAR* data, we used the strictest mode (SAAMODE = STRICT and TENTACLE = YES cut). The effective observational time reduced by these processes is shown in Table 4.2 and Table 4.3.

Table 4.2: Log of *Chandra* observations

Name	Obs ID	Effective time (ks)	Date	RA (deg)	Dec (deg)	Roll (deg)
G1.9+0.3	6708	23.9	2007-02-10	267.2	-27.2	91.8
G1.9+0.3	8521	25.7	2007-03-03	267.2	-27.2	91.8
G1.9+0.3	10111	68.3	2009-07-23	267.2	-27.2	270.0
G1.9+0.3	10112	50.8	2009-07-18	267.2	-27.2	283.2
G1.9+0.3	10928	35.4	2009-07-13	267.2	-27.2	270.2
G1.9+0.3	10930	82.1	2009-07-26	267.2	-27.2	270.0
G1.9+0.3	12689	155.6	2011-07-14	267.2	-27.2	277.3
G1.9+0.3	12690	48.2	2011-05-16	267.2	-27.2	79.2
G1.9+0.3	12691	184.0	2011-05-09	267.2	-27.2	79.2
G1.9+0.3	12692	162.6	2011-05-12	267.2	-27.2	79.2
G1.9+0.3	12693	127.5	2011-05-18	267.2	-27.2	79.2

Table 4.2: Log of *Chandra* observations (*continued*)

Name	Obs ID	Effective time (ks)	Date	RA (deg)	Dec (deg)	Roll (deg)
G1.9+0.3	12694	159.3	2011-05-20	267.2	-27.2	79.2
G1.9+0.3	12695	39.5	2011-05-23	267.2	-27.2	79.2
G1.9+0.3	13407	48.4	2011-07-18	267.2	-27.2	277.3
G1.9+0.3	13509	55.3	2011-07-22	267.2	-27.2	277.3
G1.9+0.3	16947	38.8	2015-05-04	267.2	-27.2	86.7
G1.9+0.3	16948	39.6	2015-07-14	267.2	-27.2	271.6
G1.9+0.3	16949	9.1	2015-05-20	267.2	-27.2	75.2
G1.9+0.3	17651	111.6	2015-05-05	267.2	-27.2	86.7
G1.9+0.3	17652	26.2	2015-05-09	267.2	-27.2	86.7
G1.9+0.3	17663	56.5	2015-07-24	267.2	-27.2	271.6
G1.9+0.3	17699	19.8	2015-07-17	267.2	-27.2	271.6
G1.9+0.3	17700	14.9	2015-08-31	267.2	-27.2	260.2
G1.9+0.3	17702	36.9	2015-07-15	267.2	-27.2	271.6
G1.9+0.3	17705	9.9	2015-07-25	267.2	-27.2	271.6
G1.9+0.3	18354	29.7	2015-09-01	267.2	-27.2	260.2
(total)		1659.6				
Cassiopeia A	4634	148.6	2004-04-28	350.9	58.8	59.2
Cassiopeia A	4635	135.0	2004-05-01	350.9	58.8	59.2
Cassiopeia A	4636	143.5	2004-04-20	350.9	58.8	49.8
Cassiopeia A	4637	163.5	2004-04-22	350.9	58.8	49.8
Cassiopeia A	4638	164.5	2004-04-14	350.9	58.8	40.3
Cassiopeia A	4639	79.0	2004-04-25	350.9	58.8	49.8
Cassiopeia A	5196	49.5	2004-02-08	350.9	58.8	325.5
Cassiopeia A	5319	42.3	2004-04-18	350.9	58.8	49.8
Cassiopeia A	5320	54.4	2004-05-05	350.9	58.9	65.1
(total)		980.3				
Kepler	116	48.8	2000-06-30	262.7	-21.5	261.1
Kepler	4650	46.2	2004-10-26	262.7	-21.5	268.8
Kepler	6714	157.8	2006-04-27	262.7	-21.4	89.0
Kepler	6715	159.1	2006-08-03	262.7	-21.5	265.7
Kepler	6716	158.0	2006-05-05	262.7	-21.4	89.5
Kepler	6717	106.8	2006-07-13	262.7	-21.5	264.2
Kepler	6718	107.8	2006-07-21	262.7	-21.5	264.8
Kepler	7366	51.5	2006-07-16	262.7	-21.5	264.2
Kepler	16004	102.7	2014-05-13	262.7	-21.5	92.7
Kepler	16614	36.4	2014-05-16	262.7	-21.5	92.7
(total)		975.1				
Tycho	7639	108.9	2007-04-23	6.3	64.1	29.2
Tycho	8551	33.3	2007-04-26	6.3	64.1	29.2
Tycho	10093	118.4	2009-04-13	6.3	64.1	29.2
Tycho	10094	90.0	2009-04-18	6.3	64.1	29.2
Tycho	10095	173.4	2009-04-23	6.3	64.1	29.2
Tycho	10096	105.7	2009-04-27	6.3	64.1	29.2
Tycho	10097	107.4	2009-04-11	6.3	64.1	26.3
((total))		737.1				
G330.2+1.0	6687	50.0	2006-05-21	240.2	-51.6	3.3
G330.2+1.0	19163	74.1	2017-05-02	240.2	-51.6	30.2

Table 4.2: Log of *Chandra* observations (*continued*)

Name	Obs ID	Effective time (ks)	Date	RA (deg)	Dec (deg)	Roll (deg)
G330.2+1.0 (total)	20068	74.1 198.2	2017-05-05	240.2	-51.5	30.2
SN 1006 N	13743	92.6	2012-04-28	225.8	-41.7	19.9
SN 1006 NE	9107	68.9	2008-06-24	226.0	-41.9	280.4
SN 1006 NE	732	68.1	2000-07-10	226.0	-41.9	280.2
SN 1006 SW	13739	100.1	2012-05-04	225.6	-42.1	9.1
SN 1006 NW	1959	89.0	2001-04-26	225.6	-41.8	30.2
SN 1006 NW	13737	87.1	2012-04-20	225.6	-41.8	31.7
SN 1006 W	13738	73.5	2012-04-23	225.4	-42.0	25.3
SN 1006 W	14424	25.4	2012-04-27	225.4	-42.0	25.3
SN 1006 SE	13741	98.5	2012-04-25	226.0	-42.0	24.6
SN 1006 S (total)	13742	79.0 782.2	2012-06-15	225.8	-42.1	289.1
RX J1713.7–3946 NW	736	29.6	2000-07-25	258.0	-39.6	282.5
RX J1713.7–3946 NW	6370	29.8	2006-05-03	257.9	-39.6	64.8
RX J1713.7–3946 NW	10090	28.4	2009-01-30	257.9	-39.5	98.6
RX J1713.7–3946 NW	10091	29.6	2009-05-16	257.9	-39.5	53.8
RX J1713.7–3946 NW	10092	29.2	2009-09-10	257.9	-39.6	266.1
RX J1713.7–3946 NW (total)	12671	89.9 236.5	2011-07-01	257.9	-39.6	304.5
RCW 86	1993	92.0	2001-02-01	220.2	-62.7	80.2
RCW 86 NE	4611	71.7	2004-06-15	221.3	-62.4	295.2
RCW 86 NE	7642	69.2	2007-06-20	221.3	-62.3	299.0
RCW 86	10699	2.0	2009-06-14	220.5	-62.6	304.4
RCW86	13748	36.1	2013-02-14	220.1	-62.7	70.7
RCW 86	14890	26.7	2013-02-03	220.4	-62.2	75.2
RCW 86	15608	29.2	2013-02-05	220.4	-62.2	75.2
RCW 86	15609	37.6	2013-02-10	220.4	-62.2	75.2
RCW86	15610	23.1	2013-02-17	220.1	-62.7	70.7
RCW86	15611	25.9	2013-02-12	220.1	-62.7	70.7
RCW 86 NE (total)	16952	67.2 480.7	2015-06-25	221.3	-62.4	293.6
Vela Jr. NW	3846	39.5	2003-01-05	132.3	-45.6	30.2
Vela Jr. NW	4414	34.5	2003-01-06	132.3	-45.6	30.2
Vela Jr. NORTH (total)	9123	39.7 113.7	2008-08-31	132.3	-45.7	146.2
HESS J1731–347	9139	29.2	2008-04-28	263.0	-34.7	81.2
SN 1987A	122	8.6	2000-01-17	83.9	-69.3	327.7
SN 1987A	1967	98.8	2000-12-07	83.9	-69.3	8.6
SN 1987A	1044	17.8	2001-04-25	83.8	-69.3	228.9
SN 1987A	2831	49.4	2001-12-12	83.9	-69.3	3.9
SN 1987A	2832	44.3	2002-05-15	83.8	-69.3	210.3
SN 1987A	3829	49.0	2002-12-31	83.9	-69.3	345.3
SN 1987A	3830	45.3	2003-07-08	83.8	-69.3	158.9
SN 1987A	4614	46.5	2004-01-02	83.9	-69.3	343.0
SN 1987A	4615	48.8	2004-07-22	83.8	-69.3	144.9
SN 1987A	5579	31.9	2005-01-09	83.9	-69.3	335.2

Table 4.2: Log of *Chandra* observations (*continued*)

Name	Obs ID	Effective time (ks)	Date	RA (deg)	Dec (deg)	Roll (deg)
SN 1987A	5580	23.7	2005-07-11	83.9	-69.3	153.2
SN 1987A	6668	42.3	2006-01-28	83.9	-69.3	316.4
SN 1987A	6669	36.4	2006-07-27	83.9	-69.3	139.9
SN 1987A	7636	33.5	2007-01-19	83.9	-69.3	325.1
SN 1987A	7637	25.7	2007-07-13	83.9	-69.3	153.7
SN 1987A	9142	6.6	2008-01-09	83.9	-69.3	335.2
SN 1987A	9143	8.6	2008-07-04	83.9	-69.3	161.8
SN 1987A	10130	6.0	2009-01-05	83.9	-69.3	339.4
(total)		623.2				

Table 4.3: Log of *NuSTAR* observations

Name	ObsID	Effective time (ks)	Date	RA (deg)	Dec (deg)	PA (deg)
G1.9+0.3	40001015003	85.4	2013-07-08	267.2	-27.2	327.3
G1.9+0.3	40001015005	121.6	2013-07-14	267.2	-27.2	327.3
G1.9+0.3	40001015007	144.7	2013-07-27	267.2	-27.2	327.3
(total)		351.7				
Cassiopeia A	40021002002	270.9	2012-11-23	350.8	58.8	338.3
Cassiopeia A	40021002006	135.6	2013-03-02	350.9	58.8	248.7
Cassiopeia A	40021002008	189.3	2013-03-05	350.9	58.8	248.7
Cassiopeia A	40021003003	197.8	2013-05-28	350.9	58.8	151.2
Cassiopeia A	40021001002	170.1	2012-08-27	350.8	58.8	75.7
Cassiopeia A	40021001004	25.7	2012-10-07	350.7	58.8	33.0
Cassiopeia A	40021001005	184.5	2012-10-07	350.8	58.8	33.0
Cassiopeia A	40021002010	12.4	2013-03-09	350.9	58.8	248.7
Cassiopeia A	40021003002	12.4	2013-05-28	350.9	58.8	151.2
Cassiopeia A	40021011002	235.1	2013-10-30	350.9	58.8	6.8
Cassiopeia A	40021012002	205.8	2013-11-27	350.8	58.8	335.2
Cassiopeia A	40021015002	74.4	2013-12-21	350.9	58.8	312.3
Cassiopeia A	40021015003	136.9	2013-12-23	350.9	58.8	312.2
(total)		1850.9				
Tycho	40020001002	338.7	2014-04-12	6.4	64.1	222.9
Tycho	40020001004	262.1	2014-07-18	6.4	64.1	124.2
Tycho	40020011002	146.8	2014-05-31	6.4	64.1	169.1
(total)		672.1				
Kepler	40001020002	212.8	2014-10-11	262.7	-21.5	336.2
Kepler	90201021002	106.6	2017-02-07	262.7	-21.5	158.2
Kepler	90201021004	41.4	2017-04-22	262.7	-21.4	156.1
Kepler	90201021006	47.0	2017-10-08	262.6	-21.5	336.4
Kepler	90201021008	35.0	2018-06-04	262.7	-21.4	147.8
Kepler	90201021010	31.3	2018-06-17	262.6	-21.6	6.3
Kepler	10501005002	86.1	2019-03-17	262.7	-21.4	157.2
(total)		560.2				
SN1006 NE	40110001002	198.5	2016-03-02	225.9	-41.8	180.0
SN1006 SW	40110002002	204.8	2016-03-08	225.5	-42.0	180.0

Table 4.3: Log of *NuSTAR* observations (*continued*)

Name	ObsID	Effective time (ks)	Date	RA (deg)	Dec (deg)	PA (deg)
RX J1713.7–3946 NW	40111001002	43	2015-09-27	257.86	–39.52	343.3
RX J1713.7–3946 NW	40111002002	49	2016-03-30	257.93	–39.58	165.6
(total)		92.0				
Vela Jr. NW	40101011002	69.0	2015-07-07	132.2	–45.7	40.4
Vela Jr. NW	40101011004	102.1	2015-07-16	132.2	–45.7	44.4
(total)		142.2				
SN1987A	40001014002	57.5	2012-09-07	84.0	–69.2	149.1
SN1987A	40001014003	113.3	2012-09-08	84.0	–69.2	149.1
SN1987A	40001014004	198.2	2012-09-11	83.9	–69.2	149.2
SN1987A	40001014006	45.2	2012-10-20	84.0	–69.3	190.5
SN1987A	40001014007	173.2	2012-10-21	83.9	–69.3	190.5
SN1987A	40001014010	160.0	2012-12-12	83.9	–69.3	242.9
SN1987A	40001014013	403.1	2013-06-29	83.8	–69.2	80.1
SN1987A	40001014015	83.5	2014-04-21	83.8	–69.3	13.1
SN1987A	40001014016	379.4	2014-04-22	83.8	–69.3	13.1
SN1987A	40001014018	170.5	2014-06-15	83.8	–69.2	65.0
SN1987A	40001014020	237.4	2014-06-19	83.8	–69.2	70.2
SN1987A	40001014023	397.7	2014-08-01	83.9	–69.2	111.4
(total)		2419.0				

4.3 Analysis and results

4.3.1 Images

The flux images are shown in Figure 4.1, Figure 4.2, Figure 4.3, and Figure 4.4. Note that all the epochs were combined, the exposure was corrected, and the background was not subtracted. We used `merge_obs` to produce the *Chandra* images. For the *NuSTAR* images, we created a count map using `XSELECT`¹ and the exposure map using `nuexpomap` with no vignetting correction (“`vignflag=no`” set). Finally, we divided the count map by the exposure map to generate the flux image using `XIMAGE`². In Figure 4.1, Figure 4.2, and Figure 4.3, we present three-color (red, green, and blue (RGB)) images with *Chandra*. For SNRs with strong thermal emissions (i.e., Cassiopeia A, Kepler, and Tycho), the RGB bands were set to be 1.7–2 keV (line emissions from Si), 6.4–7 keV (Fe), and 4–6 keV (continuum), respectively. For the other SNRs, which are relatively dominated by nonthermal radiation, the RGB bands were 0.5–1.2 keV, 1.2–2 keV, and 2–7 keV, respectively. These RGB images helped us to avoid contamination by thermal line emissions and to extract selectively the spectrum from the synchrotron-dominated (nonthermal) region in which we were interested.

The synchrotron spectrum is a powerful means of exploring the accelerated electrons, although some SNRs have strong thermal line emissions in addition to the synchrotron component, making it difficult to extract the pure synchrotron spectrum. In the RGB image, the hard X-ray band (in blue) can be dominated by nonthermal radiation, whereas the soft X-ray band (in red and green) can be contaminated by thermal line emissions. The rims or the filament-like structures, which are likely located in the outermost regions, appear bluish in the RGB images in Figure 4.1, Figure 4.2, and Figure 4.3. These regions are expected to contain synchrotron emissions from electrons accelerated at the forward shock and are thus the best targets for our analysis to study particle acceleration in SNRs. We defined the regions to extract the spectra along these bluish rims. We also defined subregions along those regions where the proper motions were measured in the previous works: e.g., Kepler (Katsuda et al., 2008b) and RCW 86 (Yamaguchi et al., 2016). It should be noted that the great angular resolution of *Chandra* enabled us to extract the spectrum from relatively small subregions, but the spectrum with *NuSTAR* was integrated over more extended regions. The regions used for spectral analyses using both *Chandra* and *NuSTAR* are indicated by thick-solid lines, whereas those with only *Chandra* are indicated by thin-solid lines. The regions for background extraction are indicated by dashed lines.

Note that we show the images of the entire remnants taken with *XMM-Newton* and *Suzaku* for RX J1713.7–3946 and Vela Jr., respectively. These images were kindly provided by Acero et al. (2009) for RX J1713.7–3946 and Fukuyama et al. (2019) for Vela Jr.

¹<https://heasarc.gsfc.nasa.gov/ftools/xselect/>

²<https://heasarc.gsfc.nasa.gov/docs/xanadu/ximage/ximage.html>

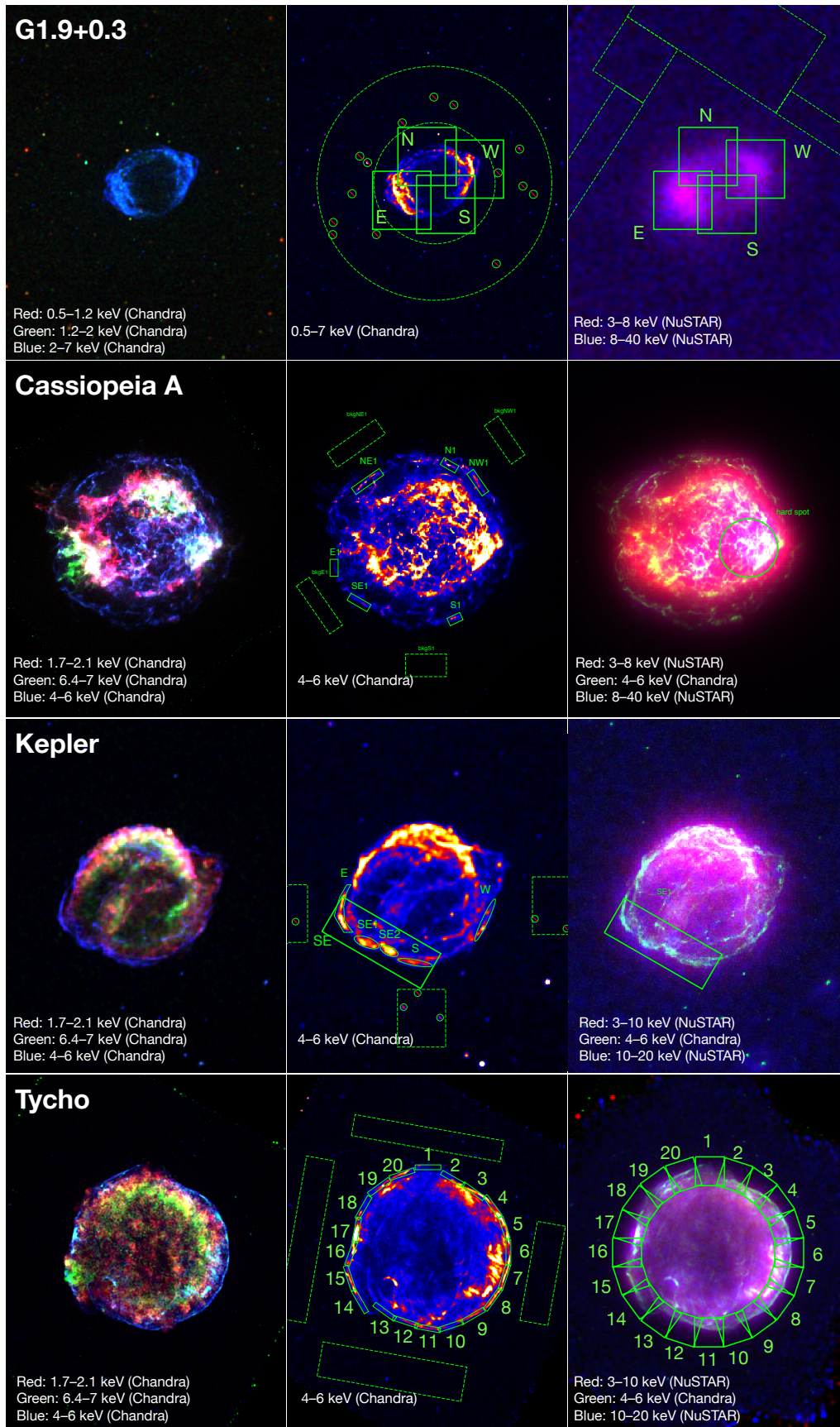


Figure 4.1: Three-color flux images using *Chandra* (left), *Chandra* images of continuum band (middle), and *NuSTAR* images (right) of G1.9+0.3, Cassiopeia A, Kepler, and Tycho from the top. The detailed energy bands are shown in each panel. Thick-solid regions indicate the regions used for joint fitting using *Chandra* and *NuSTAR*, whereas thin-solid regions indicate regions used for fitting with *Chandra*. The background regions are indicated by dashed-line regions.

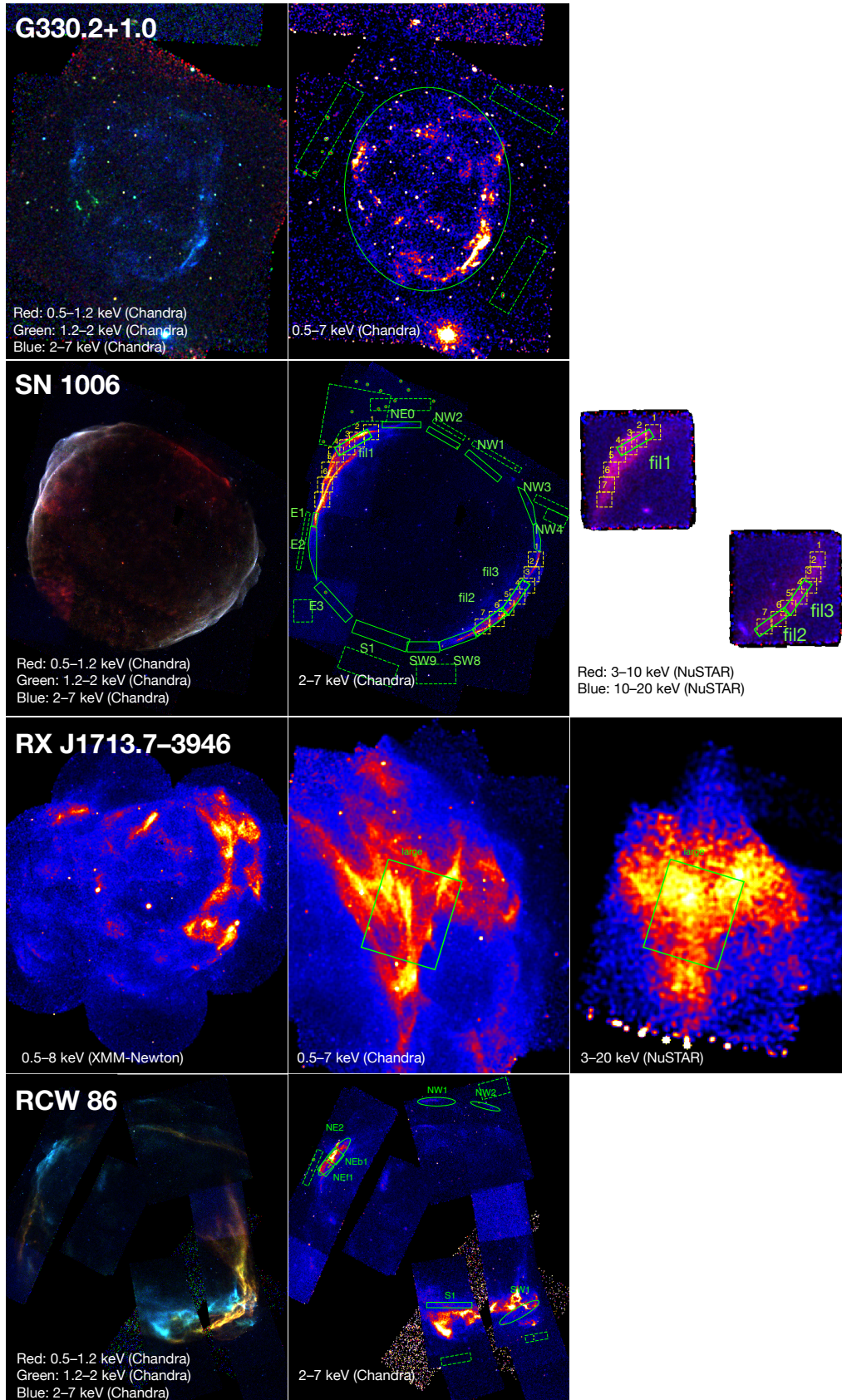


Figure 4.2: Three-color flux images using *Chandra* (left), *Chandra* images of continuum band (middle), and *NuSTAR* images (right) of G330.2+1.0, SN 1006, RX J1713.7–3946, and RCW 86 from the top.

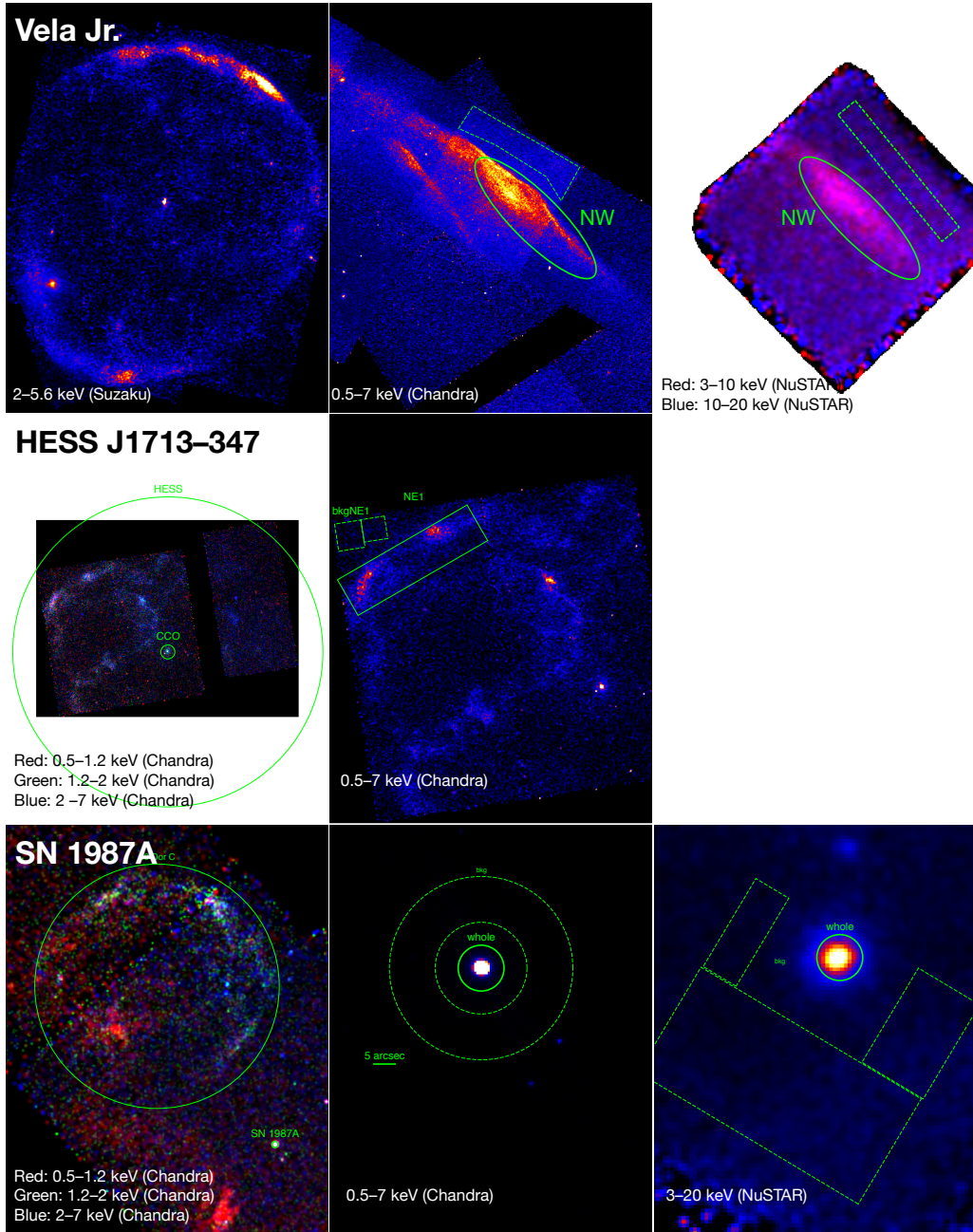


Figure 4.3: Three-color flux images using *Chandra* (left), *Chandra* images of continuum band (middle), and *NuSTAR* images (right) of Vela Jr., HESS J1713–347, and SN 1987A from the top.

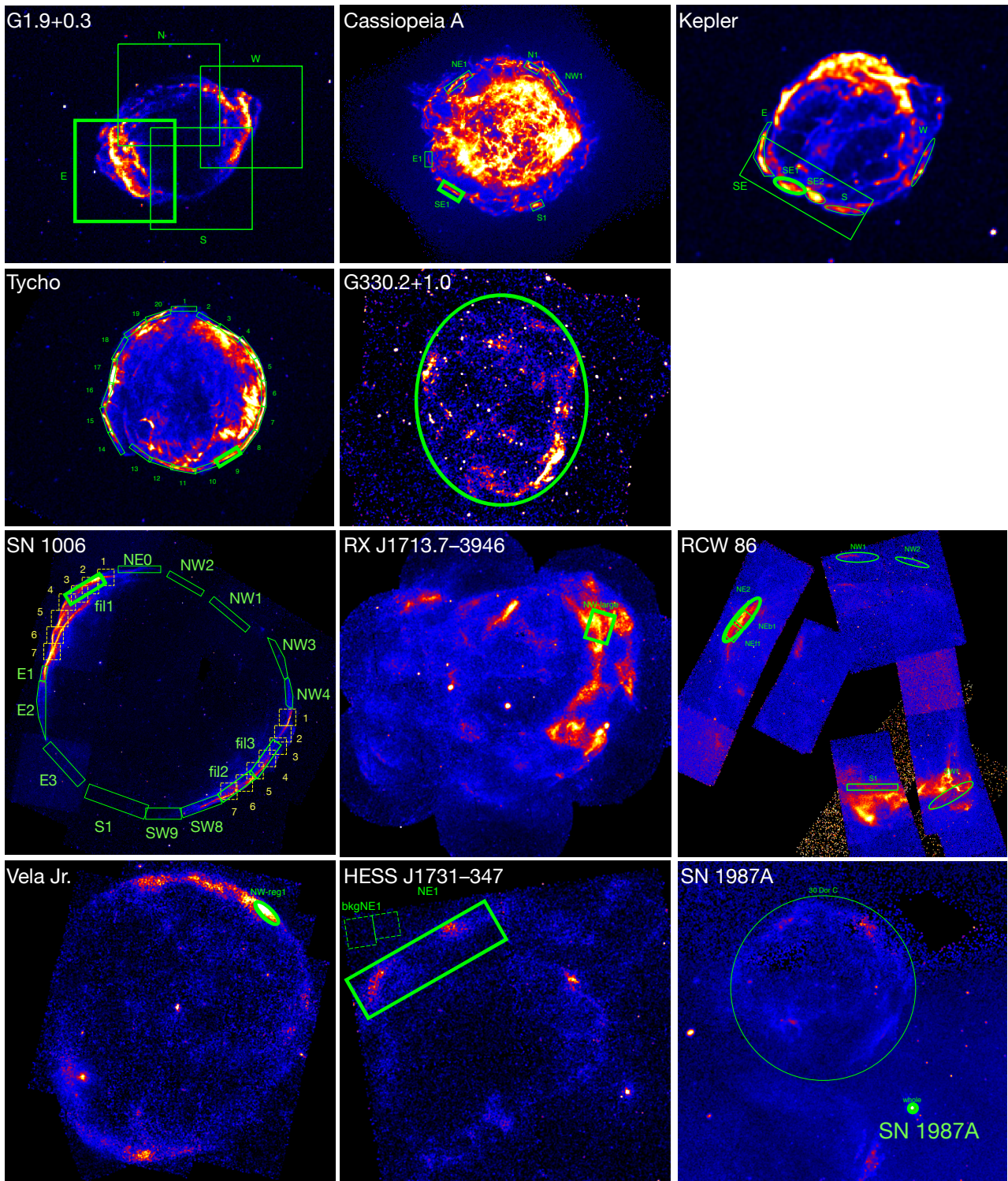


Figure 4.4: Flux images in nonthermal-dominated energy bands taken with *Chandra*, except for RX J1713.7–3946 and Vela Jr. taken with *XMM-Newton* and *Suzaku*, respectively. The color is shown in square-root scale in Cassiopeia A, RCW 86, HESS J 1731–347, and SN 1987A for visibility. The region highlighted by the thick line is used in the analysis in Section 4.4.3.

4.3.2 Spectrum

To extract spectra, we used `specextract` and `nuproducts` for observations using *Chandra* and *NuSTAR*, respectively. The “extended=yes” set was applied to all spectra using *NuSTAR* except for SN 1987A, which is spatially compatible with a point-like source. The source and background regions are shown in Figure 4.1, Figure 4.2, and Figure 4.3. The spectra of different epochs and different detector modules were combined using `addaspcaspec`. Most of the SNRs examined in this thesis showed expanding motions, particularly at the outermost rims. However, we could safely combine the spectra of different epochs because the extracted regions were substantially larger than the shifts due to their proper motions.

Note that the background spectrum with *NuSTAR* does include the uncertainty of non-uniform distribution due to the stray light and the instrumental components that are mentioned in Section 3.2.3. Thus, the use of *NuSTAR* spectra was reduced to a minimum for safety; we used them for G1.9+0.3, Kepler, Vela Jr., and SN 1987A. Because G1.9+0.3 and SN 1987A showed small angular sizes, and the background was extracted from the surrounding region of the source, the non-uniform distribution of the background did not largely affect the results. Particularly for Kepler and Vela Jr., which were spatially extended across nearly the entire FoV, careful treatment with a non-uniform background should be necessary. We simply checked that changing normalization of the present background by $\pm 10\%$ and 20% resulted in differences in the spectral parameters within 7% and 15% , respectively.

We performed spectral fitting of the broadband X-ray observations (i.e., *Chandra* + *NuSTAR* joint fitting). For the *Chandra* and *NuSTAR* spectra, the energy band was set to be 0.5–7 keV and 3–20 keV, respectively, unless otherwise mentioned.

We applied the ZA07 model, given by the equations that follow (i.e., the synchrotron radiation from cooling-limited electron as proposed in Zirakashvili and Aharonian (2007) and as mentioned in Section 2.6),

$$\frac{dN_e}{dE} \propto \left(\frac{E}{E_0}\right)^{-3} \left[\left\{ 1 + 0.523 \left(\frac{E}{E_0}\right)^{\frac{9}{4}} \right\}^2 - 0.0636 \left(\frac{E}{E_0}\right)^2 \left\{ 1 + 1.7 \left(\frac{E}{E_0}\right)^3 \right\}^{\frac{5}{6}} \right] \exp \left[- \left(\frac{E}{E_0}\right)^2 \right] \quad (4.1)$$

for electrons, and

$$\frac{dN_X}{d\varepsilon} \propto \left(\frac{\varepsilon}{\varepsilon_0}\right)^{-2} \left[1 + 0.38 \left(\frac{\varepsilon}{\varepsilon_0}\right)^{\frac{1}{2}} \right]^{\frac{11}{4}} \exp \left[- \left(\frac{\varepsilon}{\varepsilon_0}\right)^{\frac{1}{2}} \right], \quad (4.2)$$

for synchrotron X-rays (the same as Equation 2.117). In these models, we adopted the $\kappa = \sqrt{1/11}$ case in which κ is a ratio of the upstream magnetic field to the downstream magnetic field, $\kappa = B_{\text{up}}/B_{\text{down}}$ (Section 2.6). This indicates an enhancement of the random isotropic magnetic field due to the standard shock compression with a ratio of $\sigma = 4$. The interstellar absorption is considered by the TBabs model in XSEPC. The model is described with TBabs \times ZA07 for the synchrotron-dominated SNRs. For the SNRs which have non-negligible thermal emission, the thermal model was added (i.e., TBabs \times (ZA07 + thermal)), and the parameters of the thermal components, except for the normalization, were fixed to known values obtained in the previous work. The thermal model is described using VNEI³ in Cassiopeia A, VNEI + 6.43 keV Gaussian in Kepler (Bamba et al., 2005; Sun and Chen, 2019), VNEI in Tycho (Sato and Hughes, 2017), Vpshock⁴ in RCW 86 (Tsubone et al., 2017), and Vpshock + 6.6 keV Gaussian in SN 1987A (Frank et al., 2016). The details of spectral analysis for each SNR are presented in Section 4.4.2. Spectral fitting was performed using XSPEC version 12.9.0.

The spectra with the best-fit model are shown in Figure 4.5, and the best-fit parameters are listed in Table 4.4. The resulting cutoff energy parameters roughly ranged from 0.1 to 2 keV. $\varepsilon_0 \leq 0.5$ keV indicates that the cutoff started below the energy channel of *Chandra*. However, it should be emphasized that the ε_0 parameter did not exactly correspond to the cutoff energy ε_c , which yielded a e^{-1} drop-off, and $\varepsilon_c \sim 10\varepsilon_0$ approximately (Zirakashvili and Aharonian, 2007). Because the observed ε_0 ranged from 0.1 to 2 keV, ε_c was roughly 1–20 keV, which appeared in the energy bands we were observing. In addition, we measured the ε_0 parameter separately using only the *Chandra* and *NuSTAR* spectra, showing the consistent results with the joint fit.

³Variable non-equilibrium ionization (<https://heasarc.gsfc.nasa.gov/xanadu/xspec/manual/node193.html>).

⁴Variable plane-parallel shocked plasma model (<https://heasarc.gsfc.nasa.gov/xanadu/xspec/manual/node212.html>).

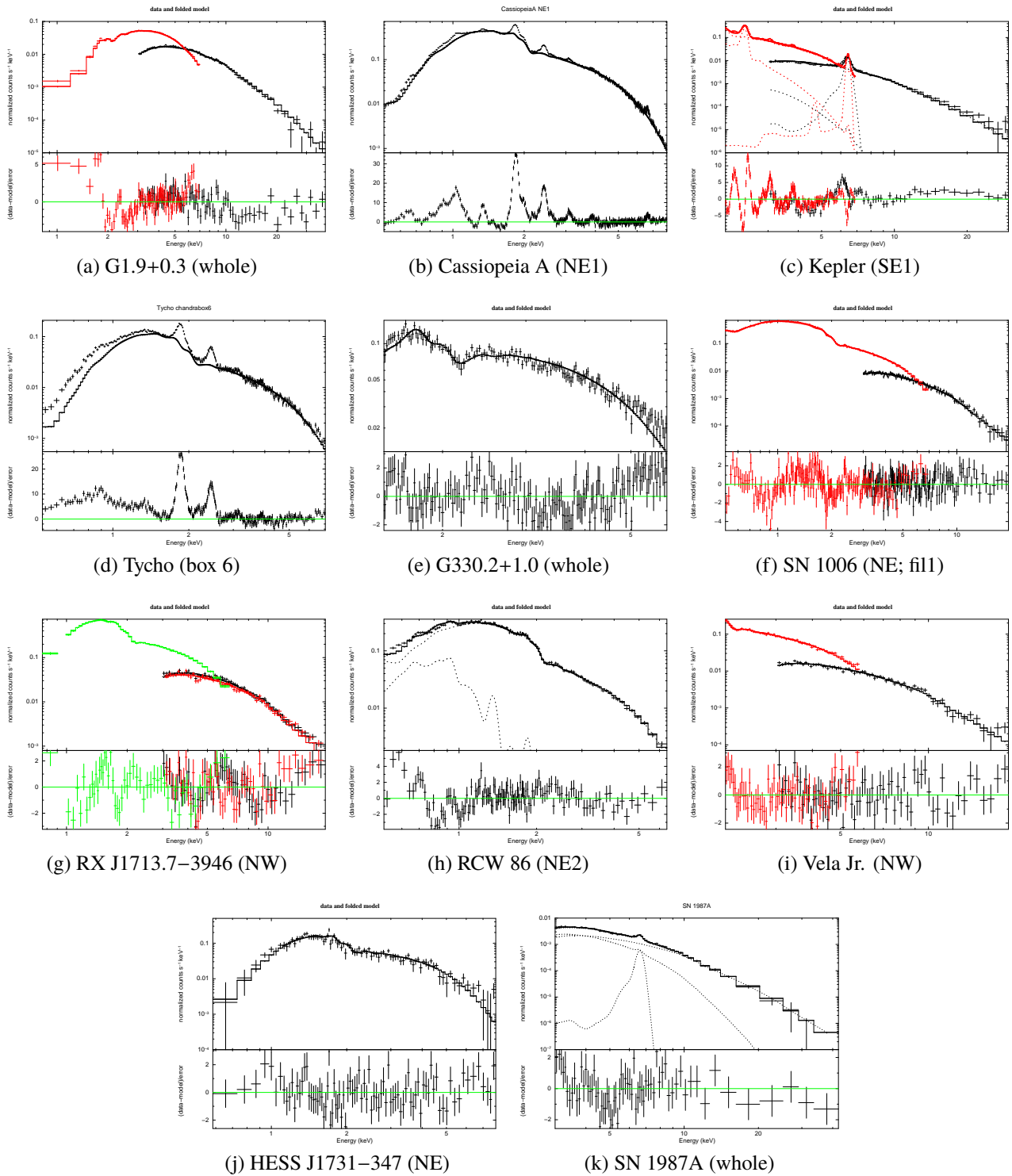


Figure 4.5: Spectrum of the typical region of each SNR with the best-fit model. For Cassiopeia A and Tycho, the fitting is performed in higher X-ray energy band (see the text for details), and the spectrum is shown from the softer band.

Table 4.4: Best-fit parameters of spectral analysis (*continued*)

Name	Region	X-ray data [†]	N_H (10^{22} cm^{-2})	ϵ_0 (keV)	χ^2	d.o.f
Table 4.4: Best-fit parameters of spectral analysis						
Name	Region	X-ray data [†]	N_H (10^{22} cm^{-2})	ϵ_0 (keV)	χ^2	d.o.f
G1.9+0.3	whole	CN	6 ± 0.04	1.2 ± 0.1	902.2	585
G1.9+0.3	N	CN	5.4 ± 0.1	1.2 ± 0.1	697.3	477
G1.9+0.3	E	CN	6 ± 0.1	1.4 ± 0.1	654.2	492
G1.9+0.3	S	CN	5.7 ± 0.1	0.9 ± 0.1	573.5	479
G1.9+0.3	W	CN	6.2 ± 0.1	1.1 ± 0.1	641.5	480
Cassiopeia A	N1	C	0.8 (fixed)	0.47 ± 0.03	280.0	200
Cassiopeia A	NE1	C	0.8 (fixed)	$0.96^{+0.08}_{-0.07}$	301.7	232
Cassiopeia A	E1	C	0.8 (fixed)	$0.47^{+0.09}_{-0.07}$	96.8	102
Cassiopeia A	SE1	C	0.8 (fixed)	$1.9^{+0.5}_{-0.34}$	158.8	178
Cassiopeia A	S1	C	0.8 (fixed)	0.39 ± 0.03	209.3	173
Cassiopeia A	NW1	C	0.8 (fixed)	$0.68^{+0.05}_{-0.04}$	278.4	226
Kepler	SE	CN	0.52 (fixed)	$0.53^{+0.02}_{-0.01}$	1067.7	507
Kepler	E	C	0.52 (fixed)	0.44 ± 0.04	157.7	142
Kepler	SE1	C	0.52 (fixed)	$0.74^{+0.12}_{-0.1}$	116.5	109
Kepler	SE2	C	0.52 (fixed)	$0.4^{+0.05}_{-0.04}$	123.0	97
Kepler	S	C	0.52 (fixed)	$0.56^{+0.1}_{-0.08}$	90.0	74
Kepler	W	C	0.52 (fixed)	$0.33^{+0.04}_{-0.03}$	239.1	99
Tycho	1	C	0.7 (fixed)	0.1 ± 0.01	289.0	42
Tycho	2	C	0.7 (fixed)	0.11 ± 0.01	316.9	63
Tycho	3	C	0.7 (fixed)	0.29 ± 0.03	142.8	116
Tycho	4	C	0.7 (fixed)	0.35 ± 0.03	209.0	136
Tycho	5	C	0.7 (fixed)	0.25 ± 0.02	890.6	145
Tycho	6	C	0.7 (fixed)	0.34 ± 0.03	273.0	135
Tycho	7	C	0.7 (fixed)	0.29 ± 0.02	224.0	135
Tycho	8	C	0.7 (fixed)	$0.33^{+0.04}_{-0.03}$	126.6	107
Tycho	9	C	0.7 (fixed)	$0.37^{+0.05}_{-0.04}$	165.8	95
Tycho	10	C	0.7 (fixed)	0.17 ± 0.02	693.7	79
Tycho	11	C	0.7 (fixed)	$0.32^{+0.04}_{-0.03}$	119.6	102
Tycho	12	C	0.7 (fixed)	$0.31^{+0.04}_{-0.03}$	158.1	88
Tycho	13	C	0.7 (fixed)	$0.25^{+0.04}_{-0.03}$	66.5	52
Tycho	14	C	0.7 (fixed)	0.24 ± 0.03	312.0	80
Tycho	15	C	0.7 (fixed)	0.28 ± 0.03	1203.6	130
Tycho	16	C	0.7 (fixed)	0.12 ± 0.01	2378.7	128
Tycho	17	C	0.7 (fixed)	0.39 ± 0.03	293.3	178
Tycho	18	C	0.7 (fixed)	0.12 ± 0.01	651.4	75
Tycho	19	C	0.7 (fixed)	0.23 ± 0.02	382.3	108
Tycho	20	C	0.7 (fixed)	$0.31^{+0.04}_{-0.03}$	137.9	98
G330.2+1.0	whole	C	2.4 (fixed)	$0.65^{+0.07}_{-0.06}$	356.2	166
SN 1006	NE0	C	0.07 (fixed)	0.16 ± 0.01	217.5	172
SN 1006	fil 1 (NE)	CN	0.068 (fixed)	0.4 ± 0.01	526.7	407
SN 1006	E1	C	0.07 (fixed)	0.33 ± 0.01	382.0	279
SN 1006	E2	C	0.07 (fixed)	0.19 ± 0.01	408.1	313
SN 1006	E3	C	0.07 (fixed)	$0.16^{+0.04}_{-0.05}$	266.2	84

Table 4.4: Best-fit parameters of spectral analysis (*continued*)

Name	Region	X-ray data [†]	N_H (10^{22} cm $^{-2}$)	ϵ_0 (keV)	χ^2	d.o.f
SN 1006	S1	C	0.07 (fixed)	$0.38^{+0.22}_{-0.11}$	288.3	181
SN 1006	SW9	C	0.07 (fixed)	0.1 ± 0.01	201.6	128
SN 1006	SW8	C	0.07 (fixed)	0.22 ± 0.01	236.8	213
SN 1006	fil 2 (SW)	CN	0.068 (fixed)	0.32 ± 0.01	469.6	297
SN 1006	fil 3 (SW)	CN	0.068 (fixed)	0.31 ± 0.01	435.3	347
SN 1006	NW4	C	0.07 (fixed)	0.24 ± 0.01	144.0	146
SN 1006	NW3	C	0.07 (fixed)	0.12 ± 0.01	161.2	118
SN 1006	NW1	C	0.07 (fixed)	$0.13^{+0.09}_{-0.05}$	152.0	110
SN 1006	NW2	C	0.07 (fixed)	$0.18^{+0.08}_{-0.05}$	272.2	124
RX J1713.7–3946	Large box	CN	0.75 ± 0.01	1.1 ± 0.06	250.5	149
RX J1713.7–3946	box (a)	CN	0.75 ± 0.02	$1.9^{+0.45}_{-0.32}$	151.2	136
RX J1713.7–3946	box (b)	CN	0.77 ± 0.02	$0.92^{+0.14}_{-0.11}$	163.7	120
RX J1713.7–3946	box (c)	CN	0.83 ± 0.02	$1^{+0.14}_{-0.11}$	150.8	150
RX J1713.7–3946	box (d)	CN	0.76 ± 0.02	$1.3^{+0.2}_{-0.16}$	167.0	141
RX J1713.7–3946	box (f)	CN	0.49 ± 0.02	$0.6^{+0.09}_{-0.08}$	191.2	131
RCW86	NE2	C	0.33 (fixed)	$0.38^{+0.02}_{-0.01}$	396.4	340
RCW86	NEf1	C	0.33 (fixed)	0.28 ± 0.01	287.6	204
RCW86	NEb1	C	0.33 (fixed)	0.36 ± 0.02	319.8	236
RCW86	NW1	C	0.34 (fixed)	$0.24^{+0.04}_{-0.03}$	77.5	62
RCW86	NW2	C	0.34 (fixed)	$0.19^{+0.05}_{-0.04}$	23.5	26
RCW86	S1	C	0.42 (fixed)	0.36 ± 0.03	221.5	177
RCW86	SW1	C	0.42 (fixed)	$0.11^{+0}_{-0.01}$	628.3	221
Vela Jr.	whole	S	0.67 (fixed)	0.31 ± 0.01	509.9	265
Vela Jr.	reg1	CN	0.67 (fixed)	0.54 ± 0.04	138.5	122
HESS J1731–347	NE1	C	1 (fixed)	$0.97^{+0.46}_{-0.26}$	102.7	86
SN 1987A	whole	N	0.24 (fixed)	$0.69^{+0.14}_{-0.11}$	76.3	64

[†] X-ray observation data used for the spectral fitting. C: *Chandra*. N: *NuSTAR*. S: *Suzaku*.

4.4 Discussion

4.4.1 Cutoff energy v.s. shock speed

The cutoff energy parameter ε_0 is the key parameter of particle acceleration in the SNR shock because it is determined based on a balance between acceleration and synchrotron cooling in the present framework. Zirakashvili and Aharonian (2007) derived an important relation between the cutoff energy parameter and the shock velocity,

$$\varepsilon_0 = 1.55 \left(\frac{v_{\text{sh}}}{3900 \text{ km s}^{-1}} \right)^2 \eta^{-1} \text{ keV}, \quad (4.3)$$

which is the same as Equation 2.116 in Section 2.6. We note that the cutoff energy parameter in the electron spectrum, E_0 , is also obtained:

$$E_0 = 23.5 \left(\frac{v_{\text{sh}}}{3000 \text{ km s}^{-1}} \right) \left(\frac{B}{100 \mu\text{G}} \right)^{-\frac{1}{2}} \eta^{-\frac{1}{2}} \text{ TeV}, \quad (4.4)$$

which is the same as (22) in Zirakashvili and Aharonian (2007) for $\kappa = \sqrt{11}^{-1}$ and $\gamma_s = 4$. Equation 4.3 yields an equation for deriving the Bohm factor,

$$\eta = 1.55 \left(\frac{v_{\text{sh}}}{3900 \text{ km s}^{-1}} \right)^2 \left(\frac{\varepsilon_0}{\text{keV}} \right)^{-1}. \quad (4.5)$$

Combining the measured cutoff energy parameter and known shock speed, we can estimate the value of η using Equation 4.5. Table 4.5 lists the obtained η parameter as well as the shock velocity in each region of SNR analyzed in Section 4.3.2.

Figure 4.6 illustrates the relation between the cutoff energy parameter measured in Section 4.3.2 and the shock speed in the literature. Each plot shown in Figure 4.6 represents the largest- ε_0 region of each SNR, which is highlighted by the thick line in Figure 4.4 and nearly corresponds to the maximum shock-speed region. Apparently, varieties of both the cutoff energy parameter and the shock velocity exist. In the following subsections, we discuss the nature of particle acceleration of individual SNRs (Section 4.4.2) and the systematical tendency of particle acceleration of young SNRs (Section 4.4.3).

Table 4.5: Properties of particle acceleration

Name	Region	X-ray data [†]	v_{sh} [‡] (km s ⁻¹)	m^*	ε_0 (keV)	η	B_{low}^* (μG)
G1.9+0.3	whole	CN	13000±1000	1.1±0.2	1.23±0.05	14.0±2.8	38
G1.9+0.3	N	CN	3600±500	0.4±0.2	1.18±0.09	1.1±0.4	39
G1.9+0.3	E	CN	13000±1000	1.1±0.2	1.43±0.09	12.1±2.6	36
G1.9+0.3	S	CN	3600±500	0.4±0.2	0.87±0.06	1.5±0.5	43
G1.9+0.3	W	CN	13000±1000	1.1±0.2	1.13±0.07	15.2±3.3	39
G1.9+0.3	N-RS [◊]	CN	5000±1000	0.4±0.2	1.18±0.09	2.2±1.0	39
G1.9+0.3	S-RS [◊]	CN	5000±1000	0.4±0.2	0.87±0.06	2.9±1.4	43
Cassiopeia A	NW1	C	4512±483	0.7±0.1	0.68±0.04	3.1±0.8	32
Cassiopeia A	S1	C	5479±483	0.7±0.1	0.39±0.03	7.8±1.9	38
Cassiopeia A	SE1	C	5157±644	0.7±0.1	1.87±0.34	1.4±0.6	23
Cassiopeia A	E1	C	5157±322	0.7±0.1	0.47±0.07	5.7±1.6	36
Cassiopeia A	NE1	C	4835±483	0.7±0.1	0.96±0.07	2.5±0.7	28
Cassiopeia A	N1	C	4351±322	0.7±0.1	0.47±0.03	4.1±0.9	36
Cassiopeia A	RS [◊] (Sato et al., 2018)	CN	8000±1000	0.7±0.1	1.15±0.25	5.7±2.6	27
Kepler	SE	CN	5000±1000	0.6±0.1	0.53±0.01	4.8±2.0	30
Kepler	E	C	3792±303	0.7±0.1	0.44±0.04	3.3±0.8	32
Kepler	SE1	C	5726±910	1.0±0.2	0.74±0.10	4.5±2.0	27
Kepler	SE2	C	3375±569	0.6±0.1	0.40±0.04	2.9±1.3	33
Kepler	S	C	4588±474	0.8±0.1	0.56±0.08	3.8±1.3	29
Kepler	W	C	3545±568	0.6±0.1	0.33±0.03	3.9±1.6	35

Table 4.5: Properties of particle acceleration (*continued*)

Name	Region	X-ray data [†]	v_{sh} [‡] (km s ⁻¹)	m^*	ε_0 (keV)	η	B_{low}^* (μ G)
Tychor	3	C	3200±320	0.6±0.1	0.29±0.03	3.6±1.0	35
Tychor	4	C	3580±358	0.6±0.1	0.35±0.03	3.8±1.1	33
Tychor	6	C	3850±385	0.6±0.1	0.34±0.03	4.4±1.3	33
Tychor	7	C	3920±648	0.6±0.1	0.29±0.02	5.4±2.2	35
Tychor	8	C	3980±418	0.6±0.1	0.33±0.03	4.9±1.5	34
Tychor	9	C	4060±634	0.6±0.1	0.37±0.04	4.6±1.9	33
Tychor	11	C	3240±486	0.6±0.1	0.32±0.03	3.4±1.3	34
Tychor	12	C	3480±538	0.6±0.1	0.31±0.03	3.9±1.6	34
Tychor	13	C	3330±333	0.6±0.1	0.25±0.03	4.6±1.5	37
Tychor	17	C	2000±400	0.6±0.1	0.39±0.03	1.1±0.5	32
Tychor	20	C	3660±366	0.6±0.1	0.31±0.03	4.4±1.3	35
G330.2+1.0	whole	C	7000±2000	0.9±0.3	0.83±0.09	6.0±4.1	18
SN 1006	NE0	C	6500±500	0.5±0.1	0.16±0.01	26.3±5.1	24
SN 1006	NE (fil1)	CN	5900±500	0.5±0.1	0.40±0.01	9.0±1.7	18
SN 1006	E1	C	4900±500	0.5±0.1	0.33±0.01	7.3±1.8	19
SN 1006	E2	C	5800±500	0.5±0.1	0.19±0.01	17.9±3.6	23
SN 1006	E3	C	7000±1200	0.5±0.1	0.16±0.05	31.7±20.8	25
SN 1006	S1	C	7200±1000	0.5±0.1	0.38±0.11	13.7±7.9	18
SN 1006	SW9	C	5000±800	0.5±0.1	0.10±0.01	26.0±10.1	29
SN 1006	SW8	C	5000±800	0.5±0.1	0.22±0.01	11.4±4.1	22
SN 1006	SW (fil2)	CN	5500±500	0.5±0.1	0.32±0.01	9.6±2.0	19
SN 1006	SW (fil3)	CN	5900±800	0.5±0.1	0.31±0.01	11.4±3.4	20
SN 1006	NW4	C	5500±500	0.5±0.1	0.24±0.01	12.7±2.9	21
SN 1006	NW3	C	7000±1000	0.5±0.1	0.12±0.01	40.0±14.5	27
SN 1006	NW1	C	3000±1200	0.5±0.1	0.13±0.05	7.0±8.1	26
SN 1006	NW2	C	3000±1200	0.5±0.1	0.18±0.05	5.2±5.6	24
RX J1713.7–3946	NW	CN	3900±300	0.7±0.1	1.14±0.06	1.4±0.3	9
RX J1713.7–3946	box (a)	CN	3900±300	0.7±0.1	1.90±0.32	0.8±0.3	8
RX J1713.7–3946	box (b)	CN	1200±300	0.2±0.1	0.92±0.11	0.2±0.1	10
RX J1713.7–3946	box (c)	CN	1400±200	0.3±0.0	1.03±0.11	0.2±0.1	9
RX J1713.7–3946	box (d)	CN	2900±200	0.7±0.1	1.26±0.16	0.7±0.2	9
RX J1713.7–3946	box (e)	CN	800±300	0.2±0.1	1.44±0.23	0.0±0.0	8
RX J1713.7–3946	box (f)	CN	800±300	0.2±0.1	0.60±0.08	0.1±0.1	11
RX J1713.7–3946	whole	S	3900±300	0.7±0.1	0.94±0.03	1.7±0.5	9
RCW 86	NE2	C	2500±700	0.3±0.1	0.30±0.01	2.1±1.3	13
RCW 86	NEf1	C	3000±340	0.4±0.0	0.28±0.01	3.2±0.9	13
RCW 86	NEb1	C	1780±240	0.3±0.0	0.36±0.02	0.9±0.3	12
RCW 86	NW1	C	810±150	0.1±0.0	0.24±0.03	0.3±0.1	14
RCW 86	NW2	C	810±150	0.1±0.0	0.19±0.04	0.4±0.2	15
RCW 86	S1	C	800±300	0.1±0.0	0.36±0.03	0.2±0.1	12
RCW 86	SW1	CN	800±300	0.1±0.0	0.11±0.01	0.6±0.5	18
Vela Jr.	whole	S	2000±600	0.5±0.2	0.31±0.01	1.3±0.8	9
Vela Jr.	NW (reg1)	CN	2000±600	0.5±0.2	0.55±0.04	0.7±0.5	8
HESS J1731–347	NE	C	2000±500	0.5±0.1	0.97 ^{+0.46} _{-0.26}	0.4 ^{+0.6} _{-0.3}	6
SN 1987A	whole	N	6711±787	0.9±0.1	0.69±0.11	6.6±2.6	164
SN 1987A	whole-RS [◦]	N	4767±300	0.9±0.1	0.69±0.11	3.4±1.0	164

[†] X-ray observation data used for the spectral fitting. C: *Chandra*. N: *NuSTAR*. S: *Suzaku*.

[‡] References (see also the text). G1.9+0.3: Borkowski et al. (2017). Cassiopeia A: Patnaude and Fesen (2009). Kepler: Vink (2008); Katsuda et al. (2008b). Tycho: Katsuda et al. (2010); Williams et al. (2013). G330.2+1.0: Borkowski et al. (2018). SN 1006: Winkler et al. (2014). RX J1713.7–3946: Tsuji and Uchiyama (2016); Acero et al. (2017). RCW 86: Yamaguchi et al. (2016). Vela Jr.: Katsuda et al. (2008a); Allen et al. (2015). HESS J1731–347: H. E. S. S. Collaboration (2011). SN 1987A: Frank et al. (2016).

* Expansion parameter.

* Lower limit of magnetic field required for cooling-limited assumption.

◦ RS: Assuming the reverse shock or reflection shock.

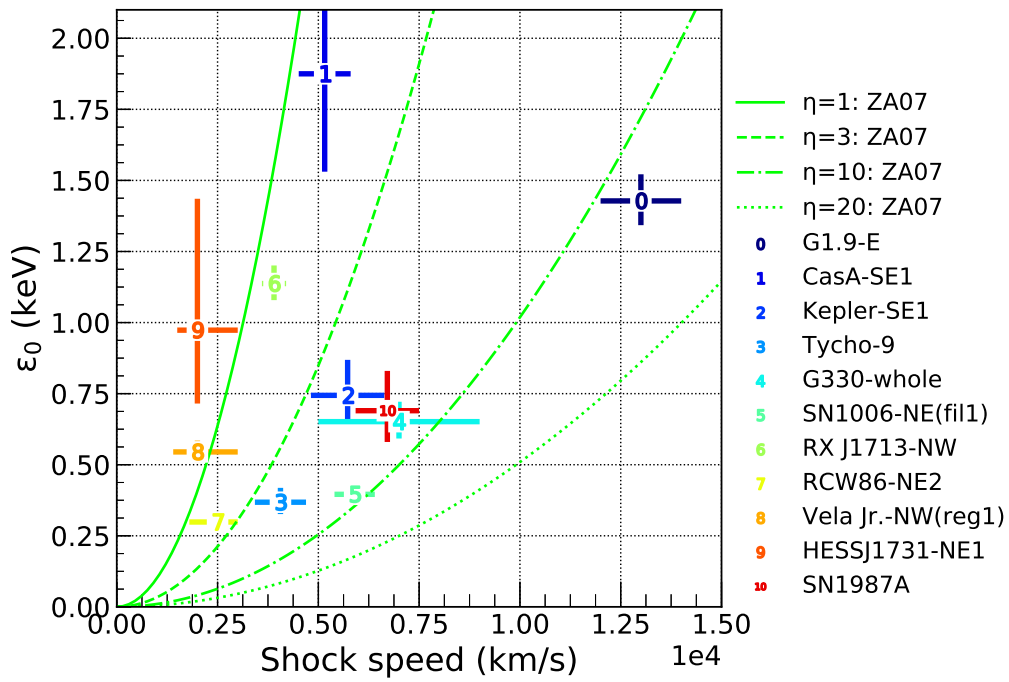


Figure 4.6: $v_{sh}-\epsilon_0$ diagram. Each plot is taken from the region having the largest ϵ_0 (or the maximum v_{sh}) in each SNR, where the region is highlighted in Figure 4.4.

4.4.2 Acceleration efficiency in individual source

G1.9+0.3

G1.9+0.3 is known as the youngest SNR in our galaxy. The observed strong absorption suggested that G1.9+0.3 is located near the galactic center, and the distance to the source is approximately 8.5 kpc. The age is roughly 150–190 years, estimated from its angular size of $1.5'$ and the fast proper motion of $\sim 14000 \text{ km s}^{-1}$ assuming the distance is 8.5 kpc (Borkowski et al., 2014). The X-ray spectrum is strongly dominated by synchrotron radiation in the bright rim of G1.9+0.3, whereas some thermal line emissions have been detected in the central void region (Borkowski et al., 2010). The *NuSTAR* observations revealed hard X-ray morphology, detected up to $\sim 30 \text{ keV}$, was roughly in agreement with the soft X-ray (Zoglauer et al., 2015). Aharonian et al. (2017) found that particle acceleration in G1.9+0.3 is approximately one order of magnitude more inefficient than the maximum rate (i.e., Bohm factor with $\eta \sim 20$) as derived from the measured cutoff energy and the shock speed. This leads us to a new insight into particle acceleration in such a young SNR. Deeper follow-up observations using *Chandra* and detailed analysis revealed the asymmetric expansion: the expansion velocity is $\sim 13000 \text{ km s}^{-1}$ in the east (E) to west (W) axis and $\sim 3600 \text{ km s}^{-1}$ in the north (N) to south (S) axis (Borkowski et al., 2017). The slower speed in the northern rim is indicative of an interaction between the SNR shock and the molecular cloud. Although the X-ray image shows the bilateral structure, the (synchrotron) radio image is ring-like, and the north part is brighter than the other regions (Borkowski et al., 2010). Brose et al. (2019) performed sophisticated one-dimensional numerical simulations that simultaneously solved the cosmic-ray transport, magnetic field transport, and hydrodynamical equations for gas flow. They suggested the morphological difference in radio and X-ray is interpreted as the radio synchrotron emission comes from the reverse shock (RS), while the X-ray synchrotron is attributed to the forward shock.

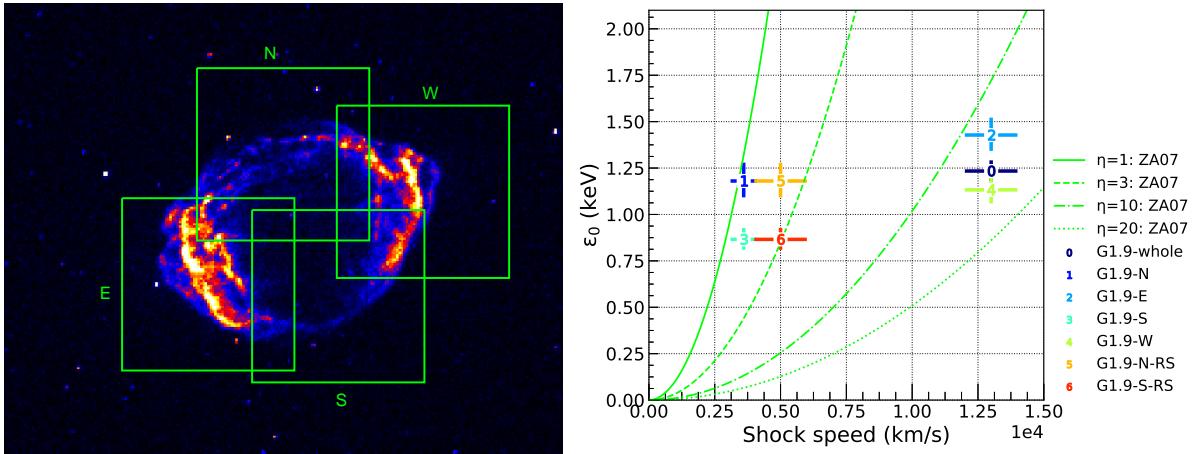


Figure 4.7: The flux image and region definition (left), and $v_{\text{sh}}-\epsilon_0$ diagram (right) in G1.9+0.3. The reverse shock speed is calculated by Equation 4.6 in the N (the plot with ID of 5 in the right panel) and S (ID 6) rims.

We extracted the spectra using *Chandra* and *NuSTAR* from four subregions named N, E, S, and W, as well as the entire remnant. The angular size of each subregion was $1.2' \times 1.2'$. The energy band of *NuSTAR* was set to be 3–40 keV. Figure 4.7 illustrates the relation between the observed ϵ_0 and v_{sh} , and the theoretical prediction given by Equation 4.3. The cutoff energy parameter of the entire remnant was measured to be 1.2 keV. This indicates the acceleration efficiency of $\eta = 13$ assuming a shock speed of 14000 km s^{-1} , which was roughly consistent with $\eta \sim 20$ obtained in Aharonian et al. (2017).

The spatially resolved spectral fitting indicates that the cutoff energy parameters in the western and northern regions were compatible with that of the entire remnant ($\epsilon_0 \approx 1.1\text{--}1.2 \text{ keV}$), whereas it was slightly higher in the eastern rim ($\epsilon_0 \approx 1.4 \text{ keV}$) and lower in the southern part ($\epsilon_0 \approx 0.9 \text{ keV}$). It should be noted that these differences in the measured cutoff energy parameters may have been underestimated because of the overlapped subregions and the limited angular resolution of *NuSTAR*. In the case of forward shock, the Bohm factor was estimated to be ~ 10 in the bright rim of E and W, with the faster shock velocity of $\sim 13000 \text{ km s}^{-1}$. However, η

was 1–2 in the fainter area of N and S, with the slower shock speed of $\sim 4000 \text{ km s}^{-1}$. If we assume the outward proper motions in the N and S rims, which were measured in Borkowski et al. (2017), correspond to the reverse shock, the upstream speed in the rest frame of the reverse shock is given by

$$u_1 = \frac{R_{\text{ref}}}{t_{\text{age}}} - v_{\text{obs}}, \quad (4.6)$$

which is introduced in Sato et al. (2018). Indeed the reverse shock might play a major role in the northern region where the radio synchrotron is strong and the proper motion is reduced, as proposed in (Brose et al., 2019). Using Equation 4.6, u_1 in N and S is approximately calculated to be 5000 km s^{-1} , resulting in $\eta \sim 2\text{--}3$ (Figure 4.7). We apparently see a significant difference in the acceleration efficiency across the remnant: The Bohm factor in the bright E–W rim is approximately one order of magnitude higher than that in the N–S part in the case of either the forward shock or reverse shock.

Cassiopeia A

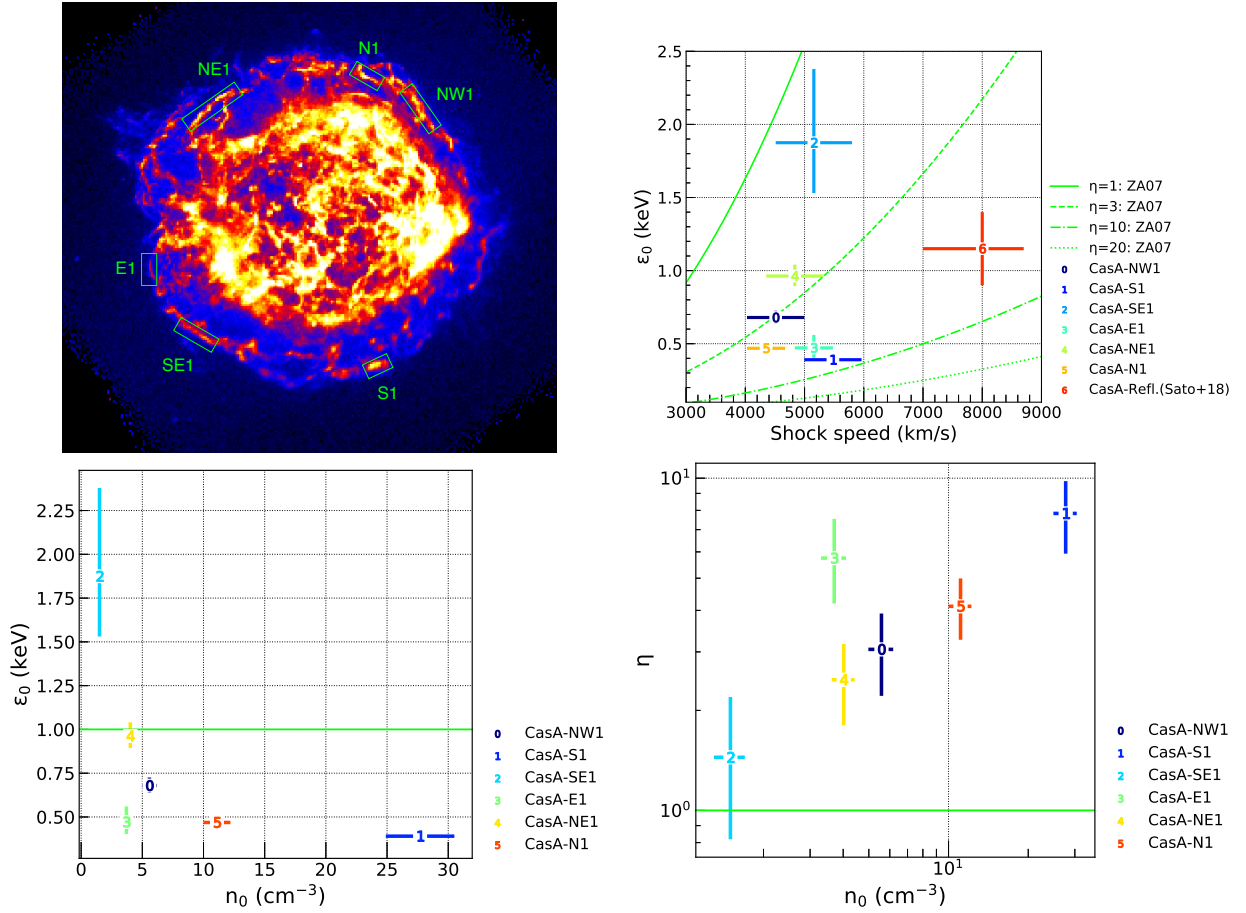


Figure 4.8: Top: Same as Figure 4.7 for Cassiopeia A. The flux image is shown in a square-root scale. The reflection shock is taken from Sato et al. (2018). Bottom: ϵ_0 (left) and the η parameter (right) as a function of the number density n_0 .

Cassiopeia A is a remnant of a core-collapse supernova explosion, which would likely be SN1680. Both of its strong thermal and nonthermal X-ray emissions make Cassiopeia A one of the best-studied galactic SNRs. It has been well-studied not only with X-rays but also with other wavelength observations from radio to TeV gamma-rays. Synchrotron X-ray radiation was confirmed in the outer thin filaments, indicating a forward shock and in the inner regions, indicating a reverse shock (Stage et al., 2006; Uchiyama and Aharonian, 2008). Stage

et al. (2006) showed the significant variation of roll-off energies (using SRCUT⁵ in XSPEC) across the remnant, resulting in the η value being lower in NE and SE assuming the shock speed is constant (5000 km s⁻¹) throughout the remnant. A later study confirmed that the proper-motion velocities were roughly comparable from region to region (Patnaude and Fesen, 2009). Recent hard X-ray observations with *NuSTAR* revealed some interesting aspects about particle acceleration in Cassiopeia A. Grefenstette et al. (2015) found a hard spot, which is located in the interior of the remnant near the reverse shock and is dominant in the hard X-ray image above 15 keV. The steeper spectrum of the hard spot, combined with the faster shock speed in the upstream region of the reverse (or reflection) shock, results in $\eta = 3-8$ in the inner shock but $\eta \sim 1$ in the forward shock (Sato et al., 2018).

We defined six sectors (N1, NE1, E1, SE1, S1, and NW1), which are roughly compatible with the regions Patnaude and Fesen (2009) measured proper motions. It has been previously shown that the proper-motion speeds are constant (~ 5000 km s⁻¹) in these outermost rims, assuming a distance of 3.4 kpc. Because the widths of all subregions are 15'' and the lengths range from 26''(S1) to 63''(NE1), we used only the *Chandra* data for spectral fitting. The *Chandra* spectra were fitted in 3.3–8 keV except for 6.4–6.8 keV (Fe line emission) using the absorbed ZA07 model with a fixed column density (N_H) of 0.8×10^{22} cm⁻². The results were consistent when fitting with the ZA07 plus thermal (VNEI) model in 0.5–8 keV. The cutoff energy parameters indicate significant varieties, which were highest in the SE rim and lowest in the S region. Because of the constant shock speeds and different cutoff energy parameters, the η values were also varied from ~ 1 in SE and ~ 8 in S, which was consistent with the previous results of Stage et al. (2006). In the case of the forward shock in Cassiopeia A, the variation of ε_0 produced the different values of η , whereas the variable shock speed was responsible for the differences of η in G1.9+0.3.

Because Cassiopeia A is the remnant of a core-collapse supernova explosion, a fluctuation in density likely occurs due to the strong stellar wind of the progenitor. We also present the cutoff energy parameter as a function of the number density (Figure 4.8) to investigate how particle acceleration depends on the fluctuating density. In the plasma model, the normalization was characterized by using the emission measure (EM):

$$\text{EM} = \frac{10^{-14}}{4\pi d^2} \int n_e n_H dV \quad (4.7)$$

$$= \frac{10^{-14}}{4\pi d^2} n_0^2 A dl, \quad (4.8)$$

where d , n_e , and n_H are the distance to the source, electron density, and hydrogen density, respectively. Here, we assume $n_0 = n_e = n_H$ and a volume of plasma (dV) is given by a product of the surface area (A) of each spectral extraction region and the line-of-sight plasma column depth (dl) of 0.25 pc corresponding to 15'' at $d = 3.4$ kpc. The value of n_0 was estimated from the EM parameter, which was obtained by fitting the spectrum with the absorbed thermal (VNEI) plus ZA07 model. In Figure 4.8, the ε_0 tends to be smaller in the denser region. If the kinetic energy of shock is transferred to a greater extent to the thermal components in the denser region, particle acceleration is expected to become inefficient and the cutoff energy in turn becomes smaller. Therefore, the variable ε_0 with the constant v_{sh} in Cassiopeia A might be indicative of the difference in number density.

Kepler's SNR

Kepler's SNR is well-known as one of the historical SNRs in the literature, namely, SN 1604, thus classifying it as a young SNR with an age of 400 years. The SN explosion is expected to be Type Ia. The nonthermal filament located in the outermost rim of the SNR has been studied using soft X-ray observations (Cassam-Chenai et al., 2004; Bamba et al., 2005). The proper motion of the outer rim has previously been measured: Vink (2008) estimated the proper-motion velocities in equivalently divided six sectors, and Katsuda et al. (2008b) obtained the proper-motion speeds from small 14 regions defined along the outermost rim. Both measurements showed significant variations in proper motions from region to region of 3000–7000 km s⁻¹.

The spectra of SE, with an angular size of $2.8' \times 1.0'$, were extracted using both *Chandra* and *NuSTAR*, and fitted using the absorbed ZA07 plus thermal (VNEI + Gaussian line at 6.43 keV) model in an energy range

⁵SRCUT is a model of synchrotron radiation from a cutoff power-law distribution of electrons (Reynolds (1998); Reynolds and Keohane (1999)). The cutoff shape has a simple form of $\exp(-E/E_0)$ and is different from that in Zirakashvili and Aharonian (2007)

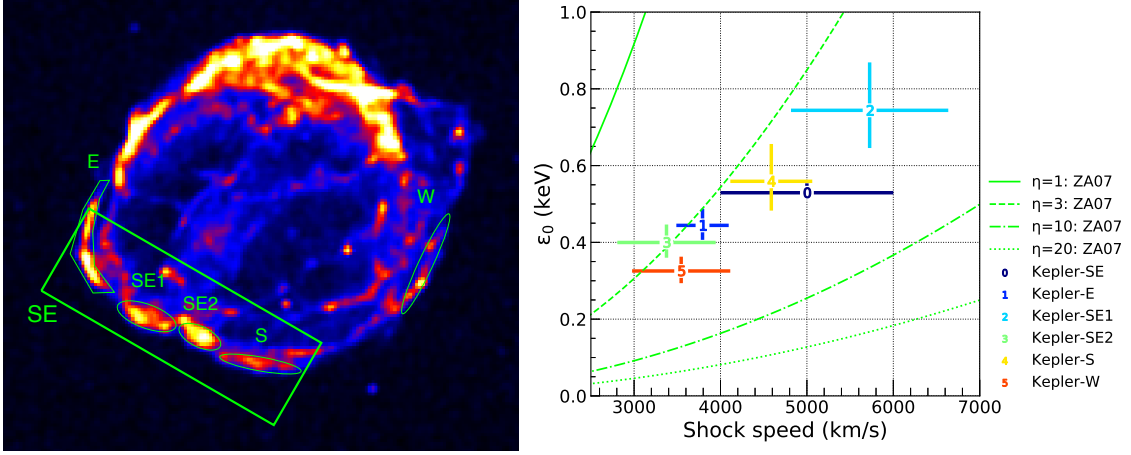


Figure 4.9: Same as Figure 4.7 for Kepler.

of 2.5–7 keV using *Chandra* and 3–30 keV using *NuSTAR*. The column density and parameters of the thermal emission were fixed based on Bamba et al. (2005); Sun and Chen (2019) (i.e., $N_H = 0.52 \times 10^{22} \text{ cm}^{-2}$, $kT = 0.6$ keV, and $nt = 10^{10} \text{ cm}^{-3} \text{ s}$). Five subregions (E, SE1, SE2, S, and W) were analyzed using only *Chandra*, because these small structures could not be spatially resolved by *NuSTAR* due to the angular resolution of $1'$. The smaller elliptical radius of each subregion is roughly comparable to the width of the nonthermal filament of $\sim 10''$. The spectral fittings of the subregions were performed in 2.5–8 keV using the absorbed ZA07 model. Note the results were consistent when fitting using the ZA07 plus thermal (VNEI) model in 0.5–8 keV. Because the plasma temperatures were as low as 0.3–1.2 keV, the spectra above ~ 3 keV were dominated by nonthermal (synchrotron) radiation.

The observed $v_{\text{sh}}-\epsilon_0$ diagram is given as Figure 4.9. The nonthermal spectrum of SE1 using *Chandra* and *NuSTAR* is nicely described with ϵ_0 of 0.53 ± 0.01 keV. Combined with the shock speed of $5000 \pm 1000 \text{ km s}^{-1}$ in the SE rim, the Bohm factor was estimated to be 4.8 ± 2.0 . Our analysis, for the first time, found that the particle acceleration in Kepler at the evolutionary age of ~ 400 years significantly deviates from the maximum rate (i.e., Bohm limit of $\eta = 1$).

The subregions (E, SE1, SE2, S, and W) correspond to the locations where the proper-motion velocities were measured by Katsuda et al. (2008b). Therefore, we could directly produce and investigate the relation between the cutoff energy parameter and the shock speed. Figure 4.9 shows a clear correlation of ϵ_0 and v_{sh} (i.e., the higher the shock speed is, the larger the cutoff energy parameter is). In addition, the correlation is well described with the theoretical curve with η of 3–5. This clarifies that the acceleration efficiency is constant ($\eta = 3\text{--}5$) and independent of the sites within the forward shock located in the outermost rim of Kepler.

Tycho's SNR

Tycho is one of the best-studied Type Ia SNRs. Its age is approximately 440 years, as it is associated with the historical supernova explosion SN 1572. The X-ray emission is mainly dominated by thermal components radiated from shocked ejecta and shocked interstellar medium. The nonthermal (synchrotron) radiation is detected from the forward shock, which is a thin and filamentary structure located at the outermost rim around the remnant. The nonthermal emission is also dominant in the “stripe” structure located in the southwestern part. This stripe structure is unique for Tycho, and the origin has been in debate. Katsuda et al. (2010) measured the proper motion in Tycho, revealing that the expansion velocity of the forward shock varies from region to region. With the *NuSTAR* observations, the spatially resolved hard X-ray was detected up to ~ 50 keV, and the hard X-ray above 10 keV is nearly concentrated in the stripe structure (Lopez et al., 2015). They also investigated the relation between the roll-off energy (ν_{roll} in the SRCUT model in XSPEC (see Reynolds (1998); Reynolds and Keohane (1999) for details) and the expansion speed (see Lopez et al. (2015) for more details of the $v_{\text{sh}}-\nu_{\text{roll}}$ relation in the other regions; note that the synchrotron model used in Lopez et al. (2015) (i.e.,

SRCUT in XSPEC) was different from our model).

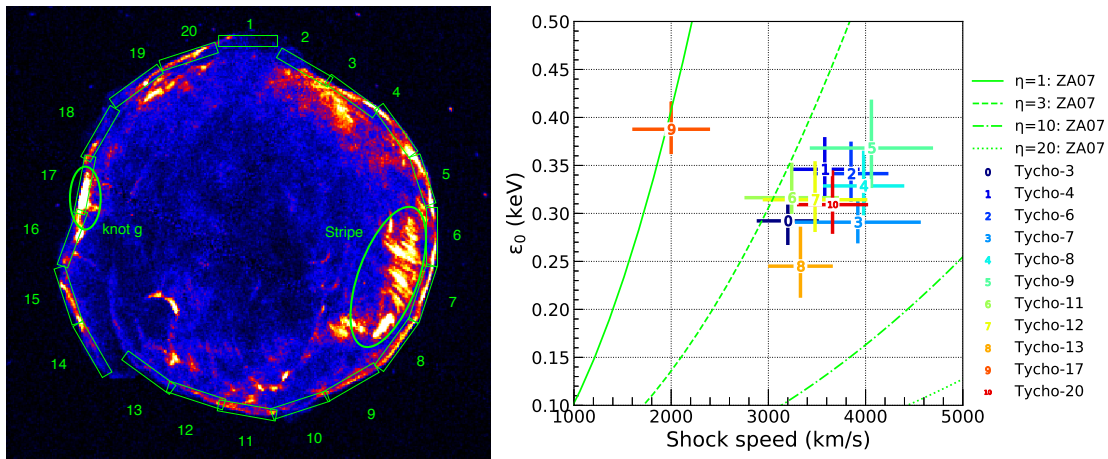


Figure 4.10: Same as Figure 4.7 for Tycho. Only results of the regions dominated by nonthermal radiation are shown. The box 17 (id 9 in the right panel) indicates the precursor and *knot g* (Lee et al., 2010; Ghavamian et al., 2000).

Twenty subregions are defined along the outer rim. The angular sizes of the subregions using *Chandra* and *NuSTAR* were $80'' \times 15''$ and $1.5' \times 1.5'$, respectively. The *Chandra* spectra in 3–7 keV were separately fitted from the *NuSTAR* spectra in 10–50 keV using the absorbed ZA07 model for both spectra with fixed N_H of $0.7 \times 10^{22} \text{ cm}^{-2}$. This resulted in approximately two times higher cutoff energy parameters in the *NuSTAR* spectra than those in the *Chandra* spectra. We assumed the fitting results using *Chandra* were more acceptable because the *NuSTAR* spectra of the larger area were heavily contaminated by the other emissions, such as the thermal components.

Figure 4.10 presents the $v_{\text{sh}}-\varepsilon_0$ scatter plot measured in Tycho. Note that nine subregions (boxes 1, 2, 5, 10, 14, 15, 16, 18, and 19) are dominated by the thermal components, which result in larger reduced chi-squared values with $\chi_{\text{red}}^2 \geq 3$ (Table 4.4), and these thermal regions are removed in Figure 4.10. This leads to Tycho showing slightly variable and theoretical predicted plots with $\varepsilon_0 = 0.25\text{--}0.40 \text{ keV}$ and $v_{\text{sh}} = 3000\text{--}4000 \text{ km s}^{-1}$ (Katsuda et al., 2010; Williams et al., 2013). This corresponds to nearly constant acceleration efficiency with η of 3–8 in the forward shock of Tycho. One exceptional region is box 17 located in the eastern rim. The η value should be ~ 1 on box 17, inferred from slow shock speed of 2000 km s^{-1} and a relatively higher cutoff energy parameter of 0.39 keV. This synchrotron radiation in the E rim might be unique and behave differently from the other parts because precursors have been detected (Lee et al., 2010) and dense clumps known as *knot g* have been shown to be present (see, for example, Ghavamian et al. (2000)). The dense density might affect the lower shock velocity in *knot g*. Our result was roughly consistent with that of Lopez et al. (2015), although the model and region definition were different (i.e., they also showed the greater roll-off energies in the higher shock speeds and the exception of *knot g*).

G330.2+1.0

G330.2+1.0 is known for its dominant synchrotron radiation. The thermal line emission was detected in a smaller spot in the eastern part. The CCO, associated with this remnant, was previously confirmed (Park et al., 2006). Nonthermal radiation was studied in Park et al. (2009). No significant spectral variation existed across the remnant (Williams et al., 2018). The proper motion was measured in Borkowski et al. (2018), showing an expansion speed of $\sim 7000\text{--}9000 \text{ km s}^{-1}$ at a distance of 5 kpc. This very fast speed implied the SNR was at the earlier evolutionary stage, but the large uncertainty regarding the distance makes its age ambiguous.

The spectrum of the entire remnant was extracted using *Chandra* and fitted with an absorbed ZA07 model in the energy range of 1–6 keV. The column density was fixed to $2.4 \times 10^{22} \text{ cm}^{-2}$ based on Williams et al. (2018). This resulted in a cutoff energy parameter of $0.65^{+0.07}_{-0.06} \text{ keV}$. Combined with $v_{\text{sh}} = 7000 \pm 2000 \text{ km s}^{-1}$

(Borkowski et al., 2018), the acceleration efficiency (η) was 6.0 ± 4.1 . We note that the measured proper motion slightly varied across the remnant, but we could not demonstrate the $v_{\text{sh}}-\varepsilon_0$ relation because of the large uncertainties on these parameters.

SN 1006

SN 1006 is one of the best-studied and historical SNRs in our galaxy. The high galactic latitude of 14.6° makes it an ideal laboratory to demonstrate supernova explosions or particle acceleration in an SNR shock. It has been well-studied in multi-wavelengths from radio to TeV gamma-ray. The nonthermal (synchrotron) radiation of SN 1006 is concentrated in the northeastern and southwestern limbs, whereas the thermal emission is detected in the northwestern and southeastern limbs and in the interior region.

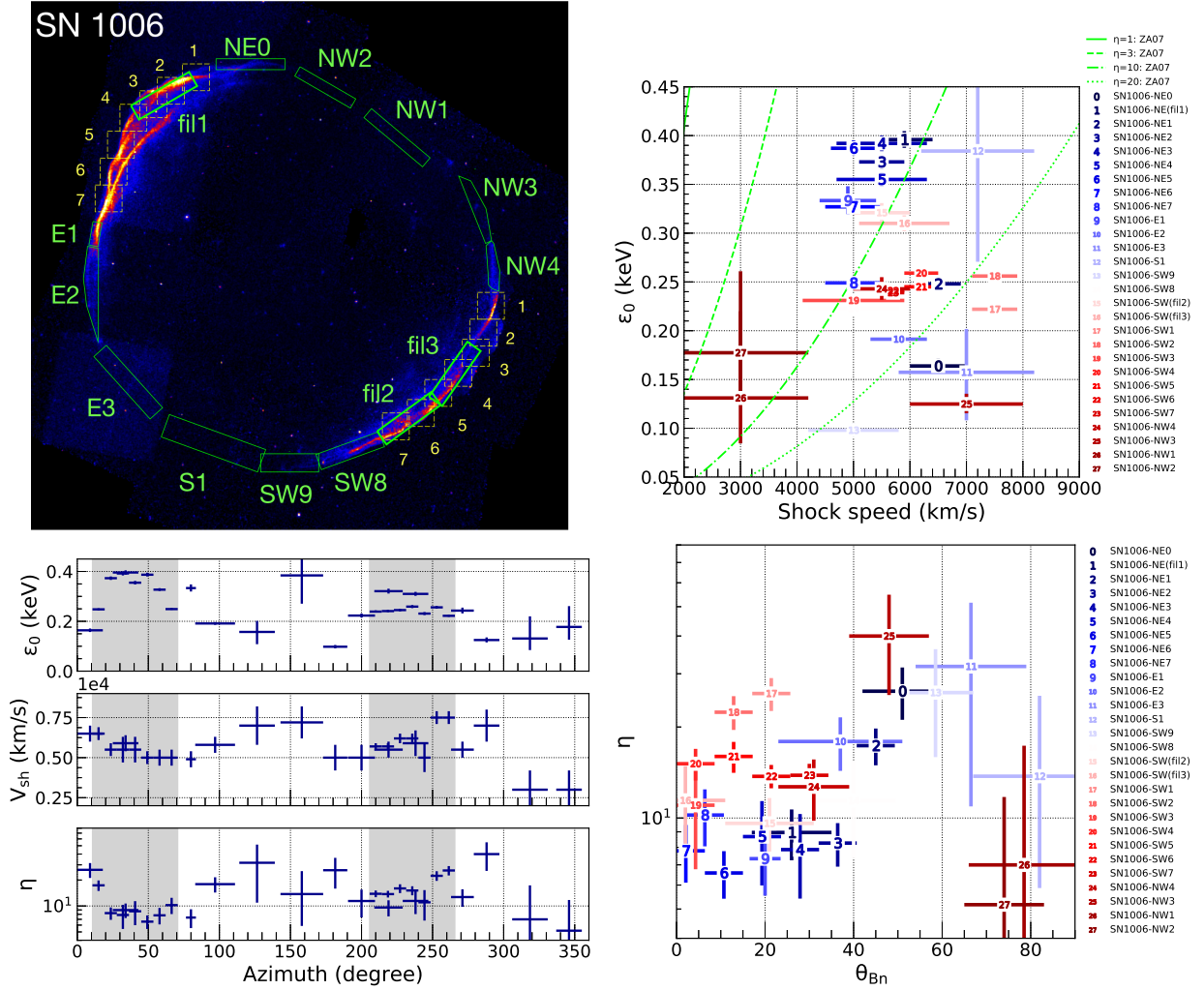


Figure 4.11: Top: Same as Figure 4.7 for SN 1006. Bottom left: The azimuthal profiles of η , ε_0 , and v_{sh} (counterclockwise from the north). The two limbs in the NE and SW are highlighted with gray bands. Bottom right: The η variation as a function of shock obliquity (assuming the shock inclination is 60° from the north).

The two limb regions, fil1–3 with an angular size of $5.0' \times 1.2'$, were analyzed using both *Chandra* and *NuSTAR*. The subregions NE1–7 and SW1–7 had angular sizes of $2.0' \times 2.0'$, for which we used the results obtained by Li et al. (2018). The other subregions (NE0, E1–3, S1, SW8–9, and NW1–4) were extracted with *Chandra* and fitted using the absorbed ZA07 plus thermal (Vpshock) model.

The filaments in the NE and SW limbs were dominated by synchrotron emission. The spectra of fil1 (NE) and fil2–3 (SW) represent the typical properties of the synchrotron radiation from this remnant. The fitting

results of these spectra using *Chandra* and *NuSTAR* were as follows (see also Figure 4.11). In fil1 (NE), the cutoff energy parameter was obtained as 0.40 ± 0.01 keV, resulting in $\eta = 9.0 \pm 1.7$ with a shock speed of 5900 ± 500 km s⁻¹. In fil2 and fil3 (SW), the cutoff energy parameter was obtained as 0.32 ± 0.01 keV, resulting in $\eta \approx 10$ with a shock speed of 5500 ± 500 km s⁻¹. Despite the relatively high shock speeds, the cutoff energy parameters appeared somewhat small, suggesting inefficient particle acceleration in SN 1006 as compared to the Bohm limit.

The $v_{\text{sh}}-\varepsilon_0$ plots of the subregions along the outermost rim of SN 1006 are shown in Figure 4.11. To produce the plots of NE1–7 and SW1–7, we used the values in the literature (i.e., the shock velocities were taken from Winkler et al. (2014), and the cutoff energy parameters were taken from Li et al. (2018) in which they derived ε_0 using *Chandra* and *NuSTAR*). The cutoff energy parameters in NE tended to appear larger than those in SW, although the spectral property of each subregion may have been mixed with that of the neighbors due to the limited angular resolution of *NuSTAR*, as noted in (Li et al., 2018). The other subregions (NE0, E1–3, S1, SW8–9, and NW1–4) were analyzed using only *Chandra*, as *NuSTAR* covered only two limbs in the NE and SW. We confirmed a possible tendency of smaller ε_0 for larger v_{sh} in Figure 4.11.

We also investigated azimuthal and shock-obliquity dependencies on particle acceleration in SN 1006. SN 1006 is a unique remnant of which the ambient magnetic field was reported to be along the galactic plane that is approximately 60° counterclockwise inclined from the north (see, for example, Reynoso et al. (2013)). This oriented magnetic field, combined with the Ia explosion in a high Galactic latitude of 14.6°, makes SN 1006 an ideal laboratory for studying the dependence of particle acceleration on magnetic field configurations (i.e., *parallel* or *perpendicular* shocks). We show the azimuthal dependence of the cutoff energy parameters in Figure 4.11. The azimuthal variations of roll-off frequencies (with the SRCUT model in XSPEC) and shock velocities were previously studied in Rothenflug et al. (2004); Miceli et al. (2009) and Winkler et al. (2014), respectively. Our measurements of azimuthal dependencies on ε_0 indicate the greater cutoff energy parameters near the polar regions (NE and SW), which is consistent with the previous studies. The observed azimuthal variations of ε_0 and v_{sh} enabled us to make a clear correlation between shock obliquity θ_{Bn} and acceleration efficiency η , as illustrated in Figure 4.11. To produce this scatter plot, we assumed the inclination of the magnetic field to be 60° from the north. The shock-obliquity dependence on particle acceleration is discussed in Section 4.4.3.

RX J1713.7–3946

The shell-type SNR RX J1713.7–3946 is well known for its strong nonthermal X-ray and gamma-ray emissions, making it one of the best-studied particle acceleration sites (Tanaka et al., 2008; Abdo et al., 2011; H. E. S. S. Collaboration, 2018b). The association between RX J1713.7–3946 and SN 393, one of the historical SNRs, was previously discussed (Wang et al., 1997; Fesen et al., 2012). Recent measurements of the proper motions in the NW and SE parts of this SNR (Tsuji and Uchiyama, 2016; Acero et al., 2017) revealed that the forward shock speed is roughly 4000 km s⁻¹. This suggests that RX J1713.7–3946 is indeed the remnant of SN 393 and kinematically young, implying that it is still in the ejecta-dominated (ED) phase. Both the fast shock velocity and early evolutionary phase were found to be consistent with the efficient acceleration of particles in the SNR.

We performed spatially resolved spectroscopy in the NW shell of RX J1713.7–3946 using *Chandra* and *NuSTAR* (see Tsuji et al. (2019) for details). We obtained ε_0 of 1.14 ± 0.06 keV and η of 1.36 ± 0.28 in the large box as typical values representing the spectral properties of the NW rim. We also report the first result of arcmin-scale spectral distribution in the hard X-ray band of the NW shell of RX J1713.7–3946. Six small regions, as denoted by boxes (a)–(f), were selected for the following reasons. Boxes (a)–(f) include clearly edge- and filament-like structures. We previously measured the proper motion velocities in these structures (Tsuji and Uchiyama, 2016) and found that the speeds were significantly different from region to region. To test the relation between the shock speed and cutoff energy, we defined boxes (a)–(f), which correspond to the regions used in Tsuji and Uchiyama (2016). The size of each box was $1.5' \times 2'$ (0.44×0.58 pc²), except for box (f) with a size of $3' \times 1'$ (0.88×1.16 pc²). Figure 4.12 demonstrates the relation between the shock speed obtained by Tsuji and Uchiyama (2016) and the cutoff energy parameter derived from the spectral fitting with the ZA07 model for each small box. The measured speeds contain uncertainties of being projected onto the line of sight. However, these uncertainties can be small because boxes (a)–(f) are located in the outer regions of the shell, and

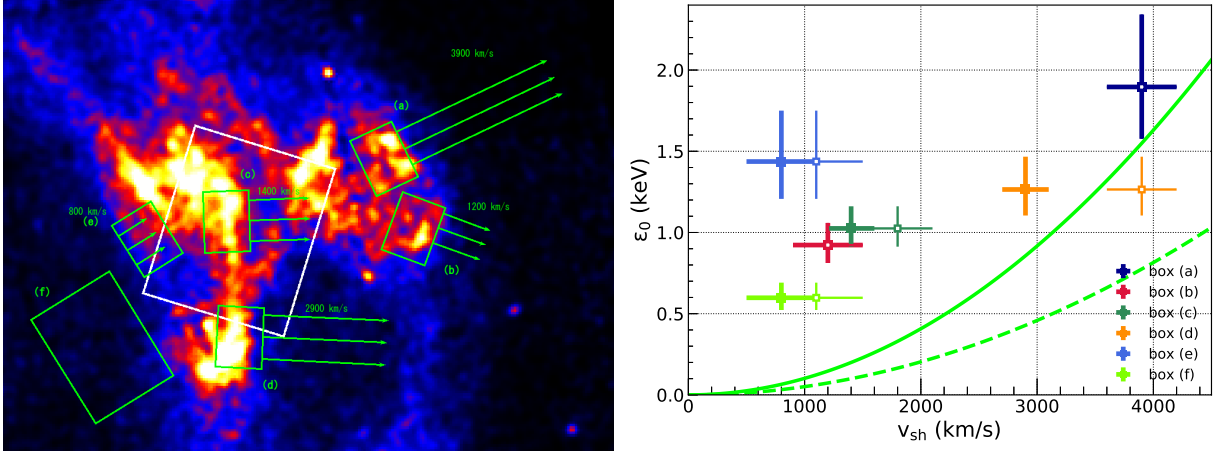


Figure 4.12: Same as Figure 4.7 for RX J1713.7–3946 NW, taken from Tsuji et al. (2019). Open markers show the projection-corrected velocities assuming a spherical shell with a radius of $30'$ (i.e., the position of box (a)). The solid and dashed green lines refer to η of 1 and 2, respectively.

the radial component is expected to be dominant in these regions. The projection-corrected speeds, plotted with open markers in Figure 4.12, are inferred by considering the projection effects (i.e., the line-of-sight velocity components), assuming spherical shell expansion (see Appendix B for details).

As shown in Figure 4.12, $v_{sh} - \epsilon_0$ relation of boxes (a) and d) can be explained by the theoretical relation with $\eta \sim 1$. TeV-scale electrons are accelerated at the maximum rate (Bohm limit) in these outermost regions, which are likely just behind the forward shock. Note that box (d), which seems to be located inside the shell, is possibly indicative of the projected forward shock (box (a)), because the projection-corrected speed is compatible with that of box (a). However, the regions with lower speeds (boxes (b), (c), (e), and (f)) do not match the theoretical prediction. This suggests that the current framework, in which we assume the synchrotron radiation derives from electrons accelerated at the SNR shock through the standard DSA mechanism and is limited by the synchrotron loss, is not applicable in these cases. The inner filament and/or edge at boxes (c), (e), and (f) may represent locally enhanced magnetic fields rather than acceleration sites. Although box (b) exists at the outermost edge, its slow speed and nonradial direction imply that the shock is decelerated and distorted because it interacts with molecular clouds (Fukui et al., 2003, 2012; Sano et al., 2015). Therefore box (b) might not be the acceleration site.

The magnetic field amplifications have been confirmed in filaments and small knot-like structures in previous works on certain young SNRs. Estimated from the width of the filamentary structure of the SNR rim just behind the shock wave, B is approximately $100 \mu\text{G}$ in these sub-parsec regions, $0.01\text{--}0.4 \text{ pc}$, (Bamba et al., 2005; Berezhko and Völk, 2006). The magnetic field is expected to be more enhanced, that is, $B \sim 1 \text{ mG}$, in the smaller (0.05 pc) region, which is derived from year-scale flux variation (Uchiyama et al., 2007; Uchiyama and Aharonian, 2008). Boxes (b), (c), (e), and (f) can be different from these filamentary and small structures in terms of location and size. The filament-like structure at box (c) and inner edge-like structure between boxes (e) and (f) are 1.8 and 2.6 pc , respectively, located from the forward shock at box (a). The box size is approximately $0.4\text{--}1 \text{ pc}$. We might require another scenario for magnetic field enhancement in these comparably large sub-parsec regions that are isolated from the shock front.

The particle acceleration at reverse shock and/or reflection shock can be feasible for the observed higher cutoff energy parameters and the slower velocities. The reflection shock, resulting from the interaction between the SNR shock and the ambient molecular cloud is reasonable in the case of RX J1713.7–3946 NW, as discussed in Okuno et al. (2018). The evidence of the molecular cloud and dense clump has been previously reported (Fukui et al., 2003, 2012; Sano et al., 2015). The shock-cloud interaction causes the deceleration of the shock, which is consistent with the measured slow speeds, and the magnetic field amplification (Inoue et al., 2012). If a reflection shock at the filament or inner edge exists, it encounters the ejecta that is freely expanding outward. Assuming SN393 is the supernova that created RX J1713.7–3946 ($t_{age} \approx 1600 \text{ years}$), u_1 (Equation 4.6) is

estimated to be $\sim 2700 \text{ km s}^{-1}$ at box (c) and $\sim 2900 \text{ km s}^{-1}$ at box (e). When the obtained u_1 is used as the shock speed in Equation 4.3, the observed cutoff energy parameter still appears slightly greater than the theoretical value (see Appendix B for details). This also suggests that the standard picture of DSA and synchrotron cooling is not the case.

The presence of magnetic turbulence can considerably affect the spectral shape of the synchrotron radiation (Zirakashvili and Aharonian, 2010; Bykov et al., 2008; Kelner et al., 2014). The turbulence can be described by different physical quantities, for example, with a probability function or with a power spectrum. The effect of a Gaussian-like distributed magnetic field in its probability function regarding the former quantity is presented in Appendix C. The latter quantity is linked to the energy dependence of the diffusion coefficient. If the diffusion coefficient deviates from the Bohm diffusion (i.e., $\alpha \neq 1$), the cutoff shape becomes somewhat different, as demonstrated in Chapter 6.

The spectrum integrated over the entire remnant indicates $\varepsilon = 0.94 \pm 0.03 \text{ keV}$ based on observations using *Suzaku* XIS and HXD (Tanaka et al., 2008; Zirakashvili and Aharonian, 2010). The expansion in the SE region of RX J1713.7–3946 was measured with *XMM-Newton*, revealing that the proper-motion speed is comparable to that in the NW, $\sim 4000 \text{ km s}^{-1}$ (Acero et al., 2017). Therefore, the η value of the whole remnant can be estimated to be 1.65 ± 0.48 , assuming the shock speed is common across the remnant, that is, $v_{\text{sh}} \approx 3900 \pm 300 \text{ km s}^{-1}$. The comparison of η in the NW shell and the entire SNR helps us understand the differences between them in terms of the properties of particle acceleration. The cutoff energy parameter appears slightly higher in the NW than in the whole remnant, whereas the η values are identical. This implies that the acceleration efficiency is constant across the remnant, or that the bright region such as the NW shell smears the information about the faint regions. Variations in the spectral properties and surface brightnesses across the remnant indeed occur (Sano et al., 2015; Okuno et al., 2018). Sano et al. (2015) showed a correlation between the photon index and surface brightness with a linear correlation coefficient of -0.62 . The velocity of the forward shock, however, is not significantly different in the NW and SE (Tsuji and Uchiyama, 2016; Acero et al., 2017). To clarify the detailed picture of particle acceleration ongoing in the whole region of RX J1713.7–3946, measuring precise values of ε_0 while using hard X-ray observations with *NuSTAR* or *Athena* and the proper-motion speeds in the other parts are all necessary. This is beyond the scope of our study and will be discussed in the future.

RCW 86

RCW 86, also known as MSH 14–63 or G315.4–2.3, was produced by the possible historical supernova explosion, SN 185 (Stephenson and Green, 2002). The distance of 2.8 kpc was estimated from optical observation (Rosado et al., 1996), and we also assume $d = 2.8 \text{ kpc}$ in this thesis. RCW 86 is a complex of thermal and nonthermal emissions: the NE rim has been studied with detection of Fe $K\alpha$ line emission and synchrotron radiation in (Vink et al., 2006; Yamaguchi et al., 2008, 2016). The nonthermal (synchrotron) studies in the NW part were also conducted in detail (Castro et al., 2013). In the SW complex, the nonthermal filament was found inside the thermal diffuse emission, suggesting the nonthermal emission can be attributed to the reverse shock because the blast-wave shock speed of $600\text{--}800 \text{ km s}^{-1}$ as determined by optical ($H\alpha$) observations (Rosado et al., 1996; Ghavamian et al., 2001) was too low to accelerate the electron radiating the synchrotron X-ray (Rho et al., 2002). The thermal and nonthermal spectral maps were produced in Tsubone et al. (2017). RCW 86 is the oldest SNR among those galactic, historical, and synchrotron-emitting SNRs, making it a great target to explore the study of particle acceleration at the evolutionary age of ~ 2000 years.

It has been argued that the proper-motion speeds estimated by X-ray and optical observations are significantly different. The optical observation of $H\alpha$ line emission traces the temperature of postshock protons. For instance, in the NE rim, Yamaguchi et al. (2016) derived the X-ray proper motion of $\sim 2000 \text{ km s}^{-1}$, whereas Helder et al. (2013) obtained the optical ($H\alpha$) proper motion of $\sim 1000 \text{ km s}^{-1}$. Optical observations showed the proper-motion velocities in the SW and NW were $600\text{--}800 \text{ km s}^{-1}$ (Rosado et al., 1996; Ghavamian et al., 2001) and $\sim 600 \text{ km s}^{-1}$ (Long and Blair, 1990), respectively, but the X-ray proper motions have yet to be measured in these parts. The differences in the X-ray and optical observations could be interpreted as follows: ambient density is inhomogeneous. The synchrotron X-ray traces the electrons in the diluted region having a fast shock speed, and the $H\alpha$ emission comes from the protons in the dense region having a slow shock speed.

We analyzed the nonthermal (synchrotron) spectrum in the NE rim where the X-ray proper motion was

well constrained. Note that the synchrotron radiation was also detected from the NW and SW, but the proper motion has yet to be measured through X-ray observations, and the proper-motion speed with X-ray and optical observations might be different. Yamaguchi et al. (2016) obtained the shock speeds in a bright region (“NEb” in Figure 4.2) and a faint region (“NEf”), which were $1780 \pm 240 \text{ km s}^{-1}$ and $3000 \pm 340 \text{ km s}^{-1}$, respectively. This variation may imply the existence of inhomogeneous density on a small-scale. The spectrum was fitted using the absorbed ZA07 plus thermal (Vpshock) model in which the thermal components were fixed following Tsubone et al. (2017). We measured the cutoff energy parameters in NEb, NEf, and an integrated large region (NE2) of $0.36 \pm 0.02 \text{ keV}$, $0.28 \pm 0.01 \text{ keV}$, and $0.30 \pm 0.01 \text{ keV}$, respectively. Assuming the shock speed was $2000\text{--}3200 \text{ km s}^{-1}$ in NE2, the η parameter was obtained as 2.1 ± 1.3 . The η values in NEb and NEf were 0.9 ± 0.3 and 3.2 ± 0.9 , respectively. We note that we obtained ε_0 of $\sim 0.2 \text{ keV}$ in NW and $\sim 0.4 \text{ keV}$ in S, thus invalidating the η values (i.e., $\eta < 1$) when combined with small shock speeds measured with optical observations.

Vela Jr.

Vela Jr. (also known as RX J0852.0–4622 or G266.2–1.2) is embedded in a complex of Vela SNR. Vela Jr. is well known for its strong nonthermal X-ray and TeV gamma-ray emission. Nonthermal X-ray studies were presented in Bamba et al. (2005); Kishishita et al. (2013); Takeda et al. (2016); Fukuyama et al. (2019). The proper motion was measured in the following two studies, which showed different values by a factor of approximately 2. The expansion in the NW rim was measured to be $0.84 \pm 0.23'' \text{ year}^{-1}$ ($2800 \pm 760 \text{ km s}^{-1}$ assuming $d = 0.7 \text{ kpc}$) based on *XMM-Newton* observations performed in 2001, 2003, 2005, and 2007 (Katsuda et al., 2008a). By contrast, that in the similar region was estimated to be $0.42 \pm 0.10'' \text{ year}^{-1}$ ($1400 \pm 330 \text{ km s}^{-1}$ assuming $d = 0.7 \text{ kpc}$) based on *Chandra* observations performed in 2003 and 2008 (Allen et al., 2015). Note that the defined regions were not exactly identical. We used $1400\text{--}3000 \text{ km s}^{-1}$ for the forward shock speed in the NW. Allen et al. (2015) calculated the hydrodynamical properties of Vela Jr. based on the measured proper motion and estimated an age of 2–4 kyr that included the uncertainty on the distance from 0.5 kpc to 0.9 kpc. MHD simulations were also performed to reproduce the morphological and spectral properties of Vela Jr. (Lee et al., 2013; Sushch et al., 2018).

We extracted the spectrum in the NW rim using *Chandra* and *NuSTAR*. We also used the spectrum from the entire remnant with *Suzaku*–XIS, which is provided by Fukuyama et al. (2019). The cutoff energy parameters of the NW filament and entire SNR were $0.54 \pm 0.04 \text{ keV}$ and $0.31 \pm 0.01 \text{ keV}$, respectively. The higher value of ε_0 in the NW rim as compared to that in the whole remnant implies a more efficient acceleration in the brighter NW region. Assuming the forward shock speed of $1400\text{--}3000 \text{ km s}^{-1}$, the η value was estimated to be 0.25–1.55 in the NE rim, indicating an acceleration approximating the maximum rate. Note that η would be 1.47 ± 0.90 for $v_{\text{sh}} = 2800 \pm 760 \text{ km s}^{-1}$ (Katsuda et al., 2008a) and 0.37 ± 0.20 for $v_{\text{sh}} = 1400 \pm 330 \text{ km s}^{-1}$ (Allen et al., 2015). The latter case is invalid since η should be larger than 1.

HESS J1731–347

Very bright shell-type TeV gamma-ray diffuse emission, that is, HESS J1731–347, was discovered with H.E.S.S. and identified as a galactic SNR (H. E. S. S. Collaboration, 2011). Follow-up X-ray observations of the western part with *Suzaku* (Bamba et al., 2012) and the entire remnant with *XMM-Newton* (Doroshenko et al., 2017) revealed good spatial correlation between the nonthermal X-ray and TeV gamma-ray. They confirmed no significant spectral variation and no thermal emission in X-ray across the remnant. The physical parameters, such as the age and the expansion speed, were not well constrained. H. E. S. S. Collaboration (2011) roughly estimated the physical parameters based on modeling the observed multi-wavelength spectral energy distribution (SED) for the following two scenarios. In the hadronic scenario for the gamma-ray emission mechanism, the SED was well reproduced with a parameter set of $n \sim 1 \text{ cm}^{-3}$, $v_{\text{sh}} \sim 410 \text{ km s}^{-1}$, and $t_{\text{age}} \sim 14000 \text{ years}$. In the leptonic scenario, the parameter set was $n \sim 0.01 \text{ cm}^{-3}$, $v_{\text{sh}} \sim 2000 \text{ km s}^{-1}$, and $t_{\text{age}} \sim 2500 \text{ years}$. Note the age was roughly estimated by the hydrodynamical evolution model (Truelove and McKee, 1999) assuming the ejecta mass of $5M_{\odot}$. We adopted the latter case in this thesis because of the X-ray and TeV gamma-ray morphological coincidence, the lack of thermal line emissions, and the flatter spectrum in the GeV gamma-ray regime (Condon et al., 2017).

The NE part of HESS J1731–347 was once observed using *Chandra* with an exposure time of 29 ks. Fixing N_H to 10^{22} cm^{-2} (Doroshenko et al., 2017), we obtained $\varepsilon_0 = 0.71\text{--}1.4 \text{ keV}$ in the NE part of HESS J1731–347. Because no spectral variation exists, the Bohm factor in this remnant can be estimated to be $\eta = 0.1\text{--}1.0$ with $v_{\text{sh}} = 2000 \pm 500 \text{ km s}^{-1}$.

SN 1987A

SN 1987A is one of the most popular astrophysical sources, as it is not only an EM emitter but also a neutrino source (see a recent review by McCray and Fransson (2016) and references therein). The soft X-ray emitted from SN 1987A is dominated by thermal components. With soft X-ray studies (e.g., Frank et al. (2016)), the X-ray spectrum below $\sim 10 \text{ keV}$ is nicely reproduced by plasma with two temperatures: $\sim 0.3 \text{ keV}$ of collisional ionization equilibrium (Vequil model in XSPEC) and $\sim 1.8 \text{ keV}$ of nonequilibrium ionization (Vpshock). Nonthermal observations and studies on particle acceleration have not been fully conducted as compared to thermal studies, as briefly summarized as follows. Radio synchrotron radiation was previously detected, showing a spectral index (α) of 0.91 at 1517 days (in 1991) and 0.73 at 9280 days (in 2012), as reported in Ng et al. (2013). Monitoring using *Chandra* has revealed that the expansion velocity in 0.5–8 keV decelerated at 6000 days from 7000 km s^{-1} to 2000 km s^{-1} , resulting from an impact of the shock and an equatorial ring that surrounds the remnant (Frank et al., 2016). *NuSTAR* confirmed a hard X-ray continuum up to 25 keV (Reynolds et al., 2015) in addition to the line emission of ^{44}Ti (Boggs et al., 2015). The *NuSTAR* spectrum in 3–25 keV itself is described using the power-law model with $\Gamma = 3.4$. Assuming the synchrotron origin of the hard X-ray, the magnetic field should be greater than $60 \mu\text{G}$ to accelerate particles emitting synchrotron X-rays within 27 years. Although gamma-ray radiation has not been detected until recently (H. E. S. S. Collaboration, 2015), Malyshev et al. (2019) reported possible detection of GeV gamma-rays from the sky in LMC containing SN 1987A.

The *NuSTAR* spectrum in 3–40 keV was fitted with fixed N_H and soft thermal emissions (i.e., 6.6 keV Gaussian line emission plus 1.8 keV Vpshock) to the values in Frank et al. (2016). Figure 4.13 presents the SED of SN 1987A in a multi-wavelength. The radio waves, GeV gamma-rays, and TeV gamma-rays were taken from Ng et al. (2013), Malyshev et al. (2019), and H. E. S. S. Collaboration (2015), respectively. The *NuSTAR* plots indicate the best-fit model to describe only nonthermal contributions. The ε_0 parameter was estimated to be 0.69 keV, resulting in η of ~ 8 for the shock speed of 6700 km s^{-1} . If we assume the nonthermal X-ray is attributed to the reverse shock, the Bohm factor was approximately 4 with $u_1 \sim 5000 \text{ km s}^{-1}$ in Equation 4.6.

Summary

To summarize the properties of particle acceleration in the individual sources, significant variations across the remnants were confirmed in G1.9+0.3, Cassiopeia A, Kepler, Tycho, SN 1006, and the NW of RX J1713.7–3946. However, spatially resolved studies could not be conducted in the other SNRs. Figure 4.14 shows the $v_{\text{sh}}\text{--}\varepsilon_0$ scatter plots of the six former SNRs, which showed significant varieties, indicating four types of $v_{\text{sh}}\text{--}\varepsilon_0$ dependencies. In G1.9+0.3 and RX J1713.7–3946 NW, the cutoff energy parameters showed no variations, but the shock speeds were different from region to region. This was the opposite case in Cassiopeia A (i.e., the cutoff energy parameters were variable), whereas the shock speeds were nearly constant. Only Kepler and Tycho (except for *knot g*) presented the $v_{\text{sh}}\text{--}\varepsilon_0$ scatter plots nicely described with the theoretical prediction of $\varepsilon_0 \propto v_{\text{sh}}^2$, whereas SN 1006 showed an inverse trend, in which the cutoff energy parameters tended to be smaller in the higher shock-speed regions.

These features were interpreted as follows. Particle acceleration in Kepler and Tycho exhibited the theoretically predicted $v_{\text{sh}}\text{--}\varepsilon_0$ relation. Therefore, the standard framework was applicable in these SNRs. However, in the other SNRs in which observed $v_{\text{sh}}\text{--}\varepsilon_0$ plots were not described by the theoretical curve, particle acceleration may have been strongly affected by the surrounding environment. In the case of SN 1006, particle acceleration was probably determined by the ambient magnetic field, because the resulting Bohm factors were correlated with the shock obliquities. In the case of Cassiopeia A, the acceleration efficiency was affected by the ambient number density. For G1.9+0.3 and RX J1713.7–3946 NW, the different shock speeds may have been caused by differences in the ambient density, resulting in variable Bohm factors across the remnant. It is more likely

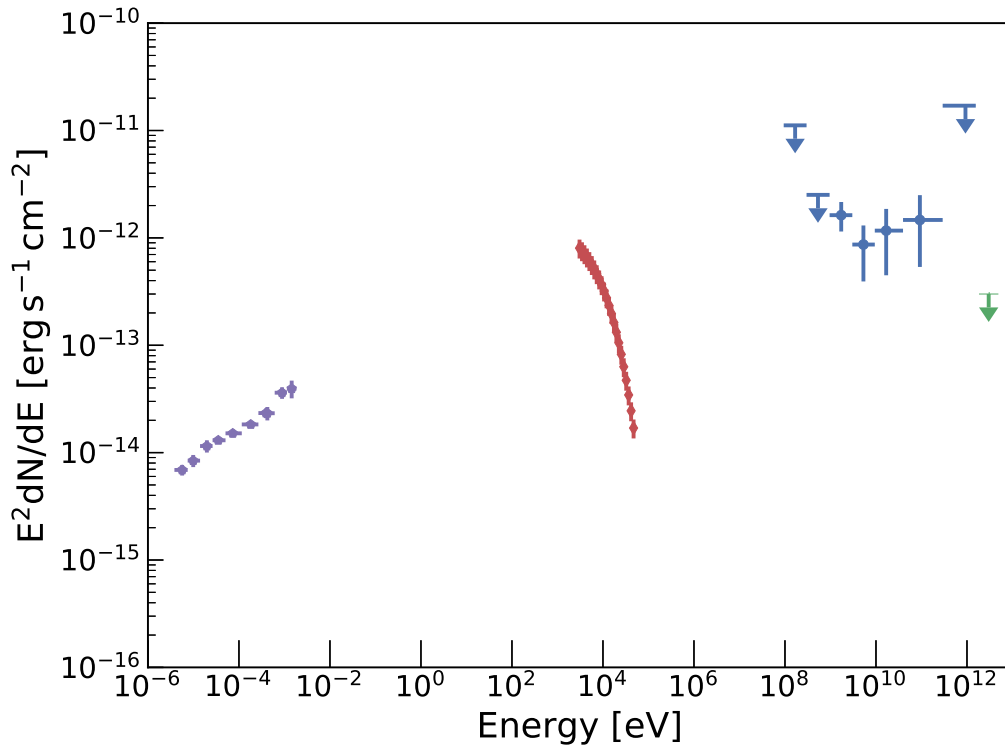


Figure 4.13: SED of SN 1987A. The purple, red, blue, and green plots are the radio (Ng et al., 2013), *NuSTAR* (this work), GeV (Malyshev et al., 2019) observations, and TeV upper limit H. E. S. S. Collaboration (2015), respectively.

that G1.9+0.3, at the age of ~ 190 years, was too young to accelerate sufficiently energetic particles, and our framework of the cooling-limited electron was not appropriate if particle acceleration in G1.9+0.3 was limited by the age. Finally, the NW rim of RX J1713.7–3946 showed the maximum rate ($\eta \approx 1$) of acceleration in the forward-shock regions and the invalid values of $\eta < 1$ in the slower-shock regions. The latter case may imply that the X-ray emission was not attributed to the acceleration site but rather to the enhancement of the magnetic field.

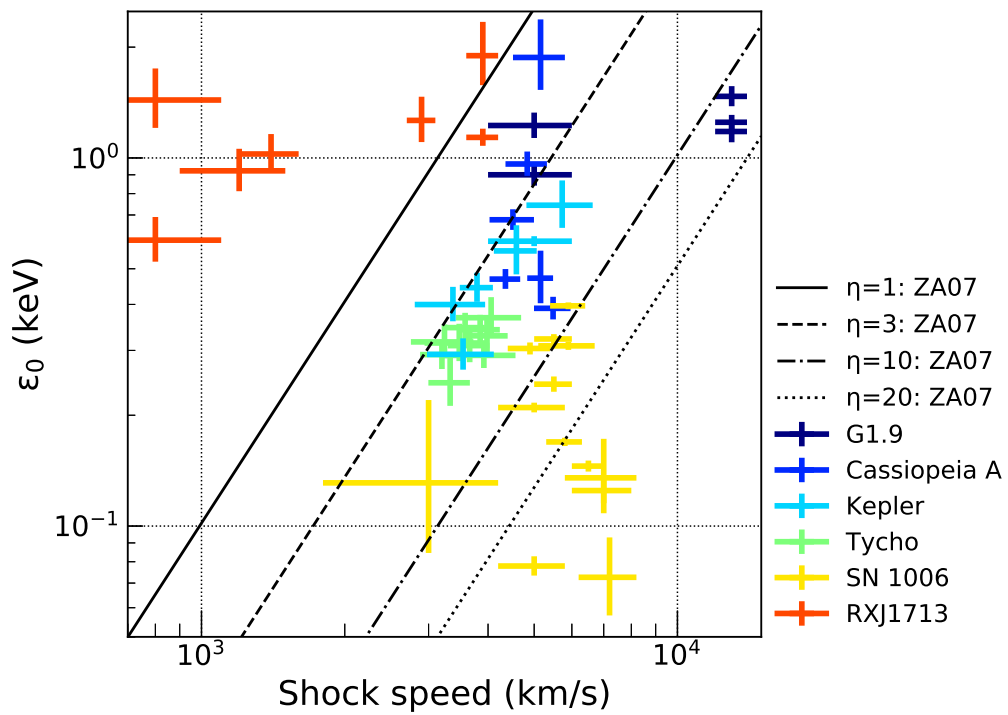


Figure 4.14: $v_{\text{sh}}-\epsilon_0$ scatter plots in G1.9+0.3, Cassiopeia A, Kepler, Tycho (expect for *knot g*), SN 1006, and RX J1713.7–3946-NW. SN 1006 does not include the subregions defined in Li et al. (2018).

4.4.3 Acceleration efficiency in young SNRs

We obtained the η values that are indicative of acceleration efficiency (Bohm factor) in the 11 individual SNRs. This subsection presents the systematic trend of η when all these SNRs are considered together. Because six SNRs showed significantly different properties of particle acceleration depending on the sites (Figure 4.14), we investigated the systematic η values estimated from the selected regions based on the following criteria: the largest- ε_0 regions, reverse shock, and supernova explosion types.

Largest- ε_0 (maximum- v_{sh}) region: evolution of η

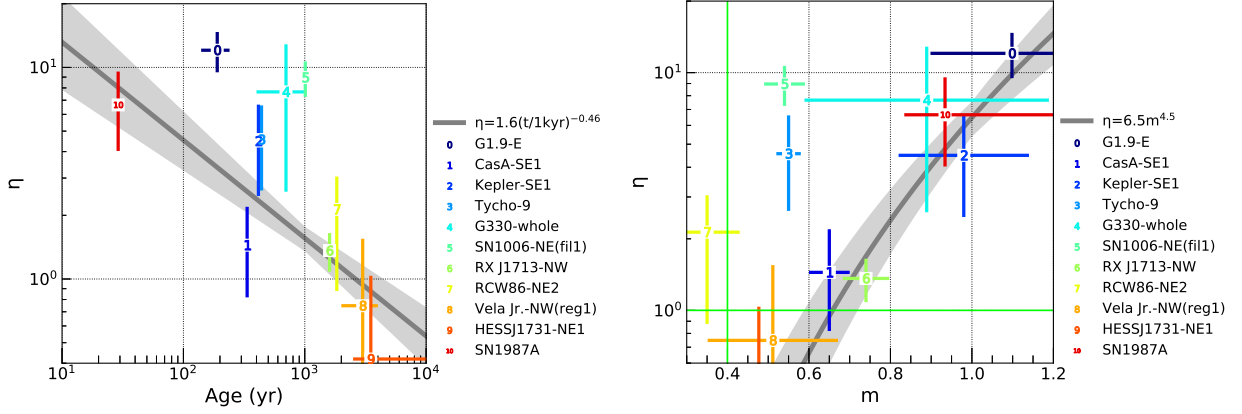


Figure 4.15: η as a function of the age (left) and expansion parameter m (right).

We investigated acceleration efficiency (η) obtained in the region with the largest ε_0 of each SNR. Note that the largest- ε_0 region nearly corresponded to the fastest- v_{sh} region, except for SN 1006, which showed an inverse correlation between ε_0 and v_{sh} . Figure 4.15 (left) presents the relation between the estimated η value and the age of each SNR. We confirmed a tendency in which η decreased as the age of SNR increased. In SNRs younger than a few 100 years, the acceleration efficiency substantially deviated from the Bohm limit (i.e., $\eta > 1$). In the later evolutionary stage older than a few 1,000 years, the acceleration proceeded at the most efficient rate (i.e., Bohm limit with $\eta \approx 1$).

To quantify the relation between η and t_{age} , we fit the observed diagram using an experimental equation:

$$\eta = C_{age} \left(\frac{t_{age}}{1 \text{ kyr}} \right)^{-\delta_{age}}, \quad (4.9)$$

where C_{age} and δ_{age} indicate a constant value of η at the age of 1 kyr and a slope of the η -age relation, respectively. With chi-squared fitting, we obtained $\delta_{age} = 0.46 \pm 0.08$ and $C_{age} = 1.6 \pm 0.2$ with χ^2 of 37.7 and degree of freedom (dof) of 10. It should be noted that the correlation coefficient of the plots in Figure 4.15 (left) was approximately -0.67 with a significance of 2.6σ . The best-fit model is indicated by the grey line, and the 1σ uncertainty is indicated by the light grey region in Figure 4.15. Equation 4.9 nicely reproduces the observation, although G1.9+0.3 and SN 1006 (and perhaps Cassiopeia A) deviate from the best-fit model. The deviations in these SNRs might arise from the fact that they are limited by some different factors, such as magnetic field, ambient density, or age, as mentioned in the summary of the previous section.

Figure 4.15 (right) indicates the observed relation between the η value and an expansion parameter m , which is an alternative parameter indicating the evolutionary phase of SNRs. Note that m refers to the evolutionary stage at which the SNR currently resides, whereas the age depends on the physical parameters surrounding the supernova explosion, such as ambient density, progenitor mass, and total energy of SNe. The radius of the SNR, R , and m are described respectively with

$$R \propto t^m, \quad (4.10)$$

and

$$m \equiv \frac{v_{\text{obs}}}{R/t_{\text{age}}}, \quad (4.11)$$

where v_{obs} is the observed expansion velocity. $m = 1$ indicates the earliest evolutionary stage (also known as the free expansion phase or ED phase). $m = 2/5$ corresponds to so-called Sedov stage at which the SNR continues to expand self-similarly. As the SNRs evolve from $m = 1$ to $2/5$, η decreases to reach ~ 1 in Figure 4.15 (right). We also fit the observed η - m diagram using an experimental model given by:

$$\eta = C_m m^{\delta_m}. \quad (4.12)$$

The best-fit values were $\delta_m = 4.5 \pm 0.7$ and $C_m = 6.5 \pm 1.1$ with χ^2 of 37.0 and dof of 10. The correlation coefficient of the plots in Figure 4.15 (right) was approximately 0.57 with a significance of 2.2σ .

Table 4.6: Properties of particle acceleration in the largest- ε_0 regions of young SNRs.

Name	Region	Age (yr)	v_{sh} (km s ⁻¹)	m	ε_0 (keV)	η	B_{low} (μG)
G1.9+0.3	E	190±50	13000±1000	1.1±0.2	1.43±0.09	12.1±2.6	36
Cassiopeia A	SE1	335±20	5157±644	0.7±0.1	1.87±0.34	1.4±0.6	23
Kepler	SE1	415±10	5726±910	1.0±0.2	0.74±0.10	4.5±2.0	27
Tycho	SW (box 9)	440±10	4060±634	0.6±0.0	0.37±0.04	4.6±1.9	33
G330.2+1.0	whole	700±300	7000±2000	0.9±0.3	0.83±0.09	6.0±4.1	18
SN 1006	NE (fil1)	1010±10	5900±500	0.5±0.1	0.40±0.01	9.0±1.7	18
RX J1713.7-3946	NW	1600±10	3900±300	0.7±0.1	1.14±0.06	1.4±0.3	9
RCW 86	NE2	1835±20	2500±700	0.3±0.1	0.30±0.01	2.1±1.3	13
Vela Jr.	NW (reg1)	3000±1000	2000±600	0.5±0.2	0.55±0.04	0.7±0.5	8
HESS J1731-347	NE	2500-14000	2000±500	0.5±0.1	0.97 ^{+0.46} _{-0.26}	0.4 ^{+0.6} _{-0.3}	6
SN 1987A	whole	30	6711±787	0.9±0.1	0.60±0.10	7.6±3.1	172

The evolution of acceleration efficiency, as previously mentioned and shown in Figure 4.15, was observationally revealed for the first time in this study. In the following, we discuss how to interpret the observational results. The Bohm factor η indicates the diffusion coefficient and is explicitly related to the magnetic turbulence. η can also be described as:

$$\eta \equiv \left(\frac{B_0}{\delta B} \right)^2, \quad (4.13)$$

where B_0 and δB are the initial background magnetic field and the turbulent magnetic field, respectively, as derived in Section 2.4.2. A higher value of η (i.e., a higher diffusion coefficient) implies that an insufficient turbulent magnetic field exists to scatter the particles. A lower value of η (i.e., a lower diffusion coefficient) implies that the magnetic field is sufficiently turbulent to scatter the particles. The observed η -age plots may suggest generation of the turbulent magnetic field is related to the evolution of SNRs: Figure 4.15 implies the turbulence of magnetic field growing with time. Here we address some open issues, such as quantitative explanation or physical meaning of the growth slope of $-\delta$.

The acceleration efficiency depends on a Mach number of the shock wave, as studied in Caprioli and Spitkovsky (2014a,b,c) using numerical simulations. Caprioli and Spitkovsky (2014c) derived the relation (Eq. (16) therein),

$$\eta \propto \mathcal{M}^{-1/2}, \quad (4.14)$$

where \mathcal{M} is the Mach number of the SNR shock. However, the Mach number decreases with the evolution of SNRs because the shock is decelerated, and η increases following Equation 4.14. Thus, the theoretical η - \mathcal{M} relation predicts the opposite tendency of the observation.

The shock obliquity (θ_{Bn}) also plays a critical role in particle acceleration in SNRs (Petruk et al., 2011; Caprioli and Spitkovsky, 2014a). Whether the acceleration occurs at parallel ($\theta_{\text{Bn}} \sim 0^\circ$) or perpendicular ($\theta_{\text{Bn}} \sim 90^\circ$) shocks remains controversial. Some numerical calculations have suggested a quasi-parallel shock produces particle injection more efficiently and generates a more amplified magnetic field (e.g., Caprioli and Spitkovsky (2014a)). They found that acceleration efficiency (ε_{cr})⁶ drastically drops off for $\theta_{\text{Bn}} \geq 45^\circ$. SN 1006 is the only target to investigate the dependence on shock obliquity, as we have known the direction of the field. Although one should be cautious about the different definitions of acceleration efficiency, our result also indicates inefficiency (larger η) above $\sim 40^\circ$ for shock obliquity in SN 1006, as shown in Figure 4.11. The observed gradual decrease of acceleration efficiency for increasing θ_{Bn} might be consistent with the simulation result with a higher Mach number, for example $\mathcal{M} = 50$. From a morphological point of view, G1.9+0.3 and Vela Jr. resemble bilateral structures similar to SN 1006, but shock obliquities are unknown. If the initial ambient field is aligned, the acceleration efficiency could depend on the shock obliquity in the earlier phase, as confirmed in SN 1006. In the later evolution stage or in the preexisting randomly turbulent field, the shock obliquity is averaged over the outer rim, resulting in efficient acceleration.

Another possible explanation for the evolving η is a nonlinear effect. In the test-particle limit, the shock front is presumed to have a clear jump. Considering the backreaction of accelerated particles, the shape of the shock is modified, and the configuration of acceleration becomes different (see, for example, Reynolds (2008) for a review of SNRs and references therein). For a fast shock wave in a young SNR, the nonlinear effect is not important. However, for a slow shock in an older SNR, the nonlinear effect becomes non-negligible, changing the acceleration efficiency.

It should be noted that the observed η -age plot is somewhat biased as a selection problem in systematical analyses. There might exist SNRs with larger Bohm factors at the older ages (a few 1,000 years), but they cannot be observed because of the inefficient acceleration. At that point, the η -age plot is considered as the lower limit of η as a function of age. Our analysis determined that younger SNRs (of a few 100 years) exhibiting efficient acceleration with $\eta \sim 1$ are hardly present except for the effective acceleration at the lower density region in Cassiopeia A.

Figure 4.16 shows the cutoff energy parameters and shock velocities taken from the same regions in Figure 4.15 as a function of age (and m). Although the decreasing v_{sh} (shock deceleration) is naturally expected, the ε_0 does not show any correlation with time. Moreover, the shock speed varies by a factor of ~ 6 at most, which should generate a difference in ε_0 by ~ 36 if the η parameter is constant. The observed cutoff energy parameters range from 0.3 to 2 keV, corresponding to the difference of a factor of ~ 7 . This inconsistency is also supportive of the time dependence on η , which is determined by the balance between ε_0 and v_{sh} .

Reverse shock

The mechanism of particle acceleration in the reverse shock has been less understood as compared to forward shock. The location of the reverse shock inside the shell of the SNR and the contamination by the projected forward-shocked components make it more difficult and challenging to observe and examine the property of reverse shock. Currently, only three SNRs exist in which the nonthermal radiation associated with the reverse shock has been reported: G1.9+0.3, Cassiopeia A, and SN 1987A.

In this section, we present the acceleration efficiency of reverse shock. The η value of the hard X-ray spot in Cassiopeia A was obtained to be 3–8 (Sato et al., 2018). Our analysis shows the acceleration efficiency was 2–3 in the N and S regions of G1.9+0.3, assuming the proper motion measured in X-ray traces the reverse shock, whereas the forward shock indicates $\eta \sim 20$ in the E and W rims. This lower value of η of the reverse shock as compared to that of the forward shock in G1.9+0.3 appears opposite to what has been seen in Cassiopeia A. The synchrotron radio emission from SN 1987A is expected to originate from the reverse shock. If we assume

⁶ ε_{cr} is defined as the fraction of the postshock energy density of particles with energies greater than a certain threshold energy. This is different from our definition of acceleration efficiency with the Bohm factor, η .

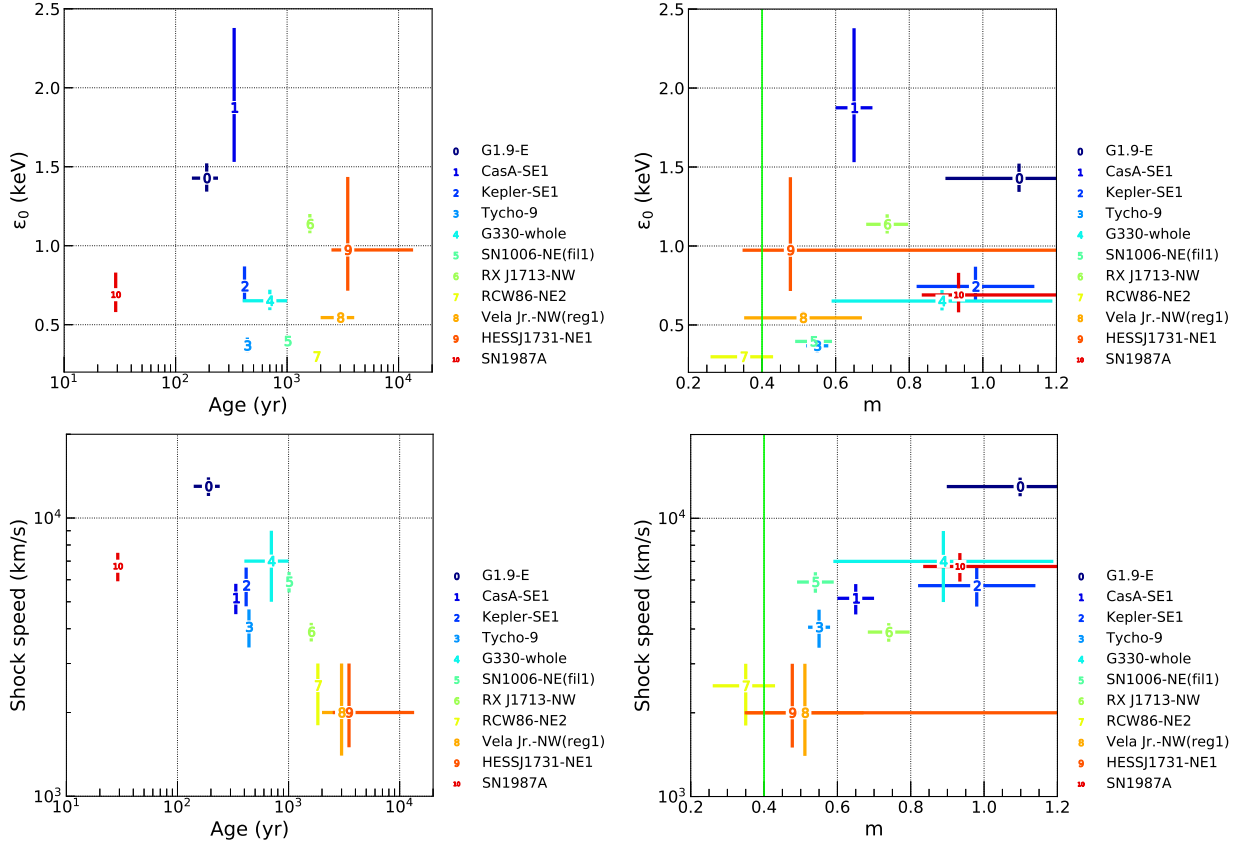


Figure 4.16: ε_0 as a function of the age (top left) and expansion parameter m (top right), and v_{sh} as a function of the age (bottom left) and expansion parameter m (bottom right).

the *NuSTAR* X-ray component is synchrotron radiation associated with the reverse shock, η is inferred to be approximately 4 with $u_1 = 4800 \text{ km s}^{-1}$ in Equation 4.6.

Figure 4.17 illustrates the η value of reverse shock in all SNRs as a function of their age. The results are also shown in Table 4.7. We found all of the η values of reverse shock were roughly identical, ranging from 2 to 6. The best-fit parameters of the η -age plot were $\delta_{age} = 0.081 \pm 0.21$ and $C_{age} = 2.4 \pm 1.4$.

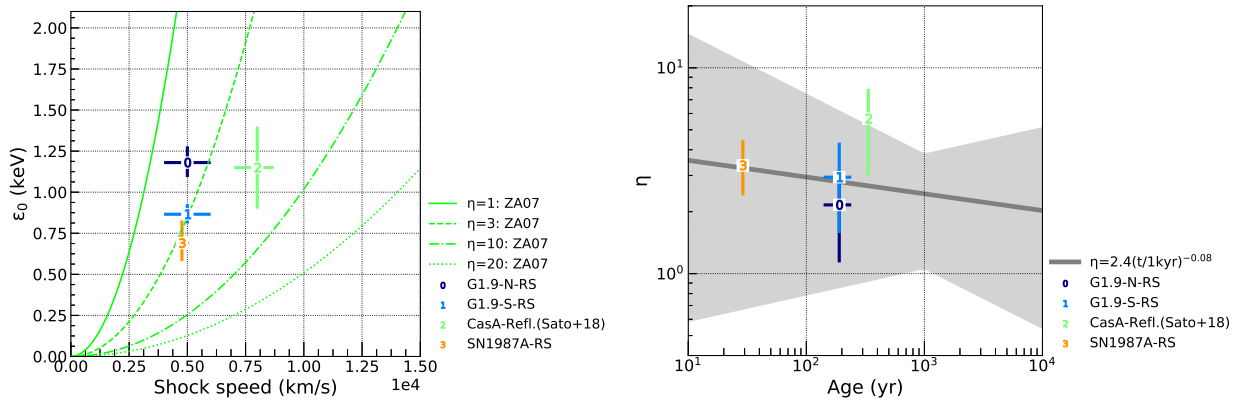


Figure 4.17: Left: v_{sh} - ε_0 diagram of the reverse-shocked regions. Right: η -age.

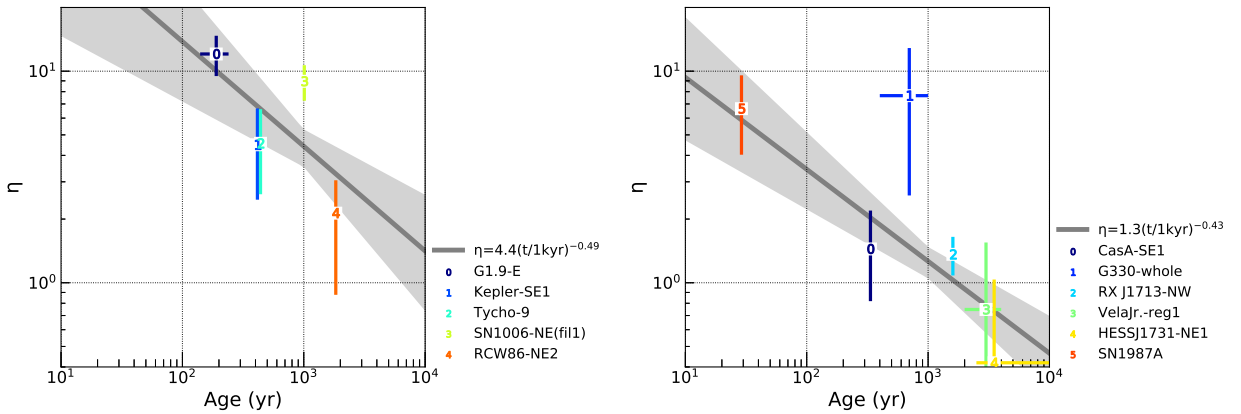
Table 4.7: Reverse-shock properties

Name	Region	Age (yr)	u_1 (km s ⁻¹)	m	ε_0 (keV)	η
G1.9+0.3	N-RS	190±50	5000±1000	0.4±0.2	1.18±0.09	2.2±1.0
G1.9+0.3	S-RS	190±50	5000±1000	0.4±0.2	0.87±0.06	2.9±1.4
Cassiopeia A	Reflection shock (Sato et al., 2018)	335±20	8000±1000	0.7±0.1	1.15±0.25	5.7±2.6
SN1987A	RS	29	4767±300	0.9±0.1	0.69 ^{+0.14} _{-0.10}	3.4±1.0

Supernova explosion type

In this subsection, we present the η values from two types of SNe. A Type Ia SN is driven by a thermonuclear explosion of a white dwarf star, and Type II is a core-collapse explosion. In general, the ambient interstellar medium of a Type Ia SNR is rarefied and thus takes longer to produce magnetic field turbulence, whereas the circumstellar medium surrounding a core-collapse SNR is clumpy and complex due to stellar wind from a massive progenitor star.

In our analysis, G1.9+0.3, Kepler, Tycho, SN 1006, and RCW 86 are classified as Type Ia, and Cassiopeia A, G330.2+1.0, RX J1713.7–3946, Vela Jr., HESS J1731–347, and SN 1987A are classified as core-collapse SNRs. We group SNRs with the CCOs as Type II. It should be noted that this may not be a precise classification. Figure 4.18 is an η –age diagram of Type Ia (left panel) and Type II (right). The best-fit parameters are $(\delta_{\text{age}}, C_{\text{age}}) = (0.49 \pm 0.18, 4.4 \pm 0.9)$ for Type Ia and $(\delta_{\text{age}}, C_{\text{age}}) = (0.43 \pm 0.11, 1.3 \pm 0.2)$ for Type II. The core-collapse SNRs have a slightly (not significant) flatter slope and a significantly lower η value at 1 kyr. For Type Ia SNRs, over 10,000 years are required for η to reach unity, whereas ~ 3000 years are required for Type II SNRs. Overall, η of core-collapse SNRs appears smaller than that of Type Ia SNRs at $t_{\text{age}} \lesssim 10000$ years. We should be careful regarding the small number of data samples and the fact that Type II SNRs presented here consist of relatively older SNRs.

Figure 4.18: η –age diagram of Type I (left) and Type II (right).

4.4.4 Limited by cooling or age?

Acceleration in SNR is expected to be limited by either energy loss (cooling), age, or escape. Our models (Equation 4.1; Equation 4.2; Equation 4.3) were based on the assumption of the cooling-limited case. We needed to first test the validity of this assumption. The characteristic timescale of electrons to gain energy via

DSA is generally given by:

$$\tau_{\text{acc}} \sim \frac{D}{u_1^2}, \quad (4.15)$$

where the diffusion coefficient of D is now assumed to be the product of η and the gyroradius. The characteristic timescale of electrons at the energy around the cutoff energy parameter ($E \approx E_0$) to suffer the synchrotron cooling is described by:

$$\tau_{\text{synch}} = \frac{E_0}{b(E_0)} \quad (4.16)$$

$$= 53 \left(\frac{v_{\text{sh}}}{3000 \text{ km s}^{-1}} \right)^{-1} \left(\frac{B}{100 \mu\text{G}} \right)^{-\frac{3}{2}} \eta^{\frac{1}{2}} \text{ yr}, \quad (4.17)$$

which is the same as (23) in Zirakashvili and Aharonian (2007) for $\kappa = \sqrt{11}^{-1}$ and $\gamma_s = 4$. Here, $b(E)$ denotes the energy loss rate of synchrotron radiation: $b(E) = 4q^4 B^2 E^2 / 9m^4 c^8$. In the synchrotron-cooling-limited case, the acceleration timescale is comparable to the synchrotron-cooling timescale and is shorter than the characteristic dynamical timescale of the source, such as the age of the accelerator. Therefore, to fulfill our assumption, the condition that follows should be satisfied:

$$\tau_{\text{acc}} \approx \tau_{\text{synch}} \leq \tau_{\text{age}}. \quad (4.18)$$

One can put a lower limit value on the magnetic field by imposing the condition of $\tau_{\text{synch}} \leq \tau_{\text{age}}$,

$$B \geq B_{\text{low}} = 12 \left(\frac{t_{\text{age}}}{1 \text{ kyr}} \right)^{-\frac{2}{3}} \left(\frac{u_1}{4000 \text{ km s}^{-1}} \right)^{-\frac{2}{3}} \eta^{\frac{1}{3}} \mu\text{G}. \quad (4.19)$$

For example, with the parameter set of RX J1713.7–3946 NW (i.e., $u_1 = 3900 \text{ km s}^{-1}$, $\eta = 1.4$, and $\tau_{\text{age}} = 1600 \text{ yr}$), B should be greater than $10 \mu\text{G}$. The lower limits of B calculated for the other SNRs are listed in Table 4.6. B_{low} is estimated to be 8–18 μG in the galactic SNRs older than G330.2+1.0. This can be reasonably achieved given the magnetic field strength in the interstellar medium of $\sim 4 \mu\text{G}$ and the standard shock compression of 4. For the younger SNRs, we obtained B_{low} of 30–40 μG , which is still acceptable when considering magnetic field amplification. Indeed, it has been reported that the magnetic field strength is enhanced up to $\sim 100 \mu\text{G}$, estimated from the filament width (e.g., Bamba et al. (2005); Berezhko and Völk (2006)). An exceptionally high value of $B_{\text{low}} = 172 \mu\text{G}$ for SN 1987A might be challenging, considering the extremely young age of the remnant. We conclude that the synchrotron-cooling-limited condition is reasonable for all of the galactic SNRs analyzed in this thesis, and the case of SN 1987A might be challenging.

4.4.5 Maximum attainable energy: Are SNRs PeVatrons?

The maximum energy attainable in SNRs was presented in Section 2.3. Because the timescale for the energy loss of a proton is significantly longer than the age of SNR in the earlier evolutionary phase, such as SNRs analyzed in this study, the maximum energy of a proton is expected to be limited by its age. With the governing equation of $\tau_{\text{acc}} = \tau_{\text{age}}$, the maximum energy of the accelerated proton is derived as:

$$E_{\text{max,age}} = \frac{3}{20} \frac{q}{c} t v_{\text{sh}}^2 B \eta^{-1}. \quad (4.20)$$

We simply assume that the shock velocity is constant in ED phase and is given by a self-similar solution in the Sedov-Taylor (ST) phase:

$$v_{\text{sh}}(t) \propto \begin{cases} t^0 & \text{(ED)} \\ t^{-3/5} & \text{(ST)}. \end{cases} \quad (4.21)$$

Note that sophisticated analytical solutions to express a smooth connection between ED and ST have been well studied (e.g., Truelove and McKee (1999); Tang and Chevalier (2017)). However, the evolution of the magnetic field is not well understood. We presume that B is dependent on the evolutionary age as:

$$B(t) \propto t^{-\mu}. \quad (4.22)$$

This work suggests that the η value also depends on the time evolution of SNR. Thus, we apply:

$$\eta(t) \propto t^{-\delta}. \quad (4.23)$$

We assume that this empirical relation holds until η becomes unity with δ being ~ 0.5 (see Figure 4.15 and Equation 4.9). Substituting into Equation 4.20, we obtain time dependence on the maximum energy of the proton:

$$E_{\max, \text{age}} \propto \begin{cases} t^{1-\mu+\delta} & \text{(ED)} \\ t^{-1/5-\mu+\delta} & \text{(ST)}. \end{cases} \quad (4.24)$$

Equation 4.24 insists that $E_{\max, \text{age}}$ can be greater than expected because of the newly added term of δ . Our result, $\delta \sim 0.5$, suggests that $E_{\max, \text{age}}$ increases as $t^{0.3}$ even in the ST stage on the assumption of $\mu = 0$.

Here, an example of Tycho is presented. The GeV gamma-ray spectrum seems likely to have a π^0 bump that is a characteristic feature in the hadronic scenario, and the TeV gamma-ray spectrum shows exponential cutoff at ~ 2 TeV. Therefore, the maximum energy of the proton in Tycho is estimated to be roughly 44 TeV (Archambault et al., 2017). Tycho is obviously not a PeVatron in the current stage with its age of 440 years. If we apply $\delta = 0.5$ and $\mu = 0$ for Equation 4.24, the maximum energy of the proton becomes 1.5 PeV at ~ 5000 years when the η value reaches 1, assuming it is still in the ED phase. This maximum energy is approximately three times greater than that in the same later stage with $\delta = 0$, which has been sometimes assumed. The time evolution of η may suggest that SNR may accelerate particles up to the PeV range.

Defining when exactly an SNR enters into the ST phase is difficult. The transition between ED and ST stages is most likely smoother than as described in Equation 4.21. The SNRs we analyzed in this study included those in both ED and ST phases, but most them were relatively young and might be in the very transition stage from ED to ST. Altogether, they indicate the Bohm factor decreases until it becomes close to unity. Our work could not fully determine the behavior of η in the later phase, particularly the phase that has significantly transitioned into ST.

4.5 Conclusions

We analyzed X-ray observations of 11 young SNRs to determine the cutoff energy parameter in the synchrotron spectrum and constrain the corresponding Bohm factor of each SNR. Our model of synchrotron radiation is based on the framework that the accelerated electron is limited by synchrotron cooling and Bohm diffusion. This assumption is reasonable for SNRs older than 1,000 years if $B = 8\text{--}18 \mu\text{G}$ and for SNRs as young as a few 100 years if $B = 30\text{--}40 \mu\text{G}$. We should be cautious about G1.9+0.3 (150–190 years) and SN 1987A (30 years) because B should be much larger for the assumption to be valid in these sources, and it is questionable for such young SNRs to be capable of enhancing magnetic fields in their short lifetimes.

The $\varepsilon_0\text{--}v_{\text{sh}}$ relations obtained for the six individual SNRs are interpreted as the following cases:

1. The $\varepsilon_0\text{--}v_{\text{sh}}$ scatter plot is nicely represented by the theoretical curve, $\varepsilon_0 \propto v_{\text{sh}}^2 \eta^{-1}$, with constant η throughout the remnant in the cases of Kepler and Tycho.
2. The acceleration is affected by a surrounding density in the case of Cassiopeia A. The different η values are attributed to the different cutoff energy parameters, which are more correlated with the ambient number density. The kinetic energy of shock is transferred to acceleration and heating in the lower and higher densities, respectively.
3. The acceleration is affected by a surrounding magnetic-field configuration in the case of SN 1006. The ε_0 , v_{sh} , and η show an azimuth variation, and we can confirm that the acceleration is more efficient near the polar limbs where quasi-parallel shocks are expected to form.

4. The different η values are attributed to the different shock speeds, which in the case of the youngest SNR in our Galaxy is G1.9. It should be noted that the cooling-limited assumption might not be appropriate for this remnant.
5. In the case of the northwest of RX J1713.7–3946, the particle acceleration is required to proceed in the regime close to the Bohm limit near the forward shock. However, we require another scenario to explain the higher cutoff energy than theoretically predicted in the regions with slow speeds, such as the inner edge and the filamentary structure. The parsec-scale amplification of the magnetic field and/or the acceleration at the reflection shock might be the case.

With all 11 SNRs together, including G330.2+1.0, RCW 86, Vela Jr., HESS J1731–347, and SN 1987A, the systematic tendency of the Bohm factor has been unveiled for the first time. The η in the maximum- ε_0 (or maximum- v_{sh}) region of each SNR depends on the evolutionary age as $\eta = 1.6(t_{\text{age}}/1 \text{ kyr})^{-0.46}$ or on the expansion parameter as $\eta = 6.5m^{4.5}$. This can be related to the turbulent generation (i.e., the turbulence becomes more self-generated as particles become more accelerated with time). Comparing the time dependence on η between Types I and II supernova explosions, Type II shows a relatively lower η value and a flatter rate of the growth. Although the difference between SNe is not significant, a lower η of Type II might be expected because it exploded in the more complex surroundings of the circumstellar medium and could facilitate the turbulence to grow. We also present the evolution of η at the reverse shock. In addition to the known reverse shock of Cassiopeia A, possible reverse shocks were reported in G1.9+0.3 and SN 1987A, showing η greater than 1. Finally, if we consider the time dependence on η as $\eta \propto t^{-\delta}$ with $\delta \approx 0.46$, which has not been expected before, and assume this condition holds until η reaches unity even in the Sedov-Taylor phase, the attainable maximum energy appears greater by the term of δ , possibly in the PeV range.

Chapter 5

Gamma-ray observations of young supernova remnants: Bohm diffusion

The nonthermal gamma-ray spectrum can be a new diagnostic method to investigate acceleration efficiency in shock waves of supernova remnants. We apply the same prescription presented in Chapter 4 to the TeV gamma-ray spectra of SNRs. There are two problems to be addressed: the gamma-ray spectrum here is assumed to be dominated by leptonic components (inverse Compton scattering radiation), but this is very controversial in some SNRs. The other issue is that the gamma-ray spectrum was obtained as an integrated spectrum over a larger area, and thus lost its local and smaller structures, such as a thin rim or a filament, because of the limited spatial resolution. We found the cutoff shape of the TeV gamma-ray spectrum is nicely reproduced by the model of IC emitted from electrons limited by cooling and Bohm diffusion, resulting in the cutoff energy parameter of the parental electron of 20–50 TeV. Combined with the shock speed, we estimate Bohm factor, which tends to be slightly larger than that estimated with X-ray observations. This could be attributed to different regions to extract the X-ray and gamma-ray spectra and an underestimation of magnetic field strength probably caused by the spatial difference of the spectra. Future gamma-ray telescopes (e.g., Cherenkov Telescope Array (CTA)), would provide us with more spatially resolved spectra in the TeV gamma-ray range, allowing to determine Bohm factor with higher accuracy.

5.1 Gamma-ray observations

We apply our model (presented in Section 2.6) to five TeV gamma-ray emitting SNRs: SN 1006, RX J1713.7–3946, RCW 86, Vela Jr., and HESS J1731–347, shown in Figure 5.1 and Figure 5.2. The gamma-ray spectra of these SNRs presented in this thesis are taken from the literature, as summarized in Table 5.1. It should be noted the radiation mechanism of the observed gamma-ray is controversial for some sources (e.g., RX J1713.7–3946). In order to apply the electron model and compare the results with X-ray observations, it is presumed that the gamma-ray is a leptonic origin (i.e., IC radiated from high-energy electrons). This assumption is supported by relatively flatter GeV gamma-ray spectra with $\Gamma = 1.5\text{--}1.8$ and good spatial correlations between the synchrotron X-rays and TeV gamma-rays. GeV gamma-rays are expected to be radiated from electrons that are not affected by the synchrotron cooling, while TeV gamma-rays are subject to the cooling-steepened electrons. Therefore we use only the TeV gamma-ray spectrum taken with H.E.S.S. to determine the cutoff shape including the cutoff energy parameter.

A deeper observation makes it possible to provide the spatially resolved spectroscopy at arcmin scale with H. E. S. S. The spatially resolved spectral analysis was performed, for example, in RX J1713.7–3946 by dividing the entire remnant into 29 regions with each box size of 4.8×4.8 arcmin² (H. E. S. S. Collaboration, 2018b). We utilize the TeV gamma-ray spectrum of the NW region (Reg 09 in (H. E. S. S. Collaboration, 2018b)) in addition to the integrated spectrum. For SN 1006, the spectra of two limbs in the northeast and southwest are individually provided (Acero et al., 2010). The integrated spectra over the entire remnant are used for the other SNRs.

Table 5.1: Dataset of gamma-ray observations

Name	Distance (kpc)	GeV spectrum	TeV spectrum	B^\dagger (μG)
SN 1006	2.0	Condon et al. (2017); Xing et al. (2019)	Acero et al. (2010)	24
RX J1713.7–3946	1.0	Abdo et al. (2011); Fed- erici et al. (2015)	H. E. S. S. Collaboration (2018b)	15
RCW 86	2.0	Ajello et al. (2016)	Aharonian et al. (2009)	10.2
Vela Jr.	0.7	Tanaka et al. (2011)	H. E. S. S. Collaboration (2018c)	12
HESS J1731–347	3.2	Condon et al. (2017)	H. E. S. S. Collaboration (2011)	25

[†] The magnetic field, B , is taken from each literature, which was estimated from the observed flux ratio of the X-ray and gamma-ray spectra.

5.2 Spectral fitting and results

We apply the IC model radiated from electrons that are limited by synchrotron cooling and Bohm diffusion, as described with Equation 2.106 and recalled below,

$$N_0 \propto p^{-4} \left[1 + 0.523 \left(\frac{p}{p_0} \right)^{\frac{9}{4}} \right]^2 \exp \left[- \left(\frac{p}{p_0} \right)^2 \right]. \quad (5.1)$$

Naima (Zabalza, 2015)¹ is used for modeling and calculating IC radiation including the Klein-Nishina effect. Note that we obtain directly the cutoff energy parameter of the electron ($E_0 = cp_0$) with KN-regime model. The

¹A python package for computation of nonthermal radiation from relativistic particle populations and Markov Chain Monte Carlo (MCMC) fitting of radiative models to observed spectra (<https://naima.readthedocs.io/en/latest/>).

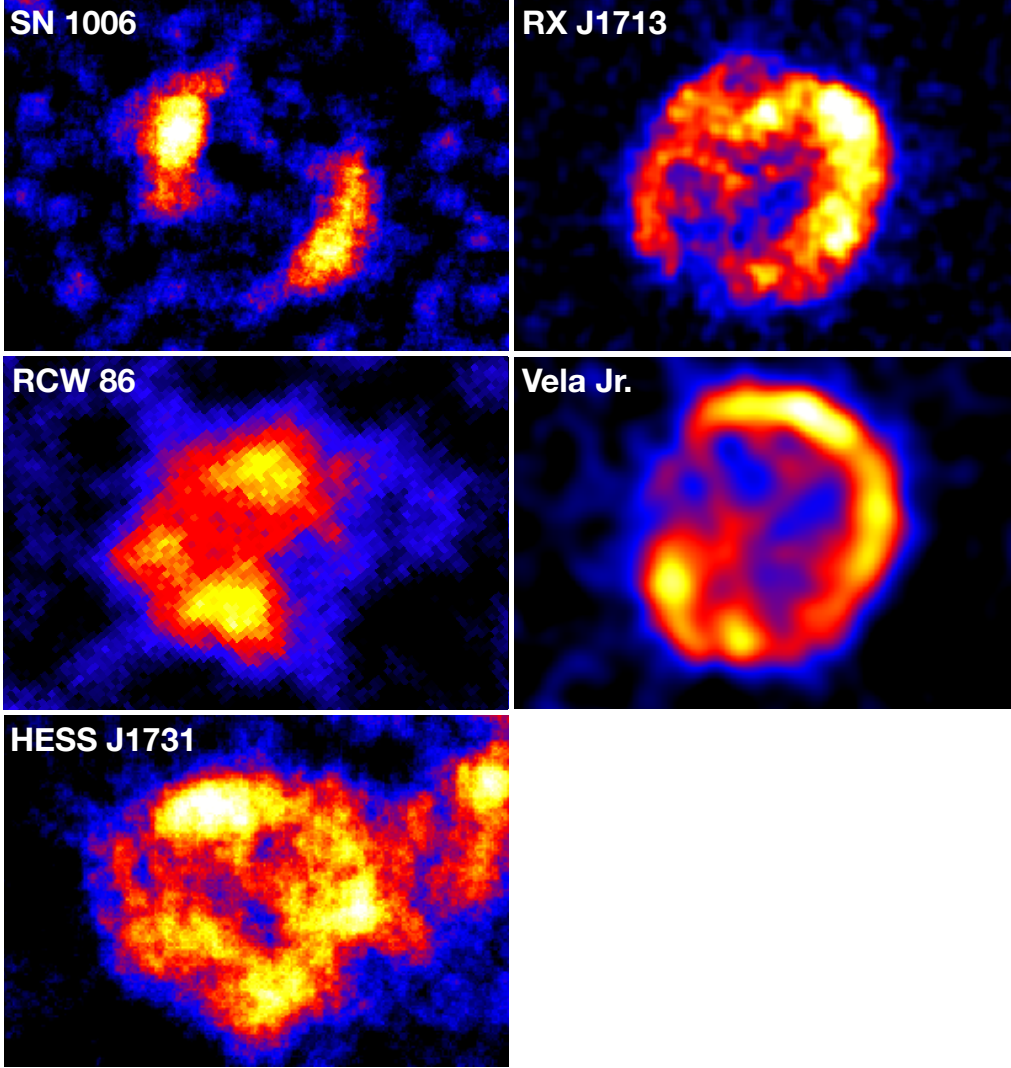


Figure 5.1: H. E. S. S. images which are taken from the previous studies in Table 5.1, except that RCW 86 is taken from the image of H. E. S. S. Galactic Plane Survey (HGPS; H. E. S. S. Collaboration (2018d)).

spectra with the best-fit models are shown in Figure 5.3, and the best-fit parameters are listed in Table 5.2. We assume that the target photon is only CMB with the temperature (T) of 2.72 K and the energy density of 0.261 eV cm^{-3} .

In addition to the physical model introduced above, we fit the spectra with power law and power law with a super exponential cutoff. The cutoff power-law model is described as

$$\frac{dN_\gamma}{d\varepsilon} \propto \varepsilon^{-\Gamma} \exp \left[- \left(\frac{\varepsilon}{\varepsilon_c} \right)^{\beta_\gamma} \right], \quad (5.2)$$

where Γ , ε_c , and β_γ are the photon index, cutoff energy, and cutoff slope, respectively. For the cutoff power-law model, we present the results with all three parameters (Γ , ε_c , and β_γ) free and with fixed photon index to 2. The best-fit parameters are shown in Table 5.3.

Our model well reproduces the gamma-ray cutoff spectral shape, as shown in Figure 5.3 and Table 5.2. The power-law models are confidently rejected from the chi-squared values, but the differences between the cutoff power-law models and our physical model are not significant with the current dataset (Table 5.2 and Table 5.3).

Table 5.2: Spectral fitting in Bohm diffusion

Name	E_0 (TeV)	W_e (10^{45} erg)	B (μG)	v_{sh} (km s^{-1})	η_γ	χ^2	dof
SN 1006 (NE)	47^{+31}_{-11}	24 ± 2	24.0	5000 ± 1000	$2.9^{+4.0}_{-1.8}$	9.6	11
SN 1006 (SW)	24^{+10}_{-6}	16 ± 3	24.0	5000 ± 1000	$12^{+11}_{-7.5}$	10.6	4
RX J1713.7–3946 (whole)	48^{+4}_{-3}	360^{+7}_{-8}	15.0	3900 ± 300	$2.7^{+0.7}_{-0.6}$	45.9	26
RX J1713.7–3946 (NW; Reg09)	35^{+5}_{-4}	25 ± 1	15.0	3900 ± 300	$5.2^{+1.6}_{-1.4}$	34.7	23
RCW 86 (whole)	26 ± 2	440^{+25}_{-28}	10.2	2500 ± 700	$5.4^{+3.2}_{-3.2}$	30.5	18
Vela Jr. (whole)	33^{+3}_{-23}	$250^{+7.6}_{-8.4}$	12.0	2200 ± 800	$2.3^{+1.7}_{-1.7}$	13.8	11
HESS J1731–347 (whole)	19 ± 2	480^{+32}_{-22}	25.0	2000 ± 500	$2.6^{+1.6}_{-1.5}$	15.8	20

Table 5.3: Best-fit parameters with power-law (PL) and cutoff power-law (CPL) models

Name	Model	Γ	ε_c (TeV)	β_γ	χ^2	dof
SN 1006 (NE)	PL	2.2 ± 0.1	—	—	4.8	11
SN 1006 (SW)	PL	2.3 ± 0.1	—	—	8.8	5
SN 1006 (SW)	CPL	2 (fixed)	14 ± 6.5	0.93 ± 1.3	6.5	4
RX J1713.7–3946 (whole)	PL	2.3 ± 0.02	—	—	147.2	26
RX J1713.7–3946 (whole)	CPL	1.8 ± 0.3	2.7 ± 7	0.46 ± 0.25	35.3	24
RX J1713.7–3946 (whole)	CPL	2 (fixed)	15 ± 1.6	0.78 ± 0.1	37.7	25
RX J1713.7–3946 (NW)	PL	2.3 ± 0.04	—	—	66.8	23
RX J1713.7–3946 (NW)	CPL	1.6 ± 0.7	1.8 ± 7.9	0.53 ± 0.53	32.0	21
RX J1713.7–3946 (NW)	CPL	2 (fixed)	11 ± 1.9	1.1 ± 0.28	33.2	22
RCW 86 (whole)	PL	2.9 ± 0.1	—	—	72.5	18
RCW 86 (whole)	CPL	2 (fixed)	8 ± 2.2	1.2 ± 0.31	13.6	17
Vela Jr. (whole)	PL	2.3 ± 0.03	—	—	77.4	11
Vela Jr. (whole)	CPL	2 (fixed)	11 ± 1	1.5 ± 0.28	7.6	10
HESS J1731–347 (whole)	PL	2.4 ± 0.1	—	—	11.9	20
HESS J1731–347 (whole)	CPL	1.9 ± 1.0	2.7 ± 16	0.65 ± 1.4	6.8	18
HESS J1731–347 (whole)	CPL	2 (fixed)	4.3 ± 1.7	0.8 ± 0.41	6.9	19

Note that the cases which are not well fitted (i.e., CPL with Γ being free) are omitted here.

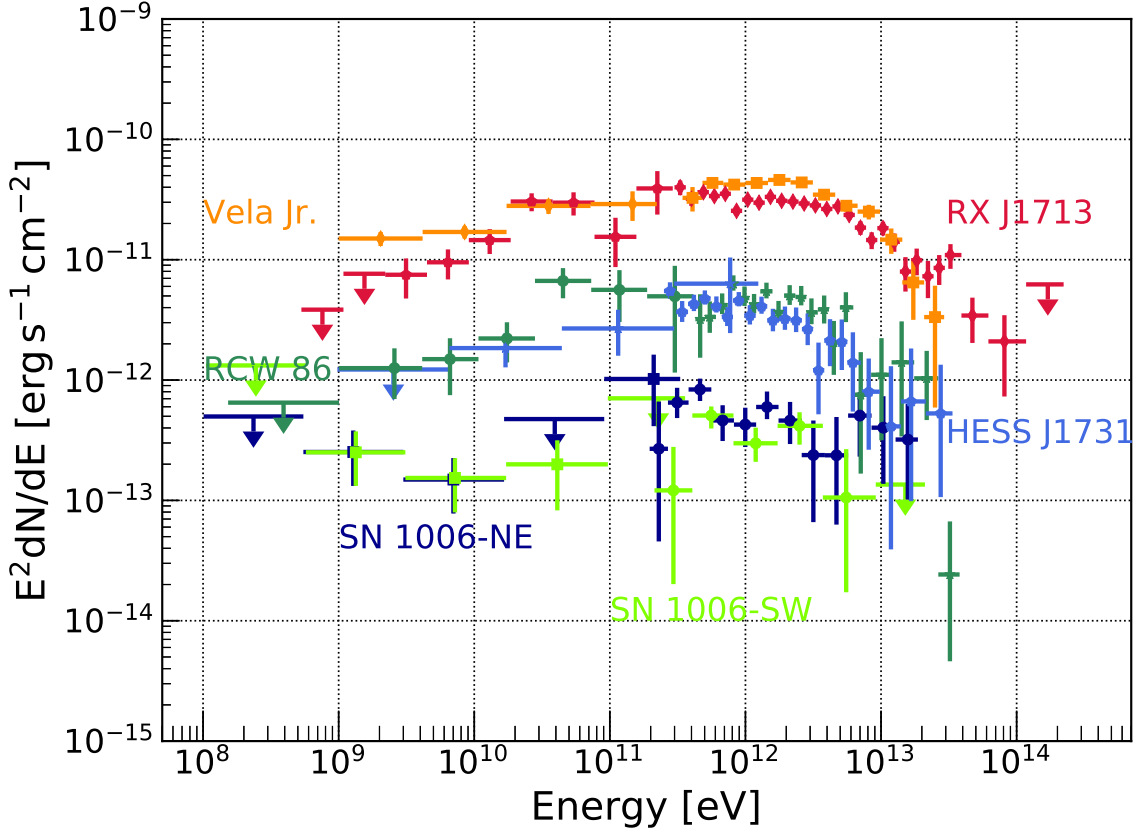


Figure 5.2: Gamma-ray spectra which are taken from the previous studies in Table 5.1.

5.3 Discussion

The observed cutoff energy parameter of the electron, combined with the shock speed and magnetic field (B), puts a constraint on the Bohm factor (η_γ). In Klein-Nishina regime, we obtain the electron cutoff energy parameter directly from spectral fitting, then we estimate η_γ by formulating Equation 2.105:

$$\eta = \frac{27m^4c^4}{2q^3\gamma_s^2} \left(1 + \frac{1}{\sqrt{\kappa\xi}}\right)^{-2} u_1^2 (B\rho_0^2)^{-1} \quad (\text{KN regime}). \quad (5.3)$$

For B , the value in the literature (Table 5.1) is used (i.e., it is estimated from the flux ratio of the observed synchrotron X-ray and IC gamma-ray radiation). We showed that the gamma-ray observation can be a new tool to estimate Bohm factor by using Equation 5.3 based on the assumption of leptonic-dominated gamma-ray radiation.

Figure 5.4 presents the Bohm factor obtained with gamma-ray observations (referred to as η_γ) and that with X-ray observations (η_X). In Figure 5.4, η_γ is roughly comparable with η_X , although it tends to be slightly larger than η_X in some SNRs. This might arise from the fact that the spectral regions are not exactly identical in X-ray and gamma-ray observations. The X-ray spectrum is extracted from a relatively small and filamentary region where the accelerated electron is concentrated, while the gamma-ray spectrum is taken from a larger region due to the limited angular resolution of the current telescope and the poor statistics. Indeed, the different regions in X-ray and gamma-ray spectra cause an underestimate of the magnetic field. B could be much locally enhanced, in particular in such a filament and rim observed in X-rays. This underestimation of B results in larger Bohm factor (see Equation 5.3) obtained with the gamma-ray observations, while B does not depend on determination of η_X . Thus we might have obtained the larger η_γ than η_X , as shown in Figure 5.4.

To avoid the issue of the different size of the spectra, an integration of the X-ray spectrum with larger area is a possible solution at the current stage. However this does not help because the integrated X-ray spectrum smears the smaller structures such as a filament or a narrow rim. In fact the larger η_γ appears in the NW and

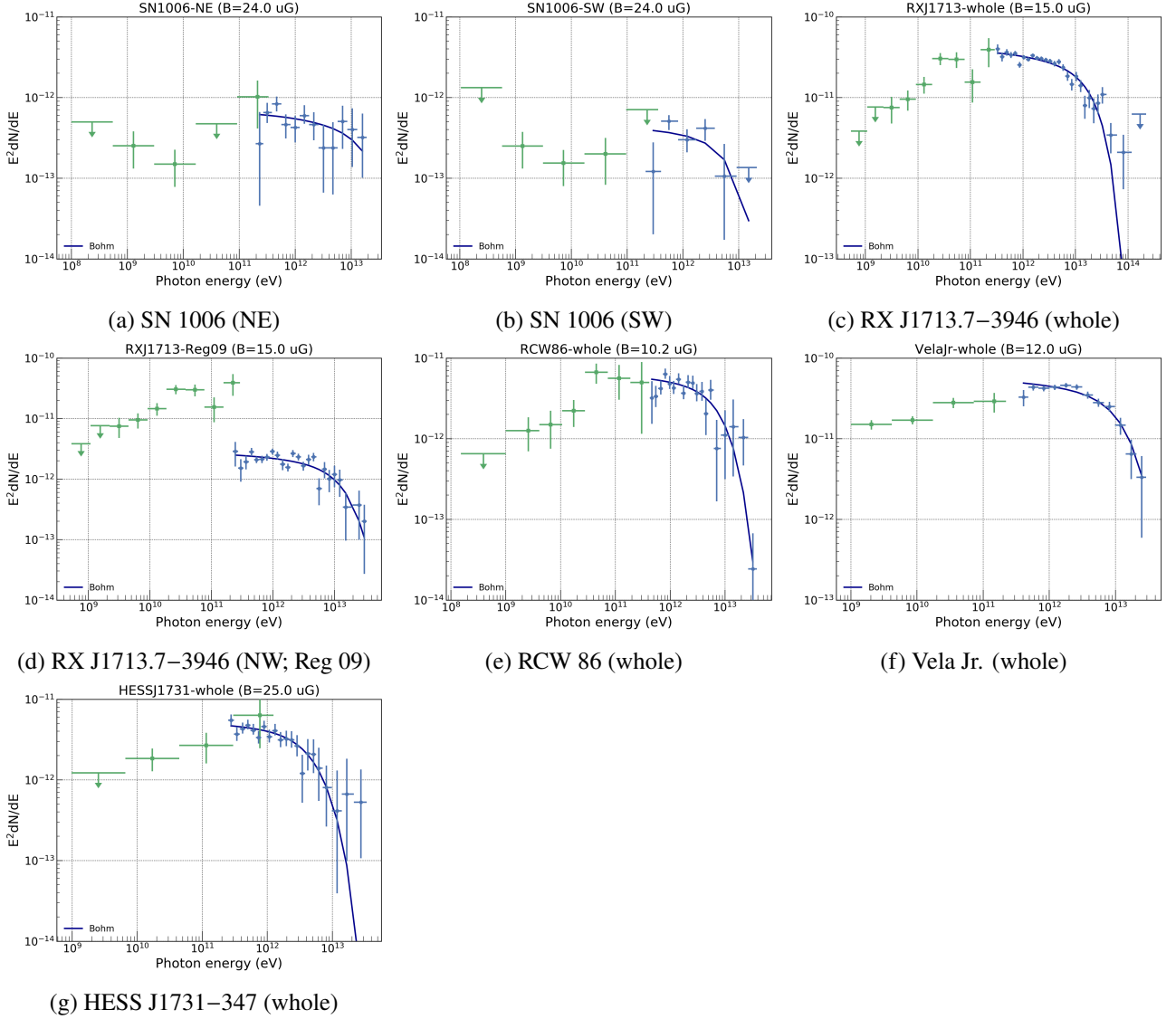


Figure 5.3: The gamma-ray spectra (plots) with the best-fit models (blue solid lines) in KN regime. The blue and green plots present the H.E.S.S. and *Fermi* spectra, respectively.

the entire remnant of RX J1713.7–3946, of which the spectra are extracted from the roughly same regions. To compare the X-ray and gamma-ray spectra in details, we need a gamma-ray spectroscopy of which the angular resolution is as good as that of the X-ray spectroscopy.

The integrated gamma-ray spectrum over the larger area might smear a contribution of a reverse shock, which should be taken into account separately from the forward shock (e.g., Zirakashvili and Aharonian (2010)). Another possibility is that the observed gamma-ray spectrum contains a non-negligible hadronic component, making the assumption of the leptonic-dominated gamma-ray spectrum invalid. In either case, the future IACT, such as CTA (promising IACT), will spatially resolve TeV gamma-ray, providing us with a more precise comparison with X-ray observations.

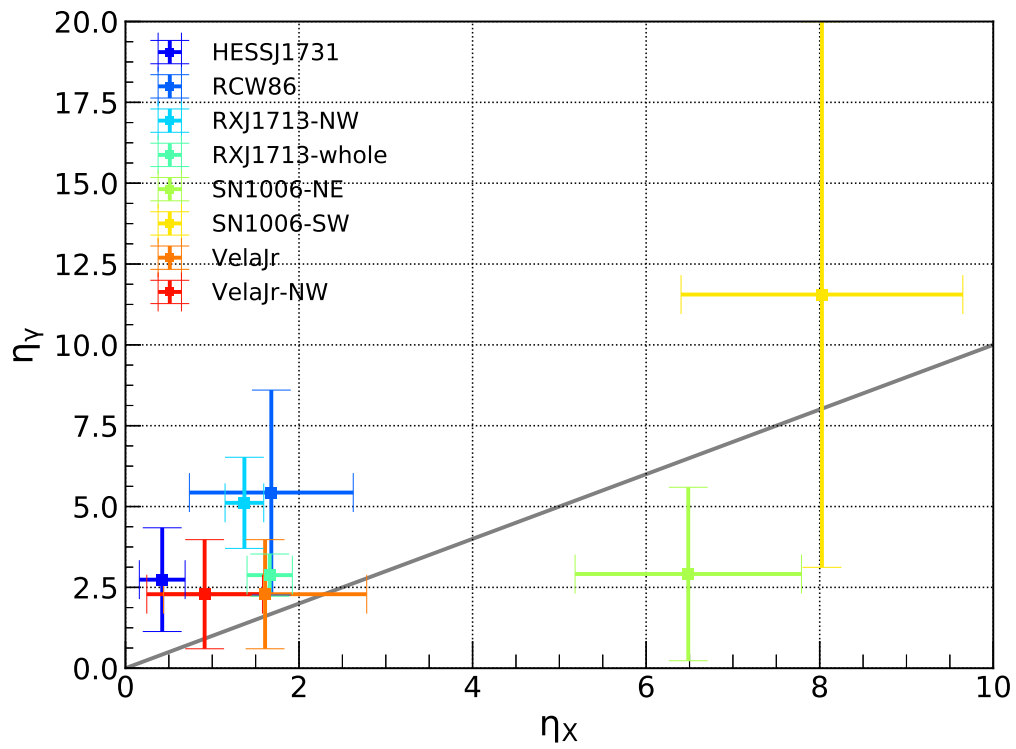


Figure 5.4: Comparison of Bohm factor (η) obtained with X-ray and gamma-ray observations. The grey line indicates $\eta_X = \eta_\gamma$.

Chapter 6

Non-Bohm diffusion

6.1 Introduction

Cosmic rays diffusively travel in space. This motion is characterized by a diffusion coefficient (D), which is in general described as

$$D(E) = k_0 D_{\text{Bohm}}(E_c) \left(\frac{E}{E_c} \right)^\alpha. \quad (6.1)$$

Here α indicates energy dependence on the diffusion coefficient, and D is the product of a constant k_0 and the Bohm-limit diffusion coefficient at characteristic energy of $E = E_c$. The coefficient of Bohm-limit diffusion is described with

$$D_{\text{Bohm}}(E) = \frac{1}{3} cr_g = \frac{1}{3} \frac{cE}{qB}. \quad (6.2)$$

In the interstellar medium, the diffusion coefficient is constrained to be $\sim 10^{28} \text{ cm}^2 \text{ s}^{-1}$ at 10 GeV with $\alpha = 1/3$, inferred from the observations of CR B/C ratio (e.g., The AMS Collaboration (2016)). The diffusion coefficient of ISM is shown in Figure 6.1. Recent measurements of multi-TeV gamma-rays with Water Cherenkov Detector, High-Altitude Water Cherenkov (HAWC), placed a new constraint on the diffusion coefficient of CRs. They detected multi-TeV gamma-ray diffuse emissions (referred to as “TeV halo”), that are spatially extended up to the radii of 20 pc, around two nearby pulsars, Geminga and PSR B0656+14 (Abeysekara et al., 2017). This implies that the diffusion coefficient is required to be $\sim 5 \times 10^{27} \text{ cm}^2 \text{ s}^{-1}$ at 100 TeV assuming $\alpha = 1/3$ to explain these extended sources. It turned out that the diffusion coefficient of these TeV halos is about two orders of magnitude lower than that of ISM, which suggested CRs accelerated in the pulsars are confined in the TeV-halo regions. The discovery of the TeV halos drew attention to the diffusion of CRs and encouraged theoretical studies to reproduce the lower diffusion coefficient in the TeV halo: a two-zone model of the diffusion coefficient, for example, has been proposed (Tang and Piran, 2019).

At the acceleration site (or in DSA), Bohm diffusion ($\alpha = 1$) is widely accepted. In Bohm diffusion, the coefficient is given by the product of Bohm factor η and Bohm-limit diffusion coefficient (Equation 6.2). In order for a particle to get accelerated up to at least the TeV range in a typical lifetime of young SNRs (a few thousand years), the mean free path of the particle should be as large as its gyroradius ($\eta \approx 1$). In fact, numerical calculations successfully produced Bohm-like ($\alpha = 1$) diffusion coefficient (Caprioli and Spitkovsky, 2014c). The Bohm diffusion coefficient is much lower than that of ISM and the TeV halo detected by HAWC, as shown in Figure 6.1. The CR diffusion coefficient changes not only its absolute value (k_0) but also its energy dependency (α) as cosmic rays transit from being accelerated in the sources to propagating in the ISM. The validity of Bohm diffusion in the acceleration site, however, has barely been demonstrated. Especially non-Bohm type diffusion (i.e., $\alpha \neq 1$) should be observationally tested. It is technically too difficult to simulate realistic situations including an accurate treatment of both MHD shock waves and individual relativistic particles. The results in Caprioli and Spitkovsky (2014c) were, therefore, limited to mildly relativistic particles. Observational constraints on the diffusion coefficient of particles, especially, in the relativistic regime are desired. The energy

dependence on the diffusion coefficient (α) is related to the wave spectrum described with $W(k) \propto k^{-p}$ as $\alpha = 2 - p$ (see also Section 2.4.1 and Table 6.1). Since the mechanism of turbulent generation is not fully understood with theoretical studies, it is meaningful to put observational constraints.

In this chapter, we explore arbitrary (non-Bohm) diffusion cases with arbitrary α parameters. Note that the case of Bohm diffusion was presented in Chapter 4 and Chapter 5. In Section 6.2, we investigate the model of electrons on the assumption of the non-Bohm diffusion regimes. We also derive the corresponding radiation models of synchrotron X-ray and IC gamma-ray. The applications to nonthermal X-ray and gamma-ray observations of young SNRs are presented in Section 6.3 and Section 6.4, respectively.

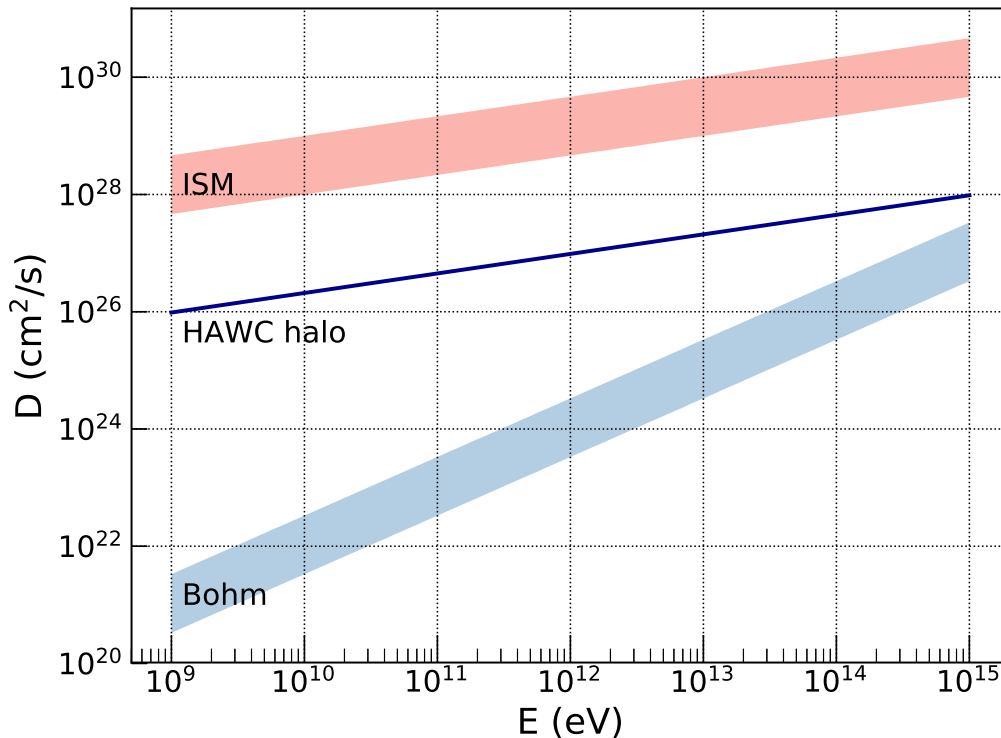


Figure 6.1: Diffusion coefficient of CRs. For the value in the ISM, see, e.g., Yüksel et al. (2009); Adriani et al. (2014). The value of the HAWC halo is taken from Abeysekara et al. (2017). Bohm diffusion is shown with $B = 10\text{--}100 \mu\text{G}$.

Table 6.1: Diffusion coefficient and turbulent wave spectrum

	α	p †	Cooling-limit	Age-limit	Escape-limit
			β ‡	β ‡	β ‡
Bohm	1	1	2	2	1
Kolmogorov	1/3	5/3	4/3	2/3	1/3
Kraichnan	1/2	3/2	3/2	1	1/2
Wave dumping due to ion-neutral collision	≈ 2	0	3	4	2
Constant	0	2	1	0	0

† Diffusion coefficient ($D \propto E^\alpha$) and wave spectrum ($E_k \propto k^{-p}$) are related as $\alpha = 2 - p$.

‡ Electron spectrum ($dN_e/dE \propto \exp(-E^\beta)$) is related to diffusion coefficient as $\beta = \alpha + 1$ in synchrotron-cooling-limited case, $\beta = 2\alpha$ in age-limited case, and $\beta = \alpha$ in escape-limited case.

6.2 Model

In Section 2.6, the analytical expression of electrons around the SNR shock wave in Bohm diffusion is derived. Here the calculation is expanded to non-Bohm diffusion regimes.

6.2.1 Electron

In Section 2.6, we present the electron distribution at the shock front (N_0 ; Equation 2.97), upstream ($F_1(p)$; Equation 2.98), and downstream ($F_2(p)$; Equation 2.99). Here we recall these equations:

$$N_0 \propto \sqrt{\frac{b}{p}} \exp \left[-\frac{\gamma_s^2}{u_1^2} \left(1 + \frac{1}{\sqrt{\xi \kappa}} \right)^2 \int_0^p \frac{dp'}{p'^2} b(p') D(p') \right], \quad (6.3)$$

$$F_1(p) = \frac{\xi}{1 + \sqrt{\kappa \xi}} \frac{u_1 p}{\gamma_s b(p)} N_0(p), \quad (6.4)$$

$$F_2(p) = \frac{\sqrt{\kappa \xi}}{1 + \sqrt{\kappa \xi}} \frac{u_1 p}{\gamma_s b(p)} N_0(p). \quad (6.5)$$

Equation 6.3, Equation 6.4, and Equation 6.5 represent the general spectral forms in the higher energies which particles effectively lose their energies. In the lower energies, since the energy loss is negligible, the particles are simply distributed in the power-law form. Note that one should perform numerical calculations to obtain the transition between the lower and higher energies. This is beyond the scope of this thesis, and the results of numerical calculations are taken from Zirakashvili and Aharonian (2007) and Blasi (2010).

Spectrum in full-energy band

In the lower energies, the particle distribution that is not cooled by synchrotron radiation can be predicted from the standard DSA:

$$N_0 \propto p^{-\gamma_s}, \quad (6.6)$$

$$F_{1,2} \propto p^{-(\gamma_s+1)}, \quad (6.7)$$

where a spectral index is $\gamma_s = 3\sigma/(\sigma - 1) = 4$ for a strong shock with a compression ratio of $\sigma = 4$. In the higher energies, the synchrotron cooling becomes non-negligible. Now we apply the arbitrary diffusion for $D(p)$ (Equation 6.1 for $p = E/c$) and synchrotron cooling for $b(p)$ (Equation 2.101) to the general expression given by Equation 6.3, then we obtain

$$N_0 \propto p^{\frac{1}{2}} \exp \left[-\left(\frac{p}{p_0} \right)^{\alpha+1} \right], \quad (6.8)$$

where a cutoff energy parameter, p_0 , is described as

$$p_0 = \left[\frac{\gamma_s^2}{u_1^2} \left(1 + \frac{1}{\sqrt{\kappa \xi}} \right)^2 \frac{4q^3}{27m^4 c^4} \frac{1}{\beta} k_0 B p_c^2 \right]^{-\frac{1}{\beta}} p_c. \quad (6.9)$$

Note that energy E and momentum p can be replaced by $E = pc$. In Equation 6.8, we derive an important relation between the energy dependence on the diffusion coefficient (α) and the cutoff energy slope of the electron spectrum in the higher energies (β):

$$\beta = \alpha + 1. \quad (6.10)$$

The exponential cutoff form of the electron spectrum deviates from a simple form such as $\exp(-p)$ unless we assume the non-energy-dependent diffusion coefficient with $\alpha = 0$. It should be noted that the cutoff form appears sharper than the simple cutoff (i.e., $\exp(-p^\beta)$ with $\beta > 1$ for $\alpha > 0$). We also note that Equation 6.10

is valid for the cooling-limited case, whereas $\beta = 2\alpha$ in the age-limited case (Kang et al., 2009) and $\beta = \alpha$ in the escape-limited case (Ohira et al., 2010).

In the entire energy band, the asymptotic expression of the electron spectrum is given by

$$N_0 \propto p^{-4} \left[1 + a \left(\frac{p}{p_0} \right)^b \right]^c \exp \left[- \left(\frac{p}{p_0} \right)^\beta \right], \quad (6.11)$$

where a , b , and c are constant parameters. The transition function, $T(p) = \left[1 + a \left(\frac{p}{p_0} \right)^b \right]^c$, is determined by performing a numerical calculation of diffusion-convection equation (Equation 2.88) and requiring a smooth connection between the lower and higher energy bands. In the higher energies ($p \gg p_0$) in Equation 6.11, N_0 becomes proportional to $p^{-4+bc} \exp(-p^\beta)$. This should be identical to the solution in the higher energies given by Equation 6.8, then we obtain the condition of $bc = 9/2$.

Zirakashvili and Aharonian (2007) obtained the analytical expression in the case of Bohm diffusion, as presented in Section 2.6. Blasi (2010) also derived the electron spectrum in the same framework that assumes injection of accelerated electrons in the shock front, the energy loss due to synchrotron emission, and the diffusion in the arbitrary regime. Although the method in Blasi (2010) somewhat differs from Zirakashvili and Aharonian (2007) at a point of its semi-analytically solving the diffusion convection equation, their results are consistent. In addition to Bohm diffusion, Blasi (2010) calculated the cases of constant and Kolmogorov diffusion with α of 0 and 1/3, respectively. The parameters of the transition function (a , b , c) are listed in Table 6.2, and the model spectra in those diffusion cases are shown in Figure 6.2. It is clear that the difference of α appears in the higher energies (i.e., the smaller α is, the flatter the spectrum becomes). Therefore the precise measurement of the spectral shape in the higher energies would distinguish the α parameter.

Cutoff energy parameter of electron

In Equation 6.9, let us suppose that the characteristic energy p_c , which determines the diffusion coefficient, is comparable to p_0 . Note the choice of p_c is completely arbitrary, and the assumption of $p_c = p_0$ means one can estimate the value of the diffusion coefficient at the cutoff energy parameter of the electron. We define Π as the product of the electron cutoff energy parameter and square-root magnetic field: $\Pi = cp_0\sqrt{B}$. Governing $p_c = p_0$ in Equation 6.9 gives

$$\Pi_0(\beta, k_0, u_1) = \beta^{\frac{1}{2}} \left[\gamma_s^2 \left(1 + \frac{1}{\sqrt{\kappa\xi}} \right)^2 \frac{4q^3}{27m^4c^4} \right]^{-\frac{1}{2}} k_0^{-\frac{1}{2}} u_1. \quad (6.12)$$

Equation 6.12 is indicative of the cutoff parameter of the electron limited by synchrotron cooling and arbitrary diffusion.

Table 6.2: Model spectral parameters of electron, synchrotron radiation, and inverse Compton scattering.

	α	β	a	b	c	β_X	a	b	c	β_γ	a	b	c
	electron					synchrotron				IC [†]			
Bohm	1	2	0.523	9/4	2	1/2	0.38	0.5	11/4	1/2	0.31	0.6	25/8
Constant	0	1	0.28	1.1	4.1	1/3	0.25	0.37	4.5	1/3	0.18	0.40	5.4
Kolmogorov	1/3	4/3	0.40	1.6	2.8	2/5	0.33	0.45	3.4	2/5	0.24	0.49	4.2

Bohm case is presented in Zirakashvili and Aharonian (2007). Constant and Kolmogorov cases are presented in Blasi (2010).

[†] Calculated in Thomson limit (see Appendix D.2).

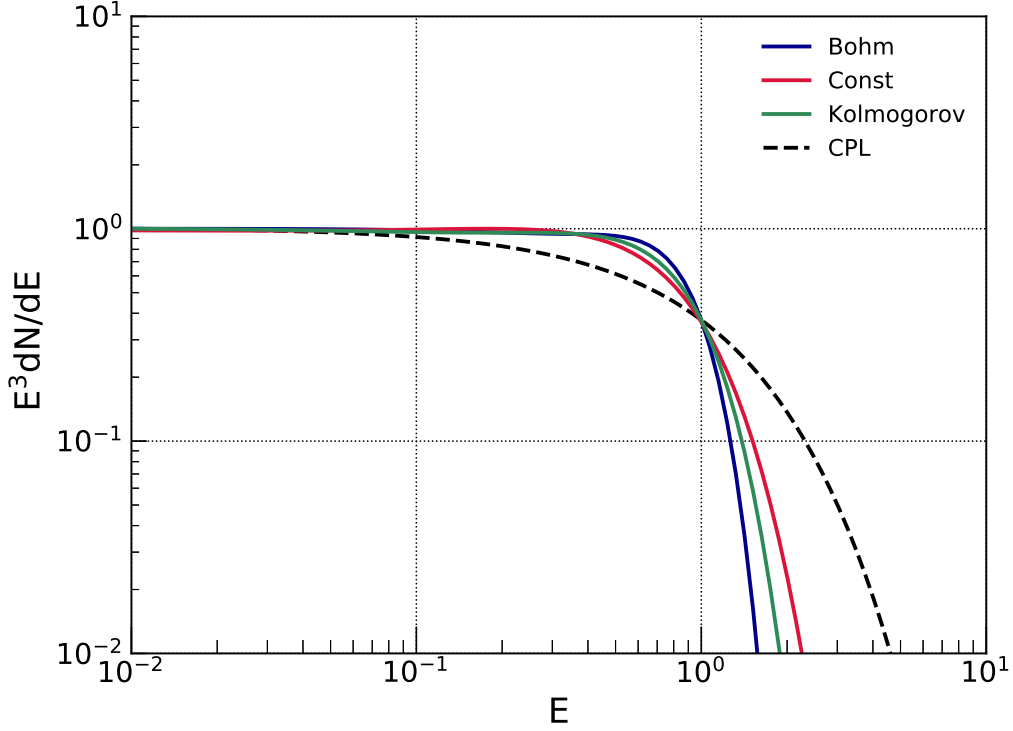


Figure 6.2: The electron spectrum limited by the synchrotron-cooling and non-Bohm diffusion regime. The x-axis is normalized by the cutoff energy which gives a e^{-1} drop.

6.2.2 Synchrotron X-ray

This section presents the synchrotron X-ray model radiated from electrons limited by the arbitrary (non-Bohm) diffusion regime and synchrotron cooling, as described in Section 6.2.1. In the lower energy band, the synchrotron photon spectrum is distributed in the power-law form:

$$\frac{dN_X}{d\varepsilon} \propto \varepsilon^{-\frac{\gamma_s}{2}}, \quad (6.13)$$

since it is radiated from the electron in the lower energies: $F(p) \propto p^{-(\gamma_s+1)}$. In the higher energy band, the synchrotron spectrum is radiated from the electron in the higher energies, which is distributed in the cutoff power-law form (Equation 6.8). Recalling Section 2.6, the synchrotron X-ray spectrum, which is radiated from the cutoff power-law distribution of electrons with a spectral index of s , cutoff energy of E_c , and cutoff slope of β , is described as

$$\frac{dN_X}{d\varepsilon} \propto \varepsilon^{-\frac{2s+3\beta-2}{2(\beta+2)}} \exp \left[- \left(\frac{\varepsilon}{\varepsilon_0} \right)^{\beta_X} \right]. \quad (6.14)$$

Here the cutoff shape slope of the X-ray spectrum (β_X) is given by $\beta_X = \beta/(\beta + 2)$. Because the electron spectrum at the shock front in the higher energies is obtained to be Equation 6.8, and the integrated spectrum $F(p)$ is described with $F(p) \propto N_0 p^{-1} \propto p^{-1/2}$, applying the spectral index of $s = 1/2$ to Equation 6.14, the photon spectrum is obtained:

$$\frac{dN_X}{d\varepsilon} \propto \varepsilon^{-\frac{3\beta-1}{2(\beta+2)}} \exp \left[- \left(\frac{\varepsilon}{\varepsilon_0} \right)^{\beta_X} \right]. \quad (6.15)$$

The cutoff energy parameter in the synchrotron X-ray spectrum is described as, recalling Equation 2.114,

$$\varepsilon_0 = \hbar \beta \left[4 \left(\frac{1}{2 + \beta} \right)^{2+\beta} \right]^{1/\beta} \frac{3q}{2m^3 c^3} B p_0^2. \quad (6.16)$$

In the entire energy band, the solution can be described with

$$\frac{dN_X}{d\varepsilon} \propto \varepsilon^{-\frac{\gamma_s}{2}} \left[1 + a \left(\frac{\varepsilon}{\varepsilon_0} \right)^b \right]^c \exp \left[- \left(\frac{\varepsilon}{\varepsilon_0} \right)^{\beta_X} \right]. \quad (6.17)$$

The transition function, $\mathcal{T}(\varepsilon) = \left[1 + a \left(\frac{\varepsilon}{\varepsilon_0} \right)^b \right]^c$, is determined by the numerical calculation, requiring the smooth connection between the lower and higher energy bands. In the higher energies ($\varepsilon \gg \varepsilon_0$) in Equation 6.17, $dN_X/d\varepsilon$ becomes $\varepsilon^{-2+bc} \exp(-\varepsilon^{\beta_X})$. This should be compatible with Equation 6.15, so we obtain the condition of $bc = (\beta + 9)/2(\beta + 2)$ for the X-ray spectrum.

In addition to Bohm diffusion, Blasi (2010) calculated the electron spectra in constant and Kolmogorov diffusion with α of 0 and 1/3, respectively. The analytical expressions of the electron spectrum in these cases are presented in Section 6.2.1. We obtain the parameters of the transition function for the synchrotron spectrum (a , b , c) by calculating synchrotron radiation from the electron spectrum described in Section 6.2.1 and fitting with Equation 6.17. The obtained parameters are listed in Table 6.2, and the model spectra in these diffusion regimes are shown in Figure 6.3. The difference of α clearly appears in the higher energies. The smaller α parameter shows the flatter spectrum above $\sim \varepsilon_0$.

Cutoff energy parameter of synchrotron X-ray

The cutoff energy parameter in the synchrotron spectrum is given by Equation 6.16. Substituting the electron cutoff energy (Equation 6.12) gives

$$\varepsilon_0 = \hbar \beta^2 \left[4 \left(\frac{1}{2 + \beta} \right)^{2+\beta} \right]^{1/\beta} \frac{81mc}{8q^2\gamma_s^2} \left(1 + \frac{1}{\sqrt{\kappa\xi}} \right)^{-2} \beta k_0^{-1} u_1^2. \quad (6.18)$$

This equation is the cutoff energy parameter of synchrotron X-ray radiated from electrons limited by synchrotron cooling and arbitrary diffusion. We note $\beta = 2$ (Bohm diffusion) gives the $\varepsilon_0 - v_{sh}$ equation, which was introduced as Equation 4.3 presented in Chapter 4.

6.2.3 Inverse Compton gamma-ray

IC spectrum in Klein-Nishina regime

As mentioned in Section 2.6, since it is too complicated to obtain the analytical expression of IC spectrum in Klein-Nishina regime, we make use of Naima (Zabalza, 2015) to calculate the IC spectrum emitted from the loss-limited electron in the arbitrary diffusion given by Equation 6.11 and Table 6.2. We apply the model to the observed gamma-ray spectrum in the TeV range, in which the effect of KN is not negligible. Thus the inverse Compton model in KN regime is favored in this thesis. The case of Thomson limit is presented in Appendix D.

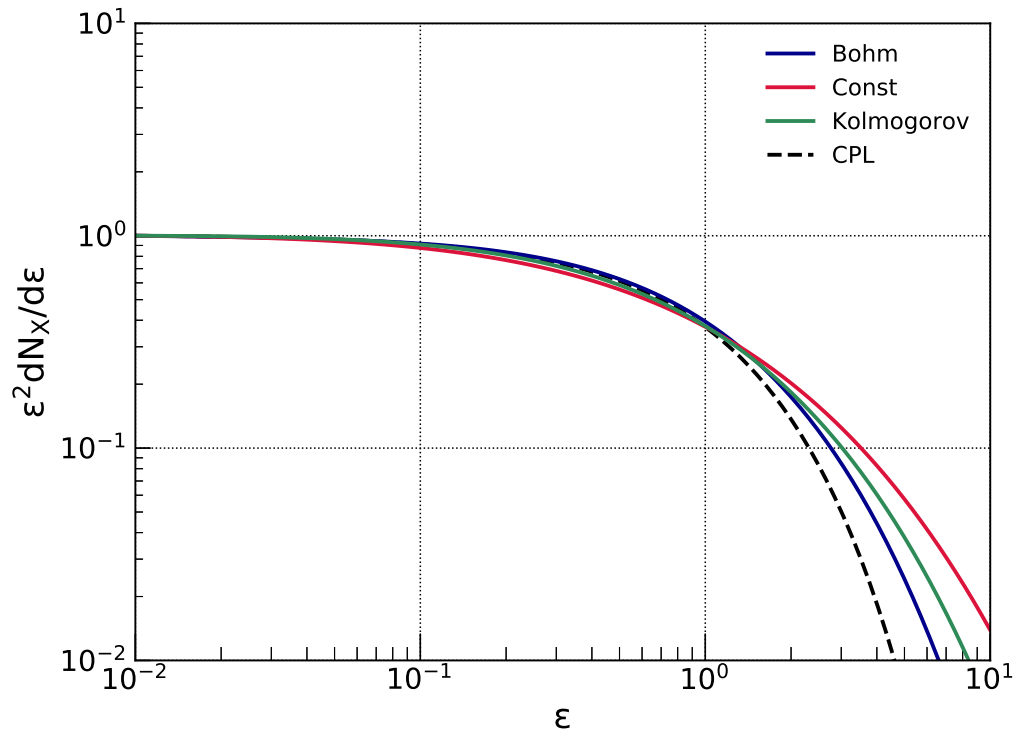


Figure 6.3: The synchrotron X-ray spectrum in non-Bohm diffusion. The x-axis is normalized by the cutoff energy which gives a e^{-1} drop.

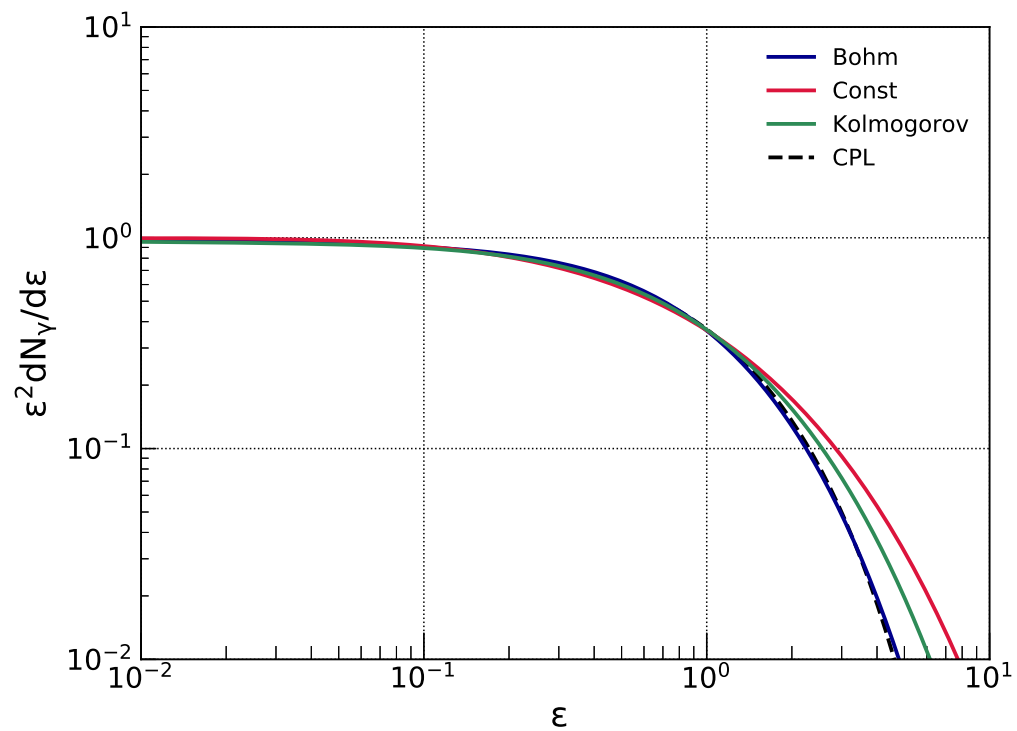


Figure 6.4: The IC gamma-ray spectrum in non-Bohm diffusion and in Klein-Nishina regime, calculated for $E_0 = 1$ TeV. The x-axis is normalized by the cutoff energy which gives a e^{-1} drop.

6.3 Nonthermal X-ray diagnostics

6.3.1 Application to X-ray observations and results

We make use of the same spectra extracted in Chapter 4. To distinguish the different models with the arbitrary α parameters, the broadband spectrum including *NuSTAR* is preferred since the difference appears clear in the higher energy band (Figure 6.3). We apply the model to the following specific regions in the young SNRs: the entire remnant of G1.9+0.3, the northeast and southwest limbs in SN 1006, the NW rim in RX J1713.7–3946, the NE rim in RCW 86, the entire remnant and NW rim in Vela Jr, and the NE rim in HESS J1731–347. They are synchrotron-dominated SNRs and strong TeV gamma-ray emitters (except that G1.9+0.3 is not a gamma-ray emitter).

The model is described as an absorbed synchrotron radiation spectrum from the synchrotron-cooling-limited electron in non-Bohm diffusion regime: the analytical expression of the synchrotron spectrum is described by Equation 6.17 and the parameters of the model are listed in Table 6.2. Note that the synchrotron model contains only two free parameters, the cutoff energy parameter ε_0 and the normalization. The interstellar absorption is taken into account using TBabs model in XSPEC.

Table 6.3: Best-fit parameters of spectral analysis

Model	N_H (10^{22} cm^{-2})	Γ	$\varepsilon_c/\varepsilon_0$ (keV)	β_X	χ^2	dof	Π_0 (TeV $\mu\text{G}^{\frac{1}{2}}$)	k_0
G1.9+0.3 (whole)								
Bohm	6 ± 0.04	–	$1.2^{+0.06}_{-0.05}$	–	902	585	270 ± 6	16 ± 1.4
Constant	6 ± 0.04	–	0.08 (fixed)	–	959	585	71 ± 2	$72^{+6.6}_{-6.4}$
Kolmogorov	6 ± 0.04	–	0.29 ± 0.01	–	915	585	130 ± 3	$34^{+3}_{-2.9}$
PL	6.4 ± 0.05	2.5 ± 0.02	–	–	1301	585		
CPL/Equation 6.19	5.6 ± 0.08	1.7 ± 0.1	$8.3^{+0.76}_{-0.66}$	1 (fixed)	787	584		
Equation 6.19	5.4 ± 0.09	0.8 ± 0.1	$0.58^{+0.11}_{-0.08}$	0.5 (fixed)	775	584		
Equation 6.19	$5.3^{+0.08}_{-0.04}$	<0.001	0.015 ± 0.003	0.3 (fixed)	773	584		
Equation 6.19	5.3 ± 0.09	0.4 ± 0.2	0.1 ± 0.02	0.4 (fixed)	773	584		
SN 1006 (NE; fil1)								
Bohm	0.07 (fixed)	–	0.4 ± 0.01	–	526	407	150 ± 2	6.5 ± 2.6
Constant	0.07 (fixed)	–	0.026 ± 0.001	–	587	407	40 ± 1	29 ± 12
Kolmogorov	0.07 (fixed)	–	0.092 ± 0.002	–	528	407	74 ± 1	14 ± 5.5
PL	0.07 (fixed)	2.5 ± 0.01	–	–	1770	407		
CPL/Equation 6.19	0.07 (fixed)	2.1 ± 0.02	$5.5^{+0.32}_{-0.29}$	1 (fixed)	572	406		
Equation 6.19	0.07 (fixed)	1.6 ± 0.04	$0.66^{+0.073}_{-0.063}$	0.5 (fixed)	505	406		
Equation 6.19	0.07 (fixed)	1.2 ± 0.1	$0.03^{+0.005}_{-0.004}$	0.3 (fixed)	496	406		
Equation 6.19	0.07 (fixed)	1.4 ± 0.1	$0.15^{+0.022}_{-0.018}$	0.4 (fixed)	499	406		
SN 1006 (SW; fil2)								
Bohm	0.07 (fixed)	–	0.32 ± 0.01	–	469	297	140 ± 2	8 ± 3.2
Constant	0.07 (fixed)	–	0.02 ± 0.001	–	519	297	34 ± 1	39 ± 16
Kolmogorov	0.07 (fixed)	–	0.073 ± 0.002	–	479	297	66 ± 1	17 ± 7
PL	0.07 (fixed)	2.6 ± 0.01	–	–	1197	297		
CPL/Equation 6.19	0.07 (fixed)	2.1 ± 0.03	$4.8^{+0.37}_{-0.33}$	1 (fixed)	467	296		
Equation 6.19	0.07 (fixed)	1.6 ± 0.1	$0.5^{+0.08}_{-0.06}$	0.5 (fixed)	471	296		
Equation 6.19	0.07 (fixed)	1 ± 0.1	$0.02^{+0.005}_{-0.004}$	0.3 (fixed)	479	296		
Equation 6.19	0.07 (fixed)	1.3 ± 0.1	0.11 ± 0.02	0.4 (fixed)	476	296		
RX J1713.7–3946 (NW)								
Bohm	0.75 ± 0.01	–	$1.1^{+0.064}_{-0.058}$	–	250	149	260 ± 7	1.4 ± 0.2
Constant	0.76 ± 0.01	–	0.082 ± 0.005	–	241	149	70 ± 2	$5.7^{+1}_{-0.9}$
Kolmogorov	0.75 ± 0.01	–	$0.27^{+0.015}_{-0.014}$	–	247	149	130^{+4}_{-3}	2.9 ± 0.5
PL	0.84 ± 0.01	2.4 ± 0.02	–	–	337	149		
CPL/Equation 6.19	0.78 ± 0.01	2.1 ± 0.04	$19^{+4.2}_{-3}$	1 (fixed)	247	148		
Equation 6.19	0.77 ± 0.02	1.9 ± 0.1	$4.2^{+2.1}_{-1.2}$	0.5 (fixed)	235	148		
Equation 6.19	0.76 ± 0.02	1.6 ± 0.1	$0.35^{+0.26}_{-0.14}$	0.3 (fixed)	233	148		

Table 6.3: Best-fit parameters of spectral analysis (*continued*)

Model	N_H (10^{22} cm $^{-2}$)	Γ	$\varepsilon_c/\varepsilon_0$ (keV)	β_X	χ^2	dof	Π_0 (TeV $\mu\text{G}^{\frac{1}{2}}$)	k_0
Equation 6.19	0.76 ± 0.02	1.8 ± 0.1	$1.4^{+0.79}_{-0.5}$	0.4 (fixed)	234	148		
RCW 86 (NE; NE2)								
Bohm	0.33 (fixed)	–	0.3 ± 0.01	–	467	407	130 ± 2	2.2 ± 1.2
Constant	0.33 (fixed)	–	0.02 (fixed)	–	483	407	33 ± 1	10 ± 5.9
Kolmogorov	0.33 (fixed)	–	0.07 (fixed)	–	470	407	64 ± 1	4.7 ± 2.6
PL	0.33 (fixed)	2.7 ± 0.01	–	–	677	407		
CPL/Equation 6.19	0.33 (fixed)	2.1 ± 0.07	$3.9^{+0.53}_{-0.42}$	1 (fixed)	470	406		
Equation 6.19	0.33 (fixed)	1.5 ± 0.1	$0.38^{+0.1}_{-0.08}$	0.5 (fixed)	460	406		
Equation 6.19	0.33 (fixed)	$0.9^{+0.2}_{-0.3}$	0.014 ± 0.005	0.3 (fixed)	458	406		
Equation 6.19	0.33 (fixed)	1.2 ± 0.2	$0.08^{+0.03}_{-0.02}$	0.4 (fixed)	459	406		
Vela Jr. (NW)								
Bohm	0.67 (fixed)	–	$0.55^{+0.04}_{-0.036}$	–	138	122	180^{+7}_{-6}	0.9 ± 0.7
Constant	0.67 (fixed)	–	0.032 ± 0.003	–	134	122	44 ± 2	4.7 ± 3.4
Kolmogorov	0.67 (fixed)	–	$0.12^{+0.01}_{-0.009}$	–	136	122	86 ± 3	2 ± 1.5
PL	0.67 (fixed)	2.7 ± 0.04	–	–	183	122		
CPL/Equation 6.19	0.67 (fixed)	2.3 ± 0.1	$11^{+3.8}_{-2.3}$	1 (fixed)	132	121		
Equation 6.19	0.67 (fixed)	1.9 ± 0.2	$1.7^{+1.3}_{-0.62}$	0.5 (fixed)	133	121		
Equation 6.19	0.67 (fixed)	1.5 ± 0.3	$0.08^{+0.13}_{-0.036}$	0.3 (fixed)	134	121		
Equation 6.19	0.67 (fixed)	$1.7^{+0.2}_{-0.3}$	$0.44^{+0.42}_{-0.2}$	0.4 (fixed)	134	121		
Vela Jr. (whole †)								
Bohm	0.67 (fixed)	–	0.31 ± 0.008	–	509	265	140 ± 2	1.6 ± 1.2
Constant	0.67 (fixed)	–	0.017 ± 0.001	–	454	265	32 ± 1	8.7 ± 6.4
Kolmogorov	0.67 (fixed)	–	0.069 ± 0.002	–	486	265	64 ± 1	3.6 ± 2.6
PL	0.67 (fixed)	2.9 ± 0.02	–	–	370	265		
HESS J1731–347 (whole †)								
Bohm	1 (fixed)	–	$0.97^{+0.46}_{-0.26}$	–	102	86	240^{+57}_{-32}	$0.42^{+0.47}_{-0.44}$
Constant	1 (fixed)	–	$0.073^{+0.041}_{-0.022}$	–	101	86	66^{+19}_{-10}	$1.7^{+1.9}_{-1.7}$
Kolmogorov	1 (fixed)	–	$0.23^{+0.11}_{-0.061}$	–	102	86	120^{+27}_{-16}	$0.89^{+0.98}_{-0.92}$
PL	1 (fixed)	2.3 ± 0.08	–	–	98	86		
CPL/Equation 6.19	1 (fixed)	$2.3^{+0.08}_{-0.16}$	>20	1 (fixed)	98	85		

 † The spectra are hardly fitted by Equation 6.19 with fixed β_X .

The best-fit parameters are listed in Table 6.3, and the spectra are presented in Figure 6.5 with the best-fit models. Figure 6.6 shows the best-fit values of ε_0 and χ^2 of each model. The cutoff energy parameter (ε_0) is obtained to be variable with different models. For instance in RX J1713.7–3946-NW, it is 1.1, 0.27, and 0.082 keV in Bohm, Kolmogorov, and constant diffusion models, respectively. It should be noted that ε_0 does not give exact cutoff energy (ε_c) which deviates from the power law by e^{-1} , because of the transition function in addition to the cutoff power-law form (Equation 6.17). As mentioned in Zirakashvili and Aharonian (2007), the cutoff energy ε_c is about one order of magnitude larger than ε_0 in Bohm diffusion. Our analysis shows that $\varepsilon_c/\varepsilon_0 \sim 17$ for Bohm diffusion in the NW of RX J1713.7–3946. In Figure 6.6, we also show 1σ , 90%, and 3σ confidence levels compared to the best synchrotron model that gives the smallest chi-squared value. For the NW of RX J1713.7–3946, the NW rim of Vela Jr., and the NE rim of HESS J1731–347, the χ^2 values of the three models (Bohm, Kolmogorov, and constant diffusion) are comparable and cannot be distinguished at 3σ confidence level. For G1.9+0.3 and the NE limb of SN 1006, however, the Bohm diffusion model is the most favored, and the constant diffusion model is rejected at 3σ . Even the Kolmogorov model is also excluded at 3σ in G1.9+0.3. Although the chi-squared value itself might imply that the Bohm model is the best, the differences of the three diffusion models appear prominent in the higher energy band above ~ 30 keV (Figure 6.5). The more accurate measurement of the cutoff shape, by deeper observations with *NuSTAR* or the next X-ray satellite such as *FORCE* and *Athena*, is necessary to distinguish the models more confidently.

In addition to the physical model derived in Section 6.2, we fit the spectrum with a power law with

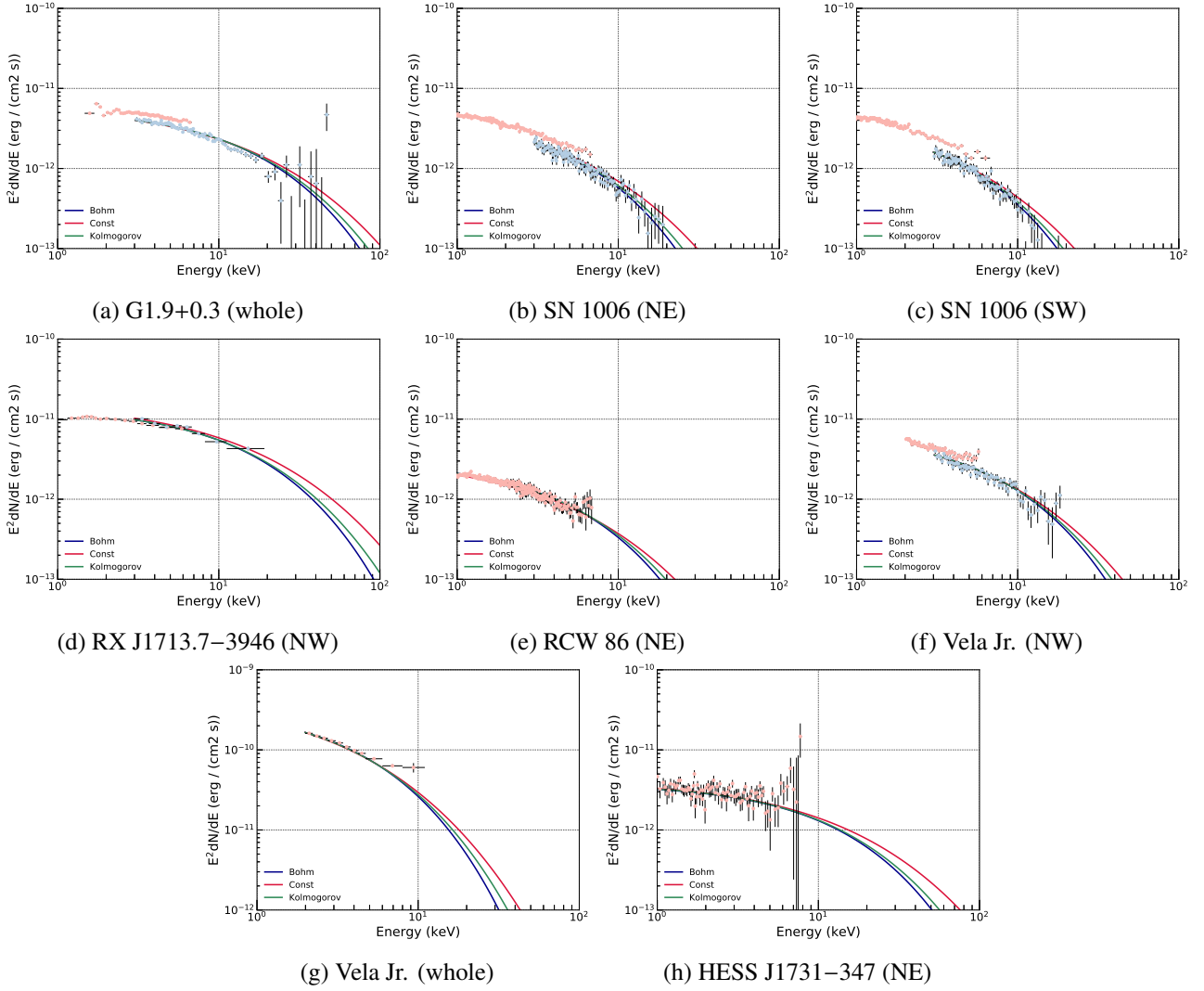


Figure 6.5: The unfolded and absorption-corrected X-ray spectra. The pink and light-blue plots respectively indicate the *Chandra* and *NuSTAR* spectra (except for the entire spectrum of Vela Jr. taken with *Suzaku* provided by Fukuyama et al. (2019)). Note that the spectra are jointly fitted by setting the spectral shape tied and only the normalization free. The best-fit models here are shown to match the *NuSTAR* spectra (or the *Chandra* spectra if no *NuSTAR* observations are available).

super-exponential cutoff that is given by

$$\frac{dN_X}{d\varepsilon} = K\varepsilon^{-\Gamma} \exp \left[- \left(\frac{\varepsilon}{\varepsilon_c} \right)^{\beta_X} \right]. \quad (6.19)$$

Here the normalization K , the photon index Γ , and the cutoff energy ε_c are set to be free, while the cutoff shape slope β_X is fixed as follows. We remind that the cutoff slope of the synchrotron X-ray spectrum (β_X) is determined by the cutoff slope of the electron spectrum (β): $\beta_X = \beta/(\beta+2)$. Therefore β_X should be less than 1. When setting the β_X parameter free in Equation 6.19, the smallest χ^2 value is sometimes obtained with $\beta_X > 1$. Since the case of $\beta_X > 1$ is not physical, we fix β_X to be 1/2, 2/5, and 1/3, which correspond to the cutoff slope of Bohm, Kolmogorov, and constant diffusion, respectively. We also use a power-law (powerlaw; PL in XSPEC) model and a conventional cutoff power-law model (cutoffpl; CPL), which the same as Equation 6.19 for $\beta_X = 1$.

The best-fit parameters with the conventional models (PL, CPL, and Equation 6.19 with fixed $\beta_X = 1/2, 1/3, 2/5$) are also shown in Table 6.3. The power law is confidently excluded for all the spectra. Some

SNRs showed that the photon index derived with Equation 6.19 significantly deviates from 2, which is expected for the synchrotron-cooling-limited electron. In G1.9+0.3, although the models given by Equation 6.19 are favored than those of the physical models at over 3σ confidence level, inferred from F-test, the photon indices derived with Equation 6.19 indicate unrealistic values such as $\Gamma \leq 1$. The northeast limb in SN 1006 also prefers to Equation 6.19 than the physical models. For the other SNRs, the differences in the simple cutoff power-law and physical models are not significant, inferred from F-test.

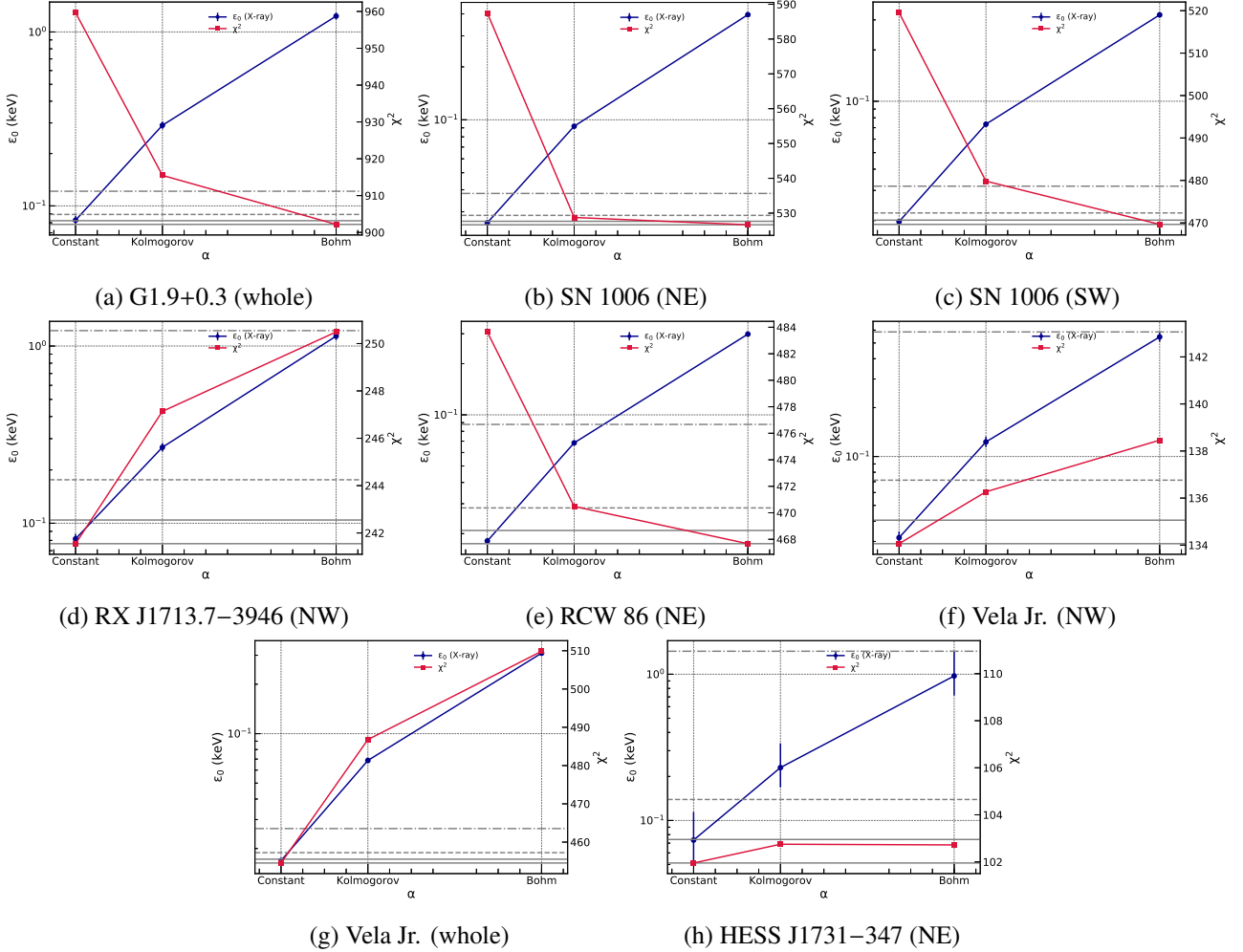


Figure 6.6: Best-fit parameters of ε_0 (in blue) and χ^2 (red). The horizontal lines indicate the minimum χ^2 , 1σ , 90%, and 3σ significances from the bottom.

6.3.2 Discussion: Estimation of diffusion coefficient

We obtained the cutoff energy parameter with each diffusion model from the spectral fitting. This ε_0 value is used to estimate the diffusion coefficient, combined with the shock velocity. The diffusion coefficient, written as Equation 6.1, is determined by k_0 and E_c (that is assumed to be equal to E_0 here) for a certain α . Equation 6.18 leads us to

$$k_0 = \hbar\beta^2 \left[4 \left(\frac{1}{2+\beta} \right)^{2+\beta} \right]^{1/\beta} \frac{81mc}{8q^2\gamma_s^2} \left(1 + \frac{1}{\sqrt{k\xi}} \right)^{-2} \beta\varepsilon_0^{-1} u_1^2. \quad (6.20)$$

Furthermore from Equation 6.16, we derive $\Pi_0 = E_0 B^{1/2}$:

$$\Pi_0 = \left[4 \left(\frac{1}{2 + \beta} \right)^{2 + \beta} \right]^{-1/2\beta} \left(\frac{2m^3 c^5}{3q\hbar\beta} \right)^{1/2} \varepsilon_0^{1/2}. \quad (6.21)$$

In summary, we make use of Equation 6.20 and Equation 6.21 to estimate respectively k_0 and Π_0 which are the characteristic parameters to determine the diffusion coefficient. The obtained k_0 and Π_0 are listed in Table 6.3 and plotted in Figure 6.7.

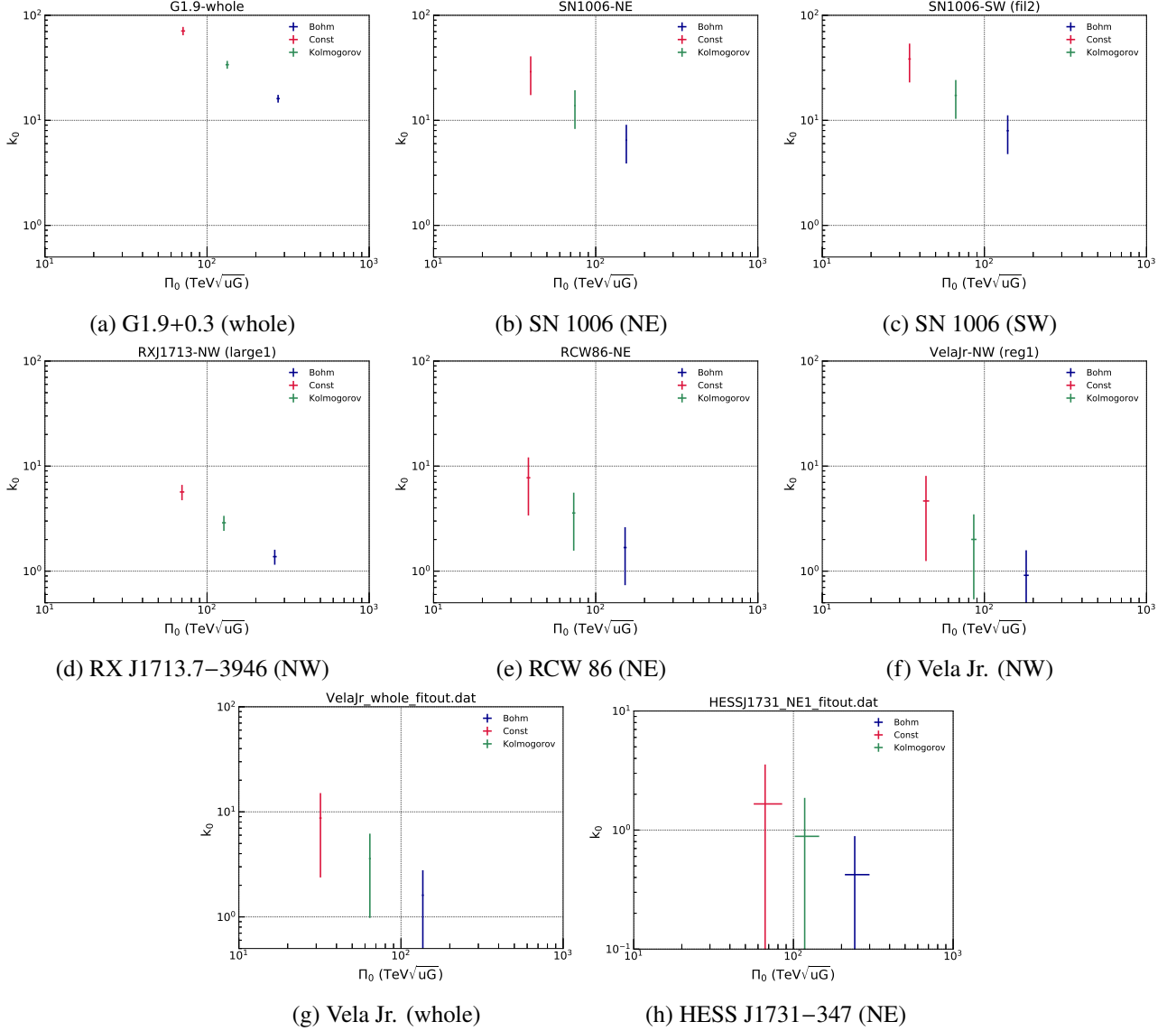


Figure 6.7: Best-fit parameters of k_0 and Π_0

We finally constrain the diffusion coefficient by the estimated k_0 and Π_0 , assuming a certain value of B . Given the magnetic field strength in the literature (see Chapter 5 for details), the diffusion coefficients with $\alpha = 1, 1/3$, and 0 are shown in Figure 6.8. Although we independently estimate the diffusion coefficients in Bohm, Kolmogorov, and constant diffusion cases, they are overlapping in a small region. This region is hereafter referred to as the characteristic range with energy of E_{ch} and diffusion coefficient of D_{ch} . For example, E_{ch} is ~ 100 TeV and D_{ch} is $3 \times 10^{26} \text{ cm}^2 \text{ s}^{-1}$ in RX J1713.7–3946 NW with $B = 15 \mu\text{G}$. In spite of the insignificant determination of the best model by the χ^2 test, we could constrain D_{ch} at $E = E_{\text{ch}}$ that is independent of the model (i.e., the α parameter).

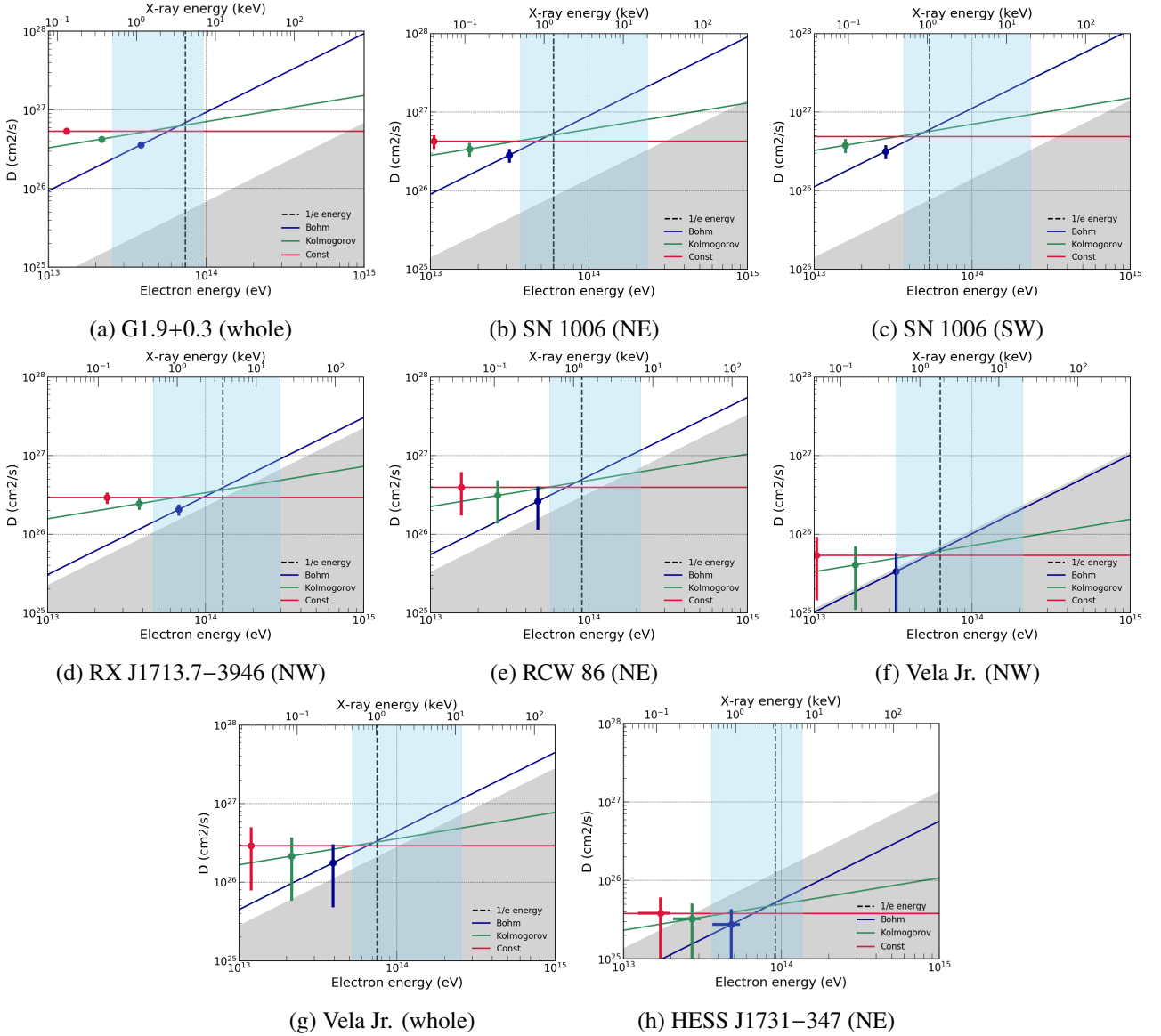


Figure 6.8: The constrained diffusion coefficient in arbitrary diffusion regimes. The scatter plots show the values of E_c and $D(E_c)$. The blue, green, and red lines show Bohm, Kolmogorov, and constant diffusions, respectively. The grey and light-blue regions indicate the range with $D \leq D_{\text{Bohm}}$ and the observed X-ray band, respectively.

Dividing Equation 6.1 by D_{Bohm} and replacing E by $\Pi = EB^{1/2}$, we obtain

$$\frac{D(E)}{D_{\text{Bohm}}(E)} = k_0 \left(\frac{\Pi}{\Pi_0} \right)^{\alpha-1}. \quad (6.22)$$

It should be emphasized that Equation 6.22 can be calculated from the observations without determining the value of the magnetic field. Equation 6.22 in the cases of $\alpha = 1$, $1/3$, and 0 is presented in Figure 6.9.

Here we consider a simple condition: the diffusion coefficient should be greater than Bohm limit. In Figure 6.8 and Figure 6.9, the diffusion coefficient smaller than Bohm limit is shown with the grey band, which is inconsistent with the condition. In the upper x -axis of these figures, we show the characteristic synchrotron energy corresponding to the electron in the lower x -axis. The condition should be satisfied at least in the energy bands which we are observing with *Chandra* (0.5–7 keV) and *NuSTAR* (from 3 to 20–50 keV). For example, in G1.9+0.3 and SN 1006, all the models (Bohm, Kolmogorov, and constant diffusion) show the

diffusion coefficient with an order of magnitude larger than Bohm limit, resulting in that the condition is always fulfilled in the *Chandra* + *NuSTAR* energy bands. On the other hand, in RX J1713.7–3946, Vela Jr., and HESS J1731–347, the diffusion coefficient of Kolmogorov and constant diffusion models appear smaller than Bohm limit in the observed energy bands, in particular, the *NuSTAR* channel. We propose two scenarios for the latter case. 1.) Bohm-type diffusion is acceptable to be consistent with the condition, and 2.) the diffusion coefficient has a break (up-turn) structure around E_{ch} ; it follows Kolmogorov or constant diffusion regimes at $E \leq E_{\text{ch}}$ and Bohm diffusion at $E \geq E_{\text{ch}}$. The broken power-law diffusion has not been considered before. Although it might be interesting to calculate and discuss the case of the diffusion coefficient with a break, this is beyond the scope of the thesis.

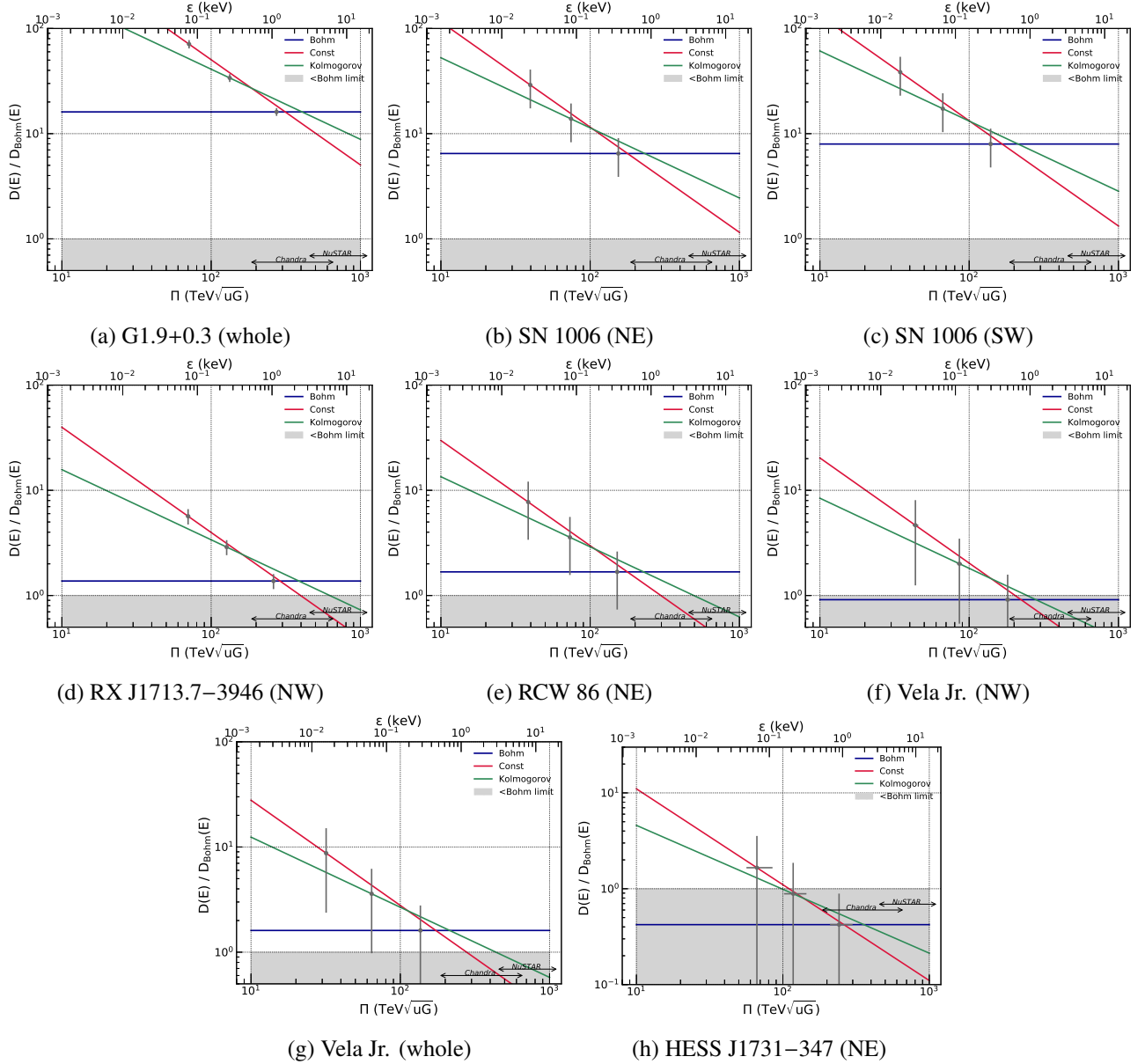


Figure 6.9: Diffusion coefficient over Bohm limit (Equation 6.22). The red, green, and blue lines show Bohm, Kolmogorov, and constant diffusion, respectively. The best-fit k_0 and Π_0 are also plotted with grey markers.

6.4 Nonthermal gamma-ray diagnostics

6.4.1 Application to gamma-ray observations and results

We apply our model to five TeV gamma-ray emitting SNRs: SN 1006, RX J1713.7–3946, RCW 86, Vela Jr., and HESS J1731–347, presented in Chapter 5. We utilize the IC model radiated from the electron that is limited by synchrotron cooling and non-Bohm diffusion, described with Equation 6.11. Naima (Zabalza, 2015) is used to calculate IC radiation including the Klein-Nishina effect. Note that we obtain directly the cutoff energy parameter of electron (E_0) with KN-regime model. The spectra with the best-fit models are shown in Figure 6.10, and the best-fit parameters are listed in Table 6.4. We assume that the target photon is only CMB with the temperature (T) of 2.72 K and the energy density of 0.261 eV cm^{-3} .

Table 6.4: The best-fit parameters with IC model in KN regime

Name	Model	E_0 (TeV)	W_e (10^{45} erg)	B (μG)	v_{sh} (km s^{-1})	η_γ/k_0	χ^2	dof
SN 1006 (NE)	Bohm	47^{+31}_{-11}	24 ± 2	24.0	5000 ± 1000	$2.9^{+4.0}_{-3.8}$	9.6	11
SN 1006 (NE)	Kolmogorov	$27^{+7.5}_{-8.3}$	25^{+2}_{-3}	24.0	5000 ± 1000	$5.7^{+3.8}_{-4.1}$	9.8	11
SN 1006 (NE)	Constant	$21^{+9.7}_{-3.7}$	24 ± 2	24.0	5000 ± 1000	$7.2^{+7.3}_{-3.9}$	9.6	11
SN 1006 (SW)	Bohm	24^{+10}_{-6}	16 ± 3	24.0	5000 ± 1000	$12^{+11}_{-7.5}$	10.6	4
SN 1006 (SW)	Kolmogorov	$18^{+14}_{-4.2}$	15 ± 3	24.0	5000 ± 1000	$13^{+21}_{-8.2}$	10.4	4
SN 1006 (SW)	Constant	$12^{+4.4}_{-2.5}$	15 ± 3	24.0	5000 ± 1000	24^{+21}_{-14}	10.6	4
RX J1713.7–3946 (whole)	Bohm	48^{+4}_{-3}	360^{+7}_{-8}	15.0	3900 ± 300	$2.7^{+0.7}_{-0.6}$	45.9	26
RX J1713.7–3946 (whole)	Kolmogorov	$31^{+2.1}_{-2.4}$	360 ± 7	15.0	3900 ± 300	$4.5^{+0.9}_{-1.0}$	41.6	26
RX J1713.7–3946 (whole)	Constant	$21^{+1.8}_{-1.6}$	350 ± 7	15.0	3900 ± 300	$7.3^{+1.7}_{-1.6}$	38.4	26
RX J1713.7–3946 (NW)	Bohm	35^{+5}_{-4}	25 ± 1	15.0	3900 ± 300	$5.2^{+1.6}_{-1.4}$	34.7	23
RX J1713.7–3946 (NW)	Kolmogorov	$22^{+2.2}_{-2.4}$	24 ± 1	15.0	3900 ± 300	$8.4^{+2.1}_{-2.3}$	34.2	23
RX J1713.7–3946 (NW)	Constant	$15^{+2.4}_{-1.6}$	24 ± 1	15.0	3900 ± 300	14^{+5}_{-4}	34.5	23
RCW 86 (whole)	Bohm	26 ± 2	440^{+25}_{-28}	10.2	2500 ± 700	5.4 ± 3.2	30.5	18
RCW 86 (whole)	Kolmogorov	$15^{+1.4}_{-1.4}$	450 ± 26	10.2	2500 ± 700	11 ± 6	32.0	18
RCW 86 (whole)	Constant	$9^{+0.79}_{-0.68}$	470^{+23}_{-28}	10.2	2500 ± 700	23 ± 14	39.3	18
Vela Jr. (whole)	Bohm	33^{+3}_{-23}	250 ± 8	12.0	2200 ± 800	2.3 ± 1.7	13.8	11
Vela Jr. (whole)	Kolmogorov	$22^{+1.6}_{-1.6}$	240 ± 7	12.0	2200 ± 800	3.5 ± 2.6	14.1	11
Vela Jr. (whole)	Constant	$14^{+1.9}_{-1}$	240 ± 8	12.0	2200 ± 800	$6.1^{+4.6}_{-4.5}$	16.6	11
HESS J1731–347 (whole)	Bohm	19 ± 2	480^{+32}_{-22}	25.0	2000 ± 500	$2.6^{+1.6}_{-1.5}$	15.8	20
HESS J1731–347 (whole)	Kolmogorov	$13^{+2.7}_{-1.4}$	480 ± 30	25.0	2000 ± 500	$4.2^{+2.8}_{-2.3}$	15.7	20
HESS J1731–347 (whole)	Constant	$8.1^{+1.3}_{-1}$	470 ± 30	25.0	2000 ± 500	$7.5^{+4.3}_{-4.2}$	15.1	20

6.4.2 Discussion: Comparison of X-ray and gamma-ray results

Table 6.4 summarizes the fitting results of application of non-Bohm diffusion models to the TeV gamma-ray observations. With the current dataset, the three diffusion models (i.e., $\alpha = 0, 1/3,$ and 1) are not firmly distinguished at least 3σ confidence level, inferred from the chi-square values.

Although the fitting itself does not distinguish the significance of α , we try to explore another way to put a constraint on the α parameter, particularly combining the X-ray and gamma-ray observations. Given the magnetic field strength listed in Table 5.1, which is inferred from the X-ray and gamma-ray flux ratio, the $\Pi_0 = E_0 B^{1/2}$ value can be also estimated from the gamma-ray spectral fitting. Figure 6.11 compares Π_0 taken with the X-ray and gamma-ray observations in the different α models. Note that the X-ray results are extracted from the narrower regions compared to the gamma-ray observations because of the better angular resolution. In the case of the entire remnant from Vela Jr., Π_0 with the X-ray and gamma-ray spectrum becomes comparable for $\alpha = 1/3$ (Kolmogorov-type diffusion): the combination of X-ray and gamma-ray observations implies that

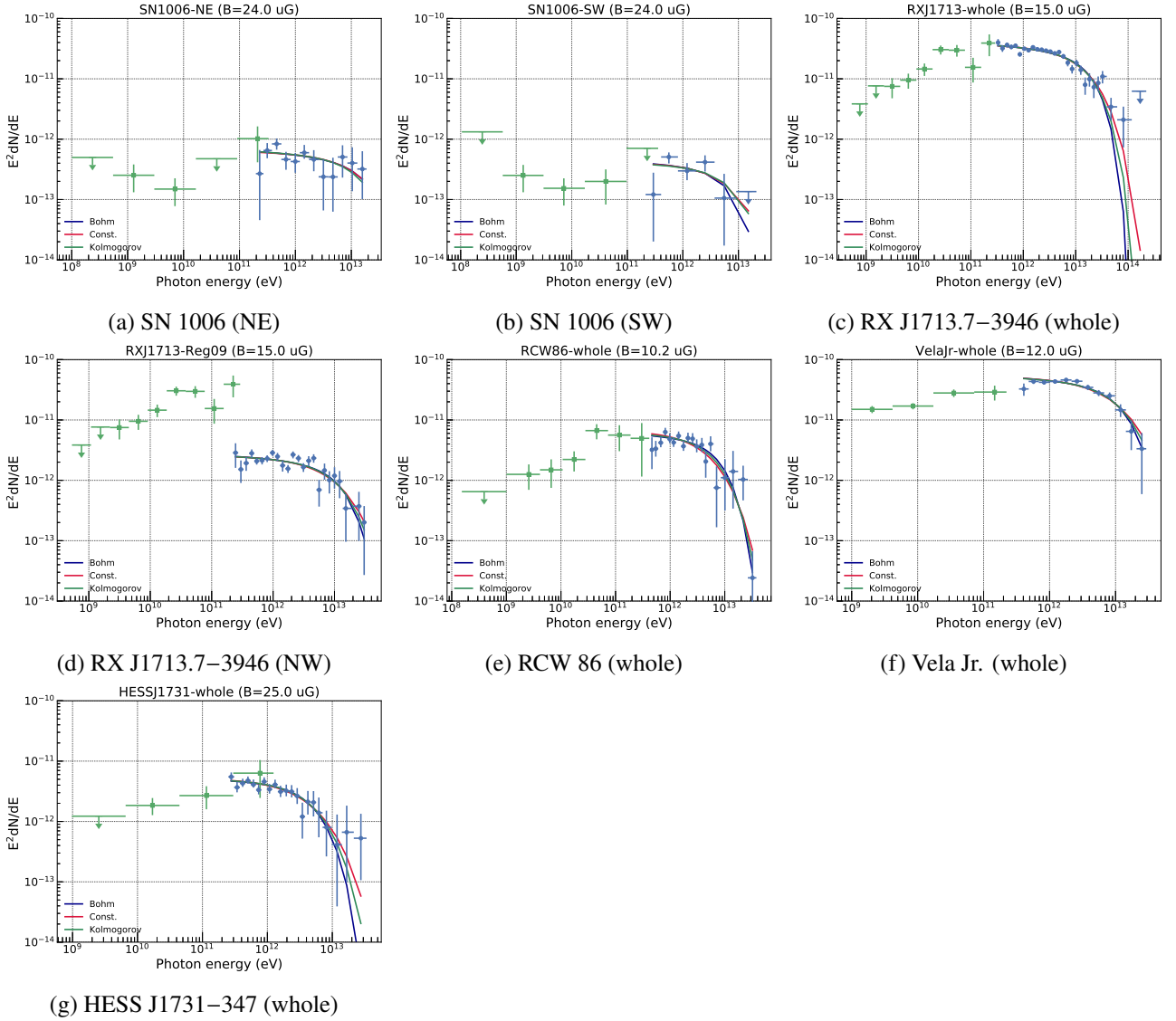


Figure 6.10: The gamma-ray spectra with the best-fit models with Bohm (shown in blue), Kolmogorov (red), and constant (green) diffusion regimes in KN regime. The blue and green plots present the *Fermi* and H.E.S.S. spectra, respectively.

Kolmogorov diffusion is preferred. The other SNRs show the larger Π_0 values with X-ray observations than those with gamma-rays, except for the two limbs of SN 1006. It should be cautious that the different region of spectral extraction causes underestimating the B value. In fact, changing B results in Figure 6.12 for the case of the NW rim in RX J1713.7–3946 with $B = 50 \mu\text{G}$. This shows the coincidence of the Π_0 parameter in the all models.

We present the scatter plots of k_0 and Π_0 obtained with X-ray and gamma-ray spectra in Figure 6.13. Because the Π_0 values are significantly different in the X-ray and gamma-ray observations as shown in Figure 6.11, the resulting k_0 values are also different. The k_0 – Π_0 plots with X-ray and gamma-ray are not identical, except for Vela Jr. in the $\alpha = 1/3$ case. We could not test the validity of α with the present dataset. This will be more constrained with deeper observations and/or more spatially resolved gamma-ray observations provided with the next-generation IACT, such as CTA.

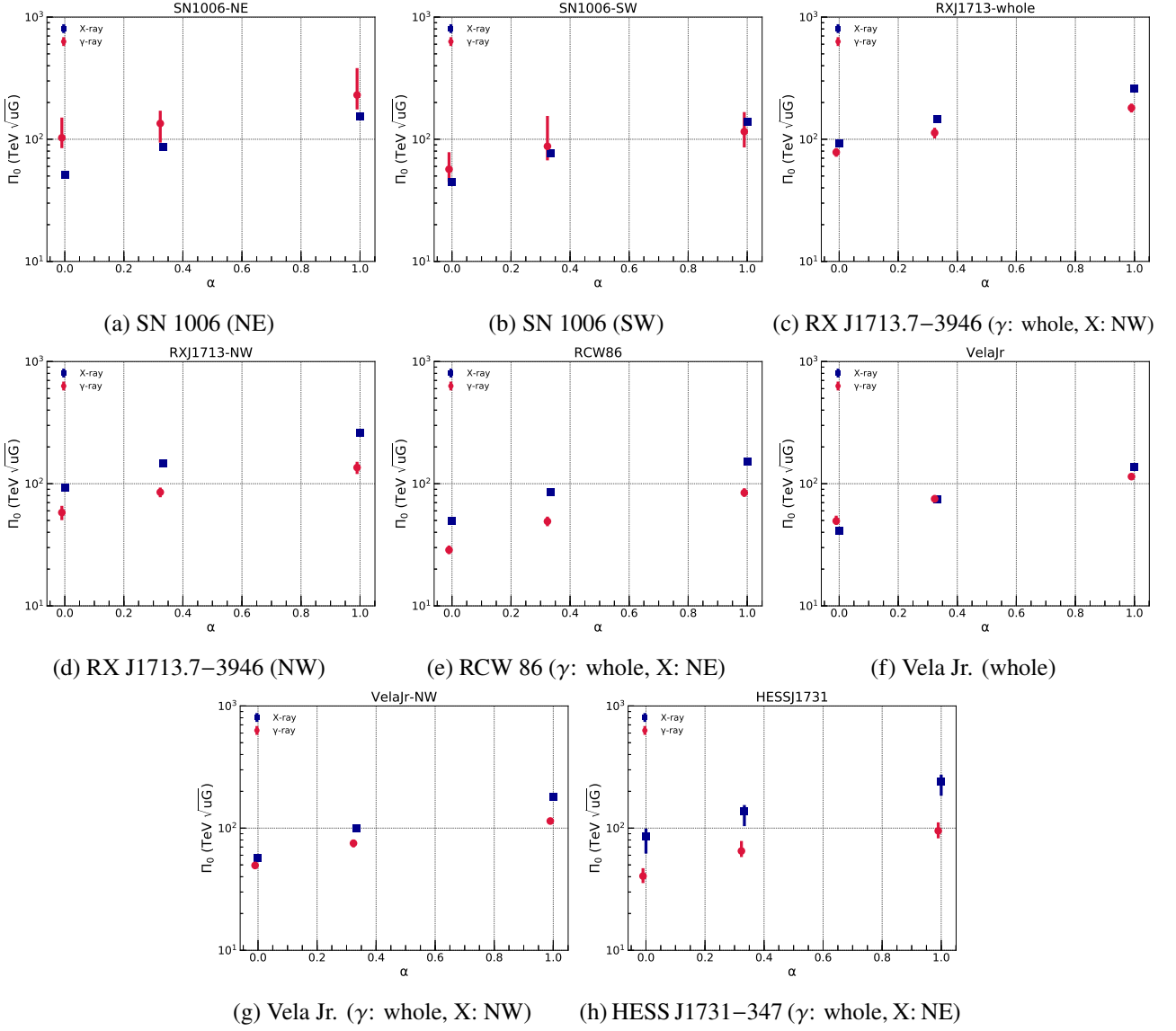


Figure 6.11: Comparison of the Π_0 parameters obtained with X-ray (shown in blue) and gamma-ray (red) observations.

6.5 Conclusions

In this chapter, we investigate the validity of Bohm diffusion ($D \propto E^\alpha$ with $\alpha = 1$) near the SNR shock by using the spectral shape of the particle (electron) distribution. Expanding calculation of Zirakashvili and Aharonian (2007), we derived the spectral cutoff shape with arbitrary α and obtained the full-energy-band analytical expressions of the electron distribution, and the corresponding synchrotron and IC radiation. The difference in α appears much clear in the higher energies (e.g., the spectrum becomes flattened for the smaller α). We applied the models with $\alpha = 0$, $1/3$, and 1 , which respectively correspond to constant, Kolmogorov, and Bohm diffusion regimes, to the nonthermal X-ray and TeV gamma-ray spectra presented in Chapter 4 and Chapter 5. The spectral fitting, unfortunately, does not enable us to demonstrate the different values of α due to the limited statistics of the current data, in particular, in the higher energy domains. However, a combination of X-ray and gamma-ray results suggested that the α parameter can be more constrained, as already Vela Jr. may show an indication of $\alpha = 1/3$. The future gamma-ray telescope, CTA, will provide us with more spatially resolved TeV gamma-ray observations, allowing to compare with X-ray observations with greater accuracy. This would put a tight constraint on α , that is, the corresponding self-generated turbulent spectrum which is difficult to access

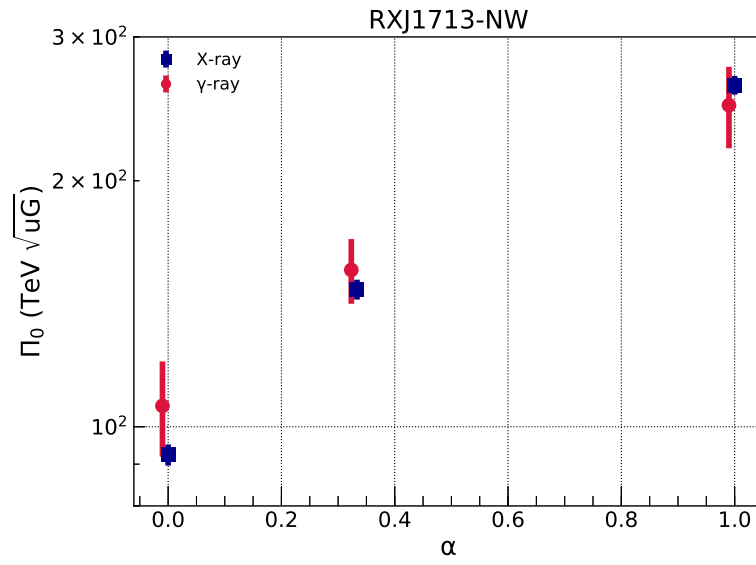


Figure 6.12: Same as Figure 6.11 for NW of RX J1713.7–3946 with $B = 50 \mu\text{G}$.

and demonstrate with theoretical studies or with numerical simulations.

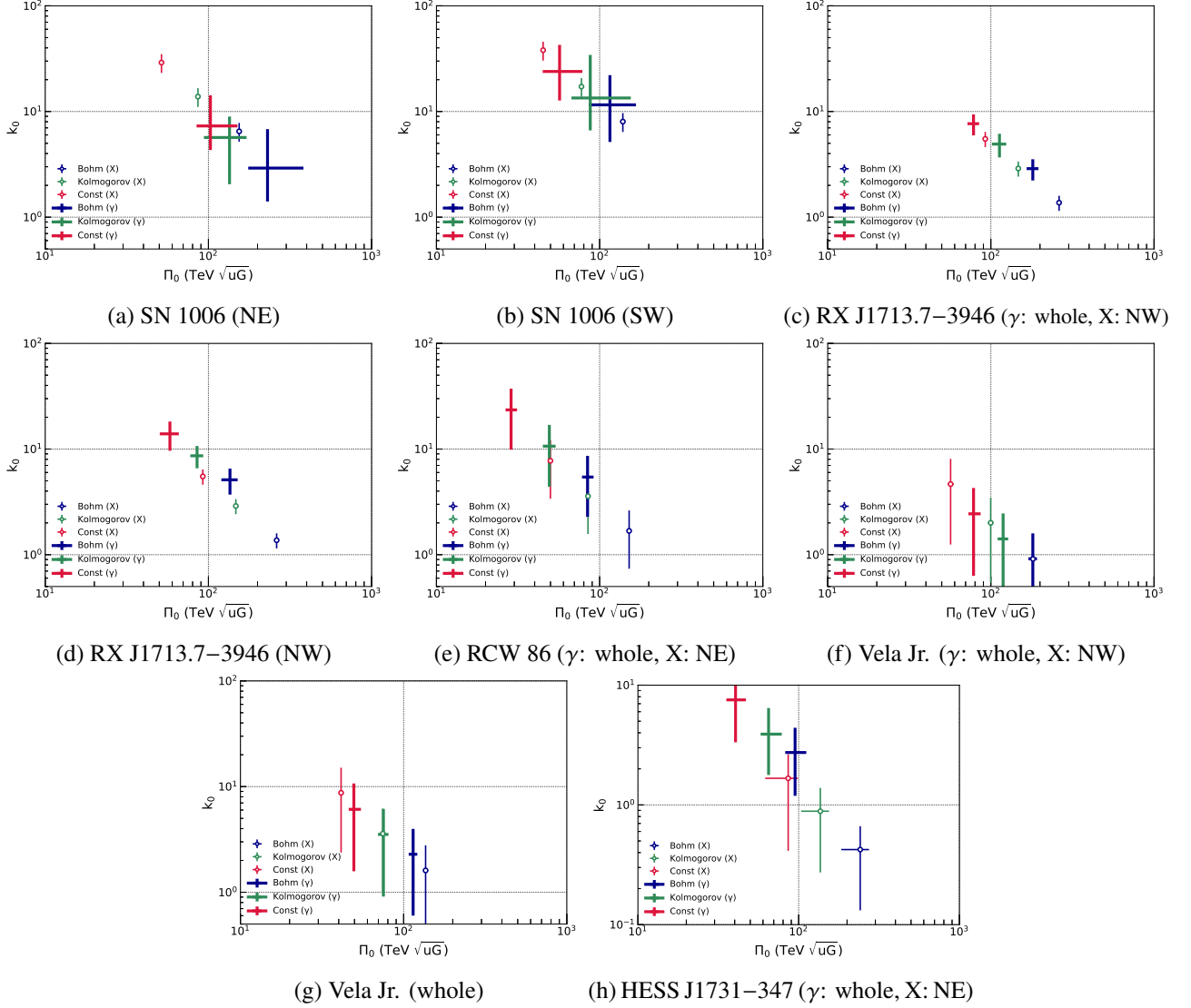


Figure 6.13: k_0 – Π_0 diagram. Thick plots are obtained with gamma-ray observations, while thin and open markers are with X-ray observations.

Chapter 7

Summary and conclusions

A particle diffusively moves back and forth across an astrophysical shock wave and stochastically gains energy in DSA. The standard DSA predicts that the energy spectrum of the accelerated particle is distributed in a power-law form of E^{-2} . The particle accelerated in the shock via DSA diffuses into the upstream and downstream regions and loses its energy due to effective radiation. We assume that the diffusion is Bohm-type of which the diffusion coefficient is proportional to the particle energy as $D(E) \propto E$, and that the energy loss is limited by synchrotron emission. This picture is applicable to accelerated electrons in the vicinity of the SNR shock. In this framework, one derives an analytical expression of the electron spectrum as $\propto E^{-3} \exp(-(E/E_0)^2)$. The corresponding synchrotron spectrum is described as $\propto \varepsilon^{-2} \exp(-(\varepsilon/\varepsilon_0)^{-1/2})$ with the cutoff energy parameter of $\varepsilon_0 \propto v_{\text{sh}}^2 \eta^{-1}$. Since it is too complicated to analytically solve the given conditions to obtain the inverse Compton gamma-ray spectrum in Klein-Nishina regime, we make use of Naima to calculate the IC spectrum. We apply these radiation models to the nonthermal observations of SNRs in order to determine the cutoff energy parameter. The obtained cutoff energy parameter, combined with the shock speed in the literature, leads to Bohm factor (η) that is indicative of an acceleration efficiency.

We analyzed X-ray observations of 11 young SNRs, measured the cutoff energy parameter in the synchrotron spectrum, and constrained the corresponding Bohm factor of each SNR. The ε_0 - v_{sh} relations of the six individual SNRs showed a variety. The obtained ε_0 - v_{sh} scatter plot is well reproduced by the theoretical curve in the cases of Kepler and Tycho (*standard* acceleration), while it is hardly explained by the theoretical curve in the other SNRs (i.e., not standard acceleration). For the latter case, the acceleration could be more affected by the surrounding environment, such as a number density in Cassiopeia A and a magnetic field obliquity in SN 1006. In addition, our assumption of the cooling-limited electrons might not be applicable for G1.9+0.3 and the interior region in the northwestern rim of RX J1713.7-3946 most likely because of a young age and slow shock speeds, respectively. With all 11 SNRs together, including G330.2+1.0, RCW 86, Vela Jr., HESS J1731-347, and SN 1987A, the systematic tendency of the Bohm factor has been unveiled for the first time. In the maximum- ε_0 (or maximum- v_{sh}) region of each SNR, the η parameter depends on the evolutionary age as $\eta = 1.6(t_{\text{age}}/1 \text{ kyr})^{-0.46}$ or on the expansion parameter as $\eta = 6.5m^{4.5}$. This might imply that the magnetic field becomes turbulent and more self-generated as particles become more accelerated with time. If we consider the time dependence on η as $\eta \propto t^{-\delta}$ with δ of 0.46, the maximum energy achieved in SNRs appears greater by the term of δ and possibly in the PeV range.

The inverse Compton gamma-ray model, calculated with Naima, is applied to the TeV gamma-ray spectra of five SNRs taken with H.E.S.S. These five SNRs are strong TeV emitters and have flatter GeV spectra, which support for the leptonic (IC) scenario. It should be noted that there may exist non-negligible hadronic components, but we assume the leptonic radiation in order to compare the gamma-ray and X-ray results. We utilize the magnetic field estimated by the ratio of the X-ray and gamma-ray flux in this leptonic framework. The TeV gamma-ray spectra are well reproduced by the IC model. The estimated Bohm factor with gamma-rays appears compatible with or slightly larger than that with X-rays. This might arise from the different size of spectral extraction, since the gamma-ray spectrum is extracted from a larger area due to its angular resolution.

While Bohm diffusion is widely accepted, one needs to demonstrate non-Bohm diffusion type. It is quite important to put observational constraints on the diffusion type which is reflected by the turbulent field, because the

turbulent spectrum is difficult to determine by theoretical studies or numerical simulations. In the case of an arbitrary diffusion regime (i.e., $D(E) \propto E^\alpha$), the cutoff shape of the electron spectrum is derived as $\exp(-(E/E_0)^{\alpha+1})$, and the corresponding synchrotron spectrum follows the cutoff shape of $\exp(-(\varepsilon/\varepsilon_0)^{(\alpha+1)/(\alpha+3)})$. The different α appears clear in the higher energies above ~ 20 keV in X-ray and ~ 30 TeV in gamma-ray. To distinguish the difference in α , a deeper observation is required to measure the cutoff shape with more accuracy, or a combination of the X-ray and gamma-ray observations with better angular resolution, such as CTA, would be able to constrain the α value. Observational constraint on α is desired for theoretical studies, leading us to the determination of the unknown turbulent spectrum and the mechanism of turbulent production.

In summary, we obtained the cutoff energy parameter and constrained the relevant diffusion coefficient of accelerated particles around the SNR shock by making use of the nonthermal X-ray and TeV gamma-ray observations. We showed that the spatially resolved analysis with *Chandra*, combined with the available *NuSTAR* data, provides us with precise measurements of the cutoff energy parameters. This unveils the variable properties of particle acceleration in the young SNRs and the evolving acceleration efficiency as an overall tendency. It is difficult and challenging to determine the diffusion type due to the current limited statistics and the angular resolution of gamma-ray observations. We finally address the prospect for tight constraints on the diffusion coefficient in the forthcoming CTA era.

Appendices

Appendix A

Radiation spectrum from cutoff power-law electron

This section represents a detailed calculation to derive the model spectrum of synchrotron radiation (Section A.1) and inverse Compton scattering (Section A.2) radiated from cutoff power-law electrons. The electron is described using the momentum $p = E/c$, and the photon is described using the frequency $\omega = \varepsilon/\hbar$.

A.1 Synchrotron radiation

Here we assume that the energy distribution of electrons has a power-law form with an exponential cutoff,

$$F(p) \propto p^{-s} \exp\left[-\left(\frac{p}{p_0}\right)^\beta\right], \quad (\text{A.1})$$

where s , p_0 , and β are a spectral index, cutoff energy, and cutoff slope. The synchrotron spectrum is obtained by

$$J(\omega) = \int dp F(p) p^2 R\left(\frac{\omega}{\omega_c}\right), \quad (\text{A.2})$$

where

$$R\left(\frac{\omega}{\omega_c}\right) = \frac{1.81 \exp\left(-\frac{\omega}{\omega_c}\right)}{\sqrt{\left(\frac{\omega_c}{\omega}\right)^{2/3} + \left(\frac{3.62}{\pi}\right)^2}}. \quad (\text{A.3})$$

Substituting Equation A.1 and Equation A.3 to Equation A.2,

$$J(\omega) = \int dp f(p) \exp[-g(p)], \quad (\text{A.4})$$

where

$$f(p) = p^{2-s} \frac{1.81}{\sqrt{\left(\frac{\omega}{Ap^2}\right)^{2/3} + \left(\frac{3.62}{\pi}\right)^2}}, \quad (\text{A.5})$$

$$g(p) = \left(\frac{p}{p_0}\right)^\beta + \frac{\omega}{\omega_c} = \left(\frac{p}{p_0}\right)^\beta + \frac{\omega}{Ap^2}. \quad (\text{A.6})$$

Here we denote ω_c by Ap^2 with A being $1.5qB/m^3c^3$.

The function $f(p)$ and $g(p)$ are shown in Figure A.1. As seen in Figure A.1, $g(p)$ has the minimal value at $p = p_*$. In the following, we expand $\exp(-g(p))$ around p_* , assuming that the contribution around p_* is dominant. p_* which gives $g'(p_*) = 0$, $g(p_*)$, and $g''(p_*)$ are, respectively,

$$p_* = \left[\frac{2\omega p_0^\beta}{\beta A} \right]^{\frac{1}{\beta+2}}, \quad (\text{A.7})$$

$$g(p_*) = \frac{2 + \beta}{\beta} \frac{\omega}{Ap_*^2}, \quad (\text{A.8})$$

$$g''(p_*) = 2(2 + \beta) \frac{\omega}{Ap_*^4}. \quad (\text{A.9})$$

Expanding the function $g(p)$ around p_* ,

$$g(p) \simeq g(p_*) + g'(p_*)(p - p_*) + \frac{1}{2}g''(p_*)(p - p_*)^2 \quad (\text{A.10})$$

$$\simeq \frac{2 + \beta}{\beta} \frac{\omega}{Ap_*^2} + (2 + \beta) \frac{\omega}{Ap_*^4} (p - p_*)^2. \quad (\text{A.11})$$

Then we substitute this to Equation A.4 and expand the function $f(p)$ around p_* as well,

$$\begin{aligned} J(\omega) &= \int dp \left[f(p_*) + f'(p_*)(p - p_*) + \frac{1}{2}f''(p_*)(p - p_*)^2 \right] \times \exp \left[- \left\{ \frac{2 + \beta}{\beta} \frac{\omega}{Ap_*^2} + (2 + \beta) \frac{\omega}{Ap_*^4} (p - p_*)^2 \right\} \right] \\ &= f(p_*) \exp \left[- \frac{2 + \beta}{\beta} \frac{\omega}{Ap_*^2} \right] \times \int_{-\infty}^{\infty} dp \exp \left[- (2 + \beta) \frac{\omega}{Ap_*^4} (p - p_*)^2 \right] \\ &= f(p_*) \exp [-g(p_*)] \times \int_{-\infty}^{\infty} dp \exp \left[- \frac{1}{2}g''(p_*)(p - p_*)^2 \right] \\ &= f(p_*) \exp [-g(p_*)] \sqrt{\frac{2\pi}{g''(p_*)}} \end{aligned} \quad (\text{A.12})$$

In the expansion of $f(p)$, the first order differentiation is zero, and the second order differentiation is ignored approximately. To derive the last form of Equation A.12, we use Gauss integration¹. The final expression of the synchrotron spectrum is given by Equation A.12, where $f(p)$ is Equation A.5, p_* is Equation A.7, $g(p_*)$ is Equation A.8, and $g''(p_*)$ is Equation A.9.

If we take only the power-law component of the synchrotron spectrum given by Equation A.12, the energy spectrum is described as

$$J(\omega) \propto \omega^{\frac{6-\beta-2s}{2(\beta+2)}}, \quad (\text{A.13})$$

and the photon spectrum is described as,

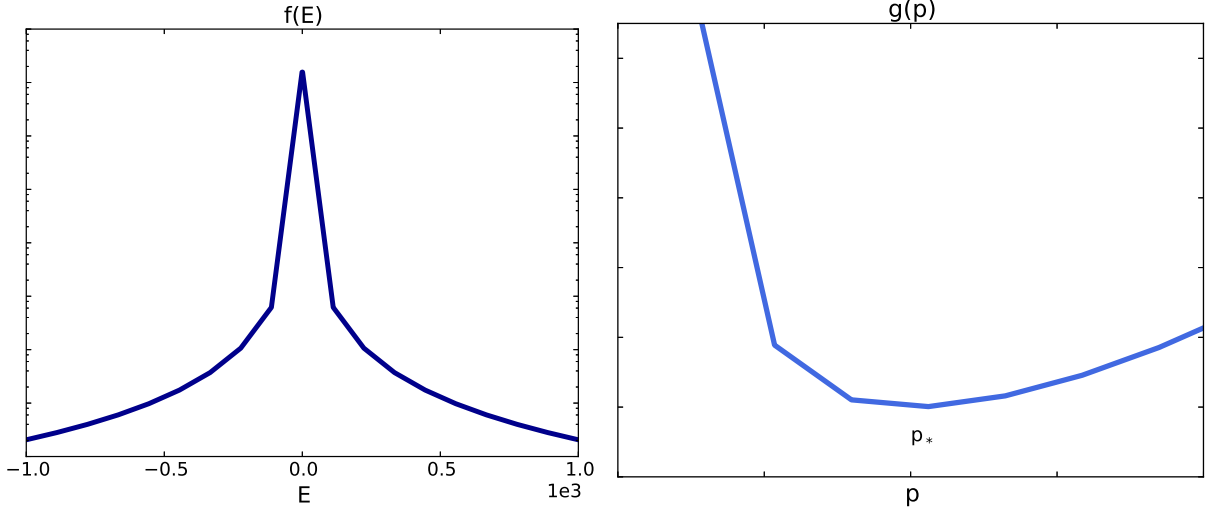
$$\frac{dN_X}{d\varepsilon} = J\omega^{-1} \propto \varepsilon^{-\frac{2s+3\beta-2}{2(\beta+2)}}. \quad (\text{A.14})$$

Hence the photon index is obtained to be $\Gamma = \frac{2s+3\beta-2}{2(\beta+2)}$.

We furthermore expand the exponential cutoff part in Equation A.12 to obtain the cutoff shape:

$$\begin{aligned} J(\omega) &\propto \exp [-g(p_*)] \\ &\propto \exp \left[- \left\{ \left(\frac{(\beta + 2)^{\beta+2}}{4} \right)^{1/\beta} \frac{\omega}{\beta A p_0^2} \right\}^{\frac{\beta}{\beta+2}} \right] \\ &\propto \exp \left[- \left(\frac{\omega}{\omega_0} \right)^{\frac{\beta}{\beta+2}} \right], \end{aligned} \quad (\text{A.15})$$

¹Gauss integration: $\int_{-\infty}^{\infty} dx \exp(-ax^2) = \sqrt{\pi/a}$

Figure A.1: Left: Function $f(E)$. Right: Function $g(p)$.

where

$$\omega_0 = \beta \left[4 \left(\frac{1}{2 + \beta} \right)^{2 + \beta} \right]^{1/\beta} \frac{3q}{2m^3 c^3} B p_0^2. \quad (\text{A.16})$$

Here we obtain the relation between the cutoff slope of the electron (β) and synchrotron (β_X) spectra as $\beta_X = \beta/(\beta + 2)$.

A.2 Inverse Compton in Thomson limit

At the higher energies $\omega \gg \gamma^2 kT/\hbar$, the IC emissivity from a single electron in Thomson regime is given by $\epsilon_{\text{IC}} \propto \omega \exp(-\hbar\omega/4\gamma^2 kT)$. Integrating the emissivity over the electron of Equation A.1, the IC spectrum is described as

$$J(\omega) = \int p^2 dp \epsilon_{\text{IC}} F(p), \quad (\text{A.17})$$

$$= \int dp p^{-s+4} \exp \left[- \left\{ \frac{\hbar}{4kTm^2c^2} \frac{\omega}{p^2} + \left(\frac{p}{p_0} \right)^\beta \right\} \right]. \quad (\text{A.18})$$

Here we assume that the up-scattered photon energy is proportional to the electron energy squared (i.e., $\epsilon \propto \gamma^2 \propto p^2$). Equation A.18 can be reduced to Equation A.4 by replacing $s \rightarrow s - 2$ and $4kTm^2c^2/\hbar \rightarrow A$. Therefore the replacements simply lead to the IC spectrum by the same procedure mentioned in Section A.1. Supposing that the resulting IC photon spectrum is given by

$$\frac{dN_\gamma}{d\epsilon} = \epsilon^{-\Gamma} \exp \left[- \left(\frac{\omega}{\omega_\gamma} \right)^{\beta_\gamma} \right], \quad (\text{A.19})$$

the photon index and the cutoff energy parameters are respectively obtained as

$$\Gamma = \frac{2s + 3\beta - 6}{2(\beta + 2)}, \quad (\text{A.20})$$

$$\omega_\gamma = \beta \left[4 \left(\frac{1}{2 + \beta} \right)^{2 + \beta} \right]^{1/\beta} \frac{4kT}{m^2 c^2} p_0^2, \quad (\text{A.21})$$

$$\beta_\gamma = \frac{\beta}{\beta + 2}. \quad (\text{A.22})$$

Appendix B

Projection effect on proper-motion measurements

Here, we argue the effect of the projection regarding the X-ray observations of the northwest rim of SNR RX J1713.7–3946. The measured proper-motion velocities in Tsuji and Uchiyama (2016) have the uncertainty of being projected onto the line of sight. We present three types of corrected speed: projection-corrected velocity (V_{cor}), projected velocity of the forward shock onto each box (V_{proj}), and upstream velocity in the rest frame (u_1).

V_{cor} indicates the projection-corrected speed of each box assuming the spherical shell. This is given by

$$V_{\text{cor, box}(X)} = V_{\text{obs, box}(X)} \frac{\theta_{\text{box}(a)}}{\theta_{\text{box}(X)}}, \quad (\text{B.1})$$

where $V_{\text{obs, box}(X)}$ and $\theta_{\text{box}(X)}$ are respectively the observed speed and the radius from the SNR center of each box. Here we assume that the remnant has a spherical shape with the radius being at the position of box (a) (probably tracing the forward shock), therefore $\theta_{\text{box}(a)}$ is fixed to 29.8 arcmin, i.e., 8.68 pc assuming the distance of the SNR is 1 kpc.

V_{proj} is the projected speed of the forward shock, box (a), assuming the spherical shell:

$$V_{\text{proj, box}(X)} = V_{\text{obs, box}(a)} \frac{\theta_{\text{box}(X)}}{\theta_{\text{box}(a)}}. \quad (\text{B.2})$$

u_1 describes the upstream speed in the rest frame of each box. In the rest frame of each box, the shock hits the ejecta that is freely moving outward. The speed of the free expansion is described with $\theta_{\text{box}(X)}/t_{\text{age}}$, where t_{age} is the age of the SNR, namely 1618 (=2011–393) years. Then the upstream speed is given by

$$u_{1, \text{box}(X)} = \theta_{\text{box}(X)}/t_{\text{age}} - V_{\text{obs, box}(X)}, \quad (\text{B.3})$$

which is same as Equation 4.6. See also, e.g., Sato et al. (2018).

The results of these corrected speeds are listed in Table B.1. The $v_{\text{sh}}-\varepsilon_0$ relation, using these corrected velocities above as the shock speed, is illustrated with the open markers in Figure B.1 for the $\kappa = \sqrt{11}^{-1}$ case and in Figure B.2 for the $\kappa = 1$ case.

Table B.1: Proper motion measurement

box	Velocity		Radius		$\dot{\theta}/\theta$ (kry ⁻¹)	V_{cor} (km s ⁻¹)	V_{proj} (km s ⁻¹)	R/t_{age} (km s ⁻¹)	u_1 (km s ⁻¹)	m^\dagger
	$\dot{\theta}$ (″ yr ⁻¹)	V (km s ⁻¹)	θ (′)	R (pc)						
(a)	0.82 ± 0.06	3900 ± 300	29.8	8.68	0.459	—	—	5246	1345	0.74 ± 0.06
(b)	0.25 ± 0.06	1200 ± 300	29.6	8.62	0.141	1200 ± 300	3873 ± 298	5210	4010	0.23 ± 0.06
(c)	0.30 ± 0.05	1400 ± 200	23.5	6.84	0.213	1800 ± 300	3073 ± 236	4134	2734	0.34 ± 0.05
(d)	0.61 ± 0.05	2900 ± 200	22.3	6.50	0.456	3900 ± 300	2921 ± 225	3928	1028	0.74 ± 0.05
(e)	0.17 ± 0.06	800 ± 300	20.1	6.11	0.135	1100 ± 400	2745 ± 211	3692	2892	0.22 ± 0.08

[†] m is the expansion parameter: $R \propto t^m$, where m is derived as (proper motion) / R/t_{age} .

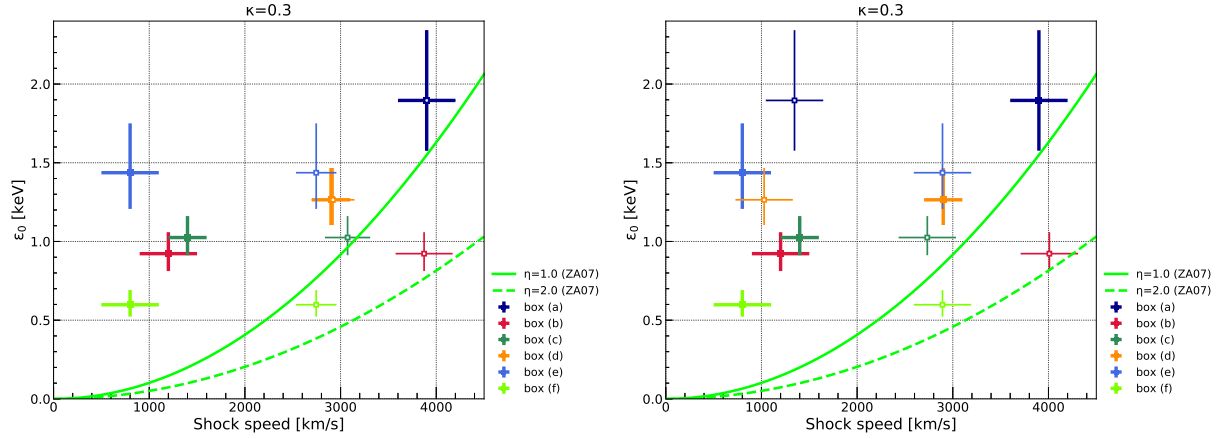


Figure B.1: Relation between the cutoff energy parameter and the shock velocity in the case of $\kappa = \sqrt{11}^{-1}$, with the open markers being the projection velocity (V_{proj}) in the left panel, and the upstream velocity at the rest frame of the shock (u_1) in the right panel.

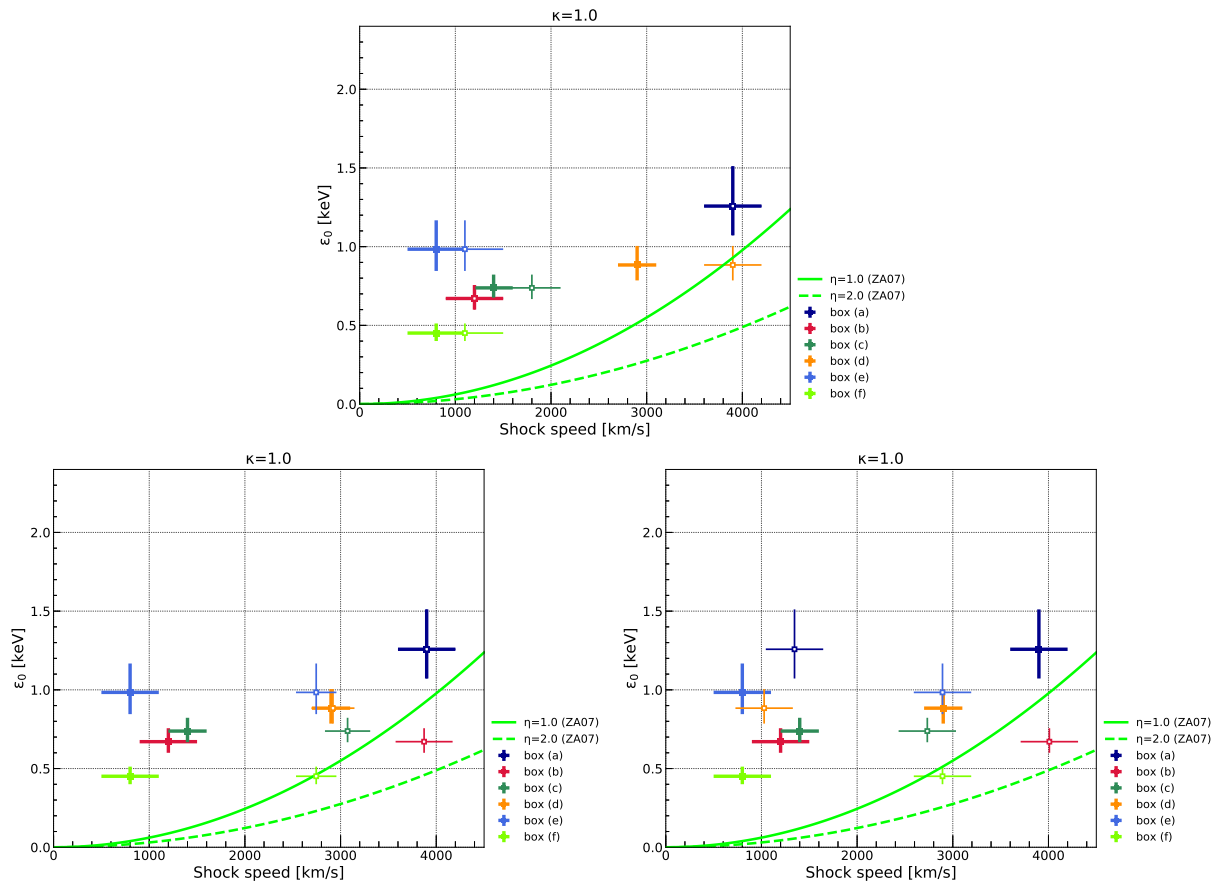


Figure B.2: Relation between the cutoff energy parameter and the shock velocity in the case of $\kappa = 1$, with the open markers being the projection-corrected velocity (V_{cor}) in the top panel, the projection velocity (V_{proj}) in the bottom left panel, and the upstream velocity at the rest frame of the shock (u_1) in the bottom right panel.

Appendix C

Synchrotron radiation in distributed field

When magnetic field is distributed (or turbulent) rather than it is described with a single (monochromatic) value, configuration of synchrotron radiation is modified. For instance, in the case of Gaussian-like turbulence of magnetic field, the cutoff shape of synchrotron spectrum follows $\exp(\varepsilon^{-1/3})$ rather than $\exp(\varepsilon^{-1/2})$ that is derived with the single value of the field. This chapter gives a brief description of the turbulent-field model (Section C.1) and applications to the observations (Section C.2).

C.1 Model

The synchrotron emissivity introduced in Section 2.6 presumes that magnetic field is monochromatic where B is given by a single value. In realistic cases, the field can be more distributed (turbulent), and the strength of magnetic field consists of various values. Let assume the magnetic field is described with probability of $P(B)$. The synchrotron emissivity using P function is given by

$$\epsilon(\omega) = \frac{\sqrt{3}q^3}{2\pi mc^2} \int dB P(B) \int p^2 dp N(p) R\left(\frac{\omega}{\omega_c}\right). \quad (\text{C.1})$$

Note that Equation C.1 yields the same as Equation 2.108 in the single-value (B_0) field with $P(B) = \delta(B - B_0)$.

Zirakashvili and Ptuskin (2008) found that the probability distribution of $P(B)$ was written in an analytical form:

$$P(B) = \frac{6B}{B_{\text{rms}}^2} \exp\left(-\frac{\sqrt{6}B}{B_{\text{rms}}}\right), \quad (\text{C.2})$$

based on numerical simulations of non-resonant streaming instability. Here $B_{\text{rms}} = \langle B^2 \rangle^{1/2}$ indicates the square root of the mean square of the random magnetic field. When the field is distributed like in Equation C.2, the analytical expression of the R function, which gives the synchrotron power radiated by a single electron, is described as

$$R_1(x) = 1.50x^{1/3} \left(1 + 1.53x^{1/2}\right)^{11/6} \exp\left(-96^{1/4}x^{1/2}\right), \quad (\text{C.3})$$

where $x = \omega/\omega_c$ (Zirakashvili and Aharonian, 2010). Figure C.1 compares the R functions in the single-value and distributed fields.

Zirakashvili and Aharonian (2010) obtained an analytical expression of synchrotron radiation in the distributed magnetic field using the same method by Zirakashvili and Aharonian (2007), i.e., they calculated the emissivity using the R function of Equation C.3 instead of Equation A.3. The spectral model of synchrotron

radiation in the entire energies is

$$\frac{dN_X}{d\varepsilon} \propto \varepsilon^{-2} \left[1 + 0.185 \left(\frac{\varepsilon}{\varepsilon_1} \right)^{0.4} \right]^{25/(12 \times 0.4)} \exp \left[- \left(\frac{\varepsilon}{\varepsilon_1} \right)^{\frac{1}{3}} \right] \quad (\kappa = 1/\sqrt{11}), \quad (\text{C.4})$$

$$\frac{dN_X}{d\varepsilon} \propto \varepsilon^{-2} \left[1 + 0.172 \left(\frac{\varepsilon}{\varepsilon_1} \right)^{0.46} \right]^{25/(12 \times 0.46)} \exp \left[- \left(\frac{\varepsilon}{\varepsilon_1} \right)^{\frac{1}{3}} \right] \quad (\kappa = 1), \quad (\text{C.5})$$

where Bohm diffusion ($\beta = 2$) is assumed. The cutoff energy parameter, denoted by ε_1 , is described as

$$\varepsilon_1 = \frac{\sqrt{6}}{128(1 + \kappa^{1/2})^2} \frac{\hbar mc}{q^2} v_{\text{sh}}^2 \eta^{-1}. \quad (\text{C.6})$$

Equation C.4 is shown in Figure C.1, together with the ZA07 model which is obtained in single-value magnetic field. Equation C.4 and Figure C.1 indicate that the synchrotron spectrum appears somewhat flatter, particularly, in the higher energy band. Therefore precise measurement of the cutoff shape of the synchrotron spectrum, which can be accessible with *NuSTAR*, would verify whether or not the magnetic field is distributed rather than monochromatic.

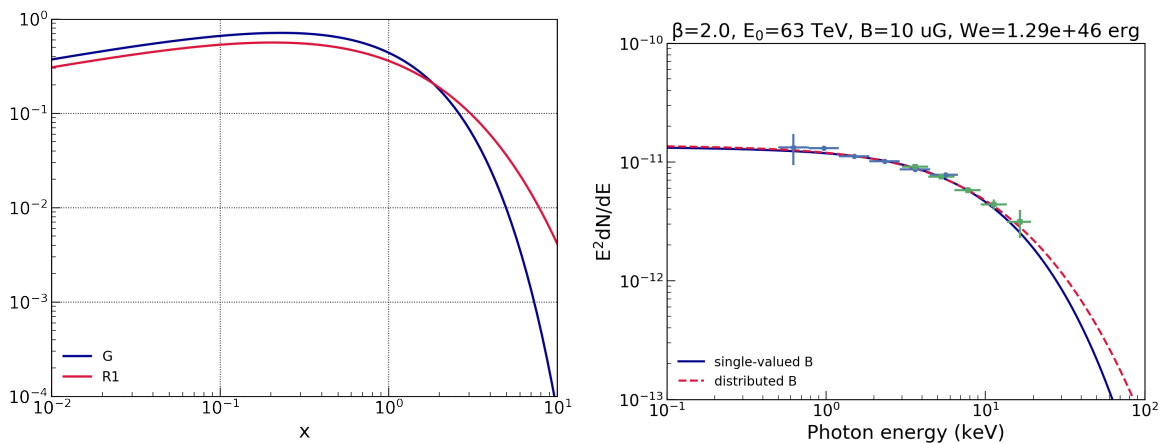


Figure C.1: Left: $R(x)$ functions in the case of single-value field (blue) and distributed field (red). Right: Synchrotron radiation spectrum in the case of single-value field (blue) and distributed field (red). The plots show the unfolded and absorption-corrected spectrum of RX J1713.7–3946-NW with *Chandra* (blue) and *NuSTAR* (green).

C.2 Application to observations

We apply the synchrotron radiation model in the distributed magnetic field to the nonthermal X-ray observations of supernova remnants. The same spectra extracted in Chapter 4 are used. The best-fit parameters are listed in Table C.1. The fitting results using the single-value model (referred to as “ZA07”) are also shown to compare with the distributed model (“ZA10”). The limited statistics, especially in the higher energies, make it difficult to distinguish the two models. G1.9+0.3 and the northeast limb of SN 1006, however, significantly prefer to the single-value model at the confidence level of $\sigma > 3$, inferred from the chi-squared value. This may imply that the field is not distributed and more concentrated in the single value in the two remnants. Although it seems challenging to demonstrate the distributed field with only X-ray data, a combination with more spatially-resolved gamma-ray observation would be a powerful tool because the magnetic field does not affect the inverse Compton spectrum.

Table C.1: Best-fit parameters of synchrotron radiation in distributed field

Name	Region	Model	N_H (10^{22} cm^{-2})	$\varepsilon_0/\varepsilon_1$ (keV)	χ^2	dof
G1.9+0.3	whole	ZA07	6 ± 0.04	$1.3^{+0.059}_{-0.055}$	902.2	585
G1.9+0.3	whole	ZA10	6 ± 0.04	0.052 ± 0.003	936.0	585
Cassiopeia A	SE1	ZA07	0.8 (fixed)	$1.9^{+0.5}_{-0.3}$	158.8	178
Cassiopeia A	SE1	ZA10	0.8 (fixed)	$0.083^{+0.024}_{-0.016}$	158.7	178
Kepler	SE1	ZA07	0.52 (fixed)	$0.74^{+0.12}_{-0.10}$	116.5	109
Kepler	SE1	ZA10	0.52 (fixed)	$0.03^{+0.006}_{-0.005}$	115.7	109
Tycho	SW (box9)	ZA07	0.7 (fixed)	$0.37^{+0.05}_{-0.04}$	165.8	95
Tycho	SW (box9)	ZA10	0.7 (fixed)	0.013 ± 0.002	162.7	95
G330.2+1.0	whole	ZA07	2.4 (fixed)	$0.65^{+0.07}_{-0.06}$	356.2	166
G330.2+1.0	whole	ZA10	2.4 (fixed)	0.027 ± 0.003	349.8	166
SN 1006	NE (fil1)	ZA07	0.068 (fixed)	0.4 ± 0.01	526.7	407
SN 1006	NE (fil1)	ZA10	0.068 (fixed)	0.016 ± 0.0004	550.7	407
RX J1713.7-3946	NW	ZA07	0.75 ± 0.008	1.1 ± 0.06	250.5	149
RX J1713.7-3946	NW	ZA10	0.76 ± 0.008	0.048 ± 0.003	243.4	149
RCW 86	NE	ZA07	0.33 (fixed)	0.38 ± 0.02	286.8	128
RCW 86	NE	ZA10	0.33 (fixed)	0.015 ± 0.001	295.9	128
Vela Jr.	NW (reg1)	ZA07	0.67 (fixed)	0.54 ± 0.04	138.5	122
Vela Jr.	NW (reg1)	ZA10	0.67 (fixed)	0.021 ± 0.002	134.8	122
HESS J1731-347	NE	ZA07	1 (fixed)	$0.97^{+0.46}_{-0.26}$	102.7	86
HESS J1731-347	NE	ZA10	1 (fixed)	$0.042^{+0.022}_{-0.012}$	102.4	86

Appendix D

Inverse Compton scattering in Thomson regime

We adopted the inverse Compton spectrum model in the Klein-Nishina regime in Chapter 5 and Chapter 6, because the TeV gamma-ray spectrum analyzed in this thesis is notably modified by the KN effect. Although it is too complicated to obtain an analytical expression for the IC spectrum by calculating the cross section in the KN regime, one can derive an analytical model in the Thomson limit. The results using the Thomson-limit model are presented as follows.

D.1 Thomson regime in Bohm diffusion

The IC model in Thomson regime is given by Equation 2.127 and recalled here:

$$\frac{dN_\gamma}{d\varepsilon} \propto \varepsilon^{-2} \left[1 + 0.31 \left(\frac{\varepsilon}{\varepsilon_\gamma} \right)^{0.6} \right]^{25/8} \exp \left[- \left(\frac{\varepsilon}{\varepsilon_\gamma} \right)^{1/2} \right]. \quad (\text{D.1})$$

We obtain the gamma-ray (ε_γ) with Thomson-limit model. The fitting results in Thomson limit are listed in and Table D.1.

In Thomson limit, Equation 2.126 leads us to the Bohm factor (η_γ) and E_0 parameter described as

$$\eta_\gamma = \frac{27m^2c^2kT}{2q^3\gamma_s^2} \left(1 + \frac{1}{\sqrt{\kappa\xi}} \right)^{-2} B^{-1}\varepsilon_\gamma^{-1}u_1^2 \quad (\text{Thomson limit}), \quad (\text{D.2})$$

$$E_0 = mc^2 \left(\frac{\varepsilon_\gamma}{kT} \right)^{1/2} \quad (\text{Thomson limit}). \quad (\text{D.3})$$

The η_γ and E_0 values estimated in Thomson regime are listed in Table D.1. Compared to the results of KN regime (Table 5.2), the cutoff energy parameter of the electron is smaller. Since the Thomson-limit model is not suppressed in the higher energies, the smaller E_0 (or ε_γ) reproduces the observed spectrum. This results in a higher value of η_γ than that in KN-regime model. The different results between Thomson and Klein-Nishina models clarify that the accurate treatment of the KN effect is required for the observed gamma-ray spectrum, which is radiated by multi-TeV electrons in the leptonic scenario.

D.2 Thomson regime in non-Bohm diffusion

In Thomson limit, the analytical expression of IC spectrum can be derived as follows. In the lower energy band, the IC spectrum, which is radiated from the electron in the lower energies as described by $F(p) \propto p^{-(\gamma_s+1)}$, has the power-law form:

$$\frac{dN_\gamma}{d\varepsilon} \propto \varepsilon^{-\frac{\gamma_s}{2}}. \quad (\text{D.4})$$

Table D.1: Spectral fitting in Thomson regime (Bohm diffusion)

Name	ε_γ (TeV)	E_0 (TeV)	B (μG)	v_{sh} (km s^{-1})	η_γ	χ^2	dof
SN 1006 (NE)	0.59±0.49	26±11	24.0	5000±1000	9.8±9	6.4	11
SN 1006 (SW)	0.53±0.071	24±2	24.0	5000±1000	11±4.6	6.6	5
RX J1713.7–3946 (whole)	0.53±0.039	24±1	15.0	3900±300	10±1.8	29.2	20
RX J1713.7–3946 (NW)	0.38±0.058	21±2	15.0	3900±300	15±3.2	32.6	23
RCW 86 (whole)	0.25±0.043	17±2	10.2	2500±700	14±8.1	13.3	18
Vela Jr. (whole)	0.38±0.038	21±1	12.0	2200±800	5.8±4.2	7.0	11
HESS J1731–347 (whole)	0.16±0.036	14±2	25.0	2000±500	5.3±2.9	7.4	20

Integrating the IC emissivity in Thomson limit (Equation 2.122) over the electron in the higher energies given by Equation 6.8, the photon spectrum is obtained:

$$\frac{dN_\gamma}{d\varepsilon} \propto \varepsilon^{-\frac{3\beta-5}{2(\beta+2)}} \exp\left[-\left(\frac{\varepsilon}{\varepsilon_0}\right)^{\beta_\gamma}\right], \quad (\text{D.5})$$

where $\beta_\gamma = \beta/(\beta + 2)$. The cutoff energy parameter in the IC spectrum in Thomson regime is derived as

$$\varepsilon_\gamma = \beta \left[4 \left(\frac{1}{2+\beta} \right)^{2+\beta} \right]^{1/\beta} \frac{4kT}{m^2 c^2} P_0^2 \quad (\text{Thomson limit}). \quad (\text{D.6})$$

See Appendix A for the detailed derivations.

In the entire energy band, the solution is described by

$$\frac{dN_\gamma}{d\varepsilon} \propto \varepsilon^{-\frac{\gamma_s}{2}} \left[1 + a \left(\frac{\varepsilon}{\varepsilon_\gamma} \right)^b \right]^c \exp\left[-\left(\frac{\varepsilon}{\varepsilon_\gamma}\right)^{\beta_\gamma}\right]. \quad (\text{D.7})$$

The transition function, $\mathcal{T}(\varepsilon) = \left[1 + a \left(\frac{\varepsilon}{\varepsilon_\gamma} \right)^b \right]^c$, is determined by the numerical calculation, requiring the smooth connection between the lower and higher energy bands. In the higher energies ($\varepsilon \gg \varepsilon_\gamma$) in Equation D.7, $dN_\gamma/d\varepsilon$ becomes $\varepsilon^{-2+bc} \exp(-\varepsilon^{\beta_\gamma})$. This should be compatible with Equation D.5, so we obtain the condition of $bc = (\beta + 13)/2(\beta + 2)$.

In the case of non-Bohm diffusion, we obtain the parameters of the transition function for the IC spectrum (a , b , c) by calculating IC radiation from electron spectrum described in Section 6.2.1 and fitting with Equation D.7. The parameters in the $\alpha = 0$ and $1/3$ are listed in Table 6.2.

The IC model in Thomson regime, given by Equation D.7, is applied to the observations. We obtain the gamma-ray cutoff energy parameter (ε_γ) with Thomson-limit model. The best-fit parameters are listed in Table D.2.

Table D.2: The best-fit parameters with IC model in Thomson regime

Name	Model	ε_γ (TeV)	E_0 (TeV)	B (μG)	v_{sh} (km s^{-1})	η_γ/k_0	χ^2	dof
SN 1006 (NE)	Bohm	0.59±0.49	26±11	24.0	5000±1000	9.8±9	6.4	11
SN 1006 (NE)	Kolmogorov	0.14±0.11	15±6.1	24.0	5000±1000	20±18	6.0	11
SN 1006 (NE)	Constant	0.053±0.053	10±5	24.0	5000±1000	32±35	5.6	11
SN 1006 (SW)	Bohm	0.53±0.071	24±1.6	24.0	5000±1000	11±4.6	6.6	5
SN 1006 (SW)	Kolmogorov	0.15±0.025	15±1.3	24.0	5000±1000	18±7.8	6.4	5
SN 1006 (SW)	Constant	0.053±0.011	10±1.1	24.0	5000±1000	32±14	6.4	5

Table D.2: The best-fit parameters with IC model in Thomson regime (*continued*)

Name	Model	ε_γ (TeV)	E_0 (TeV)	B (μG)	v_{sh} (km s^{-1})	η_γ/k_0	χ^2	dof
RX J1713.7–3946 (whole)	Bohm	0.53 ± 0.039	24 ± 0.89	15.0	3900 ± 300	10 ± 1.8	29.2	20
RX J1713.7–3946 (whole)	Kolmogorov	0.16 ± 0.014	16 ± 0.67	15.0	3900 ± 300	17 ± 2.9	21.6	20
RX J1713.7–3946 (whole)	Constant	0.056 ± 0.0056	10 ± 0.52	15.0	3900 ± 300	29 ± 5.4	20.6	20
RX J1713.7–3946 (NW)	Bohm	0.38 ± 0.058	21 ± 1.6	15.0	3900 ± 300	15 ± 3.2	32.6	23
RX J1713.7–3946 (NW)	Kolmogorov	0.11 ± 0.019	13 ± 1.1	15.0	3900 ± 300	23 ± 5.3	32.8	23
RX J1713.7–3946 (NW)	Constant	0.041 ± 0.008	8.8 ± 0.86	15.0	3900 ± 300	40 ± 10	34.9	23
RCW 86 (whole)	Bohm	0.25 ± 0.043	17 ± 1.5	10.2	2500 ± 700	14 ± 8.1	13.3	18
RCW 86 (whole)	Kolmogorov	0.056 ± 0.0096	9.3 ± 0.79	10.2	2500 ± 700	29 ± 17	17.2	18
RCW 86 (whole)	Constant	0.015 ± 0.0027	5.3 ± 0.48	10.2	2500 ± 700	67 ± 39	22.1	18
Vela Jr. (whole)	Bohm	0.38 ± 0.038	21 ± 1	12.0	2200 ± 800	5.8 ± 4.2	7.0	11
Vela Jr. (whole)	Kolmogorov	0.11 ± 0.013	13 ± 0.78	12.0	2200 ± 800	9.3 ± 6.8	12.0	11
Vela Jr. (whole)	Constant	0.04 ± 0.0056	8.7 ± 0.61	12.0	2200 ± 800	16 ± 12	19.0	11
HESS J1731–347 (whole)	Bohm	0.16 ± 0.036	14 ± 1.5	25.0	2000 ± 500	5.3 ± 2.9	7.4	20
HESS J1731–347 (whole)	Kolmogorov	0.049 ± 0.013	8.7 ± 1.1	25.0	2000 ± 500	8.6 ± 4.8	6.9	20
HESS J1731–347 (whole)	Constant	0.017 ± 0.0053	5.7 ± 0.87	25.0	2000 ± 500	15 ± 9	6.8	20

References

- Abdo, A. A. *et al.* (2011). Observations of the Young Supernova Remnant RX J1713.7-3946 with the Fermi Large Area Telescope. *ApJ*, 734(1):28.
- Abeysekara, A. U. *et al.* (2017). Extended gamma-ray sources around pulsars constrain the origin of the positron flux at Earth. *Science*, 358:911–914.
- Abramowski, A. *et al.* (2014). Discovery of the Hard Spectrum VHE γ -Ray Source HESS J1641-463. *ApJ*, 794:L1.
- Acero, F. *et al.* (2010). First detection of VHE γ -rays from SN 1006 by HESS. *A&A*, 516:A62.
- Acero, F. *et al.* (2009). A joint spectro-imaging analysis of the XMM-Newton and HESS observations of the supernova remnant RX J1713.7-3946. *A&A*, 505(1):157–167.
- Acero, F., Katsuda, S., Ballet, J., Petre, R. (2017). Measurement of the X-ray proper motion in the south-east rim of RX J1713.7-3946. *A&A*, 597:A106.
- Ackermann, M. *et al.* (2013). Detection of the Characteristic Pion-Decay Signature in Supernova Remnants. *Science*, 339(6121):807–811.
- Adriani, O. *et al.* (2014). Measurement of Boron and Carbon Fluxes in Cosmic Rays with the PAMELA Experiment. *ApJ*, 791(2):93.
- Aharonian, F. *et al.* (2006). Observations of the Crab nebula with HESS. *A&A*, 457(3):899–915.
- Aharonian, F. *et al.* (2009). Discovery of Gamma-Ray Emission From the Shell-Type Supernova Remnant RCW 86 With Hess. *ApJ*, 692(2):1500–1505.
- Aharonian, F., Sun, X.-n., Yang, R.-z. (2017). Energy distribution of relativistic electrons in the young supernova remnant G1.9+0.3. *A&A*, 603:A7.
- Aharonian, F. A. *et al.* (2004). High-energy particle acceleration in the shell of a supernova remnant. *Nature*, 432(7013):75–77.
- Ajello, M. *et al.* (2016). Deep Morphological and Spectral Study of the SNR RCW 86 with Fermi-LAT. *ApJ*, 819(2):98.
- Allen, G. E. *et al.* (2015). On the Expansion Rate, Age, and Distance of the Supernova Remnant G266.2-1.2 (Vela Jr.). *ApJ*, 798(2):82.
- Archambault, S. *et al.* (2017). Gamma-Ray Observations of Tycho’s Supernova Remnant with VERITAS and Fermi. *ApJ*, 836(1):23.
- Armstrong, J. W., Rickett, B. J., Spangler, S. R. (1995). Electron Density Power Spectrum in the Local Interstellar Medium. *The Astrophysical Journal*, 443:209.
- Atkin, E. *et al.* (2018). New Universal Cosmic-Ray Knee near a Magnetic Rigidity of 10 TV with the NUCLEON Space Observatory. *Soviet Journal of Experimental and Theoretical Physics Letters*, 108(1):5–12.

- Axford, W. I., Leer, E., Skadron, G. (1977). The Acceleration of Cosmic Rays by Shock Waves. *International Cosmic Ray Conference*, 11:132.
- Baade, W., Zwicky, F. (1934). Cosmic Rays from Super-novae. *Proceedings of the National Academy of Science*, 20(5):259–263.
- Bamba, A. *et al.* (2012). Suzaku Observations of the Non-thermal Supernova Remnant HESS J1731-347. *ApJ*, 756(2):149.
- Bamba, A., Yamazaki, R., Yoshida, T., Terasawa, T., Koyama, K. (2005). A Spatial and Spectral Study of Nonthermal Filaments in Historical Supernova Remnants: Observational Results with Chandra. *ApJ*, 621(2):793–802.
- Bell, A. R. (1978). The acceleration of cosmic rays in shock fronts - I. *MNRAS*, 182:147–156.
- Berezhko, E. G., Völk, H. J. (2006). Theory of cosmic ray production in the supernova remnant RX J1713.7-3946. *A&A*, 451(3):981–990.
- Berge, D., Funk, S., Hinton, J. (2007). Background modelling in very-high-energy γ -ray astronomy. *A&A*, 466(3):1219–1229.
- Bernlöhr, K. *et al.* (2003). The optical system of the H.E.S.S. imaging atmospheric Cherenkov telescopes. Part I: layout and components of the system. *Astroparticle Physics*, 20(2):111–128.
- Blandford, R., Eichler, D. (1987). Particle acceleration at astrophysical shocks: A theory of cosmic ray origin. *Phys. Rep.*, 154(1):1–75.
- Blandford, R. D., Ostriker, J. P. (1978). Particle acceleration by astrophysical shocks. *ApJ*, 221:L29–L32.
- Blasi, P. (2010). Shock acceleration of electrons in the presence of synchrotron losses - I. Test-particle theory. *MNRAS*, 402(4):2807–2816.
- Blasi, P. (2018). Diffusive Shock Acceleration. *DIAS summer school 2018*: <https://www.dias.ie/cappa/SummerSchool2018/>.
- Blumenthal, G. R., Gould, R. J. (1970). Bremsstrahlung, Synchrotron Radiation, and Compton Scattering of High-Energy Electrons Traversing Dilute Gases. *Reviews of Modern Physics*, 42:237–271.
- Blümer, J., Engel, R., Hörandel, J. R. (2009). Cosmic rays from the knee to the highest energies. *Progress in Particle and Nuclear Physics*, 63(2):293–338.
- Boggs, S. E. *et al.* (2015). ^{44}Ti gamma-ray emission lines from SN1987A reveal an asymmetric explosion. *Science*, 348(6235):670–671.
- Boldt, E. (1987). The cosmic X-ray background. *Phys. Rep.*, 146(4):215–257.
- Borkowski, K. J. *et al.* (2017). Asymmetric Expansion of the Youngest Galactic Supernova Remnant G1.9+0.3. *ApJ*, 837(1):L7.
- Borkowski, K. J. *et al.* (2010). Radioactive Scandium in the Youngest Galactic Supernova Remnant G1.9+0.3. *ApJ*, 724(2):L161–L165.
- Borkowski, K. J. *et al.* (2014). Nonuniform Expansion of the Youngest Galactic Supernova Remnant G1.9+0.3. *ApJ*, 790(2):L18.
- Borkowski, K. J., Reynolds, S. P., Williams, B. J., Petre, R. (2018). Expansion and Age of the X-Ray Synchrotron-dominated Supernova Remnant G330.2+1.0. *ApJ*, 868(2):L21.

- Brose, R. *et al.* (2019). Non-thermal emission from the reverse shock of the youngest galactic Supernova remnant G1.9+0.3. *arXiv e-prints*, page arXiv:1906.02725.
- Bykov, A. M., Uvarov, Y. A., Ellison, D. C. (2008). Dots, Clumps, and Filaments: The Intermittent Images of Synchrotron Emission in Random Magnetic Fields of Young Supernova Remnants. *ApJ*, 689:L133.
- Caprioli, D., Spitkovsky, A. (2014a). Simulations of Ion Acceleration at Non-relativistic Shocks. I. Acceleration Efficiency. *ApJ*, 783(2):91.
- Caprioli, D., Spitkovsky, A. (2014b). Simulations of Ion Acceleration at Non-relativistic Shocks. II. Magnetic Field Amplification. *ApJ*, 794(1):46.
- Caprioli, D., Spitkovsky, A. (2014c). Simulations of Ion Acceleration at Non-relativistic Shocks. III. Particle Diffusion. *ApJ*, 794(1):47.
- Cassam-Chenaï, G. *et al.* (2004). XMM-Newton observation of Kepler's supernova remnant. *A&A*, 414:545–558.
- Castro, D. *et al.* (2013). A Chandra View of Non-thermal Emission in the Northwestern Region of Supernova Remnant RCW 86: Particle Acceleration and Magnetic Fields. *ApJ*, 779(1):49.
- Condon, B., Lemoine-Goumard, M., Acero, F., Katagiri, H. (2017). Detection of Two TeV Shell-type Remnants at GeV Energies with FERMI LAT: HESS J1731-347 and SN 1006. *ApJ*, 851(2):100.
- Doroshenko, V. *et al.* (2017). XMM-Newton observations of the non-thermal supernova remnant HESS J1731-347 (G353.6-0.7). *A&A*, 608:A23.
- Federici, S., Pohl, M., Telezhinsky, I., Wilhelm, A., Dwarkadas, V. V. (2015). Analysis of GeV-band γ -ray emission from supernova remnant RX J1713.7-3946. *A&A*, 577:A12.
- Fermi, E. (1949). On the Origin of the Cosmic Radiation. *Physical Review*, 75(8):1169–1174.
- Fesen, R. A., Kremer, R., Patnaude, D., Milisavljevic, D. (2012). The SN 393-SNR RX J1713.7-3946 (G347.3-0.5) Connection. *AJ*, 143(2):27.
- Frank, K. A. *et al.* (2016). Chandra Observes the End of an Era in SN 1987A. *ApJ*, 829(1):40.
- Fukui, Y. *et al.* (2003). Discovery of Interacting Molecular Gas toward the TeV Gamma-Ray Peak of the SNR G 347.3–0.5. *PASJ*, 55:L61–L64.
- Fukui, Y. *et al.* (2012). A Detailed Study of the Molecular and Atomic Gas toward the γ -Ray Supernova Remnant RX J1713.7-3946: Spatial TeV γ -Ray and Interstellar Medium Gas Correspondence. *ApJ*, 746(1):82.
- Fukuyama, T., Uchiyama, Y., Mori, K., Takahashi, T. (2019). Study of synchrotron X-ray emission from supernova remnant RX J0852.0-4622 with Suzaku. *PASJ*, in prep.
- Funk, S. (2015). Ground- and Space-Based Gamma-Ray Astronomy. *Annual Review of Nuclear and Particle Science*, 65:245–277.
- Funk, S. *et al.* (2004). The trigger system of the H.E.S.S. telescope array. *Astroparticle Physics*, 22(3-4):285–296.
- Gabici, S. (2018). Propagation of Cosmic Rays. *DIAS summer school 2018*: <https://www.dias.ie/cappa/SummerSchool2018/>.
- Ghavamian, P., Raymond, J., Hartigan, P., Blair, W. P. (2000). Evidence for Shock Precursors in Tycho's Supernova Remnant. *ApJ*, 535(1):266–274.

- Ghavamian, P., Raymond, J., Smith, R. C., Hartigan, P. (2001). Balmer-dominated Spectra of Nonradiative Shocks in the Cygnus Loop, RCW 86, and Tycho Supernova Remnants. *ApJ*, 547(2):995–1009.
- Green, D. A. (2019). A revised catalogue of 294 Galactic supernova remnants. *Journal of Astrophysics and Astronomy*, 40(4):36.
- Grefenstette, B. W. *et al.* (2015). Locating the Most Energetic Electrons in Cassiopeia A. *ApJ*, 802(1):15.
- H. E. S. S. Collaboration. (2018a). A search for new supernova remnant shells in the Galactic plane with H.E.S.S. *A&A*, 612:A8.
- H. E. S. S. Collaboration. (2018b). H.E.S.S. observations of RX J1713.7-3946 with improved angular and spectral resolution: Evidence for gamma-ray emission extending beyond the X-ray emitting shell. *A&A*, 612:A6.
- H. E. S. S. Collaboration. (2018c). Deeper H.E.S.S. observations of Vela Junior (RX J0852.0-4622): Morphology studies and resolved spectroscopy. *A&A*, 612:A7.
- H. E. S. S. Collaboration. (2018d). The H.E.S.S. Galactic plane survey. *A&A*, 612:A1.
- H. E. S. S. Collaboration. (2011). A new SNR with TeV shell-type morphology: HESS J1731-347. *A&A*, 531:A81.
- H. E. S. S. Collaboration. (2015). The exceptionally powerful TeV γ -ray emitters in the Large Magellanic Cloud. *Science*, 347(6220):406–412.
- Harrison, F. A. *et al.* (2013). The Nuclear Spectroscopic Telescope Array (NuSTAR) High-energy X-Ray Mission. *ApJ*, 770(2):103.
- Haug, E. (1975). Bremsstrahlung and pair production in the field of free electrons. *Zeitschrift Naturforschung Teil A*, 30:1099–1113.
- Helder, E. A. *et al.* (2013). Proper motions of H α filaments in the supernova remnant RCW 86. *MNRAS*, 435(2):910–916.
- Hess, V. (2018). On the Observations of the Penetrating Radiation during Seven Balloon Flights. *arXiv e-prints*, page arXiv:1808.02927.
- Hinton, J. (2018). Gamma-ray Astronomy - very high energies. *DIAS summer school 2018*: <https://www.dias.ie/cappa/SummerSchool2018/>.
- Inoue, T., Yamazaki, R., Inutsuka, S.-i., Fukui, Y. (2012). Toward Understanding the Cosmic-Ray Acceleration at Young Supernova Remnants Interacting with Interstellar Clouds: Possible Applications to RX J1713.7-3946. *ApJ*, 744(1):71.
- Kafexhiu, E., Aharonian, F., Taylor, A. M., Vila, G. S. (2014). Parametrization of gamma-ray production cross sections for p p interactions in a broad proton energy range from the kinematic threshold to PeV energies. *Phys. Rev. D*, 90(12):123014.
- Kang, H., Ryu, D., Jones, T. W. (2009). Self-Similar Evolution of Cosmic-Ray Modified Shocks: The Cosmic-Ray Spectrum. *ApJ*, 695(2):1273–1288.
- Katsuda, S. *et al.* (2015). Evidence for Thermal X-Ray Line Emission from the Synchrotron-dominated Supernova Remnant RX J1713.7-3946. *ApJ*, 814(1):29.
- Katsuda, S. *et al.* (2010). X-ray Measured Dynamics of Tycho's Supernova Remnant. *ApJ*, 709(2):1387–1395.
- Katsuda, S., Tsunemi, H., Mori, K. (2008a). The Slow X-Ray Expansion of the Northwestern Rim of the Supernova Remnant RX J0852.0-4622. *ApJ*, 678(1):L35.

- Katsuda, S., Tsunemi, H., Uchida, H., Kimura, M. (2008b). Forward Shock Proper Motions of Kepler's Supernova Remnant. *ApJ*, 689(1):225–230.
- Kelner, S. R., Lefa, E., Rieger, F. M., Aharonian, F. A. (2014). The Beaming Pattern of External Compton Emission from Relativistic Outflows: The Case of Anisotropic Distribution of Electrons. *ApJ*, 785:141.
- Khangulyan, D., Aharonian, F. A., Kelner, S. R. (2014). Simple Analytical Approximations for Treatment of Inverse Compton Scattering of Relativistic Electrons in the Blackbody Radiation Field. *ApJ*, 783:100.
- Kishishita, T., Hiraga, J., Uchiyama, Y. (2013). Nonthermal emission properties of the northwestern rim of supernova remnant RX J0852.0-4622. *A&A*, 551:A132.
- Kolmogorov, A. (1941). The Local Structure of Turbulence in Incompressible Viscous Fluid for Very Large Reynolds' Numbers. *Akademiia Nauk SSSR Doklady*, 30:301–305.
- Koyama, K. *et al.* (1995). Evidence for shock acceleration of high-energy electrons in the supernova remnant SN1006. *Nature*, 378(6554):255–258.
- Kraichnan, R. H. (1965). Inertial-Range Spectrum of Hydromagnetic Turbulence. *Physics of Fluids*, 8:1385–1387.
- Krivonos, R. *et al.* (2007). Hard X-ray emission from the Galactic ridge. *A&A*, 463(3):957–967.
- Krymskii, G. F. (1977). A regular mechanism for the acceleration of charged particles on the front of a shock wave. *Akademiia Nauk SSSR Doklady*, 234:1306–1308.
- Kulsrud, R. M. (2005). *Plasma physics for astrophysics*.
- Laming, J. M., Hwang, U. (2003). On the Determination of Ejecta Structure and Explosion Asymmetry from the X-Ray Knots of Cassiopeia A. *ApJ*, 597(1):347–361.
- Landau, L., Lifshitz, E. (2013). *Fluid Mechanics*. Number volume 6. Elsevier Science.
- Lee, J.-J. *et al.* (2010). Resolved Shock Structure of the Balmer-dominated Filaments in Tycho's Supernova Remnant: Cosmic-ray Precursor? *ApJ*, 715(2):L146–L149.
- Lee, S.-H., Slane, P. O., Ellison, D. C., Nagataki, S., Patnaude, D. J. (2013). A CR-hydro-NEI Model of Multi-wavelength Emission from the Vela Jr. Supernova Remnant (SNR RX J0852.0-4622). *ApJ*, 767(1):20.
- Li, J.-T. *et al.* (2018). Spatially Resolved Broadband Synchrotron Emission from the Nonthermal Limbs of SN1006. *ApJ*, 864(1):85.
- Long, K. S., Blair, W. P. (1990). The Identification of Balmer-dominated Filaments in RCW 86. *ApJ*, 358:L13.
- Longair, M. S. (2011). *High Energy Astrophysics*.
- Lopez, L. A. *et al.* (2015). A Spatially Resolved Study of the Synchrotron Emission and Titanium in Tycho's Supernova Remnant Using NuSTAR. *ApJ*, 814(2):132.
- Malkov, M. A., Drury, L. O. (2001). Nonlinear theory of diffusive acceleration of particles by shock waves. *Reports on Progress in Physics*, 64(4):429–481.
- Malyshev, D., Pühlhofer, G., Santangelo, A., Vink, J. (2019). Evidence for recent GeV brightening of the SN 1987A region. *arXiv e-prints*, page arXiv:1903.03045.
- McCray, R., Fransson, C. (2016). The Remnant of Supernova 1987A. *ARA&A*, 54:19–52.
- Miceli, M. *et al.* (2009). Thermal emission, shock modification, and X-ray emitting ejecta in SN 1006. *A&A*, 501(1):239–249.

- Moretti, A. *et al.* (2009). A new measurement of the cosmic X-ray background. *A&A*, 493:501–509.
- Ng, C. Y. *et al.* (2013). Evolution of the Radio Remnant of Supernova 1987A: Morphological Changes from Day 7000. *ApJ*, 777(2):131.
- Nobukawa, K. K. *et al.* (2018). Evidence for a Neutral Iron Line Generated by MeV Protons from Supernova Remnants Interacting with Molecular Clouds. *ApJ*, 854(2):87.
- Ohira, Y., Murase, K., Yamazaki, R. (2010). Escape-limited model of cosmic-ray acceleration revisited. *A&A*, 513:A17.
- Okuno, T., Tanaka, T., Uchida, H., Matsumura, H., Tsuru, T. G. (2018). Spatially resolved spectroscopy of non-thermal X-rays in RX J1713.7-3946 with Chandra. *PASJ*, 70(4):77.
- Park, S. *et al.* (2009). Nonthermal X-Rays from Supernova Remnant G330.2+1.0 and the Characteristics of its Central Compact Object. *ApJ*, 695(1):431–441.
- Park, S. *et al.* (2006). Discovery of a Candidate Central Compact Object in the Galactic Nonthermal SNR G330.2+1.0. *ApJ*, 653(1):L37–L40.
- Parsons, R. D., Hinton, J. A. (2014). A Monte Carlo template based analysis for air-Cherenkov arrays. *Astroparticle Physics*, 56:26–34.
- Patnaude, D. J., Fesen, R. A. (2009). Proper Motions and Brightness Variations of Nonthermal X-ray Filaments in the Cassiopeia A Supernova Remnant. *ApJ*, 697:535–543.
- Petruk, O., Orlando, S., Beshley, V., Bocchino, F. (2011). Radio, X-ray and γ -ray surface brightness profiles as powerful diagnostic tools for non-thermal SNR shells. *MNRAS*, 413(3):1657–1670.
- Reville, B., O’Sullivan, S., Duffy, P., Kirk, J. G. (2008). The transport of cosmic rays in self-excited magnetic turbulence. *MNRAS*, 386(1):509–515.
- Revnivtsev, M., Sazonov, S., Gilfanov, M., Churazov, E., Sunyaev, R. (2006). Origin of the Galactic ridge X-ray emission. *A&A*, 452(1):169–178.
- Reynolds, S. P. (1998). Models of Synchrotron X-Rays from Shell Supernova Remnants. *ApJ*, 493(1):375–396.
- Reynolds, S. P. (2008). Supernova remnants at high energy. *ARA&A*, 46:89–126.
- Reynolds, S. P., Keohane, J. W. (1999). Maximum Energies of Shock-accelerated Electrons in Young Shell Supernova Remnants. *ApJ*, 525:368–374.
- Reynolds, S. P., Zoglauer, A., Boggs, S. E., Harrison, F., NuSTAR Team (2015). NuSTAR Observations of Hard X-ray Continuum from SN 1987A. In *American Astronomical Society Meeting Abstracts #225*, volume 225 of *American Astronomical Society Meeting Abstracts*, page 140.22.
- Reynoso, E. M., Hughes, J. P., Moffett, D. A. (2013). On the Radio Polarization Signature of Efficient and Inefficient Particle Acceleration in Supernova Remnant SN 1006. *AJ*, 145(4):104.
- Rho, J., Dyer, K. K., Borkowski, K. J., Reynolds, S. P. (2002). X-Ray Synchrotron-emitting Fe-rich Ejecta in Supernova Remnant RCW 86. *ApJ*, 581(2):1116–1131.
- Rosado, M., Ambrocio-Cruz, P., Le Coarer, E., Marcelin, M. (1996). Kinematics of the galactic supernova remnants RCW 86, MSH 15-56 and MSH 11-61A. *A&A*, 315:243–252.
- Rothenflug, R. *et al.* (2004). Geometry of the non-thermal emission in SN 1006. Azimuthal variations of cosmic-ray acceleration. *A&A*, 425:121–131.
- Rybicki, G. B., Lightman, A. P. (1986). *Radiative Processes in Astrophysics*.

- Sano, H. *et al.* (2015). A Detailed Study of Non-thermal X-Ray Properties and Interstellar Gas toward the γ -Ray Supernova Remnant RX J1713.7-3946. *ApJ*, 799(2):175.
- Sato, T., Hughes, J. P. (2017). Direct Ejecta Velocity Measurements of Tycho's Supernova Remnant. *ApJ*, 840(2):112.
- Sato, T. *et al.* (2018). X-Ray Measurements of the Particle Acceleration Properties at Inward Shocks in Cassiopeia A. *ApJ*, 853(1):46.
- Sato, T., Koyama, K., Takahashi, T., Odaka, H., Nakashima, S. (2014). Discovery of recombining plasma in the supernova remnant 3C 391. *PASJ*, 66(6):124.
- Schekochihin, A. A., Cowley, S. C. (2007). *Turbulence and Magnetic Fields in Astrophysical Plasmas*, page 85.
- NuSTAR Science Operations Center (2016). NuSTAR Observatory Guide. https://heasarc.gsfc.nasa.gov/docs/nustar/nustar_obsguide.pdf.
- Stage, M. D., Allen, G. E., Houck, J. C., Davis, J. E. (2006). Cosmic-ray diffusion near the Bohm limit in the Cassiopeia A supernova remnant. *Nature Physics*, 2(9):614–619.
- Stephenson, F. R., Green, D. A. (2002). Historical Supernovae and their Remnants. *ApJ*, 835(1):34.
- Sun, L., Chen, Y. (2019). Spatially Resolved X-Ray Spectroscopy of Kepler's Supernova Remnant: Distinct Properties of the Circumstellar Medium and the Ejecta. *ApJ*, 872(1):45.
- Sushch, I., Brose, R., Pohl, M. (2018). Modeling of the spatially resolved nonthermal emission from the Vela Jr. supernova remnant. *A&A*, 618:A155.
- Takeda, S. *et al.* (2016). Suzaku observations of the hard X-ray spectrum of Vela Jr. (SNR RX J0852.0-4622). *PASJ*, 68:S10.
- Tanaka, T. *et al.* (2011). Gamma-Ray Observations of the Supernova Remnant RX J0852.0-4622 with the Fermi Large Area Telescope. *ApJ*, 740(2):L51.
- Tanaka, T. *et al.* (2008). Study of Nonthermal Emission from SNR RX J1713.7-3946 with Suzaku. *ApJ*, 685(2):988–1004.
- Tanaka, T. *et al.* (2018). NuSTAR Detection of Nonthermal Bremsstrahlung from the Supernova Remnant W49B. *ApJ*, 866(2):L26.
- Tang, X., Chevalier, R. A. (2017). Shock evolution in non-radiative supernova remnants. *MNRAS*, 465(4):3793–3802.
- Tang, X., Piran, T. (2019). Positron flux and γ -ray emission from Geminga pulsar and pulsar wind nebula. *MNRAS*, 484(3):3491–3501.
- The AMS Collaboration. (2015a). Precision Measurement of the Helium Flux in Primary Cosmic Rays of Rigidities 1.9 GV to 3 TV with the Alpha Magnetic Spectrometer on the International Space Station. *Phys. Rev. Lett.*, 115(21):211101.
- The AMS Collaboration. (2015b). Precision measurement of the proton flux in primary cosmic rays from rigidity 1 gv to 1.8 tv with the alpha magnetic spectrometer on the international space station. *Phys. Rev. Lett.*, 114:171103.
- The AMS Collaboration. (2014). Electron and positron fluxes in primary cosmic rays measured with the alpha magnetic spectrometer on the international space station. *Phys. Rev. Lett.*, 113:121102.

- The AMS Collaboration. (2016). Precision measurement of the boron to carbon flux ratio in cosmic rays from 1.9 gv to 2.6 tv with the alpha magnetic spectrometer on the international space station. *Phys. Rev. Lett.*, 117:231102.
- The Pierre Auger Collaboration. (2017). Observation of a large-scale anisotropy in the arrival directions of cosmic rays above 8×10^{18} ev. *Science*, 357(6357):1266–1270.
- The Telescope Array Collaboration. (2018). Evidence of Intermediate-scale Energy Spectrum Anisotropy of Cosmic Rays $E \geq 10^{19.2}$ eV with the Telescope Array Surface Detector. *ApJ*, 862(2):91.
- Truelove, J. K., McKee, C. F. (1999). Evolution of Nonradiative Supernova Remnants. *ApJS*, 120(2):299–326.
- Tsubone, Y., Sawada, M., Bamba, A., Katsuda, S., Vink, J. (2017). A Systematic Study of the Thermal and Nonthermal Emission in the Supernova Remnant RCW 86 with Suzaku. *ApJ*, 835(1):34.
- Tsuji, N., Uchiyama, Y. (2016). Expansion measurements of supernova remnant RX J1713.7-3946. *PASJ*, 68(6):108.
- Tsuji, N. *et al.* (2019). NuSTAR Observations of the Supernova Remnant RX J1713.7-3946. *ApJ*, 877(2):96.
- Uchiyama, Y., Aharonian, F. A. (2008). Fast Variability of Nonthermal X-Ray Emission in Cassiopeia A: Probing Electron Acceleration in Reverse-Shocked Ejecta. *ApJ*, 677(2):L105.
- Uchiyama, Y., Aharonian, F. A., Tanaka, T., Takahashi, T., Maeda, Y. (2007). Extremely fast acceleration of cosmic rays in a supernova remnant. *Nature*, 449(7162):576–578.
- Verzi, V., Ivanov, D., Tsunesada, Y. (2017). Measurement of Energy Spectrum of Ultra-High Energy Cosmic Rays. *arXiv e-prints*, page arXiv:1705.09111.
- Vink, J. (2008). The Kinematics of Kepler’s Supernova Remnant as Revealed by Chandra. *ApJ*, 689(1):231–241.
- Vink, J. *et al.* (2006). The X-Ray Synchrotron Emission of RCW 86 and the Implications for Its Age. *ApJ*, 648(1):L33–L37.
- Wang, Z. R., Qu, Q. Y., Chen, Y. (1997). Is RX J1713.7-3946 the remnant of the AD393 guest star? *A&A*, 318:L59–L61.
- Weekes, T. C. *et al.* (1989). Observation of TeV Gamma Rays from the Crab Nebula Using the Atmospheric Cerenkov Imaging Technique. *ApJ*, 342:379.
- Weisskopf, M. C. *et al.* (2002). An Overview of the Performance and Scientific Results from the Chandra X-Ray Observatory. *PASP*, 114(791):1–24.
- Wik, D. R. *et al.* (2014). NuSTAR Observations of the Bullet Cluster: Constraints on Inverse Compton Emission. *ApJ*, 792:48.
- Williams, B. J. *et al.* (2013). Azimuthal Density Variations around the Rim of Tycho’s Supernova Remnant. *ApJ*, 770:129.
- Williams, B. J., Hewitt, J. W., Petre, R., Temim, T. (2018). A Deep X-Ray View of the Synchrotron-dominated Supernova Remnant G330.2+1.0. *ApJ*, 855(2):118.
- Winkler, P. F. *et al.* (2014). A High-resolution X-Ray and Optical Study of SN 1006: Asymmetric Expansion and Small-scale Structure in a Type Ia Supernova Remnant. *ApJ*, 781(2):65.
- Xing, Y., Wang, Z., Zhang, X., Chen, Y. (2019). Fermi LAT detection of the supernova remnant SN 1006 revisited: The southwest limb. *PASJ*, page 69.

- Chandra* X-ray Center (2018). The Chandra Proposers' Observatory Guide. <http://cxc.cfa.harvard.edu/proposer/POG/html/index.html>.
- Yamaguchi, H. *et al.* (2016). The Refined Shock Velocity of the X-Ray Filaments in the RCW 86 Northeast Rim. *ApJ*, 820(1):L3.
- Yamaguchi, H. *et al.* (2008). Suzaku Observation of the RCW86 Northeastern Shell. *PASJ*, 60:S123.
- Yuasa, T., Makishima, K., Nakazawa, K. (2012). Broadband Spectral Analysis of the Galactic Ridge X-Ray Emission. *ApJ*, 753(2):129.
- Yüksel, H., Kistler, M. D., Stanev, T. (2009). TeV Gamma Rays from Geminga and the Origin of the GeV Positron Excess. *Phys. Rev. Lett.*, 103(5):051101.
- Zabalza, V. (2015). Naima: a Python package for inference of particle distribution properties from nonthermal spectra. In *34th International Cosmic Ray Conference (ICRC2015)*, volume 34 of *International Cosmic Ray Conference*, page 922.
- Zirakashvili, V. N., Aharonian, F. (2007). Analytical solutions for energy spectra of electrons accelerated by nonrelativistic shock-waves in shell type supernova remnants. *A&A*, 465:695–702.
- Zirakashvili, V. N., Aharonian, F. A. (2010). Nonthermal Radiation of Young Supernova Remnants: The Case of RX J1713.7-3946. *ApJ*, 708(2):965–980.
- Zirakashvili, V. N., Ptuskin, V. S. (2008). Diffusive Shock Acceleration with Magnetic Amplification by Nonresonant Streaming Instability in Supernova Remnants. *ApJ*, 678(2):939–949.
- Zoglauer, A. *et al.* (2015). The Hard X-Ray View of the Young Supernova Remnant G1.9+0.3. *ApJ*, 798(2):98.

Acknowledgement

First of all, I would like to thank Professor Uchiyama for his expert advice and encouragement throughout the past six years of my research in bachelor's degree, master's degree, and doctoral course. I would like to express my gratitude to Dr. Khangulyan for his constructive comments and helpful discussion. My heartfelt appreciation goes to Professor Aharonian and Professor Safi-Harb for their extraordinary supports in this thesis process, including hosting me at Max-Planck-Institut für Kernphysik in 2018 and at University of Manitoba in 2019.

I am deeply grateful to the advisory committee (Professor Kitamoto, Professor Nakayama, and Professor Uchiyama) for their valuable comments and advice about this thesis, and to the other professors of Physics department in Rikkyo University, especially the professors in Astro and Solar-Terrestrial Physics Laboratories for their fruitful comments and discussion in the weekly seminar. I would like to thank Dr. Ichinohe and Dr. Hayashida for giving me helpful and professional advice in our group meeting. I also want to show my special thanks to H. Iwasaki, M. Arakawa, R. Higurashi, the other members of our laboratory group, and H. Yoneda from University of Tokyo. You greatly supported me, helped me, and made my research life full of joy.

I would like to express my gratitude to Dr. Shimoda and the SNR community in Japan. Without their invaluable help this thesis would not have been materialized. I truly appreciate technical advice from Dr. Krivonos, Dr. Mori, and Dr. Wik about the detailed analysis of *NuSTAR* observations.

I would like to offer my special thanks to my friends, who have been with me and given me warm encouragement. Finally I would like to show my greatest appreciation to my family for being tolerant and supportive.

This thesis made use of data obtained from the Chandra Data Archive and the Chandra Source Catalog, and software provided by the Chandra X-ray Center (CXC) in the application package CIAO. This thesis also has made use of data from the NuSTAR mission, a project led by the California Institute of Technology, managed by the Jet Propulsion Laboratory, and funded by the National Aeronautics and Space Administration. I appreciate the NuSTAR Operations, Software, and Calibration teams for support with the execution and analysis of these observations. I have received support by the Japan Society for the Promotion of Science (JSPS) KAKENHI grant No. JP17J06025.